



Generalized Reliability Methodology Applied to Brittle Anisotropic Single Crystals

Jonathan A. Salem
Glenn Research Center, Cleveland, Ohio

The NASA STI Program Office . . . in Profile

Since its founding, NASA has been dedicated to the advancement of aeronautics and space science. The NASA Scientific and Technical Information (STI) Program Office plays a key part in helping NASA maintain this important role.

The NASA STI Program Office is operated by Langley Research Center, the Lead Center for NASA's scientific and technical information. The NASA STI Program Office provides access to the NASA STI Database, the largest collection of aeronautical and space science STI in the world. The Program Office is also NASA's institutional mechanism for disseminating the results of its research and development activities. These results are published by NASA in the NASA STI Report Series, which includes the following report types:

- **TECHNICAL PUBLICATION.** Reports of completed research or a major significant phase of research that present the results of NASA programs and include extensive data or theoretical analysis. Includes compilations of significant scientific and technical data and information deemed to be of continuing reference value. NASA's counterpart of peer-reviewed formal professional papers but has less stringent limitations on manuscript length and extent of graphic presentations.
- **TECHNICAL MEMORANDUM.** Scientific and technical findings that are preliminary or of specialized interest, e.g., quick release reports, working papers, and bibliographies that contain minimal annotation. Does not contain extensive analysis.
- **CONTRACTOR REPORT.** Scientific and technical findings by NASA-sponsored contractors and grantees.

- **CONFERENCE PUBLICATION.** Collected papers from scientific and technical conferences, symposia, seminars, or other meetings sponsored or cosponsored by NASA.
- **SPECIAL PUBLICATION.** Scientific, technical, or historical information from NASA programs, projects, and missions, often concerned with subjects having substantial public interest.
- **TECHNICAL TRANSLATION.** English-language translations of foreign scientific and technical material pertinent to NASA's mission.

Specialized services that complement the STI Program Office's diverse offerings include creating custom thesauri, building customized data bases, organizing and publishing research results . . . even providing videos.

For more information about the NASA STI Program Office, see the following:

- Access the NASA STI Program Home Page at <http://www.sti.nasa.gov>
- E-mail your question via the Internet to help@sti.nasa.gov
- Fax your question to the NASA Access Help Desk at 301-621-0134
- Telephone the NASA Access Help Desk at 301-621-0390
- Write to:
NASA Access Help Desk
NASA Center for Aerospace Information
7121 Standard Drive
Hanover, MD 21076



Generalized Reliability Methodology Applied to Brittle Anisotropic Single Crystals

Jonathan A. Salem
Glenn Research Center, Cleveland, Ohio

National Aeronautics and
Space Administration

Glenn Research Center

Acknowledgments

First, the author would like to express his appreciation for the patience displayed by everyone involved in this project. In particular this applies to my advisor Professor Jenkins. Regarding the research aspects of this dissertation, I would like to especially thank Ron Noebe for his interest in the work. The mound of references he collected on NiAl was quite helpful. A special thanks is also extended to Jane Manderscheid, whose knowledge of elasticity was invaluable in working with the stress solutions. Additionally, a special thanks is extended to Ram Darolia of General Electric Aircraft Engines, Evendale, Ohio, who made and supplied the NiAl single crystal material for the study. Finally, special thanks are extended to the members of my advisory committee: Professors Albert Kobayashi, Mamidala Ramulu and Per Reinhall. Of course, many others provided support and deserve recognition. These include Kurt Munson, Matt Kokaly, and many others. The National Aeronautics Administration, Glenn Research Center, Cleveland, Ohio provided financial support for this work.

Available from

NASA Center for Aerospace Information
7121 Standard Drive
Hanover, MD 21076

National Technical Information Service
5285 Port Royal Road
Springfield, VA 22100

Available electronically at <http://gltrs.grc.nasa.gov/GLTRS>

TABLE OF CONTENTS

LIST OF FIGURES	v
LIST OF TABLES	xii
NOMENCLATURE	xiv
ABBREVIATIONS	xxi
ACKNOWLEDGEMENTS	xxii
 CHAPTER 1: INTRODUCTION.....	 1
1.1 BACKGROUND ON NICKEL ALUMINIDES	1
1.2 PROBLEM STATEMENT	6
1.3 OBJECTIVES.....	6
 CHAPTER 2: REVIEW OF PREVIOUS WORK.....	 7
2.1 FRACTURE OF BRITTLE, SINGLE CRYSTALS	7
2.2 CLEAVAGE OF NiAl SINGLE CRYSTALS.....	9
2.3 ANISOTROPIC FRACTURE MECHANICS	12
2.4 MECHANICAL TESTING OF BRITTLE, ANISOTROPIC MATERIALS.....	15
2.4.1 Elastic Properties.....	15
2.4.2 Uniaxial Flexure Testing	16
2.4.3 Biaxial Flexure Testing	19
2.4.4 Uniaxial Tensile Testing	25
2.4.5 Torsional Testing	26
2.5 DETERMINISTIC DESIGN CRITERIA FOR BRITTLE MATERIALS	30
2.5.1 Stress-Based Criteria	30
2.5.1.1 Maximum Principal Stress	30
2.5.1.2 The Modified Mohr Theory and the Tsai-Wu Theory	31
2.5.1.3 Principle of Independent Action	31
2.5.2 Fracture Mechanics Criteria	32
2.5.2.1 Mode I Failure (MP)	36
2.5.2.2 The Maximum Hoop Stress Factor (MHSF)	36
2.5.2.3 The Coplanar Energy Release Rate (CERR).....	36
2.5.2.4 The Maximum Noncoplanar Energy Release Rate (NERR)	36
2.5.2.5 Criteria for Porous Media	37

2.6 PROBABILISTIC DESIGN CRITERIA FOR BRITTLE MATERIALS	38
2.6.1 <i>The Weibull Model</i>	38
2.6.2 <i>The Batdorf Model</i>	40
2.6.3 <i>Criteria for Anisotropic Materials</i>	42
CHAPTER 3: THEORY: ANISOTROPIC RELIABILITY MODEL	47
3.1 MODELS BASED ON THE PRINCIPLE OF INDEPENDENT ACTION.....	47
3.2 A GENERALIZED WEIBULL RELIABILITY MODEL FOR BRITTLE MATERIALS WITH STRENGTH AND ELASTIC ANISOTROPY	50
3.3 A FAILURE CRITERION FOR ELASTICALLY ANISOTROPIC MATERIALS	54
3.4 RELIABILITY PREDICTION FORMULATIONS.....	55
3.4.1 <i>Isotropic Material</i>	55
3.4.2 <i>Anisotropic Material</i>	58
CHAPTER 4: EXPERIMENTAL PROCEDURES: MATERIAL PROPERTIES AND VERIFICATION TESTING	62
4.1 TEST SPECIMEN PREPARATION	62
4.1.1 <i>Isotropic Materials</i>	62
4.1.2 <i>Anisotropic Materials</i>	62
4.2 MEASUREMENT OF ELASTIC PROPERTIES.....	63
4.3 UNIAXIAL STRENGTH TESTING	63
4.4 BIAXIAL TEST RIG DESIGN AND ANALYSIS.....	65
4.4.1 <i>Stress State in a Pressurized Plate: Okubu's Approximate Solution</i>	67
4.4.2 <i>Okubu's Exact Solution</i>	69
4.4.3 <i>Generalization of Okubu's Solution to Variable Radius</i>	72
4.5 BIAXIAL TEST RIG VERIFICATION.....	79
4.5.1 <i>The Isotropic Case</i>	79
4.5.2 <i>The Anisotropic Case</i>	85
4.6 BIAXIAL STRENGTH TESTING.....	89
4.6.1 <i>Isotropic Material</i>	89
4.6.2 <i>Anisotropic Material</i>	90
CHAPTER 5: EXPERIMENTAL RESULTS: MATERIAL PROPERTIES AND VERIFICATION TESTING	91
5.1 ELASTIC PROPERTIES.....	91
5.2 UNIAXIAL STRENGTH.....	91

5.2.1 <i>Isotropic Material</i>	91
5.2.2 <i>Anisotropic Material</i>	92
5.3 FRACTOGRAPHY OF THE FLEXURE SPECIMENS	92
5.4 BIAXIAL STRENGTH.....	104
5.4.1 <i>Isotropic Material</i>	104
5.4.2 <i>Anisotropic Material</i>	106
5.4.3 <i>Macroscopic Failure Analysis of the Disk Test Specimens</i>	107
5.4.4 <i>Fractography of the Disk Test Specimens</i>	113
CHAPTER 6: VERIFICATION OF THE ANISOTROPIC RELIABILITY MODEL.....	122
6.1 RELIABILITY-BASED STRENGTH PREDICTIONS FOR ISOTROPIC MATERIALS.....	122
6.2 RELIABILITY-BASED STRENGTH PREDICTIONS FOR ANISOTROPIC MATERIALS: UNIAXIAL STRESS STATES.....	124
6.3 ESTIMATION OF THE SCALE PARAMETER.....	126
6.4 RELIABILITY PREDICTION FOR ANISOTROPIC MATERIALS: MULTIAXIAL STRESS STATES	128
6.4.1 <i>Assumption of Complete Isotropy</i>	128
6.4.2 <i>Assumption of Strength Isotropy</i>	128
6.4.3 <i>Assumption of Complete Anisotropy</i>	129
6.4.4 <i>Flaw Distribution Anisotropy</i>	130
CHAPTER 7: DISCUSSION OF THE RESULTS	134
7.1 DISCUSSION OF THE EXPERIMENTAL RESULTS	134
7.1.1 <i>Strength and Weibull Modulus</i>	134
7.1.2 <i>Correlation of Billet Chemistry to Flexural Strength</i>	137
7.1.3 <i>Test Specimen Preparation</i>	140
7.2 DISCUSSION OF THE PREDICTIONS	140
7.3 RESIDUAL STRESSES	145
CHAPTER 8: SUMMARY	148
CHAPTER 9: CONCLUSIONS	150
CHAPTER 10: RECOMMENDATIONS AND FUTURE WORK	152
REFERENCES	153

APPENDIX A: BIAXIAL TEST APPARATUS	164
A.1 DESCRIPTION OF THE TEST APPARATUS.....	164
A.2 SEAL ANALYSIS	172
APPENDIX B: CODE FOR CALCULATION OF STRESSES AND STRAINS IN ANISOTROPIC CIRCULAR PLATES SUBJECTED TO UNIFORM PRESSURE	174
APPENDIX C: UNIAXIAL TEST SPECIMEN DATA.....	178
APPENDIX D: BIAXIAL TEST SPECIMEN DATA.....	182
APPENDIX E: CODE FOR ESTIMATION OF THE SCALE PARAMETER OF ANISOTROPIC MATERIALS.....	184
APPENDIX F: CODE FOR ESTIMATION OF THE CHARACTERISTIC STRENGTH OF ISOTROPIC DISK TEST SPECIMENS	185
APPENDIX G: CODE FOR ESTIMATION OF THE CHARACTERISTIC STRENGTH OF ELASTICALLY ANISOTROPIC DISK TEST SPECIMENS.....	189
APPENDIX H: CODE FOR ESTIMATION OF THE CHARACTERISTIC STRENGTH OF ANISOTROPIC DISK TEST SPECIMENS	193

LIST OF FIGURES

<i>Number</i>	<i>Page</i>
Figure 1.1.1: Temperature capabilities of superalloys: temperature for 100-hour life at 140 MPa stress (Molloy 1990).	3
Figure 1.1.2: Temperature capabilities of superalloys and ceramics: blade surface temperature (courtesy H.R. Gray, NASA GRC)	4
Figure 2.2.1: The {110} dodecahedral family of surfaces	11
Figure 2.4.1: The elastic modulus $E_{\langle hkl \rangle}$ of binary NiAl as a function of orientation in (a) the {100}, and (b) the {110}. The single crystal elastic constants of Wasilewski (Wasilewski 1966) were used in the calculations	17
Figure 2.4.2: Typical fracture pattern resulting from flexural failure of a brittle material (Military Handbook 790 1992)	18
Figure 2.4.3: Schematic of the testing configurations used to generate biaxial tensile stresses in plate specimens: (a) ball-on-ring, (b) ring-on-ring, (c) pressure-on-ring and (d) top view of the pressure-on-ring configuration.	20
Figure 2.4.4.1: Tensile specimens used to test brittle materials (ASTM C1273-95a 1999). All dimensions in mm	27
Figure 2.4.4.2: Miniature test tensile specimen. All dimensions in mm	28
Figure 2.5.2.1: Basic modes of loading and displacing a crack surface	33
Figure 2.5.2.2: Normal and shear stresses resolved on a crack plane rotated at an angle to the principal stresses: (a) surface crack and (b) embedded crack	35
Figure 4.1.2.1: EDM damage along the surface of a flexural test specimen: (a) overall view and (b) detail. EDM damage was not removed prior to chemical milling	64

Figure 4.4.1: Schematic of the biaxial test fixture.....	66
Figure 4.4.1.1: Stresses in a {100} plate of unit radius and thickness subjected to a unit uniform pressure as calculated with Okubu's (Okubu 1949) approximate solution....	70
Figure 4.4.2.1: Stresses in a {100} plate of unit radius and thickness subjected to a unit uniform pressure as calculated with Okubu's (Okubu 1949) series solution	73
Figure 4.4.2.2: Comparison of stresses in a {100} plate of unit radius and thickness subjected to a unit uniform pressure as calculated with isotropic and anisotropic solutions (a) <100> direction and (b) <110> direction.....	74
Figure 4.5.1.1: 4340 steel plate with strain gage rosettes attached	81
Figure 4.5.1.2: Measured and theoretical stresses for a 4340 steel disk as a function of normalized radial position. Error bars indicate the 95% confidence intervals.	83
Figure 4.5.2.1: Measured and theoretical stresses for a {001} NiAl disk test specimen as a function of normalized radial position. The support ring was lubricated with anti-seizing compound. Error bars indicate the 95% confidence bands: (a) <100> direction and (b) <110> direction.	87
Figure 4.5.2.2: Measured strain at failure normalized to theoretical strain as calculated from Okubu's (Okubu 1949) approximate and exact solutions	88
Figure 5.2.2.1: Average <100> four-point flexural strengths and 90% confidence bands on AFN12 single crystal for NiAl billets.....	94
Figure 5.2.2.2: Average <110> four-point flexural strengths and 90% confidence bands on AFN12 single crystal for NiAl billets.....	95
Figure 5.2.2.3 Weibull distributions for the <100> and <110> orientations of AFN12 single crystal NiAl tested in three and four-point flexure	96

Figure 5.2.2.4 Mean strength as a function of orientation on the {100} for AFN12 single crystal NiAl tested in four-point flexure	97
Figure 5.2.2.5 Characteristic strength as a function of orientation on the {100} for AFN12 single crystal NiAl tested in four-point flexure	98
Figure 5.3.1: Failure origins in AFN12 NiAl single crystal flexure specimens: (a) Hf rich inclusion in a <100> test specimen and (b) EDM damage in a <110> test specimen.....	100
Figure 5.3.2: Typical bifurcation pattern observed on the surface of <110> flexure specimens: (a) overall flexure test specimen and (b) detail of a fracture location	101
Figure 5.3.3: Side view of a segment of a fractured AFN12 <110> four-point flexure specimen ..	102
Figure 5.3.4: Summary of cleavage planes in various <110> four-point flexure test specimens. Numbers are crystal <hkl> directions associated with fracture facets	103
Figure 5.3.5: Bifurcation angle plotted as a function of fracture stress in <110> four-point flexure test specimens	105
Figure 5.4.2.1: Weibull distributions for the flexural strength of AFN12 single crystal NiAl. Included in the plot are the data for the <100> and <110> tested in three and four-point flexure (beams) and the {100} tested in biaxial flexure (disks) by application of a uniform pressure	108
Figure 5.4.3.1: NiAl single crystal disk test specimens failed by application of a uniform pressure: (a) specimen B11 and (b) specimen B5	109
Figure 5.4.3.2: Standard (001) pole figure showing the macroscopic failure directions exhibited by AFN12 single crystal NiAl biaxial test specimen. Arrows on the perimeter indicate the measured mean directions and standard deviations of the cleavage directions observed on the (001).	110
Figure 5.4.3.3: Macroscopic failure locations and planes exhibited by AFN12 single crystal biaxial test specimens.....	112

Figure 5.4.4.1: Failure origin in an AFN12 single crystal NiAl biaxial test specimen	114
Figure 5.4.4.2: Energy dispersive analysis of a failure origin in an AFN12 single crystal NiAl biaxial test specimen. Hafnium, titanium and carbon are indicated implying (HfTi)C	115
Figure 5.4.4.3: Detail of a failure origin in an AFN12 single crystal NiAl biaxial test specimen. A mixture of secondary and back-scattered electrons were used for imaging	116
Figure 5.4.4.4: Mating fracture surfaces of an AFN12 single crystal NiAl biaxial test specimen. Fractured inclusion can be observed on both halves, implying inclusion fracture instead of pullout	117
Figure 5.4.4.5: (a) Tensile surface of an AFN12 single crystal NiAl biaxial test specimen and (b) and corresponding fracture surface. Jog angle relative to the macroscopic failure plane and <100> etch lines that resulted from chemical milling are shown...	118
Figure 5.4.4.6: Failure locations in AFN12 single crystal NiAl biaxial test specimens. Symmetry was invoked and the positions plotted in a single quadrant. The lines within the circles represent the local direction of failure (i.e. the jog direction) extending from the HfC origin	120
Figure 5.4.4.7: Generalized schematic failure pattern in AFN12 single crystal biaxial test specimens. Angles between the directions illustrated are based on average measurements on the {100}.....	121
Figure 6.1.2: Measured and predicted characteristic strength for tungsten carbide. The stress intensity factor coefficients of (a) a Griffith crack, (b) of Thiemeier et al. (Thiemeier 1991) and (c) Smith et al. (Smith 1967) and Smith and Sorensen (Smith and Sorensen 1994) were used. The maximum principal stress (MP), principal of independent action (PIA), normal stress (NS), coplanar energy release rate (CERR), non-coplanar energy release rate (NERR), maximum hoop stress factor (MHSF), Batdorf's for a Griffith crack (BGC) and Batdorf's for a Griffith notch (BCN) were considered.	123

Figure 6.4.1.1: Measured and predicted characteristic strength for AFN12 single crystal NiAl. Elastic and strength isotropy were assumed. The stress intensity factor coefficients of (a) a Griffith crack, (b) of Thiemeier et al. (Thiemeier 1991) and (c) Smith et al. (Smith 1967) and Smith and Sorensen (Smith and Sorensen 1994) were used. The maximum principal stress (MP), principal of independent action (PIA), normal stress (NS), coplanar energy release rate (CERR), non-coplanar energy release rate (NERR) and maximum hoop stress factor (MHSF) were considered..... 130

Figure 6.4.2.1: Measured and predicted characteristic strength for AFN12 single crystal NiAl. Strength isotropy with anisotropic elasticity was assumed. The stress intensity factor coefficients of (a) a Griffith crack, (b) Thiemeier et al. (Thiemeier 1991) and (c) Smith et al. (Smith 1967) and Smith and Sorensen (Smith and Sorensen 1994) were used. The maximum principal stress (MP), principal of independent action (PIA), normal stress (NS), coplanar energy release rate (CERR), non-coplanar energy release rate (NERR), maximum hoop stress factor (MHSF), Batdorf's for a Griffith crack (BGC) and Batdorf's for a Griffith notch (BCN) were considered..... 131

Figure 6.4.3.1: Measured and predicted characteristic strength for single crystal AFN12 NiAl. Elastic and strength anisotropy were applied. The maximum principal stress (MP), principal of independent action (PIA) and normal stress (NS) were analyzed using Equation (98) for the functional form of the scale parameter 132

Figure 6.4.3.2: Measured and predicted characteristic strength for AFN12 single crystal NiAl. Elastic and strength anisotropy were applied. The stress intensity factor coefficients of (a) a Griffith crack, (b) Thiemeier et al. (Thiemeier 1991) and (c) Smith et al. (Smith 1967) and Smith and Sorensen (Smith and Sorensen 1994) were used. The maximum principal stress (MP), principal of independent action (PIA), normal stress (NS), coplanar energy release rate (CERR), non-coplanar energy release rate (NERR), maximum hoop stress factor (MHSF), Batdorf's for a Griffith crack (BGC) and Batdorf's for a Griffith notch (BCN) were considered. Equations (144) and (145) were used for the functional form of the scale parameter..... 133

Figure 7.1.1.1: Coefficient of variation of the fracture toughness of various commercially available ceramics. No correlation between fracture toughness and the coefficient of variation is apparent	136
Figure 7.1.2.1: Mean carbon content (weight %) and 90% confidence interval for the <100> billets	138
Figure 7.1.2.2: Mean strength and 90% confidence interval as a function of <100> billet carbon content (weight %)	139
Figure 7.2.1: Measured and predicted characteristic strength for single crystal AFN12 NiAl. Elastic and strength anisotropy were applied. The three strongest <100> billets were not used in the predictions. The maximum principal stress (MP), principle of independent action (PIA) and normal stress (NS) were considered.....	141
Figure 7.2.2: Effect of flaw type on the loading mode resulting from application of a uniaxial stress state: (a) randomly oriented planar crack and (b) three-dimensional inclusion	143
Figure 7.2.3: Illustration of an inclusion shielding a crack from an applied, remote shear stress	144
Figure A.A.1: Assembly drawing for a biaxial test apparatus capable of applying a uniform pressure to a disk test specimen	165
Figure A.A.2 Section view assembly drawing for a biaxial test apparatus capable of applying a uniform pressure to a disk test specimen	166
Figure A.A.3: Test chamber for a biaxial test apparatus capable of applying a uniform pressure to a 25.4 mm disk test specimen. Units are in inches for ease of machining and minimization of cost.....	167
Figure A.A.4: Test chamber cap for a biaxial test apparatus capable of applying a uniform pressure to a 25.4 mm disk test specimen. Units are in inches for ease of machining and minimization of cost.....	168

Figure A.A.5: Test chamber reaction ring for a biaxial test apparatus capable of applying a uniform pressure to a 25.4 mm disk test specimen. Units are in inches for ease of machining and minimization of cost	169
Figure A.A.6: Test chamber centering ring for a biaxial test apparatus capable of applying a uniform pressure to a 25.4 mm disk test specimen. Units are in inches for ease of machining and minimization of cost	170
Figure A.A.7: 25.4 mm disk test specimen. Units are in inches for ease of machining and minimization of cost	171
Figure A.A.8: Cross-sectional view of the test specimen, reaction ring, O-ring and groove	173

LIST OF TABLES

<i>Number</i>	<i>Page</i>
Table 1.1.1: Physical properties of NiAl, NiAl alloys and an advanced superalloy (Walston and Darolia 1993).	5
Table 2.4.3.1: Effect of friction on the effective area, A_e , of a 25 mm diameter disk loaded between 10 and 20 mm diameter concentric rings. Poisson's ratio = 0.23. Values were calculated by numerical integration of the PIA model (Barnett et al. 1967).	24
Table 4.4.3.1: Displacement solution constants ($\times 10^{-6}$) for NiAl and graphite/epoxy plates of unit thickness and radius subjected to a unit lateral pressure	79
Table 4.5.1.1: Measured stresses, standard deviations and theoretical stresses for a 25 mm circular, 4340 steel plate subjected to 6.90 MPa uniform pressure	84
Table 4.5.2.1: Measured stresses, standard deviations and theoretical stresses for a 25 mm diameter, {100} NiAl single crystal plate supported on a lubricated steel ring and subjected to a 4.8 MPa uniform pressure	86
Table 4.6.1.1: Test specimen dimensions for the isotropic case	89
Table 4.6.2.1: Test specimen dimensions for AFN12 single crystal NiAl specimens tested in biaxial flexure	90
Table 5.2.1.1: Measured flexural strength statistics and 90% confidence intervals for WC.....	91
Table 5.2.2.1: Flexural strength of AFN12 single crystal NiAl - normal statistics	93
Table 5.2.2.2: Flexural strength of AFN12 single crystal NiAl - Weibull statistics	93

Table 5.4.1.1: Measured strength statistics and 90% confidence intervals for WC	106
Table 5.4.2.1: Measured strength statistics and 90% confidence intervals for AFN12 single crystal NiAl tested in biaxial flexure.....	106
Table 5.4.3.1: Macroscopic cleavage directions and 90% confidence interval in the (001) plane of single crystal NiAl tested in biaxial flexure. Measurements are relative to the $[\bar{1}00]$ direction. Also the listed are the angles from $[\bar{1}00]$ to the $\langle 310 \rangle$	111
Table 5.4.4.1: Orientation of failure relative to the crystal structure and stress state.....	113
Table 6.2.3: Measured and predicted strength for AFN12 single crystal NiAl tested in uniaxial flexure.....	125
Table 6.3.1: Scale parameters estimated from Eqs. (98), (100) and (101) for various failure criteria.....	126
Table 6.3.2: Scale parameters estimated from Eqs. (144) and (145) for various failure criteria.....	127
Table 7.1.2.1: Billet chemistry (weight %) and $\langle 100 \rangle$ four-point flexural strength with 90% confidence intervals	137
Table 7.3.1: Mechanical Properties of HfC (MCIC 1979)	146
Table 7.3.2: Estimated residual stresses at the interface of an HfC inclusion in an NiAl matrix. The stresses were calculated using the data in Table 7.3.1 and Table 1.1.1, and the equations of Selsing (Selsing 1961).....	147

NOMENCLATURE

a	crack length
a_c	critical crack length
A	area
A_e	effective surface area based on the PIA model
A_n	series constant in the anisotropic, plate displacement solution
A_T	total surface area
AF	anisotropy factor
b	width of a plate
b_{ij}	reduced elastic stiffness
B	width of a uniaxial flexure (beam) specimen
B_n	series constant in the anisotropic, plate displacement solution
c	free surface half-length of an elliptical crack
C	contour for unit circle integration
C_i	constants in the anisotropic displacement stress solution
C_{ij}	elastic stiffness
CV_i	coefficient of variation of the i^{th} variable
d	gage section diameter
D	half-width of a composite tensile specimen
D_{ij}	flexural rigidities
D^*	effective flexural rigidity of an anisotropic plate

D^{*cubic}	effective flexural rigidity of a cubic plate
e	eccentricity of two cylinders
E	Young's modulus
$f(\theta)$	failure criterion written in terms of a unit, uniaxial principal stress
f_a	probability density function
f_i	arbitrary function used in the displacement solution of an anisotropic plate
F	applied force
FC	failure criterion
FC_c	critical value of a failure criterion for a materials resistance to unstable crack propagation
G	shear modulus
G_I	mode I strain energy release rate
G_{Ic}	critical, mode I strain energy release rate
h	the ratio of the major to minor axes of an elliptical cavity
$H(\sigma)$	step function to account for compressive stresses
I_i	scale parameter invariant
k_i	reduced flexural rigidity
k_t	transverse sensitivity of a strain gage
k_{wps}	polyaxial crack density coefficient
\bar{k}_{wps}	average polyaxial crack density coefficient
k_{ws}	uniaxial crack density coefficient
\bar{k}_{ws}	average uniaxial crack density coefficient
k^*	effective, reduced flexural rigidity of an anisotropic plate

k^{*cubic}	effective, reduced flexural rigidity of a cubic plate
K_I	mode <i>I</i> stress intensity factor
K_I	mode <i>I</i> fracture toughness
K_{II}	mode <i>II</i> stress intensity factor
K_{III}	mode <i>III</i> stress intensity factor
l	length of the edge of a square plate (e.g. a biaxial test specimen)
m	Weibull modulus
M_o	applied moment
N	crack density for a volume element
N_t	safety factor for the tensile conditions considered
N_c	safety factor for the compressive conditions considered
\overline{N}_n^m	ratio of normal stress to strength averaged about the unit circle
p_{a_c}	probability of a single crack being critical
$p_{A\theta}$	probability of a single crack being in a location and having a particular orientation
P_e	probability of a crack existing
P_{FA}	probability of failure for surface flaws
P_{FV}	probability of failure for volume flaws
P_{Fx}	probability of failure for flaw population <i>x</i>
q	pressure
r	radial position in a biaxial disk test specimen
r_p	radius of an anisotropic biaxial disk test specimen
R	correlation coefficient for linear regression

R_c	cross sectional radius of load ring used in ring-on-ring biaxial testing
R_d	radius of an isotropic plate (e.g. an isotropic biaxial disk test specimen)
R_i	radius of inner (load) ring of ring-on-ring biaxial test fixture
R_n	reliability of a component with n cracks
R_o	radius of outer (support) ring
R_s	radius of support ring in pressure-on-ring test fixture
S	surface for unit sphere volume integration
S_i	inner span of a four-point flexure test
S_o	outer span of flexure test
S_{ij}	elastic compliance
S_{ucs}	ultimate strength in compression
S_{uts}	ultimate strength in tension
S_{UTS}^{Flex}	ultimate strength in uniaxial flexural
S_{UTS}^{POR}	ultimate biaxial strength of an isotropic material as determined by pressure-on-ring loading
$S_{UTS, cubic}^{POR}$	ultimate biaxial strength of an anisotropic material with cubic symmetry as determined by pressure-on-ring loading
SD_{xi}	standard deviation of the x_i variable
t	biaxial disk test specimen thickness
T	torque
V	volume
V_T	total volume

w	plate deflection in the z direction
w_o	particular solution for the displacement of an anisotropic plate
W	height of a uniaxial flexure (beam) specimen
x	abscissa as measured from the center of a plate or rod
\bar{x}	location on surface
y	ordinate as measured from the center of a plate or rod
z	distance from mid-surface of the plate ranging over $\pm t/2$
Y_I	mode I stress intensity factor coefficient
Y_{II}	mode II stress intensity factor coefficient
χ	ratio of tensile Weibull modulus to compressive Weibull modulus
ϵ_p	measured major principal strain component
ϵ_q	measured minor principal strain component
$\hat{\epsilon}_q$	measured minor principal strain uncorrected for transverse sensitivity
$\hat{\epsilon}_p$	measured major principal strain uncorrected for transverse sensitivity
ϵ_x	strain in the x direction
ϵ_y	strain in the y direction
$\hat{\epsilon}_i$	measured strain uncorrected for transverse sensitivity; $i = 1,2,3$
ϕ	angle from the xy plane
φ	counter clockwise angle from the x axis
Φ	phase angle between the $\langle 100 \rangle$ crystal direction and the principal stress
γ_{xy}	shear strain in the xy plane

γ_f	the fracture surface energy
$\Gamma(l/m)$	the gamma function of l/m
η	ratio of tensile strength to compressive strength
φ	counterclockwise angle from the x axis
μ	coefficient of friction
μ_i	complex root
ν	Poisson's ratio
ν_o	Poisson's ratio of strain gage manufacturer's calibration material
θ	angle from the first principal stress
Θ	angle from the <100>direction
σ_b	stress due to bending
σ_{cr}	critical stresses for flaw failure
σ_{eq}	equivalent stress
σ_{emax}	maximum effective stress (Batdorf model)
$\overline{\sigma}_{fv}^{(i)}$	average unit volume strength in the direction of the i principal stress
σ_i	i^{th} principal stress ($i = 1, 2, \text{ or } 3$)
σ_{ij}	Cartesian stress component
σ_{Ieq}	mode I equivalent stress
σ_{MAX}	maximum stress
σ_m	minimum strength in the Weibull distribution
σ_n	normal stress on the crack plane

$\sigma_{n<hkl>}$	the normal stress in the $<hkl>$ direction
σ_o	scale parameter or unit strength
$\sigma_{o<hkl>}$	scale parameter in the $<hkl>$ crystal direction.
σ_p	measured major principal stress
σ_q	measured minor principal stress
σ_t	tensile stress
σ_θ	characteristic strength (i.e. strength for a 62 % probability of failure in the Weibull distribution)
σ_{rr}	radial stress
$\sigma_{\theta\theta}$	tangential stress
$\sigma_{r\theta}$	shear stress
σ_s	correction term for the effect of lateral stresses on plate deflection
σ_x	stress in the x direction
σ_y	stress in the y direction
σ^*	critical tensile stress at the surface of an elliptical flaw
τ	shear stress resolved on the crack plane
τ_{xy}	shear stress in the xy plane
ξ	twist per unit length
Ω	solid angle
Ψ	scalar reliability function for whisker reinforced ceramics

ABBREVIATIONS

BGC Batdorf's criterion for a Griffith crack

BGN Batdorf's criterion a Griffith notch

CERR coplanar energy release rate

EDM electro-discharge machining

MHSF maximum hoop stress factor

MP maximum principal stress

NERR non-coplanar energy release rate

NS normal stress

PIA principle of independent action

P-O-R pressure-on-ring

SIFC stress intensity factor coefficient

R-O-R ring-on-ring

CHAPTER 1: INTRODUCTION

1.1 BACKGROUND ON NICKEL ALUMINIDES

The efficiency and lifetime of a turbine engine component is limited by the ability of the material comprising the component to sustain stress at elevated temperatures. In order to increase the turbine operating temperature and improve the efficiency, traditional turbine component alloys have been improved and a variety of non-traditional or advanced material systems (e.g. ceramics, intermetallics and composites) have been developed and investigated (Molloy 1990). Advanced material systems may exhibit an effect of test specimen dimensional scale on mechanical properties (e.g. ceramics), or anisotropy on both macro and micro scales (e.g. laminated composites) because the materials are no longer homogeneous isotropic mediums but structures. Design methodologies for traditional turbine alloys generally do not address such considerations, and thus new design methods need to be developed as non-traditional materials emerge and are considered viable for engine applications.

A variety of alloys of intermetallic composition have been developed (e.g. NiAl, TiAl, Ti₃Al, Nb₃Al and MoSi₂) in an attempt to further increase the operating temperature of turbine engines (Ashley 1991, Sauthoff 1995). Intermetallics have a unique atomic ordering that can result in congruent melting and unique properties. Nickel aluminide (NiAl) intermetallics, in particular, have low density, high thermal conductivity and high oxidation resistance as compared to nickel-based superalloys such as René' N5, Table 1.1.1 (Walston and Darolia 1993). A detailed review of the physical properties of intermetallic NiAl's has been given by Noebe et al. (Noebe et al. 1993). The term "NiAl" will be used to refer generically to any compound in the B2 NiAl phase field.

The beneficial properties listed in Table 1.1.1 make NiAl alloys possible candidates for turbine applications. A further step used to improve the elevated temperature capabilities of NiAl's has been the application of the creep limiting mechanisms used to improve the elevated temperature capabilities of traditional nickel-based alloys. A variety of mechanisms have been used to improve the creep resistance of traditional alloys used in turbine engines. One mechanism is the

precipitation of second phase particles throughout the matrix via modification of alloy composition and heat treatment. The second phase particles inhibit dislocation motion and the resulting creep deformation. Another improvement in traditional turbine engine alloys that occurred after the development of second phase precipitates was the generation of single crystal materials, which have been used in turbine engines for a decade. The improved creep resistance of single crystal superalloys results from the lack of grain boundaries, which act as sites for accelerated creep deformation. As a result of these improvements, the creep resistance of turbine alloys has improved substantially, thereby allowing an increase in turbine temperatures as shown in Figures 1.1.1 and 1.1.2. However, such improvements in elevated temperature capability are ultimately limited by the melting point of the alloy system and materials systems with higher melting points are desired (Fischer and Webster 1990).

The application of traditional creep limiting mechanisms (e.g. precipitation of a second phase in a single crystal) to intermetallics has resulted in single crystal NiAl alloys that are ideal candidates for turbine applications with one serious exception: a lack of ductility stemming from the limited dislocation motion and contaminant creep resistance. The room temperature fracture toughness of binary polycrystalline NiAl is on the order of 4 to 6 MPa√m (Noebe et al. 1993), and 8.7 ± 0.7 to 10 MPa√m and 4.4 ± 0.4 MPa√m for the {100} and {110} planes¹ of single crystals, respectively (Chang et al. 1992, Reuss and Vehoff 1991). Thus, these alloys “are not currently used in aircraft engines because room temperature fracture toughness and ductility are not high enough to allow assembly and maintenance operations” (Blankenship et al. 1995).

Further, because of the low fracture toughness of single crystal NiAl, the strength of NiAl may dependent on the surface finish and the flaw size distribution throughout the microstructure. Thus the fracture characteristics of some alloys are probably similar to those of classical brittle materials such as ceramics and glasses with two exceptions: elastic anisotropy, fracture toughness anisotropy and limited but possibly significant plastic deformation under specific conditions such as pure compression (Noebe et al. 1993).

¹ Conventional Miller indices and notation are used to describe crystallographic planes and directions in this dissertation: (hkl) defines a specific crystal plane; $\{hkl\}$ defines a family or group of identical crystal planes except for the arbitrary choice of the x-, y-, and z-labels on the axes. Similarly, $[hkl]$ and $\langle hkl \rangle$ correspond to specific directions and families of directions, respectively (Van Vlack 1975).

The lack of grain boundaries in single crystal NiAl results in a continuum, as in glass. However, the presence of a crystal structure and flaws such as coarse precipitates, inclusions, pores, etc. should create a material more similar to a monolithic ceramic. Also, because the material is a

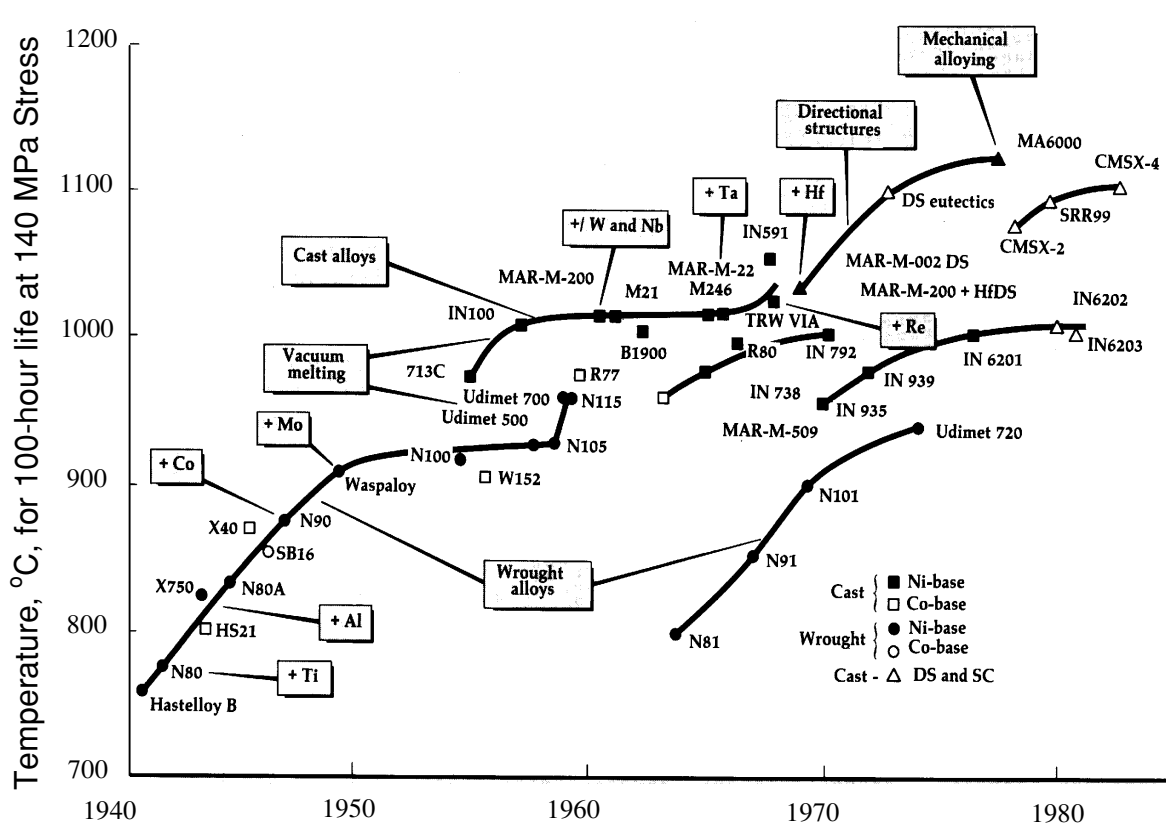


Figure 1.1.1: Temperature capabilities of superalloys: temperature for 100-hour life at a 140 MPa stress (Molloy 1990).

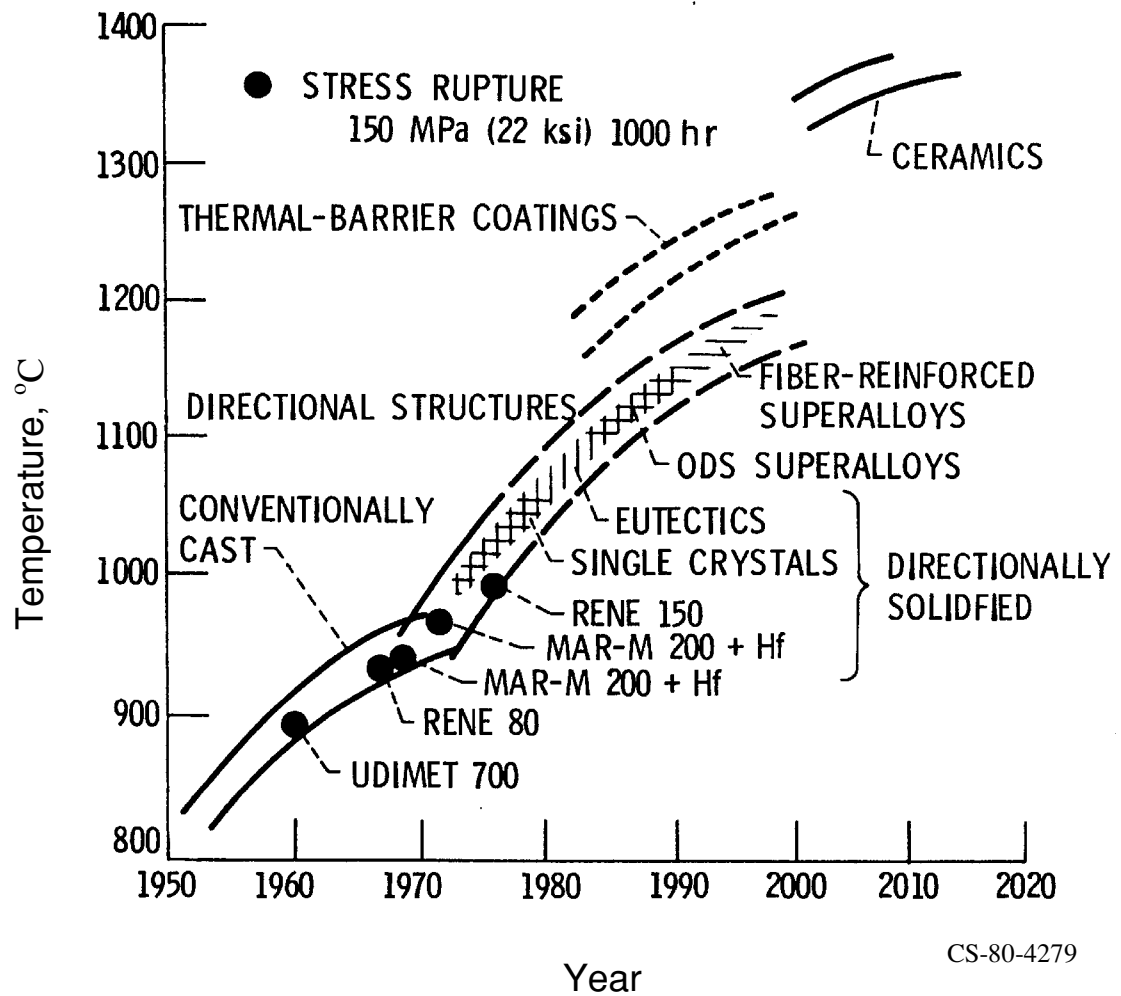


Figure 1.1.2: Temperature capabilities of superalloys and ceramics: blade surface temperature (courtesy H.R. Gray, NASA GRC).

single crystal, the fracture toughness varies with orientation, as noted previously, and a preferential fracture path(s) or cleavage plane(s) exists. This results in an anisotropic strength distribution.

It should be noted that low fracture toughness has not eliminated materials from application in turbine engines. In the case of ceramics, viable turbine vanes and nozzles in ground based auxiliary power units were achieved through better processing, machining, and handling that made the components stronger and more reliable, and through reliability analysis that accounted

Table 1.1.1: Physical properties of NiAl, NiAl alloys and an advanced superalloy (Walston and Darolia 1993).

Property	Units	Temp, °C	NiAl	NiAl alloys ^[1]	Advanced Superalloy
Bonding			Covalent/Metallic	Covalent/Metallic	Metallic
Melting Point	°C		1682	1610-1676	1390
Density	g/cm ³	RT	5.9	up to 6.30	8.60
Young's Modulus, Polycrystal	GPa	RT	188	188	205
Young's Modulus - <100>	GPa	RT	88	88	130
Anisotropy Factor		RT	3.25	~3.25 ^[2]	2.72
Shear Modulus, Polycrystal	GPa	RT	71.5	~71.5 ^[2]	74
Poisson's Ratio		RT	0.313	~0.313 ^[2]	0.380
Thermal Expansion	10 ⁻⁶ /°C	600	13.2	13.7	13.5
Specific Heat	J/g°C	600	0.64	0.61-0.64	0.46
Thermal Diffusivity	cm ² /sec	600	0.22	0.1-0.22	0.033
Thermal Conductivity	W/m°C	600	76	35-76	15
Electrical Resistivity	μohm·cm	RT	8-10	10-30	120-140

[1] NiAl alloys containing primarily β' precipitates and less than 5 atom percent alloying additions.

[2] Estimated assuming no effect of alloying on the elastic constants.

for the wide dispersion in strength (Schenk 1999, Price 1999). In the specific case of silicon nitrides, continued research on processing routes that elongate the grain structure and thereby provided “*in situ* toughening” have nearly doubled ($5 \text{ MPa}\sqrt{\text{m}}$ vs $8 \text{ MPa}\sqrt{\text{m}}$) the fracture toughness (Li and Yamanis 1989), further encouraging applications of what is a low fracture toughness material.

Thus, presuming maintenance and assembly operation can be sufficiently modified, the use of NiAl single crystals in turbine applications, such as vane and blades, will require component design methods that consider the elastic and strength anisotropy, the brittle behavior and the possibility of a wide size distribution of surface and volume distributed flaw populations.

1.2 PROBLEM STATEMENT

The guiding objective of this work is to further the knowledge and understanding of the failure of anisotropic, brittle materials and to develop component design capabilities for such materials. The overall goal of this dissertation follows:

Develop and verify a model for the structural design of anisotropic, brittle monoliths such as single crystal NiAl.

Specific objectives comprising this goal are as follows.

1.3 OBJECTIVES

- (1) Determine the elastic constants of the material.
- (2) Determine the mode of failure and the source, composition and structure of strength limiting defects.
- (3) Measure the uniaxial and biaxial strengths of the material for relevant crystal orientations.
- (4) Determine the appropriate statistical distribution for characterization of the materials strength. Develop appropriate reliability model and failure criterion.
- (5) Verify the model and criterion.

CHAPTER 2: REVIEW OF THE PREVIOUS WORK

2.1 FRACTURE OF BRITTLE, SINGLE CRYSTALS

Brittle single crystals such as sapphire, diamond, mica, etc. frequently fracture along specific planes defined by the crystal structure, even when the externally applied stresses are not a maximum on the specific planes. This phenomenon is referred to as cleavage and implies “that, other things being equal, cracking will proceed along the cleavage plane” (Fréchet 1990). The extent or quality of cleavage is typically described as “perfect, good, distinct or indistinct,” and is a result of both the nature of the crystal and the applied stress state. When the stress state is sufficiently misaligned, even crystals with a distinct cleavage plane will exhibit a ‘conchoidal’ fracture surface, or “that is, forming fracture surfaces fancied to resemble certain sea shells” (Fréchet 1990). Some crystals, such as quartz, SiO_2 , do not exhibit a distinct cleavage. Polycrystalline materials and materials without a microstructure, such as glass, fracture conchoidally with the fracture features being controlled by the stress state and crack dynamics.

Although cleavage has been described as “the separation of atomic planes in the absence of any plastic flow” (LeMay 1981), some semi-brittle metals and non-metals exhibit large dislocation densities and regions of stable crack growth on the ‘perfect’ cleavage plane. This behavior is a function of temperature and strain rate (Hirsch et al. 1992).

For ionic and covalently bonded single crystals, the cleavage plane was thought to be best predicted by a fracture energy criterion (Schultz et al. 1994, Hayashi 1982):

$$2\gamma_f = K_{Ic}^2 / E = \sigma_{cr}^2 \pi a = G_{Ic} \quad (1)$$

where γ_f is the fracture surface energy, G_{Ic} is the mode *I* strain energy release rate, K_{Ic} is some measure of the mode *I* fracture toughness and E is the elastic modulus in the direction of interest. Note however, that Equation (1) is an approximation of the energy release rate for an anisotropic material. For collinear crack extension, the conversion of the stress intensity factor into fracture energy for an orthotropic system should be done using (Sih and Leibowitz 1967)

$$G_I = \pi K_I^2 \left(\frac{S_{11} S_{22}}{2} \right)^{1/2} \left[\left(\frac{S_{22}}{S_{11}} \right)^{1/2} + \frac{2S_{12} + S_{66}}{2S_{11}} \right]^{1/2} \quad (2)$$

where the S_{ij} 's are the single crystal elastic constants (compliance's), K_I is the mode I stress intensity factor and G_I is the mode I strain energy release rate. In the case of a cubic system such as NiAl, $S_{11} = S_{22}$ and $S_{44} = S_{66}$. Self-similarity was invoked in deriving the equation and thus the crack must coincide with one of the principal axes of material symmetry (Sih 1979).

Note that there are two different formulations of Equation (2) published in two different works (Sih and Leibowitz 1967 and Sih 1979). The later publication (Sih 1979) of this formulation does not include the π term and S_{66} is replaced by S_{22} . This is a result of the form of the stress intensity factor chosen in the derivation.

Although the above solution is for the principal axes of material symmetry, Yoo and Fu (Yoo and Foo 1991) applied Eq. (2) to a {110} orientation of NiAl, which though not the principal axis of elastic symmetry is a plane of elastic symmetry. They calculated the theoretical stress intensity factor from theoretically derived energy release rates. Because the tensor for such a transformation is less populated than an orthotropic matrix, Eq. (2) should be applicable. Also, they applied Eq. (2) to the {100}, which is the principal plane of symmetry, however, it has been reported that collinear crack extension does not occur (100) (Chang et al. 1992). Note that collinear crack extension typically only occurs on the cleavage plane.

Metallically bonded materials are less prone to distinct cleavage because of the plastic flow allowed by the metallic bonding. However, iron, low carbon steel, tungsten, molybdenum, chrome, (all body centered cubic) and zinc, beryllium and magnesium (all hexagonal close packed) exhibit cleavage under the appropriate conditions. Although a stress criterion is implied by Broek (Broek 1982) for describing metallic cleavage, NiAl has a combination of covalent and metallic bonds and thus a fracture mechanics based energy criterion might be the most appropriate. Further, if small flaws exist, the reliability analysis of NiAl materials should be fracture mechanics based instead of based purely on strength relations.

2.2 CLEAVAGE OF NiAl SINGLE CRYSTALS

Cleavage of NiAl has been studied in some detail (Chang et al. 1992, Vehoff 1992). Pascoe and Newey (Pascoe and Newey 1968) reported that cleavage of a NiAl single crystal tested in compression occurred on the {110}.

Chang et al. used electro-discharge machining (EDM) notched four-point flexure specimens to estimate fracture toughness and determine the cleavage plane of various NiAl alloys. For binary NiAl, the fracture toughness and standard deviations on the {100}, {110}, and {111} families of planes were 8.28 ± 0.73 , 4.53 ± 0.44 , and 5.00 ± 0.16 MPa $\sqrt{\text{m}}$, respectively, implying a {110} cleavage plane. The fracture plane of the {100} specimens turned away from the notch plane and macroscopically aligned itself with the {110}, whereas the crack path was macroscopically coplanar for the {110} specimens, again implying {110} cleavage. It should be noted that Chang's fractograph's (Figure 6(a), pp. 2732) indicate that failure may have occurred from a point along the notch front rather than from the whole notch front in a quasi-static fashion as is assumed in calculation of the stress intensity factor. Such unstable fracture in four-point flexure can result in small errors in the calculated fracture toughness (Baratta and Dunlay 1990). However, little scatter is apparent in the data via the standard deviations listed above, and the data thus seems to illustrate the relative toughness of the planes reasonably. Another complication with Chang's data is the statement "the maximum load was used to calculate the fracture toughness, K_{c} , according to the equation ASTM E399." The American Society for Testing and Materials (ASTM) Test Method E 399 (ASTM E 399 1995) makes no provision for fracture toughness calculation from four-point bend tests or from maximum load unless specific conditions are fulfilled.

Although Chang (Chang et al. 1992) concluded that the {110} was the cleavage plane, they observed {511} transition planes at the tip of {110} EDM notched specimens. The occurrence of {511} transition planes were also noted by Bain and Darolia (Bain and Darolia, unpublished work that is reported in Chang et al. 1992) on the fracture surfaces of {100} chevron-notched flexure specimens, and on the surfaces of smooth strength specimens which also showed {110} facets and other high indices facets (Chang et al. 1992). However, on a low fracture toughness NiAl alloy (Ni-46Al, $K_{\text{c}} = 3.05 \pm 0.06$ MPa $\sqrt{\text{m}}$ for (110)<001>), no transition planes were observed (Chang et al. 1992). Although no specific explanation for the transition planes was given, it seems that the planes result from the crack dynamics and energy and constraint conditions at fracture. In the low fracture toughness material, the energy at failure can be dissipated without transition of the crack path onto planes such as the {511}. However, in the alloy with greater fracture toughness, the conditions at fracture were apparently sufficient to cause the crack to follow

multiple paths. In the {100} chevron-notched specimens (of the high fracture toughness alloy), the {511} transition planes occur because the crack can macroscopically follow the high toughness {100} notch plane, which it is macroscopically constrained via the notch, by transiting locally to {511} planes. A substantially greater fracture toughness measurement resulted. Chevron-notch measurements of the {110} were in good agreement ($4.61 \text{ MPa}\sqrt{\text{m}}$) with EDM notched data, implying equivalence, and no {511} transition was noted. The stable crack growth generated by the chevron notch probably kept the energy condition such that {511} transition was not necessary for energy dissipation. The materials tested by Bain and Darolia (Bain and Darolia unpublished work) are an early version of the material studied in this research.

DeMarco and Ardell (deMarco and Ardell 1996) concluded that neither the {100} nor the {110} were the preferred cleavage planes, but probably the {511} or {711} were, based on the work of Darolia et al. (Darolia et al. 1993) and Schneibel et al. (Schneibel et al. 1993). Note that the {110} is close to the {511} and {711}. In order to determine the cleavage plane, they indented $300 \mu\text{m}$ thick 3 mm diameter disks with a Vickers indenter at a substantial force of 5 kg such that the corners of the indenter were aligned with the $[01 \bar{1}]$ and the $[100]$ directions. The disks were then loaded in biaxial flexure between two concentric rings, thus aligning the tangential stresses on the classical (100) and (011) cleavage planes. They assumed equal probability of failure on all tangential or radial planes, which, as they note is not the exact case for an anisotropic disk. The stresses should be greater in the stiff crystallographic directions because the rings tend to enforce a displacement boundary condition and the stiff directions resist deflection the most. Further, the probability of failure is not only proportional to the stress, but to the ratio of stress relative to strength in the particular direction. Thus the probability of failure should be greater for the {110} plane because it has low fracture toughness and strength and is twice as stiff as the (100). Stress analysis might help clarify the results. Note that the disks used were “thick” for the range of plate theory (Diameter/thickness = 10) and significant shear may have developed through the section thickness (Adler 1991).

Crack extension occurred initially on the macroscopic (100) plane. However, no distinct (100) facets were visible or identifiable on the surfaces, implying that the (100) was not the cleavage plane, but a plane near the (100) such as the {511} or {711} planes. Note that the published fractographs of (100) fracture surfaces look like typical fracture surfaces in which a stress wave has interacted with the extending crack (i.e. conchoidal fracture), as would be expected for an isotropic material or an unfavorable orientation. Note that 5 kg is a very large indentation load for a $300 \mu\text{m}$ thick disk and may have induced severe deformations and residual stresses that may have influenced the results, particularly if the deformation was anisotropic.

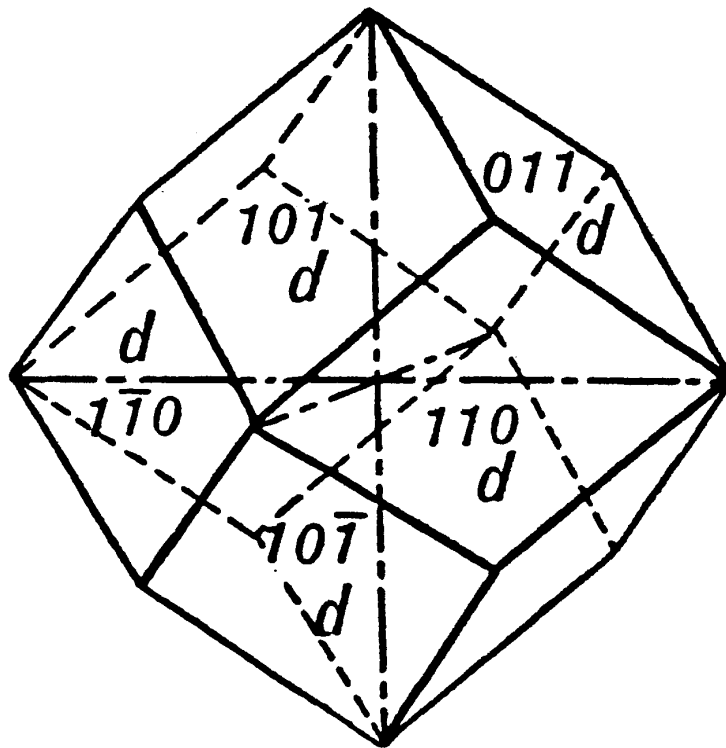


Figure 2.2.1: The $\{110\}$ dodecahedral family of surfaces.

After the initial crack extension on the (100), the test specimens were loaded until a second failure occurred. As the stresses on the (100) were probably partially relieved, failure occurred near but not exactly on the (011) from the corner of the indentation (i.e. near 90° to the first failure). Although large, flat surfaces resulted, no specific facets could be identified. Because the stress and deformation state of such a case is complex, a clear conclusion from these results is difficult. Deformation and strain energy may have driven the crack plane off the expected cleavage plane. The use of a more uniform stress concentration (e.g. spherical) or precrack along with stress analysis might have given clearer results.

The conclusion by Chang et al. that {110} is the cleavage plane of NiAl and that other high index planes such as the {511} form as a result of energy conditions and crack dynamics is in agreement with results presented in section 5.4.4. The {110} set of planes forms the dodecahedral surface shown in Figure 2.2.1.

2.3 ANISOTROPIC FRACTURE MECHANICS

As shown in section 2.2, the effects of anisotropy in fracture mechanics and energy release rate calculations are occasionally ignored either because of lacking information (e.g. elastic constants) or inattention to detail. Sih et al. (Sih, Irwin and Paris 1964) demonstrated that stress intensity factor solutions for isotropic and orthotropic materials are identical for infinite plates with symmetric and asymmetric self-equilibrating loads. Also, for finite rectangular test specimens of sufficient length subjected to tension or pure bending, the effects of orthotropic elastic properties are only marginal for a material such as wood with $E_x:E_y = 20:1$ when tested along or across the grain (Walsh 1972). A “sufficient length” is a length-to-width ratio of approximately 6:1 to 8:1 or greater. The standard flexure test specimen for strength testing of ceramics (ASTM C 1161 1990) is frequently used for fracture toughness testing (e.g. ASTM C 1421 1999). It has a constant moment section of 20 mm, a support span of 40 mm and a width of 4 mm when turned on edge, giving a ratio 10:1. Thus, standard flexure test specimens would be of “sufficient length” to avoid error when tested on the standard axes. Further, NiAl is substantially less anisotropic than common woods.

For more general cases of anisotropy (i.e. for a crack is located off the axis of elastic symmetry in an orthotropic material), Kanninen writes (Kanninen and Popelar 1985) “the stress intensity factors are in most practical cases just the same as for isotropic bodies. In particular, except

when unbalanced loads act on the crack faces, the stress intensity factors will be independent of the materials constants and therefore will be identical to the K values derived in isotropic fracture mechanics. This holds for each of the three possible modes of crack extension.” However, Kanninen and Popelar note that one complication arises: “The difficulty in the anisotropic case is that crack extension will not necessarily occur in a planar fashion. However, because the mathematical difficulties involved in treating angled cracks is prohibitive, this complication is usually ignored.” Thus, for brittle materials that exhibit small amounts of stable crack extension prior to catastrophic failure, the assumptions noted to be typically applied seem reasonable.

With the assumption given above, the main complication remaining in generation of fracture mechanic data on single crystals is the effects for off-axis testing on the stress state and thus on the stress intensity factor. However, as can be noted from the stress-strain compliance tensors below and the equation for the displacements of a beam subjected to pure bending, no twisting of the sections of cubic single crystals typically tested for cleavage energy should occur. The tensors given in Equations (3a) to (3e) were calculated from standard transformation equations (Wortman and Evans 1965, Turley and Sines 1971) The x_1' and x_2' axes are normal and parallel to the crack plane and growth direction specified below, respectively:

$$(100)\langle 001 \rangle$$

$$\begin{bmatrix} 1.0428 & -0.4210 & -0.4210 & 0 & 0 & 0 \\ -0.4210 & 1.0428 & -0.4210 & 0 & 0 & 0 \\ -0.4210 & -0.4210 & 1.0428 & 0 & 0 & 0 \\ 0 & 0 & 0 & 0.892 & 0 & 0 \\ 0 & 0 & 0 & 0 & 0.892 & 0 \\ 0 & 0 & 0 & 0 & 0 & 0.892 \end{bmatrix} \quad (3a)$$

$$(110)\langle 001 \rangle$$

$$\begin{bmatrix} 0.5339 & 0.0879 & -0.4210 & 0 & 0 & 0 \\ 0.0879 & 0.5339 & -0.4210 & 0 & 0 & 0 \\ -0.4210 & -0.4210 & 1.0427 & 0 & 0 & 0 \\ 0 & 0 & 0 & 0.8920 & 0 & 0 \\ 0 & 0 & 0 & 0 & 0.8920 & 0 \\ 0 & 0 & 0 & 0 & 0 & 2.9275 \end{bmatrix} \quad (3b)$$

$$(110)\langle\bar{1}10\rangle$$

[0.5339	-0.4210	0.0879	0.3739x10 ⁻⁵	0	0]	
[-0.4210	1.0428	-0.4210	-0.7477x10 ⁻⁵	0	0]	
[0.0879	-0.4210	0.5339	0.3739x10 ⁻⁵	0	0]	
[0.3739x10 ⁻⁵	-0.7477x10 ⁻⁵	0.3739x10 ⁻⁵	0.8920	0	0]	(3c)
[0	0	0	0	2.9275	0.7477x10 ⁻⁵]	
[0	0	0	0	0.7477x10 ⁻⁵	0.8920]	

$$(110)\langle\bar{1}12\rangle$$

[0.5339	-0.0393	-0.2937	-0.4407	0	0]	
[-0.0393	0.3749	-0.1347	-0.1102	0	0]	
[-0.2937	-0.1347	0.6293	0.5509	0	0]	(3d)
[-0.4407	-0.11018	0.5509	2.0370	0	0]	
[0	0	0	0	1.4009	-0.8814]	
[0	0	0	0	-0.8814	2.4187]	

$$(111)\langle\bar{1}10\rangle$$

[0.3643	-0.0817	-0.0817	0	0.20356x 10 ⁻⁸	0]	
[-0.0817	0.5339	-0.25137	0	-0.4798	0]	
[-0.0817	-0.2514	0.5339	0	0.4798	0]	(3e)
[0	0	0	1.5705	0	-0.9596]	
[0.2036x10 ⁻⁸	-0.4799	0.4798	0	2.2491	0]	
[0	0	0	-0.9596	0	2.2491]	

The displacement of a plate subjected to pure bending is given by (Whitney and Dauksys 1970, Ressler and Stavsky 1961)

$$w = \frac{3M_o l^2}{2h^3} [S_{11}(4x'^2 - 1) + S_{16}R(4x'y' \pm 1) + S_{12}R^2(4y'^2 - 1)] \quad (4)$$

where t is the plate thickness, b the width, l the length and $x' = x/l$, $y' = y/b$ and $R = b/l$. The positive and negative signs in the second term are associated with $S_{16} > 0$ and $S_{16} < 0$, respectively. At the corners of the plate (i.e. $x' = \pm 1/2$, $y' = \pm 1/2$) this reduces to

$$w = \frac{\pm 3M_o l^2}{t^3} [S_{16}R] \quad (5)$$

Because no S_{16} terms are present in the transformed tensors shown in Eqs. (3a) – (3e), “liftoff” (i.e. loss of contact) along the supports via twisting should not occur for cubic single crystal NiAl subjected to pure bending. However, in bending configurations with shear (e.g. three and four-point bending), shear-twist coupling will occur if S_{56} terms exists. If bend twist coupling were to occur, fixtures that do not allow articulation of the load line could induce a shear stress and a mode III stress intensity factor on precracked specimens. Such an effect would occur for the reported {511} transition plane because the tensor is fully populated, making direct measurements on such a plane difficult.

2.4 MECHANICAL TESTING OF BRITTLE, ANISOTROPIC MATERIALS

2.4.1 Elastic Properties

The single crystal elastic constants of NiAl have been measure by for a variety of conditions and compositions (Wasilewski 1966, Rusovic' and Warlimont 1977). Wasilewski determined the room temperature elastic constants of 50.6 atom percent Al NiAl by resonance of cylindrical rods in longitudinal and torsional modes. The reported constants were $C_{11} = 211.5$, $C_{12} = 143.2$, and $C_{44} = 112.1$ GPa. Note, that Wasilewski's data in lb_f/in^2 do not agree with his data in dyn/cm^2 by $\sim 1.5\%$. It appears that the data was measured in dyn/cm^2 and converted to lb_f/in^2 by a factor of 6.995 instead of the accepted value (Mechtly 1973) of 6.895. The values given in dynes/cm² are presumed to be correct and used in the following calculations made in order to give a

crystallographic perspective to the moduli. The elastic modulus varies from a minimum of 95.9 GPa in the $\langle 100 \rangle$ to a maximum of 275 GPa in the $\langle 111 \rangle$ direction, with an intermediate value of 187 GPa in the $\langle 110 \rangle$, as shown in Figure 2.4.1. Note also that Wasilewski reports a single value for the shear modulus of $\langle 110 \rangle$ specimens as determined by torsion of the $\{110\}$ plane. Actually, the shear modulus of the $\{110\}$ plane is a function of direction, and value reported is the apparent value (Hearmon 1961) given by

$$G = 2/(S_{44} + S_{55}) \quad (6)$$

For the (100) and (111) planes, the shear modulus is not a function of direction and the values reported are representative of all directions in the specified plane.

Rusovic' and Warlimont used the pulse-echo technique with wave polarization to measure the constants for 50 atom percent Al NiAl. The reported values were $C_{11} = 198.5$, $C_{12} = 137.5$, $C_{44} = 116$ GPa, in reasonable agreement with Wasilewski.

The elastic anisotropy factor ($AF = 2C_{44}/(C_{11} - C_{12})$) ranges from 3.2 to 3.3 for this data. This value is intermediate to other metallic single crystals such as aluminum which is nearly isotropic ($A = 1.2$), and β -Brass ($A = 8.5$) which is strongly anisotropic.

2.4.2 Uniaxial Flexure Testing

The requirements for uniaxial flexure testing of brittle materials have been studied in detail (Hoagland et al. 1976, Baratta et. al. 1987, Quinn 1990), and a frequently used standard test method exists (ASTM C1161 1990). The standard does not address elastically anisotropic materials specifically, but does provide for an articulated fixture so specimens with as-processed tolerances, which are typically poor, can be tested. Such a fixture might be capable of accommodating any bend-twist coupling encountered in a generally anisotropic beam, however, the effects can be severe (Whitney and Dauksys 1970). Ideally, bend-twist coupling should be avoided by testing axes of symmetry.

The standard also allows for three and four-point flexure of three different size specimens. Thus, standard test specimens can be used in the determination of size effects on strength.

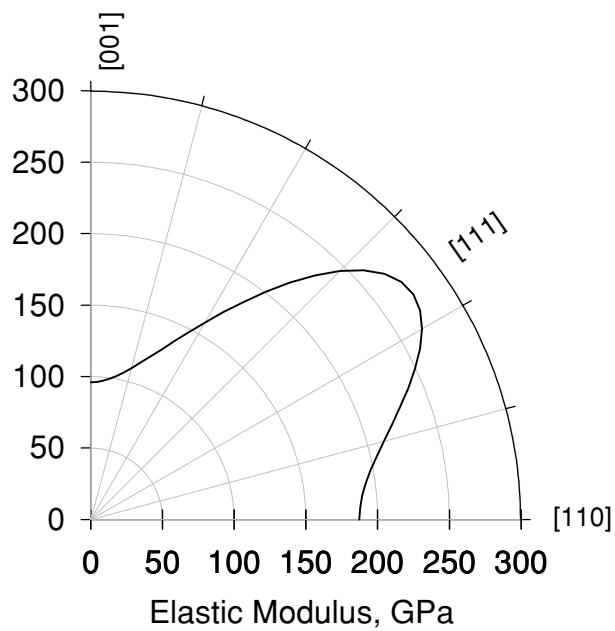
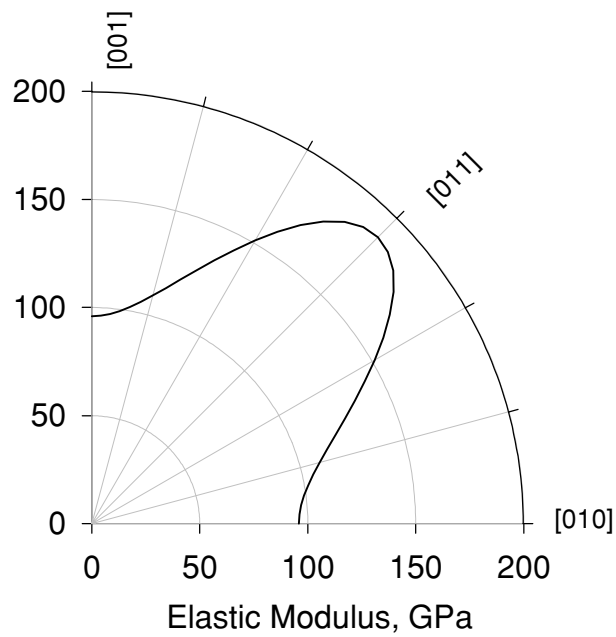


Figure 2.4.1: The elastic modulus $E_{\langle hkl \rangle}$ of binary NiAl as a function of orientation in (a) the $\{100\}$, and (b) the $\{110\}$. The single crystal elastic constants of Wasilewski (Wasilewski 1966) were used in the calculations.

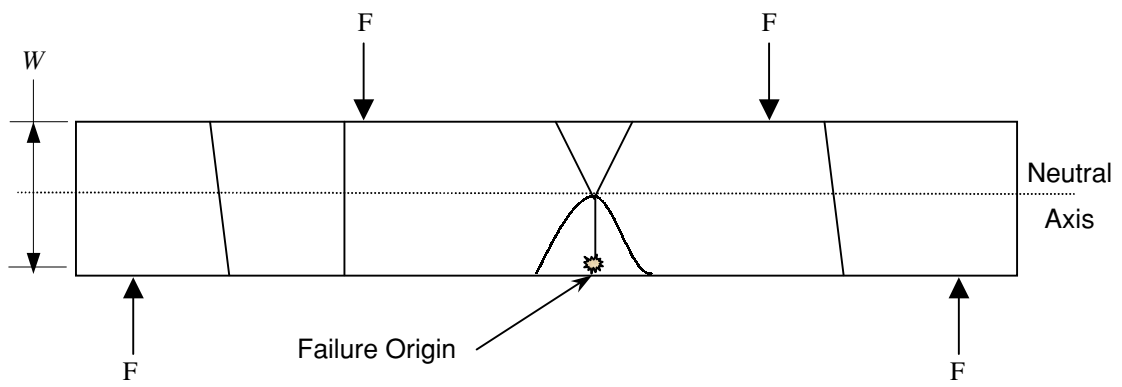


Figure 2.4.2: Typical fracture pattern resulting from flexural failure of a brittle material (Military Handbook 790 1992).

Considering the ingot sizes that were available in this study, either the “A” (1.5 by 2.0 by 25 mm in height, width and length, respectively) or “B” (3.0 by 4.0 by 50 mm, respectively) specimens were usable. For a wider range of test specimen sizes, a miniature test specimen can also be designed based on published recommendations (Hoagland et al. 1976, Baratta et. al. 1987, Quinn 1990). The advantages of flexural testing are, depending on one’s viewpoint, the small amount of required material, the simple geometry, the sensitivity to surface connected defects and the frequency of use in data measurement. One major advantage borne out in these results is the asymmetric fracture pattern that results from the primary crack intersecting the compression side of the beam, as shown in Figure 2.4.2. This pattern makes identification of the failure origin relatively easy, even when the test specimen fragments into dozens of pieces. In contrast, tensile strength tests generating a uniform stress state typically produce many symmetric failures and the primary failure plane is very difficult to identify.

2.4.3 Biaxial Flexure Testing

Biaxial flexure testing has been studied in some detail (Rickerby 1977, Adler and Mihora 1991, Vitmar and Pukh 1963, Ritter et al. 1980, Shetty et al 1983) and at least one full consensus standard exists (ASTM F 394 1978). Typically three different loading assemblies, shown in Figure 2.4.3, are used to flex circular or square plates: ball-on-ring (B-O-R), ring-on-ring (R-O-R), and pressure-on-ring (P-O-R). For model verification, the R-O-R or the P-O-R is typically used, as more of the test volume is subjected to large stresses. Very little published work (DeMarco and Ardell 1996, Chen and Leipold 1985) on biaxial testing of single crystal plates is available in the open literature. However, a review of the isotropic literature is useful as it points out some of the complications and interfaces to be avoided in the design of biaxial test rigs.

The P-O-R has the advantage that no frictional or contact stresses are developed in the highly stressed regions, thereby avoiding a “spike” in the stress distribution. However, friction will occur in P-O-R specimen at the support ring. The frictional effects can be minimized by lubricating the support ring.

The radial and tangential stresses are not equal except at the center of the disk, and thus somewhat less effective area is tested than with the R-O-R. Rickerby (Rickerby 1977) developed a system that used a neoprene membrane to transmit pressure to the test specimen (diameter/thickness ≈ 17). The reported radial and tangential stress were in excellent agreement

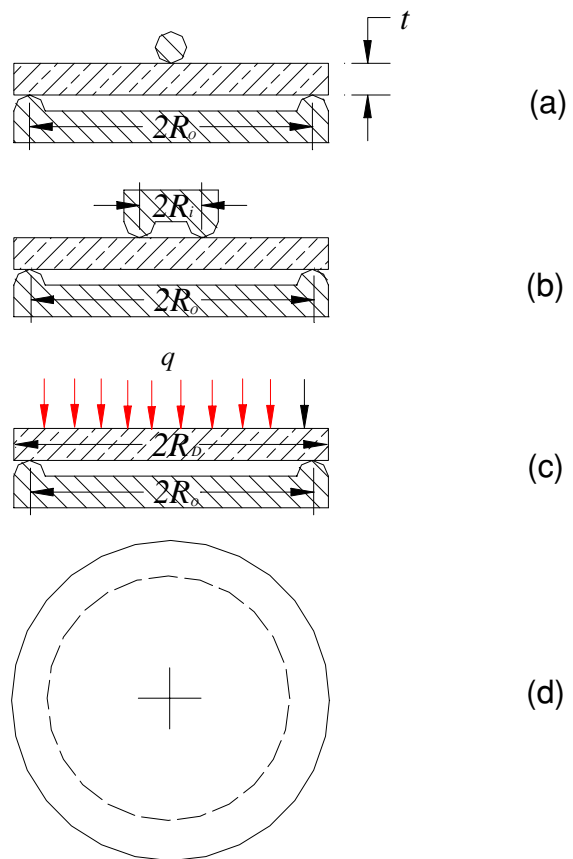


Figure 2.4.3: Schematic of the testing configurations used to generate biaxial tensile stresses in plate specimens: (a) ball-on-ring, (b) ring-on-ring, (c) pressure-on-ring and (d) top view of the pressure-ring configuration.

with plate theory at the disk center ($\ll 0.5\%$ difference). At 40 percent of the support radius the agreement was approximately 3.6 and 2.5 percent. However at 80 percent of the support radius the differences were 25 and 2.4 percent, respectively. The large difference in radial stress toward the edge of the specimen is less significant as the radial stresses is less than one-third of the maximum stresses and thus does not effect reliability as much.

The biaxial test rig used by Shetty included a 0.25 mm spring steel membrane between the specimen (diameter/thickness ≈ 13) compressive surface and the pressure source (Shetty et al. 1983). Despite the presence of a membrane, the rig resulted in stresses in reasonable agreement with plate theory. The measured stresses at the disk center were about 3.5% greater than the theoretical predictions. The radial and tangential stresses were about 1.5 and 1.9% greater at 25% of the disk radius, and at 80% of the support ring the radial stress error was 10%. Reliability calculations are strongly dependent on the peak stress region, and thus the difference must be small in the central region of the disk. Although the overall differences are not large (i.e. only 10% toward disk edge), they are significantly larger than Rickerby's (Rickerby 1977) at the high stress central region. This may be due to the restraining effect of the steel membrane.

The R-O-R specimen has display somewhat less accurate results as compared to the P-O-R specimen. Adler and Mihora (Adler and Mihora 1991), in a detailed study, used a three dimensional finite element analysis (FEA) that combined membrane stresses with bending stresses and included large shear strains. "Slide surfaces" were used in the model to eliminate the effects of friction between the load ring and plate. Thin plates (diameter/thickness > 20) were found to experience combined membrane and bending stresses. Thick disks (diameter/thickness < 10) underwent bending and shear stresses. A centerline deflection of 10% of the plate thickness introduced substantial membrane stress that increased the tension face stresses. For very thin plates the contact stresses associated with the loading ring were mirrored (i.e. wedging stresses occur) such that a tensile face stress almost as large as the compressive contact stress occurred. In the case of a ZnS disk with diameter/thickness ≈ 23 , the radial component of stress under the steel loading-ring of 3 mm cross sectional radius, as measured with strain gages, increased by 55% as compared to the expected value. Note that uniaxial strain gages were used and transverse (up to $\sim 5\%$) errors may not have been taken into account.

Adler also suggested and analyzed the use of an acrylic (Delrin) ring with a square cross section. The square cross section ring resulted in substantially lower compressive contact stresses than

even steel rings with a ratio of cross-section radius to plate thickness of 4:1. Because the analysis was done at a maximum stress of 69 MPa, which is substantially less than the stress required to fracture most intermetallic or ceramic materials, the Delrin ring may not be applicable. Note also that all of the analyses assumed no friction. Friction can create substantial errors (5 to 15%) in four-point flexure tests (Hoagland et al. 1976, Baratta et. al. 1987, Quinn 1990) and theoretical calculations indicated that errors as large as 50% can occur in R-O-R testing (Fessler and Fricker 1984). To minimize its effect, a support ring consisting of roller bearings that are allowed to roll could be used (Godfrey and St. John 1986). Use of a similar loading ring made of balls would probably generate excessive contact stresses, and thus a soft (e.g. annealed copper) continuous ring with a large cross-sectional radius, R_c , relative to the plate thickness, t , might be used (e.g. R_c/t ratio > 4). In order to minimize the friction and stress concentration from the upper ring, a thin Teflon or rubber shim could be placed between the plate and ring. Verification of such a configuration would require empirical analysis (e.g. strain gage analysis).

For the specific case of a 76.2 mm diameter disk with a Young's modulus of 100 GPa that was loaded with steel rings of 3 mm cross-section radius, FEA calculations assuming no friction resulted in radial stresses in good agreement with the thin plate theory of Vitmar and Pukh (Vitmar and Pukh 1963) for diameter to thickness ratios between 20:1 and 6:1. The corresponding ratios of ring cross-section radius to plate thickness for the example above are surprisingly small: 0.8:1 to 0.25:1. Note that the assumptions in most analytic models are that membrane stresses, transverse shears and highly concentrated loads do not exist. So the choice of specimen diameter, thickness, load-ring cross-section and elastic modulus are critical for each material

Vitman and Pukh's solution added a term (r_o^2/R^2) to the conventional solution (Roark and Young 1975 or Timoshenko and Woinowsky-Krieger 1959) to account for the extra stiffening effect of overhang:

$$\sigma_{\max} = \sigma_{rr} = \sigma_{\theta\theta} = \frac{3F}{2\pi t^2} \left[(1-\nu) \frac{R_o^2 - R_i^2}{2R_o^2} \cdot \frac{R_o^2}{R_d^2} + (1+\nu) \ln \frac{R_o}{R_i} \right] \quad (7)$$

where F is the applied force, R_i is the load or inner ring radius, R_o is the support or outer ring radius, R_d is the plate radius, t is the plate thickness and ν is Poisson's ratio. For a round plate with no overhang, the (R_o^2/R_d^2) term goes to unity and the conventional solution is obtained. The solution can be used for a square plate if an effective value of R_d that expresses the characteristic

size of the plate is used. The approximate arithmetic mean of the circles inscribed by and inscribing the square plate is suggested (Vitmar and Pukh 1963)

$$R_d = l(1 + \sqrt{2})/4 \quad (8)$$

where l is the length of the edge. The maximum deflection for such a plate can be estimated from (Vitmar and Pukh 1963)

$$\delta = \frac{3F(1-\nu^2)R_i^2}{2\pi Et^3} \left\{ \frac{R_o^2}{R_i^2} \left[1 + \frac{(1-\nu)(R_o^2 - R_i^2)R_o^2}{2(1+\nu)R_o^2} \right] - \left(1 + \ln \frac{R_o^2}{R_i^2} \right) \right\} \quad (9)$$

where E is Young's modulus.

A closed form solution including friction, shear and overhang has been derived by Fessler and Fricker (Fessler and Fricker 1984). The solution indicates that friction increases the stress in a region $\sim 0.25t$ outside of the loading ring by 50 percent for thick disks with a coefficient of friction of 0.4. Friction lowers the maximum stress within the loading ring. The result of friction is to bias the failure toward the loading ring and lower the effective area as shown in Table 2.4.3.1. The reduction in effective area is most significant for thick disks and large Weibull moduli, and results in increased observed strength. Note that Equation (15) of Fessler and Fricker's stress solution (Fessler and Fricker 1984) is missing the term $(1-\nu)(R_s^2 - R_l^2)/2R_o^2$.

Of particular importance to our material is the requirement that deflection be less than 10% of the thickness, as the strong, $\langle 001 \rangle$ orientation has the lowest stiffness ($E_{\langle 100 \rangle} = 96$ GPa). Based on the analysis of Adler and Mihora, it may be difficult to design a ring-loaded NiAl specimen that can be accurately described by Equation (7). Although strain gages and FEA could be used to estimate the actual stresses and design an accurate R-O-R test specimen, it is probably simpler to avoid the complications associated with the R-O-R specimen and to use the P-O-R specimen instead. A further complication with the R-O-R specimen is the lack of a closed form stress solution for single crystal materials. An even more compelling reason to use the P-O-R method is that a closed form displacement solution exists for an anisotropic material subjected to uniform pressure (Okubu 1949).

Table 2.4.3.1: Effect of friction on the effective area, A_e , of a 25 mm diameter disk loaded between 10 and 20 mm diameter concentric rings. Poisson's ratio = 0.23. Values were calculated by numerical integration of the PIA model (Barnett et al. 1967) model, see section 3.4.1, using the stress functions of Fessler and Fricker (Fessler and Fricker 1984).

Coefficient of Friction μ	Weibull Modulus m	Effective Area, mm ²	
		Thickness, mm	
		1	2
0	5	235	235
0.05	"	230	226
0.1	"	226	218
0.2	"	218	202
0.4	"	202	172
0	10	197	197
0.05	"	189	182
0.1	"	182	167
0.2	"	167	142
0.4	"	142	102
0	15	184	184
0.05	"	173	162
0.1	"	162	142
0.2	"	142	110
0.4	"	110	70

2.4.4 Uniaxial Tensile Testing

A variety of uniaxial, tensile test configurations for brittle, anisotropic materials have been standardized (e.g., ASTM C 1273-95a 1999). Figure 2.4.4.1 shows tensile specimens that have been used to test brittle materials. Unfortunately, most of these specimens are too large to cut from the billets available in this work. Thus, design of a smaller test specimen that can be gripped with a fixed collet system needs to be considered. The use of a fixed collet presents advantages and disadvantages: precise alignment can be made if the proper fixtures are employed, and only a short shank length is required. However, the fixed end-grip condition can result in shear stresses for anisotropic materials tested off axis.

An analysis of the effects of fixed end-grips on displacements, strains and stresses for an orthotropic material rotated about the z axis was done by Pagano and Halpin (Pagano and Halpin 1968). If the analysis is repeated for a cubic system the same equations result:

$$\begin{aligned}
 \sigma_x &= -2C_0xy - 2\frac{S_{16}}{S_{11}}C_0y^2 + C_1y + C_2 \\
 \sigma_y &= 0 \\
 \tau_{xy} &= C_0(y^2 - D^2) \\
 \epsilon_x &= S_{11}(-2C_0xy + C_1y + C_2) - S_{16}C_0(y^2 + D^2) \\
 \epsilon_y &= S_{12}\left(-2C_0xy - 2\frac{S_{16}}{S_{11}}C_0y^2 + C_1y + C_2\right) + S_{26}C_0(y^2 + D^2) \\
 \gamma_{xy} &= S_{16}\left(-2C_0xy - 2\frac{S_{16}}{S_{11}}C_0y^2 + C_1y + C_2\right) + S_{66}C_0(y^2 + D^2)
 \end{aligned} \tag{10}$$

where D is the specimen half-width and the C_i 's are combinations of the elastic constants and the applied axial load. If the analysis is applied to the typical cleavage orientations in Section 2.3, no shear stresses result in the xy (cross section) plane. However, for orientations such as the $\langle 511 \rangle$, etc., shear stresses on the order of 20 percent of the normal stress result.

Thus a small cylindrical test specimen as shown in Figure 2.4.4.2 could be used. The stress concentration factor at the gage to shank region is estimated to produce a 2 to 3% increase the

tensile stress (Peterson 1974). The concentricity tolerance requirements between the shank and the gage section can be calculated from basic stress equations for a rod

$$\begin{aligned}\sigma_t &= 4F / \pi d^2 \\ \sigma_b &= 24Fe / \pi d^3\end{aligned}\tag{11}$$

resulting in a percent bending of

$$\frac{\sigma_b}{\sigma_t} = 8 \frac{e}{d}\tag{12}$$

where d is the gage section diameter, e the eccentricity. For two percent bending a concentricity of 0.007 mm or less is required for the proposed specimen. Centerless grinding can attain such tolerances.

Another issue associated with tensile testing is that both the center and surface of the test section are subjected to the same stress, and the specimen fails from both surface and volume flaws. As the flexure specimens are biased toward surface failure, predictions of tensile behavior from flexure data is more complicated.

2.4.5 Torsion Testing

The advantage of torsion testing is that it produces a maximum shear stress equal to that of the maximum normal stress instead of the 1:2 ratio generated in tension testing. Thus the opportunity for ductile behavior is greater in the case of low ductility, and the sensitivity of the fracture strength to combined stresses or shear, can be determined. This is particularly important for determining the failure mechanisms of a material that exhibits yield under certain conditions and brittle fracture under others, as the design might be geared toward yield.

No full consensus standards exist for torsion testing of brittle materials. In addition, torsion testing of ceramics and NiAl has been performed infrequently (Blankenship et al. 1995, Petrovic and Stout 1981, Oda et al. 1988). Torsion testing of <100> and <110> binary, NiAl single crystal rods was performed by Blankenship et al. Specimens of <001> orientation exhibited $a_0<100>$ dislocations and shear strain to failure of 0.11 ± 0.03 whereas <110> orientations exhibited both $a_0<100>$ and some $a_0<110>$ dislocations with a torsional strain to failure of 0.02 ± 0.008 . The dislocation density was greater at the specimen surface than the center as would be expected for

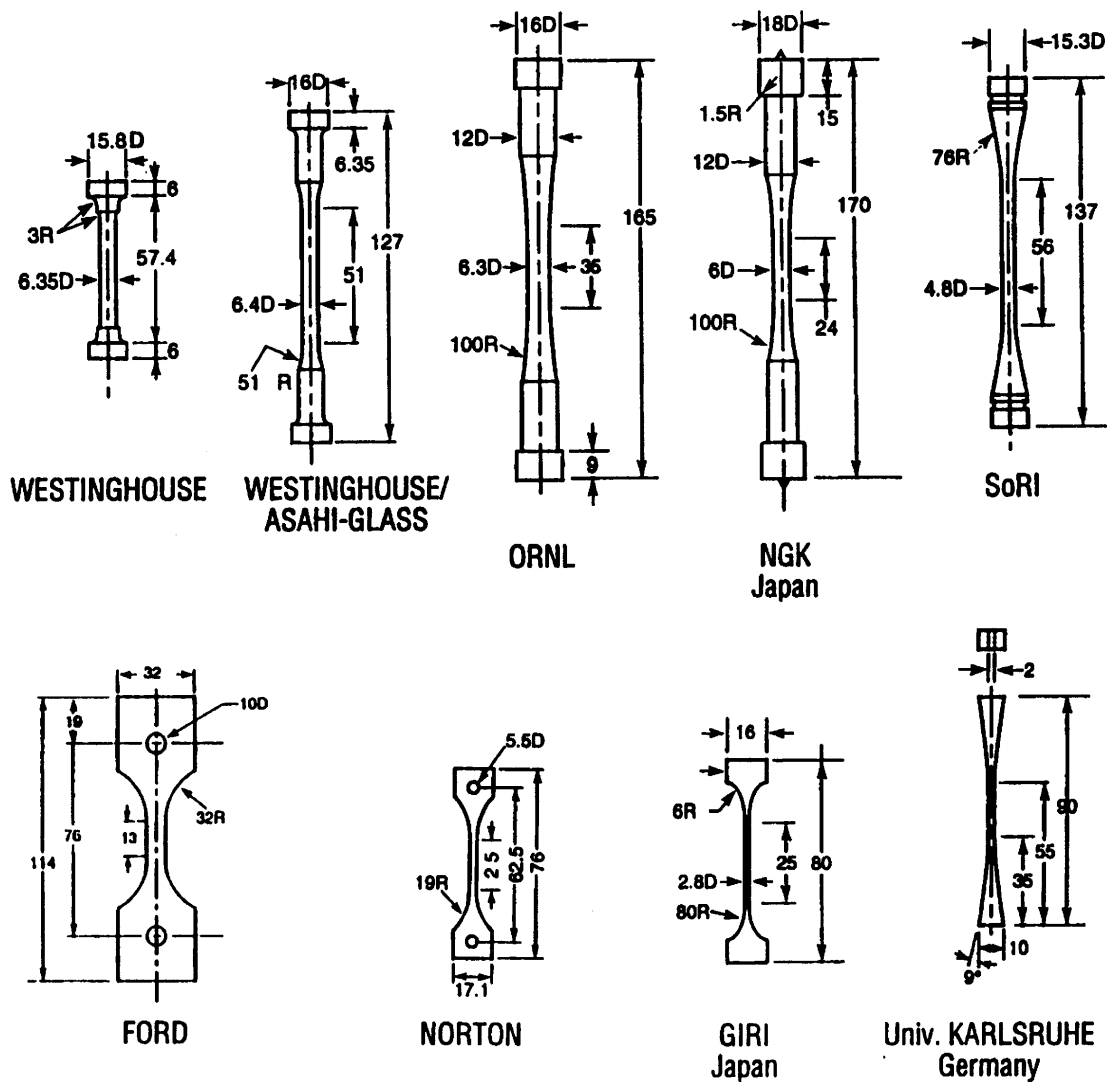


Figure 2.4.4.1: Tensile specimens used to test brittle materials (ASTM C 1273-95a 1999). All dimensions in mm.

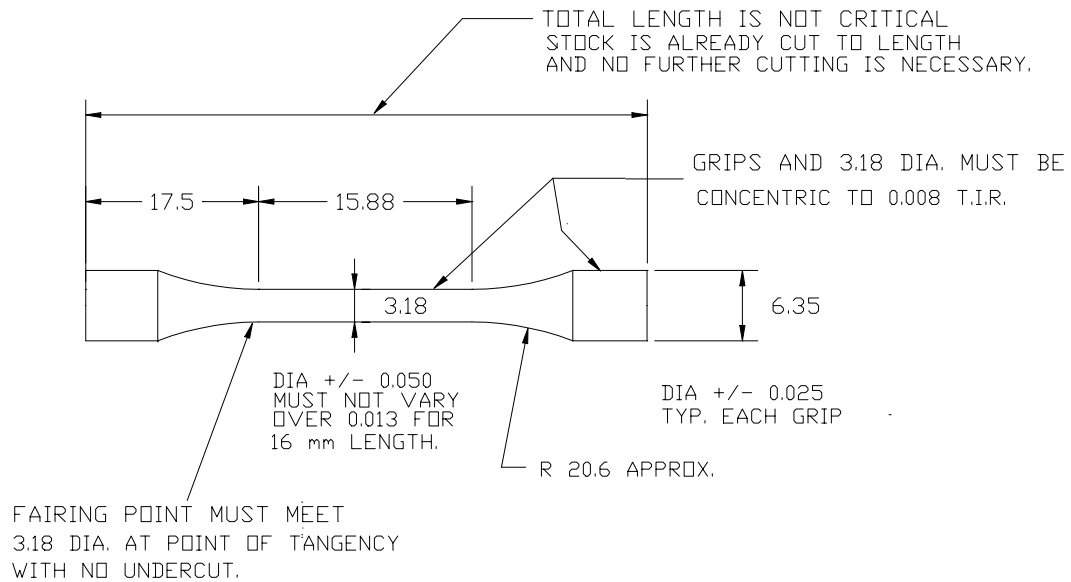


Figure 2.4.4.2: Miniature tensile test specimen. All dimensions in mm.

torsional loading. The shear modulus calculated from the tests were very different than reported by Wasilewski (Wasilewski 1966) ($G_{<100>}=153 \pm 7$ vs. 112.1 GPa and $G_{<110>}=160 \pm 27$ vs. 52.5 GPa).

In contrast to the results of Chang et al. (Chang et al. 1992) which found near {110} and {511} cleavage planes, Blankenship et al. found fracture facets oriented about 10° from the <001> or near <112> fracture surfaces, in agreement with tensile results of Schneibel (Schneibel 1993). For the <100> test specimens, their stress analysis indicated that the (112) and (110) were subjected to a large normal stress yet the actual failure planes were within 18° of the (100), which was subjected to large shear stresses. For the <110> test specimens the (100) and (112) were subjected to large normal stresses, however, the (001) and (1 $\bar{1}$ 2), which are oriented at 90° to the (110), were also subjected to large shears. Failure was observed on {001} and {112} type planes. Although no strong conclusions were put forth by Blankenship et al., it seems that local, shear induced failure occurs initially on the {100} planes and is linked together by local cleavage near the {112}. Although the {110} is thought to be the natural cleavage plane, the large orientation difference between the {110} and the shearing {100}, which is either 45° or 90° , may not have allowed failure to link onto the {110} but on a more favorably oriented {112}.

Blankenship et al. calculated stresses in NiAl with solutions for elastically isotropic materials with out specific justification. This can be examined via the solution for an orthotropic rod in torsion (Hearmon 1961). The stresses and angle of twist per unit length, ξ , are given by

$$\sigma_{23} = \phi C_{55} (C + 1) x$$

$$\sigma_{13} = \phi C_{44} (C - 1) y \quad (13)$$

$$\xi = 16T(S_{44} + S_{55})/\pi d^4$$

with

$$C = (C_{55} - C_{44})/(C_{55} + C_{44})$$

where T is the torque, d is the diameter of the cylinder, and the x_i 's are the distances along the coordinate axes. The solution was generated such that the crystal axes, coordinate axes and geometric axes of the rod were aligned. The solution applies to orthotropic materials in standard position or materials of higher symmetry transformed such that the tensor is of an orthotropic

form. For the (100)<001> and (110)< $\bar{1}10$ > tensors shown in section 2.3, the surface shear stresses reduce to

$$\sigma_{23} = -\sigma_{13} = 16T/\pi d^3 \quad (14)$$

which is the solution for an isotropic medium.

Considering the size of the billets available for this study, the complexities of test specimen design, specimen alignment and the machining costs associated with torsion testing, the use of simple beam and plate specimens to generate both uniaxial design data and multiaxial model verification data seems appropriate for brittle, anisotropic materials such as single crystal NiAl.

2.5 DETERMINISTIC DESIGN CRITERIA FOR BRITTLE MATERIALS

2.5.1 Stress-Based Criteria

2.5.1.1 Maximum Principal Stress

For materials that show little deformation or shear sensitivity upon fracture, the normal stresses should control failure. As the maximum principal stress is the largest normal stress, this theory proposes that a predefined form of failure ensues when the maximum principal stress exceeds the strength. No specific flaw is assumed. Typically, the material's tensile strength is assumed constant in all directions and a safety factor is applied to ensure survival and to account for load, geometry and material property variations (Shigley and Mischke 1989). Compressive stresses are treated in a fashion similar to tensile stresses. The criterion is formulated as

$$\begin{aligned} \sigma_1 &\geq S_{UTS} / N_t \\ \sigma_2 &\leq S_{UCS} / N_c \end{aligned} \quad (15)$$

where the three principal stresses have the algebraic order $\sigma_1 > \sigma_2 > \sigma_3$, and S_{UTS} and S_{UCS} are the tensile and compressive strengths, respectively, and N_t and N_c are appropriate safety factors for the conditions considered. The theory does not account for interactions between various principal stresses and, as mentioned above, and ignores effects of shears. A final limitation is that the theory does not account for the effects of scale (i.e. component size) exhibited by brittle materials such as ceramics and glasses.

2.5.1.2 The Modified Mohr Theory and the Tsai-Wu Theory

These theories, though more advanced than the Maximum Principal Stress Theory, have the same limitation - they do not account for the effects of scale. The Mohr theory allows for different strengths in tension and compression, and torsional failure is dominated by the tensile stress component. However, it applies only to materials with isotropic tensile and compressive strengths.

The Tsai-Wu (Tsai and Wu 1971) formulation mathematically represents the most general case of an ellipse (i.e. translated and rotated off the origin):

$$F_i \sigma_i + F_{ij} \sigma_i \sigma_j = 1 \quad (16)$$

or with expansion

$$F_1 \sigma_1 + F_2 \sigma_2 + F_{11} \sigma_1^2 + F_{22} \sigma_2^2 + F_{12} \sigma_1 \sigma_2 + F_{21} \sigma_1 \sigma_2 = 1 \quad (17)$$

which is equivalent to an ellipse translated off the origin and rotated, i.e.

$$Ax^2 + Bxy + Cy^2 + Dx + Ey + F = 0 \quad (18)$$

It is thus symmetric and convex for a discriminant less than zero (Ellis and Gulick 1978). Thus the theory cannot describe materials with equibiaxial weakening. The theory might be adapted to weakest-link materials by incorporating it into a scaling function, but the symmetry of the function makes it unlikely that it would work for brittle anisotropic materials exhibiting cleavage planes.

2.5.1.3 Principle of Independent Action

Another stress-based criterion is the principle of independent action or PIA (Barnett et al. 1967). Although this criterion was formulated for use with statistical functions, the stresses are treated as deterministic and the equivalent stress inducing failure is given as

$$\sigma_{eq} = (\sigma_1^m + \sigma_2^m + \sigma_3^m)^{1/m} \quad (19)$$

for

$$\sigma_1 > \sigma_2 > \sigma_3 > 0$$

where the σ_i 's are the principal stresses, m is the Weibull modulus (see section 2.6.1), and σ_{eq} is the equivalent stress that induces failure 100% of the time when it exceeds a specified value. Principal stresses less than zero are generally ignored.

2.5.2 Fracture Mechanics Criteria

A variety of deterministic fracture mechanics failure criteria exist. These can be reformulated in terms of an equivalent stress for failure by assuming an embedded or surface connected crack and corresponding stress intensity factor coefficient. Thus, the strength exhibited by a brittle component subjected to multiaxial stresses can be related to the fracture mechanics criterion. In general the stress intensity factors for the loading modes shown in Figure 2.5.2.1 can be formulated as

$$\begin{aligned} K_I &= Y_I \sqrt{a} \sigma_n \\ K_{II} &= Y_{II} \sqrt{a} \tau \\ K_{III} &= 0 \end{aligned} \quad (20)$$

where σ_n and τ are the normal and shear stresses on the crack plane, Y_I and Y_{II} are the mode *I* and mode *II* stress intensity factor coefficients (SIFCs), and a is the crack dimension. For a through-wall surface crack of length $2a$ in an infinite plate, the stress intensity factors are

$$\begin{aligned} K_I &= \sqrt{\pi a} \sigma_n \\ K_{II} &= \sqrt{\pi a} \tau \\ K_{III} &= 0 \end{aligned} \quad (21)$$

For a semicircular crack Smith determined the mode *I* solution for an infinite plate (Smith et al. 1967). For mode *II* Smith and Sorensen gave a value for an aspect ratio of $a/c =$ of 0.4 with a crack depth to section thickness ratio of $a/t = 0.2$ (Smith and Sorensen 1974). Note that for an a/t ratio < 0.5 , the Y_{II} value increases only slightly, and the value for $a/t = 0.2$ should approximate that for a thick plate, so

$$\begin{aligned} K_I &= 1.366 \sqrt{a} \sigma_n \\ K_{II} &= 1.241 \sqrt{a} \tau \\ K_{III} &= 0 \end{aligned} \quad (22)$$

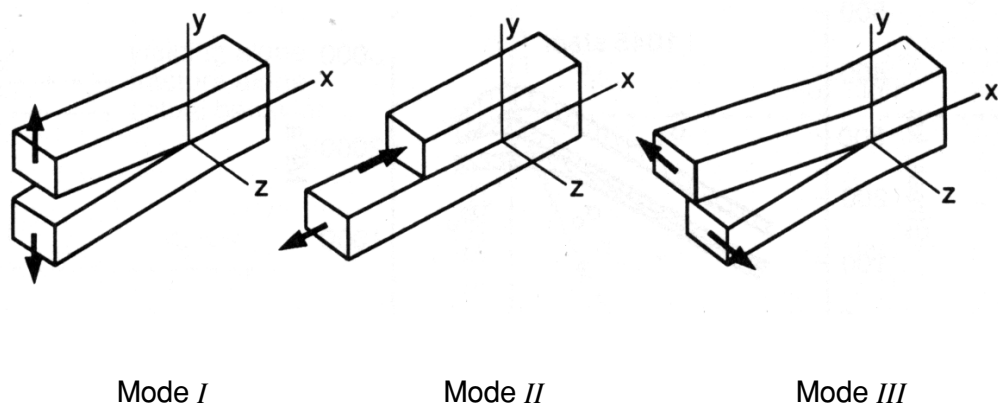


Figure 2.5.2.1: Basic modes of loading and displacing a crack surface.

SIFC's for surface cracks were also approximated from those of embedded cracks by Theimeier et al. (Theimeier et al. 1991):

$$\begin{aligned} K_I &= 1.14 \frac{2}{\sqrt{\pi}} \sqrt{a} \sigma_n \approx 1.286 \sqrt{a} \sigma_n \\ K_{II} &= 1.14 \frac{4}{\sqrt{\pi}} \frac{1}{2-\nu} \sqrt{a} \tau \approx 1.479 \sqrt{a} \tau . \\ K_{III} &= 0 \end{aligned} \quad (23)$$

The normal and shear stresses in terms of the principal stresses and polar and azimuthal angles are

$$\begin{aligned} \sigma_n &= \sigma_1 \cos^2 \theta + \sigma_2 \sin^2 \theta \\ \tau &= \frac{1}{2} |(\sigma_1 - \sigma_2) \sin(2\theta)| \end{aligned} \quad (24)$$

for a surface connected crack as shown in Figure 2.5.2.2, and by

$$\begin{aligned} \sigma_n &= (\sigma_1 \cos^2 \theta + \sigma_2 \sin^2 \theta) \cos^2 \phi + \sigma_3 \sin^2 \phi \\ \tau &= \left[\left((\sigma_1 - \sigma_2) \cos \phi \sin \theta \cos \theta \right)^2 + \left((\sigma_1 \cos^2 \theta + \sigma_2 \sin^2 \theta - \sigma_3) \cos \phi \sin \phi \right)^2 \right]^{1/2} \end{aligned} \quad (25)$$

for an embedded (volume) crack.

In general, a failure criterion can be written in terms of the applied stress intensity factors as

$$FC(K_I, K_{II}, K_{III}) \geq FC_c \quad (26)$$

where FC_c is the critical value of the materials resistance to unstable crack propagation. No stability requirements are imposed. The equivalent mode I criterion is defined as

$$FC(K_{Ieq}, 0, 0) = FC(K_I, K_{II}, K_{III}) \quad (27)$$

where the equivalent stress and stress intensity factor are related by

$$K_{Ieq} = Y_I \sqrt{a} \sigma_{Ieq} . \quad (28)$$

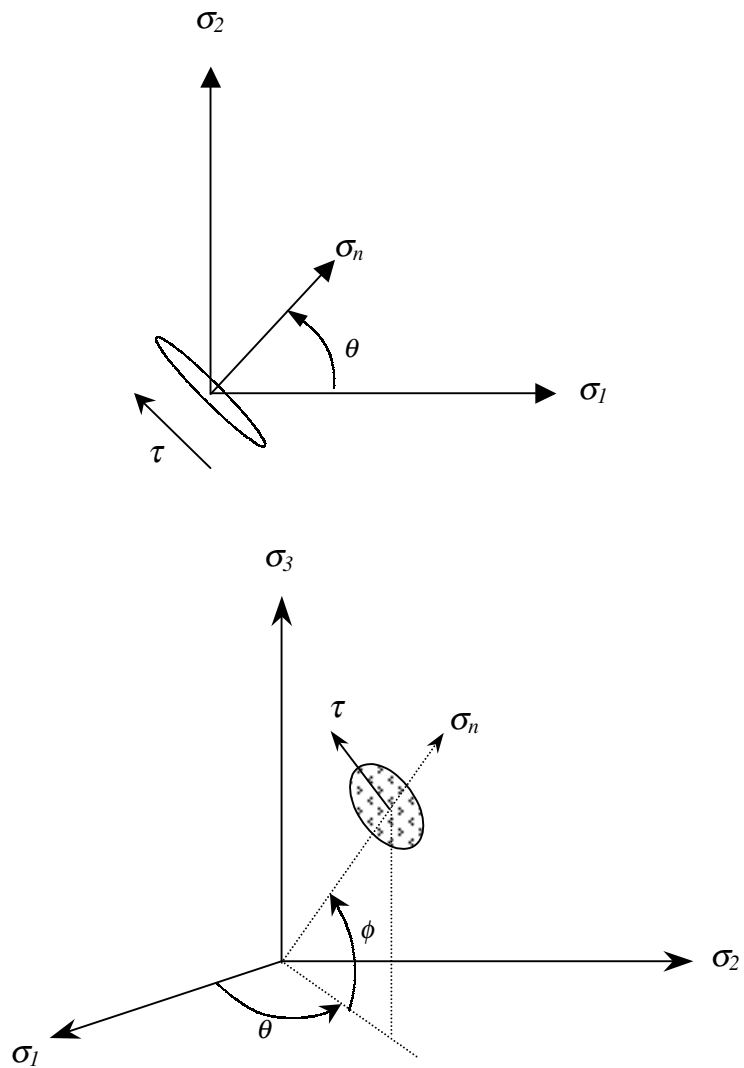


Figure 2.5.2.2: Normal and shear stresses resolved on a crack plane rotated at an angle to the principal stresses: (a) surface crack and (b) embedded crack.

Some of the existing criterion and equivalent stresses are

2.5.2.1 Mode I Failure (MP):

$$\begin{aligned} FC(K_I, K_{II}, K_{III}) &= K_I \\ FC_c &= K_{Ic} \\ \sigma_{Ieq} &= \sigma_n \end{aligned} \quad (29)$$

This is equivalent to the maximum principal stress formulation (Equation 15).

2.5.2.2 The Maximum Hoop Stress Factor (MHSF) (Erdogan and Sih 1963):

$$\begin{aligned} FC &= \frac{\sqrt{8} \left(2K_I + 6\sqrt{K_I^2 + 8K_{II}^2} \right) K_{II}^3}{\left(K_I^2 + 12K_{II}^2 - K_I \sigma_n \sqrt{K_I^2 \sigma_n^2 + 8K_{II}^2} \right)^{3/2}} \\ FC_c &= K_{Ic} \\ \sigma_{Ieq} &= \frac{\sqrt{8} \left(2\sigma_n + 6\sqrt{\sigma_n^2 + 8\tau^2 Y_{II}^2 / Y_I^2} \right) Y_{II}^3 \tau^3}{\left(Y_I^2 \sigma_n^2 + 12Y_{II}^2 \tau^2 - Y_I \sigma_n \sqrt{Y_I^2 \sigma_n^2 + 8Y_{II}^2 \tau^2} \right)^{3/2}} \end{aligned} \quad (30)$$

2.5.2.3 The Coplanar Energy Release Rate (CERR) (Paris and Sih 1965):

$$\begin{aligned} FC(K_I, K_{II}, K_{III}) &= \frac{I}{E'} \left(K_I^2 + K_{II}^2 + \frac{I}{I + \nu} K_{III}^2 \right) \\ FC_c &= \frac{K_{Ic}^2}{E'} \\ \sigma_{Ieq} &= \left(\sigma_n^2 + \frac{Y_{II}^2}{Y_I^2} \tau^2 + \frac{\tau^2}{I - \nu} \frac{Y_{III}^2}{Y_I^2} \right)^{1/2} \end{aligned} \quad (31)$$

2.5.2.4 The Maximum Noncoplanar Energy Release Rate (NERR) (Hellen and Blackburn 1975):

$$\begin{aligned}
FC(K_I, K_{II}, K_{III}) &= \frac{I}{E} \sqrt{K_I^4 + 6K_I^2 K_{II}^2 + K_{II}^4} \\
FC_c &= \frac{K_{Ic}^2}{E} \\
\sigma_{leq} &= \left(\sigma_n^4 + 6 \frac{Y_{II}^2}{Y_I^2} \sigma_n^2 \tau^2 + \frac{Y_{II}^4}{Y_I^4} \tau^4 \right)^{1/4}
\end{aligned} \tag{32}$$

Other, empirical, fracture mechanics criterion exist (Richard 1985; Shetty 1987) but these contain factors that allow variation of the solution to account for microstructural (i.e. coarse grains) effects prevent crack sliding and are thus less fundamental.

2.5.2.5 Criteria for Porous Media

The formulations of Eqs. 20 to 32 treat flaws as planar cracks. In actual materials the critical flaws are often pores, agglomerates or inclusions instead of idealized cracks. In the case of inclusions, tractions could be transmitted across the interface and in the case of pores and agglomerates, the flaw has a complex three-dimensional shape. For porous medium, Babel and Sines (Babel and Sines 1968) proposed the following biaxial fracture criterion

$$\begin{aligned}
\sigma^* &= (1 + 2h)\sigma_1 - \sigma_2 && \text{(tension quadrant)} \\
\sigma^* &= \frac{(h+1)^2 (\sigma_1 - \sigma_2)}{4h (\sigma_1 + \sigma_2)} && \text{(compression-tension quadrant)}
\end{aligned} \tag{33}$$

where h is the ratio of the major to minor axes of the elliptical cavity and σ^* is a critical tensile stress at the surface of a flaw. The value of σ^* is considered a characteristic of the material. Good agreement occurred between the model and data generated with hydrostone plaster, high-silicon cast iron and a porous zirconia. The effect of test volume was not specifically addressed, however, zirconia, like most ceramics, should exhibit a scale effect. If σ^* is equated to an equivalent stress, the criteria becomes

$$\begin{aligned}
\sigma_{eq} &= (1 + 2h)\sigma_1 - \sigma_2 && \text{for } \sigma_1 > \sigma_2 > 0 \\
\sigma_{eq} &= \frac{(h+1)^2 (\sigma_1 - \sigma_2)}{4h (\sigma_1 + \sigma_2)} && \text{for } \sigma_1 > 0 > \sigma_2
\end{aligned} \tag{34}$$

2.6 PROBABILISTIC DESIGN CRITERIA FOR BRITTLE MATERIALS

Although reliability theories that account for the variation of a variety of parameters (e.g. dimension, properties, applied loads, etc.) on the system or component reliability exist (Haugen 1980), we are predominantly concerned with a materials strength variation and any effect of scale on the measured strength. The most commonly used reliability theories that account for a brittle materials strength variation and an effect of scale are based on that of Weibull (Weibull 1939). Ideally, a useful reliability theory should require only simple laboratory data (e.g. flexural strength) to infer the reliability of components subjected to nonuniform, multiaxial stresses.

2.6.1 The Weibull Model

The most basic reliability theory applied to design brittle components is the direct application of the Weibull statistical distribution (Weibull 1939). The cumulative probability of failure or risk of rupture, P_{Fx} of a brittle component subjected to applied stresses, σ , is

$$P_{Fx} = 1 - \exp \left[- \int_x \left(\frac{\sigma - \sigma_m}{\sigma_o} \right)^m dx \right] \text{ for } \sigma > \sigma_m$$

(35)

$$P_{Fx} = 0 \quad \text{for } \sigma \leq \sigma_m$$

where m is the Weibull modulus, σ_o is the scale parameter, and σ_m is the minimum strength. The scale parameter is the strength corresponding to a unit volume or area stressed in tension. The minimum strength can be determined via data analysis if justification exists, or set to zero otherwise. The integration is carried out over the components surface area and/or volume, depending on the location of the flaws resulting in failure, and the independent variable x is replaced with area A or volume V . Flaw types include both intrinsic (*i.e.* those inherent in the material) and extrinsic (those generated on the surface of the material by external events such as machining). Examples of intrinsic flaws are pores, inclusions, coarse grains, agglomerates, etc. which are generated during processing and distributed throughout the volume and exposed at the surfaces. Extrinsic flaws are machining damage, handling scratches, nicks, etc. which are located on the surface only.

The shortcomings of the use of the Weibull distribution as a reliability theory have been discussed at length (Batdorf and Crose 1974, Batdorf 1978, Evans 1978, Lamon 1988). The Weibull model

is purely statistical and thus does not recognize the existence of flaws with specific characteristics (e.g. sharp or dull), thereby requiring empirical measure of the distribution of each flaw population. Further, it does not specifically address the effects of multiaxial stress, but implies the principal tensile stresses to act independently, thereby ignoring shear and compressive effects, which may be of importance.

The assumption of independence of the principal stresses leads to a probability of failure formulation known as the principal of independent action (PIA) (Barnett, et al. 1967, Freudenthal 1968). For surface and volume analysis, respectively, the functions are

$$P_{FA} = 1 - \exp \left\{ - \int_A \left[\frac{\sigma_1}{\sigma_o} \right]^m + \left[\frac{\sigma_2}{\sigma_o} \right]^m dA \right\} \quad (36)$$

$$P_{FV} = 1 - \exp \left\{ - \int_V \left[\frac{\sigma_1}{\sigma_o} \right]^m + \left[\frac{\sigma_2}{\sigma_o} \right]^m + \left[\frac{\sigma_3}{\sigma_o} \right]^m dV \right\} \quad (37)$$

where σ_1 , σ_2 , and σ_3 are the principal stresses. If, instead, the normal stresses in all directions are assumed to reduce reliability and averaged, the normal tensile stress averaging model proposed by Weibull (Weibull 1939) for multiaxial stresses is attained:

$$P_{Fx} = 1 - \exp \left(- \int_x k_{wps} (\bar{\sigma}_n)^m dx \right) \quad (38)$$

where k_{wps} is a polyaxial crack density coefficient. The averaged normal stress is

$$(\bar{\sigma}_n)^m = \frac{\int_x \sigma_n^m dx}{\int_x dx} \quad (39)$$

where the variable x is replaced with the contour C for surface analysis and surface S for volume analysis, and the integration is performed about a unit circle or a unit sphere, respectively. The model is capable of predicting volume effects for a uniaxial stress state (Lamon 1988).

2.6.2 The Batdorf Model

Batdorf and Crose (Batdorf and Crose 1974) proposed a model that combined the probability of a crack existing in a volume with the probability that the crack will cause fracture. The probability of a crack existing for a material with a crack density N is, for a volume element,

$$P_e = N \Delta V \quad (40)$$

Because real materials have a distribution of cracks sizes and shapes, the number of cracks in a volume ΔV that have critical stresses between σ_{cr} and $\sigma_{cr} + d\sigma_{cr}$ is needed. Defining a distribution function $N(\sigma_{cr})$ which gives the density of cracks having a critical stress less than or equal to σ_{cr} , the number of cracks is

$$dN = \Delta V \frac{dN(\sigma_{cr})}{d\sigma_{cr}} d\sigma_{cr} \quad (41)$$

The probability that the crack is critical is given by the ratio of the solid angle, Ω , containing the normals to all the orientations for which the normal stress component is greater than the cracks critical stress to the solid angle of a unit half-sphere:

$$P_c = \Omega(\Sigma, \sigma_{cr}) / 4\pi \quad (42)$$

where Σ represents the applied stress state. Though the initial theory (Batdorf and Crose 1974) was formulated for the normal stress component only, general stress states were later considered (Batdorf and Heinisch 1978). The probability of failure of a component becomes

$$P_{Fx} = 1 - \exp \left\{ \int_x \left[\int_0^{\sigma_{emax}} \frac{\Omega(\Sigma, \sigma_{cr})}{4\pi} \frac{dN_V(\sigma_{cr})}{d\sigma_{cr}} \right] dx \right\} \quad (43)$$

where σ_{emax} is the maximum effective stress that a randomly oriented flaw could experience from a general stress state.

Batdorf and Heinisch (Batdorf and Heinisch 1977, Batdorf and Heinisch 1978) also introduced effective stress criterion for the model based on the work of Oh (Oh 1970, Oh 1973) and Paul (Paul and Mirandy 1976) for the stress distribution around Griffith cracks and flat, ellipsoidal cavities. For A Griffith crack, the effective stress is

$$\sigma_e = h \left(\sigma_n + \sqrt{\sigma_n^2 + \tau^2} \right) \quad (44)$$

where h is the ratio of the major to minor axis of the ellipse. For a Griffith notch the effective stress is

$$\sigma_e = 1.12h \left(\sigma_n (1 + \nu) + \sqrt{\sigma_n^2 (1 - \nu) + (\tau^2 / 1.12)} \right) \quad (45)$$

The model shown in Eq. (43) reduced the gap between physically based fracture mechanics models and statistically based weakest link theories such as Weibull's, and avoided the assumption of independence of stress which "ignores the fact that, for some crack orientations, two principal stresses can combine to fracture a crack that would not fracture by either stress acting alone" (Batdorf and Crose 1974). The flaws were assumed to be noninteracting, randomly oriented, uniformly distributed, closed, planar entities in an isotropic medium that was subjected to macroscopic tensile stresses only. No stable or subcritical crack growth was assumed to occur prior to failure. Crack size was not explicitly treated.

Predictions of the probability of failure of graphite (Poco AFX-5Q) tubes subjected to hoop and axial stresses were made from tensile dog-bone data using volume integration only. The ratio of effective volumes was 3:1 and the prediction was within 1% when the tubes were subjected to axial loading and within 8% for hoop loading. The larger error for hoop loading was attributed to the possibility of anisotropy

Giovan and Sines (Giovan and Sines 1979) tested alumina (WESGO AL-995) in uniaxial and biaxial flexure with longitudinally ground and lapped surface conditions. Uniaxial strength data were attained by placing wide beams (i.e. plates) in four-point flexure ($A_e \cong 315 \text{ mm}^2$). The biaxial data was attained by R-O-R loading of circular plates ($A_e \cong 641 \text{ mm}^2$). The specimens were designed to have the same surface area subjected to the maximum principal stress. The machining was relatively aggressive (0.05 mm removal rate) as compared to what is now typically specified (0.002 mm per pass for the final 0.06 mm, ASTM C 1161 1990), and probably resulted in machining damage and the relatively large Weibull moduli (19 and 21 for the as-ground plates and disks, respectively, and 17 and 18 for the lapped plates and disks respectively, as estimated from data given in the paper). Also, the supports were not allowed to roll in either specimen configuration, and thus errors due to friction probably existed. Their results indicate that the Weibull and PIA models over and underestimate, respectively, the probability of failure of the

concentric ring specimens with approximately twice the effective area as the four-point flexure specimens from which the predictions (both lapped and as-ground) were made. However, the Batdorf model with the following shear-sensitive effective-stress for a penny shaped crack was satisfactory for both the lapped and as-ground conditions:

$$\sigma_e = \sqrt{\sigma_n^2 + \tau^2 / (1 - 0.5\nu)^2} \quad (46)$$

where τ is the shear stress acting on the crack plane. Eq. (46) is based on the coplanar energy release rate (Batdorf 1977). Note that the small effective area differences results in small differences in the measured strengths of the beams and disks. Thus, the ability of the model to scale over large areas was not rigorously tested. Surprisingly, the as-ground disks were not reported to fail parallel to the grinding direction as would be expected considering the aggressive grinding and the fact that the transversely ground plates exhibited lower strength than the longitudinally ground plates (235 ± 18 vs. 202 ± 20 MPa) as would be expected. Unfortunately, the specific failure origins were not identified. Both the uniaxial and biaxial specimens had the same surface area, and the disks were about eight percent weaker than the uniaxial plates for both finishes, implying a closed flaw population (i.e. equibiaxial weakening occurred).

Thiemeier and Bruckner-Foit (Thiemeier and Bruckner-Foit 1991) analyzed aluminum nitride (AlN) four-point flexure ($A_e \cong 99 \text{ mm}^2$) and R-O-R ($A_e \cong 453 \text{ mm}^2$) data using an equivalent stress approach based on the work of Batdorf et al. (Batdorf and Crose 1974, Batdorf and Heinisch 1978). Six different failure criterion were considered for through-wall and semicircular crack types: The maximum principal stress, the coplanar energy release rate (Paris and Sih 1965), the maximum hoop stress factor (Erdogan and Sih 1963), the minimum strain energy density (Sih 1974), the maximum noncoplanar energy release rate (Hellen and Blackburn 1975), and the empirical criterion of Richard (Richard 1985). The maximum noncoplanar energy release rate and the empirical criterion of Richard produced predictions within the confidence interval of the disk data for both crack types. The maximum hoop stress criterion agreed only for the through-wall crack configuration. The results illustrate well the importance of fracture criterion and confidence bands in making predictions.

2.6.3 Criteria for Anisotropic Materials

Many brittle materials are anisotropic in some sense. A material can be anisotropic in three aspects particularly relevant to the design of structures: elastic behavior, strength (by way of

fracture toughness), and flaw distribution. Single crystals, textured polycrystalline materials and composites are anisotropic in terms of elasticity and strength. The flaw populations may or may not vary with orientation.

Of such anisotropic materials, graphite has been used frequently in studies of weakest-link reliability models (Batdorf and Crose 1974, Buch 1976, Margetson 1976). Batdorf and Crose (Batdorf and Crose 1974) treated graphite as isotropic (Poco AFX-5Q) although they concluded that it might have been anisotropic.

Margetson (Margetson 1976) accounted for the anisotropic strength distribution of graphite by modifying the PIA formulation of the Weibull model (Barnett 1967, Freudenthal 1968). The principal stresses were normalized with the strength in the principal directions instead of with a single characteristic strength as done for the isotropic case. Also, to account for compressive strength being different from tensile strength, a step function was added which multiplied the direction dependent tensile strength by the ratio of compressive strength to tensile strength. The probability of failure for volume analysis was given as

$$P_{FV} = 1 - \exp \left\{ - \left(\Gamma \left(\frac{1}{m} \right) \right)^m \int_V \left[\frac{\sigma_1}{\bar{\sigma}_{fv}^{(1)} H(\sigma_1)} \right]^m + \left[\frac{\sigma_2}{\bar{\sigma}_{fv}^{(2)} H(\sigma_2)} \right]^m + \left[\frac{\sigma_3}{\bar{\sigma}_{fv}^{(3)} H(\sigma_3)} \right]^m dV \right\} \quad (47)$$

where $\Gamma(1/m)$ is the gamma function of $1/m$, and $\bar{\sigma}_{fv}^{(1)}$, $\bar{\sigma}_{fv}^{(2)}$, and $\bar{\sigma}_{fv}^{(3)}$ are the respective average unit volume strengths in the direction of the principal stresses, σ_1 , σ_2 , and σ_3 . The gamma function allows the average unit volume strengths to be used instead of the characteristic values. The step function to account for compressive stresses is

$$H(\sigma) = 1, \quad \sigma \geq 0 \quad (48)$$

$$H(\sigma) = -\eta, \quad \sigma < 0$$

where η is the ratio of the compressive and tensile strengths of the material. In terms of the scale parameter, which is typically used in Weibull type functions, the probability of failure is

$$P_{FV} = 1 - \exp \left\{ - \int_V \left[\frac{\sigma_1}{\sigma_o^{(1)} H(\sigma_1)} \right]^m + \left[\frac{\sigma_2}{\sigma_o^{(2)} H(\sigma_2)} \right]^m + \left[\frac{\sigma_3}{\sigma_o^{(3)} H(\sigma_3)} \right]^m dV \right\} \quad (49)$$

Although volume integration was specified in the model and used in the data analysis, an area integral was probably more appropriate as all the testing was done in flexure. In order to determine the materials strength envelope, three-point flexure tests were conducted on test specimens cut from graphite blocks. The strength data was fit with an ellipsoidal function that had a circular cross section in one plane (i.e. the strength was isotropic in that plane). To verify the model, circular disks were cut parallel to the isotropic plane and tested in R-O-R biaxial flexure. A ratio of compressive to tensile strength of $\eta = 8$ was assumed. The large η implies that the compressive stresses do not greatly effect the reliability. The model was slightly conservative (approximately 3%) in predicting the biaxial strength from the three-point flexure data. The slight conservatism could have resulted from friction between the loading rings and specimen or contact stresses, as no mention of lubrication is made. Note, however, that for a plate cut from the isotropic plane and tested in flexure, the material and model simplify to the isotropic case and the model was not verified for the anisotropic case.

One minor shortcoming of the model is that it assumes that the compressive strength distribution differs from the tensile distribution by only a single multiplying factor. This is probably not the case (Adams and Sines 1976) and the inclusion of compressive effects requires characterization of the compressive strength distribution as a function of orientation. If the Weibull moduli are different, the Weibull modulus could also be multiplied by a step function as follows

$$P_{FV} = 1 - \exp \left\{ - \int_V \left[\frac{\sigma_1}{\sigma_o^{(1)} H_1(\sigma_1)} \right]^{mH_2} + \left[\frac{\sigma_2}{\sigma_o^{(2)} H_1(\sigma_2)} \right]^{mH_2} + \left[\frac{\sigma_3}{\sigma_o^{(3)} H_1(\sigma_3)} \right]^{mH_2} dV \right\} \quad (50)$$

where the step function to account for compressive stresses on Weibull modulus is

$$H_2(\sigma) = 1 \quad , \quad \sigma \geq 0$$

$$H_2(\sigma) = \chi \quad , \quad \sigma < 0 \quad (51)$$

where χ is the ratio of the Weibull moduli in compressive and tensile loading of the material. Another problem with the model is that it only considers the principal planes, which may not be the weakest planes. Stress states might arise in which large normal stresses are resolved on the cleavage planes while the reliability is only a function of the stresses and strengths in the principal directions. Thus, the ratio of normal stress to strength may be a more relevant parameter in calculation of reliability. A better modification of the PIA model might include both the principal stresses and the stresses on the cleavage planes, both normalized to the appropriate strength parameters. Note that both the {100}, {110} and {111} families of cleavage planes are not typically orthogonal to each other. Generally, the occurrence of the maximum principal stresses on one planar set precludes its occurrence on another. However, the {100} and {110} and the {110} and {111} sets contain members that are orthogonal to each other and the existence of the maximum principal stress on a given cleavage plane does not preclude the resolution of the second principal on another set. Further, when the principal stresses are equal, they will be resolved onto all crystal planes a point in the body.

Duffy and Arnold (Duffy and Arnold 1990) followed the approach of Weibull (Weibull 1939) and Barnett and Freudenthal (Barnett, et al. 1967, Freudenthal 1968) to develop a reliability model for transversely isotropic whisker reinforced ceramic components. As with most weakest link type models, no interaction is assumed, and the material is a continuum that is sufficiently discretized to make stress, strain and temperature constant while still having sufficient volume to be a statistically homogenous medium. Unlike the previous models, however, they took advantage of the scalar nature of reliability functions and the contaminant tensor invariance under orthogonal transformations. The materials symmetry was accounted for via unit vectors incorporated into the reliability function. Thus, invariants related to the stress components causing fracture were developed and incorporated into a PIA like model, resulting in

$$\psi = \left[\frac{I_1^*}{\sigma_{o1}} \right]^{m_1} + \left[\frac{I_2^*}{\sigma_{o2}} \right]^{m_2} + \left[\frac{I_3^*}{\sigma_{o3}} \right]^{m_3} + \left[\frac{I_4^*}{\sigma_{o3}} \right]^{m_3} \quad (52)$$

for a unit volume where the I_i^* 's are the invariants, the m_i 's are the Weibull moduli and the σ_{oi} 's are the scale parameters. The component reliability would be given by integration of the function over the total area or volume, as for all Weibull type formulations. No verification of the model was performed.

Based on the literature reviewed, no fracture mechanics based reliability model exists for application to brittle materials exhibiting strength and elastic anisotropy. The isotropic reliability models based on the Weibull distribution offer a good starting point for the development and verification of a more general reliability model that is applicable to brittle materials exhibiting elastic and strength anisotropy.

CHAPTER 3: THEORY: ANISOTROPIC RELIABILITY MODEL

In this chapter, a reliability model for anisotropic materials will be derived from two approaches: the first from an intuitive analysis of how the strength distribution in an anisotropic body effects the reliability of the body, and the second from a probabilistic analysis of the effects of a crack distribution of random orientation and size on the reliability of an anisotropic body.

3.1 MODELS BASED ON THE PRINCIPLE OF INDEPENDENT ACTION

Per the discussion in Chapter 2, the PIA model as modified for anisotropy (Margetson 1976) does not consider that the principal stresses may not align with the cleavage planes. Thus the PIA model needs to be modified to consider the effects of normal tensile stresses on a multiplicity of planes, or at least the most significant planes, leading to

$$P_{Fx} = 1 - EXP \left\{ - \int_x \left[\sum \left(\frac{\sigma_{n<hkl>}}{\sigma_{o<hkl>}} \right)^m \right] dx \right\} \quad (53)$$

where $\sigma_{n<hkl>}$ is the normal stress in the $<hkl>$ direction, $\sigma_{o<hkl>}$ is the scale parameter or unit strength in the $<hkl>$ crystal direction. The summation is taken over the most significant planes (i.e. the weak cleavage planes and those subjected to all the principals). Two extreme cases of Equation (53) can be considered: that in which a single term in the summation dominates reliability and that in which all normal tensile stresses reduce reliability. The first case occurs if the stress distribution consists of a large tensile stress oriented on or near a weak cleavage plane; the term in the summation is the maximum ratio of normal stress to scale parameter. The second case is the limit in which the summation term becomes an integral over all crystal directions. This would appear conservative (i.e. over estimate the probability of failure) based on isotropic data, even though the normal stress component in any direction should reduce the reliability associated with three-dimensional flaws. Such an effect was proposed by Weibull for isotropic materials (Weibull 1939) via the normal stress averaging technique which was given previously in Equations (38) and (39).

Use of Equations (38) and (39) requires the crack density coefficient for a multiaxial stress state, k_{wps} , on the stressed, free surfaces of the crystal. For two dimensional isotropic cases, the approach of Gross and Gyekenyesi (Gross and Gyekenyesi 1989) might be used to estimate a k_{wps} value for an anisotropic material by averaging the uniaxial crack density coefficient, k_{ws} , over the $\langle hkl \rangle$ directions of a contour in the (mno) plane of interest

$$\bar{k}_{ws} = \frac{\int_{C(mno)} k_{ws} dC}{\int_{C(mno)} dC}. \quad (54)$$

The limits of integration depend on the symmetry of the (mno) plane. For multiple planes (i.e., a three dimensional body), a series of terms is required in Equation (53), or it can be solved on an element-by-element basis. This leads to a solution of the form

$$\bar{k}_{wps} = \frac{m\sqrt{\pi} \Gamma(m) \bar{k}_{ws}}{\Gamma\left(m + \frac{1}{2}\right)} \quad (55)$$

where \bar{k}_{wps} is an effective crack density coefficient for anisotropic surface subjected to multiaxial stresses. The obvious problem with this solution is that stresses and crack density coefficients are averaged instead of being matched on a plane-to-plane basis. Further, a function describing strength in all directions in the plane is required.

For a plate in biaxial flexure, a single free (mno) surface is stressed in tension and the contour integral is taken over the $\langle hkl \rangle$ directions. If the (100) plane is considered, the strength repeats every quadrant and the strength in a $\langle hkl \rangle$ direction might be described by

$$\sigma_{o(100)\langle hkl \rangle}(\theta) = \sigma_{o<100>} \cos^2(2\theta) + \sigma_{o<110>} \cos^2\left(2\theta + \frac{\pi}{2}\right) \quad (56)$$

where θ is the angle from the $\langle 100 \rangle$, $\sigma_{o<100>}$ and $\sigma_{o<110>}$ are the unit strengths, respectively in the $\langle 100 \rangle$ and $\langle 110 \rangle$ directions. In order to determine if the effects of multiaxial stresses on the

reliability can be predicted, more complex testing such as torsion or biaxial flexure is required. For a three-dimensional surface, a more general equation is required.

A more general approach for anisotropy might be to integrate the ratio of strength to stress about the unit circle

$$P_{FA} = 1 - \exp \left\{ - \int_A [\overline{N}_n^m] dA \right\} \quad (57)$$

with

$$\overline{N}_n^m = \frac{\int_C \left(\frac{\sigma_{n<hkl>}}{\sigma_{o<hkl>}} \right)^m dC}{\int_C dC},$$

where \overline{N}_n^m would represent an average ratio of normal stress to strength for a surface, which must be calculated element by element, and is less than unity (Batdorf 1978). Although this approach only considers effects of normal stresses, an effective stress could replace the specified normal stress. Replacing the normal stress with a mode *I* equivalent stress derived from any appropriate fracture mechanics failure criterion leads to

$$P_{fA} = 1 - \exp \left(- \int_A \frac{I}{\pi} \int_0^\pi \left(\frac{\sigma_{Ieq<hkl>}}{\sigma_{o<hkl>}} \right)^m dC dA \right) \quad (58)$$

where and $\sigma_{Ieq<hkl>}$ is the mode *I* equivalent stress parallel to the $<hkl>$ direction and normal to the (hkl) plane at a location. The same function is derived in a more rigorous fashion in the next section.

3.2 A GENERALIZED WEIBULL RELIABILITY MODEL FOR BRITTLE MATERIALS WITH STRENGTH AND ELASTIC ANISOTROPY

A general reliability model for homogenous brittle materials with strength anisotropy can be derived by modifying the approach of Thiemeier et al. (Thiemeier 1991) to consider fracture toughness, and thus strength, as a variable of orientation in the probability density function. The probability of failure of a brittle material containing randomly distributed surface flaws is related to the probability that a crack of a given orientation exists at a given location and the probability that the flaw exceeds the critical dimension for failure. If the cracks are assumed to be randomly distributed in orientation and location via a uniform distribution, the probability of a crack existing at a location with a particular orientation is

$$p_{A\theta} = \frac{1}{A_T} dA \frac{1}{\pi} d\theta \quad (59)$$

where A_T is the total surface area of the body and π is the total range of possible crack angles. The probability that a given flaw causes failure is the probability that the randomly distributed crack size (i.e. no variation in the crack size distribution and Weibull modulus with orientation) is greater than the critical crack length a_c on that plane:

$$p_{a_c} = p(a > a_c) = \int_{a_c}^{\infty} f_a(a) da \quad (60)$$

where f_a is the probability density function describing the crack size distribution and a is the randomly distributed crack size. The critical crack size on any plane of an anisotropic material is related to the fracture toughness by

$$a_c = \frac{K_{Ic}^2(\theta)}{Y_I^2 \sigma_{Ieq}^2(\theta, \bar{x})} \quad (61)$$

where $K_{Ic}(\theta)$ is the fracture toughness of the plane at angle θ , Y_I is the crack geometry factor, and $\sigma_{Ieq}(\theta, \bar{x})$ is a mode I equivalent stress at orientation θ and location \bar{x} as defined by any of applicable failure criterion for elastically anisotropic materials. Note that some of the failure

criteria in section 2.5.2 are applicable to anisotropic materials as they are independent of the elastic constants. Only the stresses and the stress intensity factor coefficients are necessary.

For a material with fracture toughness anisotropy, both the fracture toughness and equivalent stress are functions of the crack plane orientation. Thus a_c depends on the location of the crack by way of the equivalent stress and on the orientation of the crack by way of the fracture toughness and equivalent stress. The probability of a single crack causing failure in a component is thus

$$P_1 = \int_{A_T} \frac{1}{A_T} \int_0^\pi \frac{1}{\pi} \int_{a_c(\theta, \vec{x})}^\infty f_a(a) da d\theta dA \quad (62)$$

To solve Equation (62), a functional form for the crack size distribution needs to be assumed. If a power function of the form

$$f(a) = Ca^{-g} \quad (63)$$

is used, Equation (62) becomes

$$P_1 = \frac{1}{A_T} \int_{A_T} \frac{1}{\pi} \int_0^\pi \frac{Ca_c^{1-g}}{1-g} d\theta dA \quad (64)$$

for $g > 1$. The reliability of a component containing the above flaw is $R_1 = (1 - P_1)$, and the reliability of the component for n flaws is

$$R_n = (1 - P_1)^n \quad (65)$$

The probability of n cracks actually occurring in a components area for an average crack occurrence is given by the binomial distribution if the sampled areas are independent and have equal probability of a crack existing. The binomial distribution can be approximated by the Poisson distribution (Miller and Freund 1977) for a large sample area and a small probability of crack occurrence in a unit area, which should be the case for dense, well made components with small flaws. The probability of n cracks becomes:

$$p_n = \frac{\lambda^n \exp(-\lambda)}{n!} \quad (66)$$

where λ is the product of the number of sampled areas and the probability of a crack existing in a sampled area, or the expected (*i.e.* average) number of cracks. The probability of the component surviving is the sum of the product of the reliability at any crack frequency and the probability of that frequency occurring:

$$P_s = \sum_{n=1}^{\infty} p_n R_n \quad (67)$$

Substituting Equations (64), (65) and (66) into (67) and using the equality

$$\sum_{n=1}^{\infty} \frac{x^n}{n!} = \exp(x) \quad (68)$$

leads to

$$P_s = \exp(-\lambda P_1) \quad (69)$$

and

$$P_{FA} = 1 - \exp\left(-\frac{\lambda}{A_T} \int_A \frac{1}{\pi} \int_0^\pi \frac{C a_c^{1-g}}{1-r} d\theta dA\right) \quad (70)$$

The expected number of cracks and the area are not known initially. However, the total number of crack in the total area is equivalent to the average number of cracks per unit area:

$$\frac{\lambda_o}{A_o} = \frac{\lambda}{A_T} \quad (71)$$

Also, because crack length is inconvenient to measure and strength “captures” the combination of fracture toughness and crack length, Equation (60) can be substituted into (59). If the fracture

toughness is written in terms of a reference strength and crack length (*i.e.* $K_{Ic}(\theta) = \sigma_o(\theta) Y_I \sqrt{\pi a_o}$), then by substitution of (70) and (60) into Equation (69)

$$P_{FA} = 1 - \exp \left(- \frac{\lambda_o}{A_o} \int_A \frac{1}{\pi} \int_0^\pi C a_o^{m/2} \left(\frac{\sigma_{Ieq}(\theta, \bar{x})}{\sigma_o(\theta)} \right)^m d\theta dA \right) \quad (72)$$

where $m=2g-2$. Further reduction is attained by redefining the initial crack density as

$$\begin{aligned} f(a) &\equiv \frac{m a_o}{2 \lambda_o a^{m/2+1}} \\ C &\equiv \frac{m a_o^{m/2}}{2 \lambda_o} \end{aligned} \quad (73)$$

yielding the reliability function for anisotropic materials

$$P_{FA} = 1 - \exp \left(- \frac{1}{A_o} \int_A \frac{1}{\pi} \int_0^\pi \left(\frac{\sigma_{Ieq}(\theta, \bar{x})}{\sigma_o(\theta)} \right)^m d\theta dA \right). \quad (74)$$

This has the basic form of the Weibull function and is similar to the isotropic model given by Thiemeier and those frequently use for polycrystalline ceramics, except that the reference strength is a function of planar angle and any failure criterion defining coplanar crack extension can be used. A function describing the strength as a function of angle on the surface(s) considered is needed along with the stress state in the anisotropic body. Because of the symmetry of a cubic material, the fracture toughness, strength and elastic properties repeat every quadrant and the second integral can be multiplied by a factor of two, and the integration taken from 0 to $\pi/2$. For a three-dimensional component, the finite element method (FEM) can be applied to determine the stress state and perform the integrations. The element size must be sufficiently small so that the stress state is nominally constant, and any curved surfaces can be descritized to planes effectively. The model assumes coplanar extension can effectively occur on any plane.

The above analysis can be extended to volume flaws by modifying Equation (58) to

$$P_1 = \frac{1}{V_T} dV \frac{1}{\pi} d\theta \frac{1}{\phi} d\phi \quad (75)$$

leading to

$$P_1 = \int_V \frac{1}{V_T} \int_0^{\pi/2} \frac{2}{\pi} \int_0^{\pi/2} \frac{2}{\pi} \int_{a_c(\theta, x)}^{\infty} f_a(a) da d\theta d\phi dV. \quad (76)$$

where V_T is the component volume and the other variable are as defined previously.

The reliability formulation in Eq. (74) is very convenient as it allows the use of any fracture mechanics failure criterion that is applicable to elastic isotropy or anisotropy as necessary, a variety of crack shapes and a scale parameter defining the strength as a function of orientation. In order to apply the reliability function, a mode I equivalent stress failure criterion applicable to elastic anisotropy is required.

3.3 A FAILURE CRITERION FOR ELASTICALLY ANISOTROPIC MATERIALS

All of the mode I equivalent stress formulations given in section 2.5.2 are applicable to isotropic and anisotropic materials except that for the coplanar energy release rate. A mode I equivalent stress failure criterion for the coplanar energy release rate can be derive for an elastically anisotropic material by accounting for elastic anisotropy. The mode I equivalent energy release rate can be defined as (Paris and Sih 1965)

$$G_{Ieq} = G_I + G_{II} \quad (77)$$

with

$$G_I = -\frac{K_I^2}{2\pi} S_{22} \operatorname{Im} \left\{ \frac{\mu_1 + \mu_2}{\mu_1 \mu_2} \right\} \quad \text{and} \quad G_{II} = \frac{K_{II}^2}{2\pi} S_{11} \operatorname{Im} \{ \mu_1 + \mu_2 \} \quad (78)$$

where the S_{ij} 's are the single crystal elastic constants (compliances), K_I and K_{II} are the mode *I* and *II* stress intensity factors defined as $K_I = \sigma_n \sqrt{\pi a}$ and $K_{II} = \tau \sqrt{\pi a}$ where a is the crack size, σ_n is the normal stress and τ is the shear stress on the specified plane. The quantities μ_1 and μ_2 are the roots of the complex equation (Lekhnitskii 1963)

$$S_{11}\mu^4 - 2S_{16}\mu^3 + (2S_{12} + S_{66})\mu^2 - 2S_{26}\mu + S_{22} = 0 . \quad (79)$$

The equivalent stress can be derived by defining the mode *I* equivalent stress intensity as

$$K_{Ieq} = \sigma_{Ieq} \sqrt{\pi a} . \quad (80)$$

Substituting Eqs. (78) and (80) into (77) leads to

$$\sigma_{Ieq} = \sqrt{\sigma_n^2 - \tau^2 \frac{S_{11}}{S_{22}} \frac{\text{Im}(\mu_1 + \mu_2)}{\text{Im}[(\mu_1 + \mu_2)/(\mu_1 \mu_2)]}} . \quad (81)$$

Eqs. (56), (74) and (81) define energy based, probabilistic fracture mechanics functions for the reliability analysis of an elastically anisotropic, brittle surface such as a plate. For a volume analysis, more general equations are required. In order to conveniently make strength predictions with Eq. (74), it is necessary to reformulate it in terms of strength instead of probability.

3.4 RELIABILITY PREDICTION FORMULATIONS

3.4.1 *Isotropic Materials*

For the case of strength isotropic, Equation (74) reduces to

$$P_{FA} = 1 - \exp \left(- \frac{I}{A_o} \int_A \frac{1}{\pi} \int_0^\pi \left(\frac{\sigma_{Ieq}(\theta, \bar{x})}{\sigma_o} \right)^m d\theta dA \right) . \quad (82)$$

For the specific case of measured test specimen or component data, the probability formulation is

$$P_F = 1 - \exp \left[- \left(\frac{\sigma_{MAX}}{\sigma_\theta} \right)^m \right] \quad (83)$$

where σ_{MAX} is the maximum stress sustained by the specimen or the strength. The scale parameter, σ_o , in Equation (35) and (82) can be determined by equating the general form of the Weibull equation (*i.e.* Equation (82)) to that for the specific case of test specimen data (*i.e.* 83) and solving for the scale parameter:

$$1 - \exp \left[- \left(\frac{\sigma_{MAX}}{\sigma_\theta} \right)^m \right] = 1 - \exp \left(- \frac{1}{A_o} \int_A \frac{1}{\pi} \int_0^\pi \left(\frac{\sigma_{leq}(\theta, \bar{x})}{\sigma_o} \right)^m d\theta dA \right) \quad (84)$$

or, as the scale parameter is a constant

$$\sigma_o = \sigma_\theta \left[\frac{1}{A_o} \int_A \frac{1}{\pi} \int_0^\pi \left(\frac{\sigma_{leq}}{\sigma_{MAX}} \right)^m d\theta dA \right]^{1/m} \quad (85)$$

or

$$\sigma_o = \sigma_\theta A_e^{1/m} \quad (86)$$

where A_e is the “effective area” of the specimen and σ_θ is the characteristic strength of the test specimen, or the stress for which for 62% of the specimen would fail. Generally the PIA model is employed and σ_{leq} in Equation (85) replaced with the principal stress or stresses as appropriate.

Although Equation (82) can be used to predict the failure distribution of a biaxial test specimen or a component from uniaxial test data, for verification purposes it is more convenient to use characteristic strength values associated with the biaxial flexure test specimen, because the strength was experimentally measured. Rearrangement of Equation (85) provides the function

$$\sigma_{\theta} = \sigma_o \left[\frac{1}{A_o} \int_A \frac{1}{\pi} \int_0^{\pi} \left(\frac{\sigma_{leq}}{\sigma_{MAX}} \right)^m d\theta dA \right]^{-1/m} . \quad (87)$$

If Equation (87) is equated to itself for two different failure strengths and effective areas, a convenient scaling equation for a given probability of failure can be derived:

$$\sigma_{\theta 1} / \sigma_{\theta 2} = (A_{e2} / A_{e1})^{1/m} \quad (88)$$

where $\sigma_{\theta i}$ is the characteristic strength corresponding to effective area A_{ei} . The effective area for all the surfaces subjected to tension in three- or four-point flexure specimens is (Nemeth et al. 1990)

$$A_e = \left[\frac{1 + m(S_i / S_o)}{(m + 1)^2} \right] \left[1 + \frac{mW}{B + W} \right] [B + W] S_o \quad (89)$$

where m is the Weibull modulus for the surface flaw population, S_o and S_i are the outer (support) and inner (loading) spans respectively, and B and W are the depth and height of the beam respectively.

Equations (88) and (89) are generally considered capable of predicting four-point strengths from three-point strength data for brittle, isotropic materials such as polycrystalline ceramics and glasses. They are noted here because they constitute a convenient approach for verification exercises.

Note that the use of the maximum stress in Eqs. (83) and (84) is an arbitrary, but convenient and common choice as most engineering comparisons consider the maximum stress to represent strength, etc. However, Fessler and Fricker (Fessler and Fricker 1984) use a nominal stress to compare plate specimens with and without friction and generated a nondimensional value of effective area by normalizing to the total specimen surface area or volume.

For the POR biaxial flexure test configuration and the PIA failure criterion, the effective area of the disk test specimen can be calculated from

$$Ae \cong \frac{4\pi(1+\nu)}{1+m} \left(\frac{R_s}{R_d} \right)^2 \left[\frac{2R_d^2(1+\nu) + R_s^2(1-\nu)}{(3+\nu)(1+3\nu)} \right] \quad (90)$$

within 1.5% for $m > 5$, $\nu > 0.17$ and within 1% if $R_s/R_d < 0.9$ also. For the disks tested herein, $Ae = 227 \text{ mm}^2$. For the three-point flexure specimens tested herein, $Ae = 2.06 \text{ mm}^2$, implying an effective area change of $\sim 110:1$. The nominal tensile surface areas of the WC POR test specimens and the size “A” 3-point flexure specimens were 40 mm^2 and 2027 mm^2 , respectively.

3.4.2 Anisotropic Materials

For the anisotropic case, equating Equation (82) and (83) leads to

$$\sigma_\theta = \left(\frac{1}{A_o} \int_A \frac{1}{\pi} \int_0^\pi \left(\frac{1}{\sigma_o(\theta)} \frac{\sigma_{leq}(\theta, \bar{x})}{\sigma_{MAX}(\theta)} \right)^m d\theta dA \right)^{-1/m} \quad (91)$$

with the scale parameter unfactorable from the integrand because of its functionality. However, if the PIA approach is applied, the equivalent stress and scale parameter are nonzero in the principal direction only, and

$$\sigma_\theta = \sigma_o(\theta_1) \left(\frac{1}{A_o} \int_A \frac{1}{\pi} \int_0^\pi \left(\frac{\sigma_1(\theta_1, \bar{x})}{\sigma_{MAX}} \right)^m d\theta dA \right)^{-1/m} \quad (92)$$

or

$$\sigma_\theta = \sigma_o(\theta_1) \left(\frac{1}{A_o} \int_A \left(\frac{\sigma_1(\theta_1, \bar{x})}{\sigma_{MAX}} \right)^m dA \right)^{-1/m} \quad (93)$$

or

$$\sigma_o(\theta_1) = \sigma_\theta A_e^{1/m} \quad (94)$$

where θ_i is the orientation of the principal stress and the measured characteristic strength. The corresponding scale parameter is independent of the scale parameter in other directions. This is analogous to the isotropic case and scaling of uniaxial data for a specific orientation can be done as usual

$$(\sigma_{\theta 1} / \sigma_{\theta 2})_{\langle hkl \rangle} = (A_{e2} / A_{e1})_{\langle hkl \rangle}^{1/m} \quad (95)$$

where $\sigma_{\theta i}$ is the characteristic strength corresponding to effective area A_{ei} in the $\langle hkl \rangle$ direction of interest. For more general failure criterion, the scale parameter can be estimated from uniaxial characteristic strength data by noting that the equivalent stress is a function of the first principal stress and trigonometric functions. Thus, the area and unit circle integrations can be separated by grouping the terms as functions of angle or the Cartesian area coordinates

$$\sigma_{\theta} = \left(\frac{1}{A_o} \int_A \left(\frac{\sigma_1(\theta_1, \bar{x})}{\sigma_{MAX}(\theta_1)} \right)^m dA \times \frac{1}{\pi} \int_0^{\pi} \left(\frac{f(\theta)}{\sigma_o(\theta)} \right)^m d\theta \right)^{-1/m} \quad (96)$$

or

$$\sigma_{\theta} = \left(\frac{A_e}{\pi} \int_{\theta} \left(\frac{f(\theta)}{\sigma_o(\theta)} \right)^m d\theta \right)^{-1/m} \quad (97)$$

where $f(\theta)$ is the failure criterion written in terms of unit, uniaxial principal stress. Note that for the uniaxial case, the integrand in (97) is identical for any specimen size and once again equation (89) is applicable. Further, as Equation (97) can be divided by itself for two different uniaxial volumes and simplified to yield Equation (88), implying that characteristic strength is independent of failure criterion for uniaxial cases and computation of the scale parameter unnecessary. However, the scale parameter is still required for prediction of multiaxial stress cases and Equation (95) needs to be solved for σ_o for the desired failure criterion.

The functional form of the scale parameter is unknown in Eq. (96). However, because it nominally represents a scaled value of the characteristic strengths, it can be assumed to take the same form. For the (100) plane the scale parameter in any $\langle hkl \rangle$ direction can be represented as

$$\sigma_{o(100)<hkl>}(\theta) = \sigma_{o<100>} \cos^2(2\theta) + \sigma_{o<110>} \sin^2(2\theta). \quad (98)$$

where θ is the angle from the $<100>$. Note that the effective stress functions in Equations (29) – (32) are integrated about the unit circle from the first principal stress whereas the strength function has an absolute reference to the crystal orientation. Thus, a phase angle accounting for the difference between the starting angle for the scale parameter function and the orientation of the principal stress is needed. The general function in terms of the angle θ from the principal stress becomes

$$\sigma_{o(100)<hkl>} = \sigma_{o<100>} \cos^2(2\theta + 2\Phi) + \sigma_{o<110>} \sin^2(2\theta + 2\Phi) \quad (99)$$

where the angle Φ is 0 and $\theta = \theta$ for a principal stress oriented in the $<100>$ direction. For a principal stress orientated in the $<110>$ direction $\Phi = \pi/4$ and $\theta = \theta$. For experimentally measured characteristic strength data, Equation (97) can be written as

$$\sigma_{\theta<100>} = \left(2 \frac{A_e}{\pi} \int_{\theta}^{\pi/2} \left(\frac{f(\theta)}{\sigma_o(\theta)} \right)^m d\theta \right)^{-1/m} \quad (100)$$

and

$$\sigma_{\theta<110>} = \left(2 \frac{A_e}{\pi} \int_0^{\pi/2} \left(\frac{f(\theta)}{\sigma_o(\theta + \pi/4)} \right)^m d\theta \right)^{-1/m} \quad (101)$$

and the two equations used to solve for the unknown values $\sigma_{o<100>}$ and $\sigma_{o<110>}$ based on any failure criterion. For the normal stress criterion with a unit stress,

$$f(\theta) = \cos^2 \theta. \quad (102)$$

For the maximum coplanar energy release rate with a unit stress

$$f(\theta) = \left(\cos^4 \theta + \frac{1}{4} \frac{Y_{II}^2}{Y_I^2} \sin^2 2\theta \right)^{1/2}. \quad (103)$$

For maximum noncoplanar energy release rate with a unit stress

$$f(\theta) = \left(\cos^8 \theta + \frac{3}{2} \frac{Y_{II}^2}{Y_I^2} \cos^4 \theta \sin^2 2\theta + \frac{1}{16} \frac{Y_{II}^2}{Y_I^2} \sin^4 2\theta \right)^{1/4}. \quad (104)$$

In Eqs. (102) – (104) θ is the angle from the first principal stress and Y_I and Y_{II} are the mode *I* and Mode *II* SCIFs as defined in section 2.5.2.

Eq. (91) defines a function for the prediction of the characteristic strength of a component exhibiting strength and elastic anisotropy. The required inputs are the scale parameter constant in Eq. (99) as determined by simultaneous solution of Eqs. (100) and (101), and an equivalent stress as defined in section 2.5.2 or 3.3.

CHAPTER 4: EXPERIMENTAL PROCEDURES: MATERIAL PROPERTIES AND VERIFICATION TESTING

In order to assess the ability of Equation (74) to predict the strength of isotropic or anisotropic materials subjected to multiaxial stresses, the uniaxial and biaxial strengths of an isotropic and an anisotropic material were measured.

4.1 TEST SPECIMEN PREPARATION

4.1.1 Isotropic Material

The isotropic material used was a commercial grade WC with a 6% nickel binder (KZ801, Kennametal Corp., Latrobe, PA). Billets measuring 25 mm in thickness were ground and lapped on one face in order to provide a surface with minimal machining damage and isotropic strength behavior. Lapping was used because test specimens that are manufactured with typical uniaxial grinding procedures (e.g. ASTM C 1161 1990) and subsequently subjected to multiaxial stresses tend to fail from grinding damage rather than from inherent processing flaws.

4.1.2 Anisotropic Material

Single crystal billets of a NiAl alloy manufactured commercially² were mounted on goniometers and oriented by X-ray diffraction. Flexural specimens (ASTM C 1161), measuring 3 by 4 by 45 mm in height, depth and length, respectively, were then cut from the billets along the $\langle 100 \rangle$ or $\langle 110 \rangle$ axes by electro-discharge machining (EDM). The secondary orientation was not controlled relative to the beam surfaces. The resulting surfaces were sanded with 400 grit silicon carbide paper and chemically milled in a solution of phosphoric and nitric acid to remove the remaining EDM damage. The chemical milling procedure follows (Walston 1995):

1. Mix a solution of 85% phosphoric acid and 15% nitric acid.
2. Heat to 125°F while stirring constantly.

² AFN 12 - General Electric Aircraft Engines, Evendale, Ohio.

3. Submerge the specimens in the solution, making sure that the surfaces of interest are exposed to the stirred solution. Leave the specimens in the solution for 15 minutes.
4. Rinse the specimens in water.

The specimen were then inspected at ~30x magnification with an optical microscope, and if necessary the sanding and etching processes were repeated until no EDM damage was visible on the tensile or side surfaces of the specimen. An example of EDM damage on the surface of a specimen is shown in Figure 4.1.2.1.

Disk specimens for biaxial flexure were cut from a billet and prepared in a similar manner

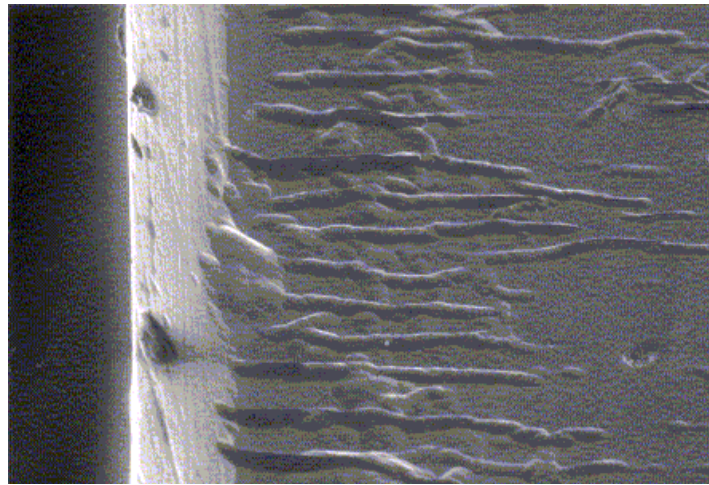
4.2 MEASUREMENT OF ELASTIC PROPERTIES

The elastic modulus and Poisson's ratio of the WC was measured by applying the impulse excitation technique (ASTM C 1259 1994) to the ten 50.8 mm diameter, 2.2 mm thick disk test specimens.

In order to determine if the elastic properties reported by Wasilewski or Rusovic' and Warlimont (Wasilewski 1966, Rusovic' and Warlimont 1977) for binary NiAl were sufficient for calculations on this alloy, the elastic modulus was determined along the <100> and <110> crystal directions. The impulse excitation technique (ASTM 1259 1994) was used on 46 <100> and 65 <110> flexural beam specimens.

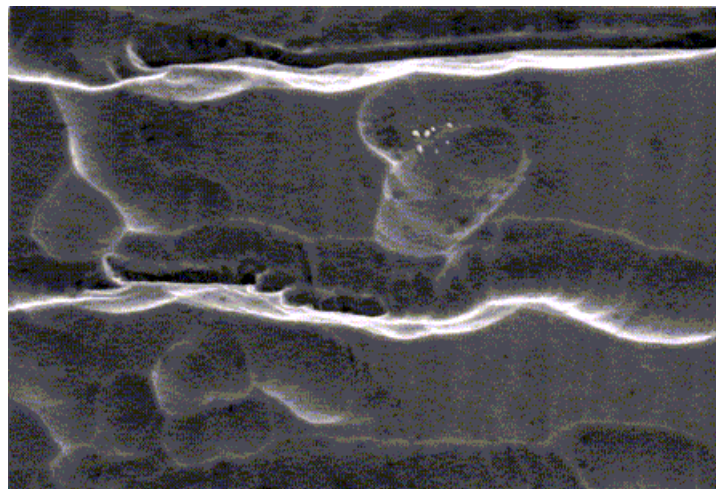
4.3 UNIAXIAL STRENGTH TESTING

The uniaxial strength of the WC was measured in three-point flexure by using twenty-nine size "A" test specimens measuring 1.5 by 2 by 25 mm in height, depth and length (ASTM C1161 1990). Flexure testing was used because it is relatively simple, requires little test material and has been standardized for brittle materials (i.e. ceramics) (ASTM C 1161 1990). The tensile surface of the test specimens corresponded to the lapped surface of the billet.



(a) Overall view

100 μm



(b) Detail

10 μm

Figure 4.1.2.1: EDM damage along the surface of a flexural test specimen: (a) overall view and (b) detail. EDM damage was not removed prior to chemical milling.

The flexural strengths of the NiAl <100> and <110> beams were measured in both three and four-point flexure. Measurement were made in both three and four-point loading because the different volumes subjected to stress provide a means to verify the model for the simple case of uniaxial stresses. Size “B” specimens (3 by 4 by 40 mm in height, depth and support span for three-point loading; a 20 mm loading span was used for four-point loading) were used. The strength was calculated from

$$S_{UTS}^{Flex} = \frac{3}{2} \frac{F(S_o - S_i)}{BW^2} \quad (105)$$

where F is the failure force, S_o and S_i are the outer (support) and inner (loading) spans respectively, and B and W are the depth and height of the beam respectively.

4.4 BIAXIAL TEST RIG DESIGN AND ANALYSIS

A biaxial test rig employing the P-O-R configuration was designed based on descriptions given in the literature (Rickerby 1977, Shetty 1983). Based on the discussion in Section 2.4.3, it was thought that a neoprene membrane or no membrane would provide the best results, particularly for NiAl because it is relatively strong, has a relatively low elastic modulus as compared to ceramics or steel, and will exhibit larger deflection at failure for a given test specimen configuration.

The membranes used previously to contain the pressurization medium on face of the test specimen were replaced by a nitrile O-ring retained in a groove. A cross section of the test rig, which accommodates 25.4 mm diameter disks is shown in Figure 4.4.1. The rig consists of a test chamber, support ring and cap, extensometer and oil inlet and drain ports. The desired pressurization cycle is supplied to the test chamber and specimen via a servo-hydraulic actuator connected to a closed loop controller. The feedback to the controller is supplied by a commercial pressure transducer connected to the oil inlet line.

The test chamber and cap are 304 stainless steel, and the support ring is cold rolled, half-hard copper or steel depending on the pressure required. Copper, being somewhat ductile, accommodated any minor misalignments or specimen curvatures. Detailed drawings of the rig are given in Appendix A.

Ideally, the test rig applies a uniform pressure on the supported surface of the disk test specimen, and allows it to deflect without rotational or sliding restraint at the support ring. The resulting biaxial stress state provides a means to estimate the biaxial strength of a material, provided that the stress state generate within the specimen can be calculated.

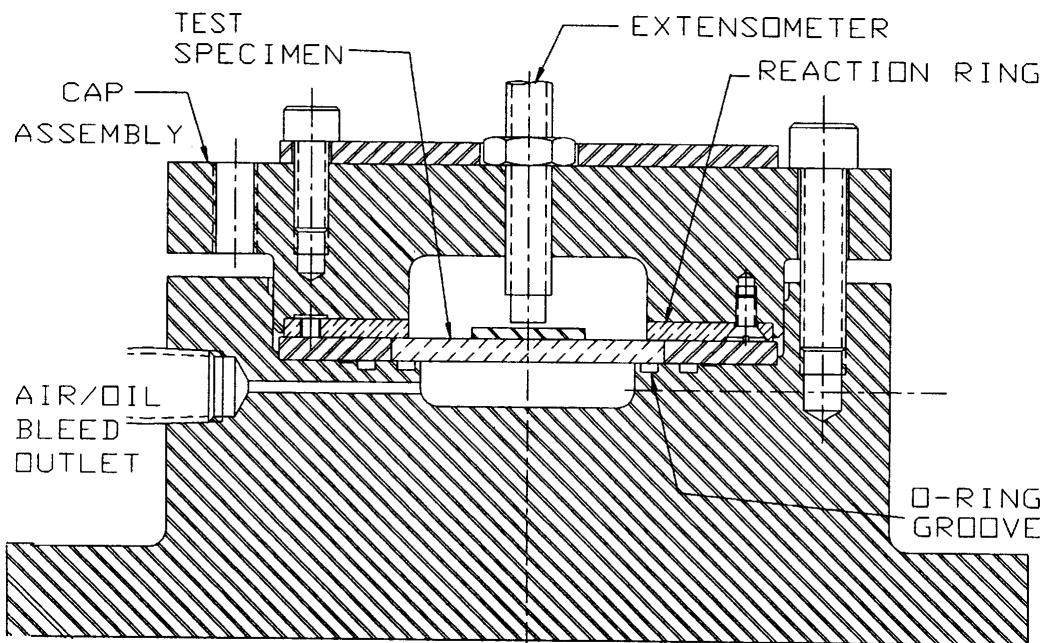


Figure 4.4.1: Schematic of the biaxial test fixture.

4.4.1 Stress State in a Pressurized Plate: Okubu's Approximate Solution

The displacement solution for a simply supported, circular, special orthotropic plate of unit radius and thickness subjected to uniform pressure was solved by Okubu (Okubu 1949) in the form of a series. An empirical solution for a plate of unit radius, similar in form to the isotropic solution (Szilard 1974), was also proposed:

$$w \cong \frac{q}{64D^*} (1 - r^2) (k^* - r^2) \quad (106)$$

where

$$D^* = \frac{1}{8} (3D_{11} + 2D_{12} + 4D_{66} + 3D_{22}) \quad (107)$$

$$k^* = \frac{7D_{11} + 10D_{12} + 12D_{66} + 7D_{22}}{2(D_{11} + 2D_{12} + D_{22})} \quad (108)$$

and

$$\begin{aligned} D_{11} &= \frac{t^3}{12} \frac{S_{22}}{S_{11}S_{12} - S_{12}^2}, \quad D_{22} = \frac{t^3}{12} \frac{S_{11}}{S_{11}S_{12} - S_{12}^2} \\ D_{12} &= \frac{t^3}{12} \frac{-S_{12}}{S_{11}S_{12} - S_{12}^2}, \quad D_{66} = \frac{t^3}{12} \frac{1}{S_{66}} \end{aligned} \quad (109)$$

where q is the applied pressure, t is plate thickness, r is the position of interest and the S_{ij} 's are the material compliances. The plate rigidities, D_{ij} 's, and associated functions are written in the more standard notation used by Hearmon (Hearmon 1961) instead of that used by Okubu (Okubu 1949). Note that Equation (106) was published by Hearmon (Hearmon 1961) for the general case of a non-unit radius:

$$w \cong \frac{q}{64D^*} (r_p^2 - r^2) (k^* - r^2). \quad (110)$$

where r_p is the radius of an anisotropic plate. However, an r_p^2 term is missing. For the general case of a plate of variable support radius the displacement should be

$$w \cong \frac{q}{64D^*} (r_p^2 - r^2) (k^* r_p^2 - r^2). \quad (111)$$

For the simpler case of cubic symmetry, the constants reduce to

$$D^{*cubic} = \frac{1}{4}(3D_{11} + D_{12} + 2D_{66}) \quad (112)$$

$$k^{*cubic} = \frac{7D_{11} + 5D_{12} + 6D_{66}}{2(D_{11} + 2D_{12})}. \quad (113)$$

Note that the effect of overhang is ignored in the displacement solution and the specimen radius is set equal to the support radius. Because the symmetry of an orthotropic or cubic crystal is orthogonal, the elastic constants are in Cartesian form and the stresses and strain need to be determined in Cartesian coordinates. The strains and stresses are determined from the curvature equation in Cartesian form and the usual strain-displacement relations for pure bending:

$$\varepsilon_{11} = -z \frac{\partial^2 w}{\partial x^2}; \quad \varepsilon_{22} = -z \frac{\partial^2 w}{\partial y^2}; \quad \varepsilon_{66} = -2z \frac{\partial^2 w}{\partial x \partial y} \quad (114)$$

$$\frac{\partial^2 w}{\partial x^2} = \frac{-q}{64D^*} [2r_p^2(k^* + 1) - 12x^2 - 4y^2]$$

$$\frac{\partial^2 w}{\partial y^2} = \frac{-q}{64D^*} [2r_p^2(k^* + 1) - 12y^2 - 4x^2] \quad (115)$$

$$\frac{\partial^2 w}{\partial x \partial y} = \frac{q}{8D^*} [xy]$$

where z is the distance from the mid-surface of the plate. The stresses are determined from the strains by (Hearmon 1961):

$$\begin{aligned}
\sigma_{11} &= -z \left(b_{11} \frac{\partial^2 w}{\partial x^2} + b_{12} \frac{\partial^2 w}{\partial y^2} \right) \\
\sigma_{22} &= -z \left(b_{12} \frac{\partial^2 w}{\partial x^2} + b_{22} \frac{\partial^2 w}{\partial y^2} \right) \\
\sigma_{12} &= -z \left(2b_{66} \frac{\partial^2 w}{\partial x \partial y} \right)
\end{aligned} \tag{116}$$

where $b_{11} = S_{22} / S_{11}S_{22} - S_{12}$, $b_{22} = S_{11} / S_{11}S_{22} - S_{12}$, $b_{66} = 1/S_{66}$ and $b_{12} = -S_{12} / S_{11}S_{22} - S_{12}$. As the plate is cylindrical, a description of the stresses in polar coordinates is more intuitive. The Cartesian values at any point in the plate can be converted as follows:

$$\begin{aligned}
\sigma_{rr} &= \sigma_{11} \cos^2 \varphi + \sigma_{22} \sin^2 \varphi + \sigma_{12} \sin 2\varphi \\
\sigma_{\theta\theta} &= \sigma_{22} \cos^2 \varphi + \sigma_{11} \sin^2 \varphi - \sigma_{12} \sin 2\varphi \\
\sigma_{r\theta} &= (\sigma_{22} - \sigma_{11}) \sin \varphi \cos \varphi + \sigma_{12} \cos 2\varphi
\end{aligned} \tag{117}$$

where φ is the counter clockwise angle from the x axis. The resultant stresses as a function of angular orientation in a (001) NiAl plate are shown in Figure 4.4.1.1. The stresses are a function of both radial position and orientation, with the tangential stresses being greater than the radial stresses at all locations except the plate center where they are equal. For any radius, the peak tangential stress in the plane of the plate occurs at the $\langle 110 \rangle$ directions, whereas the peak radial stress occurs along $\langle 100 \rangle$ directions.

4.4.2. Okubu's Exact Solution

Because Eq. (110) is approximate, its accuracy is an issue for reliability calculations. The deflection at any point in an anisotropic plate is defined as (Hearmon 1961, Timoshenko 1959)

$$D_{11} \frac{\partial^4 z}{\partial x^4} + 2(D_{12} + 2D_{66}) \frac{\partial^4 z}{\partial x^2 \partial y^2} + D_{22} \frac{\partial^4 z}{\partial y^4} = q. \tag{118}$$

Okubu defined the exact displacement solution for a plate with unit radius as

$$w = w_o + R \left[f_1(x + ik_1 y) + f_2(x + ik_2 y) + C_1 x^4 + C_2 x^2 y^2 + C_3 y^4 + C_4 x^4 + C_5 y^2 + C_6 \right] \tag{119}$$

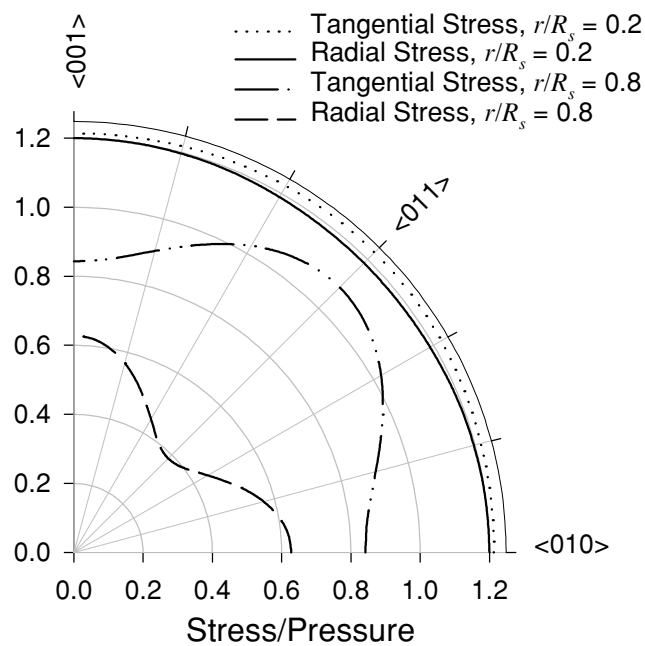


Figure 4.4.1.1: Stresses in a {100} plate of unit radius and thickness subjected to a unit uniform pressure as calculated with Okubu's (Okubu 1949) approximate solution.

with

$$\begin{aligned} f_1''(x + ik_1 y) &= \sum_2^{\infty} A_n \cosh 2n(\alpha' + i\beta') \\ f_2''(x + ik_2 y) &= \sum_2^{\infty} B_n \cosh 2n(\alpha'' + i\beta'') \end{aligned} \quad (120)$$

and

$$\begin{aligned} k_1 &= \frac{D_1^{1/2}}{\left(D_2 + D_4 + \left\{ (D_2 + D_4)^2 - D_1 D_3 \right\}^{1/2} \right)^{1/2}} \\ k_2 &= \frac{D_1^{1/2}}{\left(D_2 + D_4 - \left\{ (D_2 + D_4)^2 - D_1 D_3 \right\}^{1/2} \right)^{1/2}} \end{aligned} \quad (121)$$

This lead to

$$\begin{aligned} \frac{\partial^2 w}{\partial x^2} &= \sum_2^{\infty} (A_n \cosh 2na' + B_n \cosh 2na'') \cos 2n\beta + 6C_1 + C_2 + 2C_4 + (6C_1 - C_2) \cos 2\beta \\ \frac{\partial^2 w}{\partial y^2} &= - \sum_2^{\infty} (A_n k_1^2 \cosh 2na' + B_n k_2^2 \cosh 2na'') \cos 2n\beta + 6C_3 + C_2 + 2C_5 - (6C_3 - C_2) \cos 2\beta \\ \frac{\partial^2 w}{\partial x \partial y} &= - \sum_2^{\infty} (A_n k_1 \sinh 2na' + B_n \sinh 2na'') \sin 2n\beta + 2C_2 \sin 2\beta \end{aligned} \quad (122)$$

on the boundaries of a plate with a unit radius. The A_n 's, B_n 's and C_i 's can be determined by applying the boundary conditions that the displacement and moments disappear at the edge of the on the boundaries of a plate. The necessary functions are given by Okubu (Okubu 1949). The terms c' and a' are dependent on the elastic constants only and can be derived from the Cartesian to curvilinear transformation equations provided by Okubu:

$$\begin{aligned} x + iy &= e^{\alpha + i\beta} \\ x + ik_1 y &= c' \cosh(\alpha' + i\beta') \\ x + ik_2 y &= c'' \cosh(\alpha'' + i\beta'') \end{aligned} \quad (123)$$

$$\text{with} \quad c' \cosh a' = 1, c' \sinh a' = k_1, c'' \cosh a'' = 1, c'' \sinh a'' = k_2 \quad (124)$$

for a plate of unit radius. The resultant stresses as a function of angular orientation in a (001) NiAl plate are shown in Figure 4.4.2.1. The stresses are a function of both the radial position and the orientation, with the tangential stresses being greater than the radial stresses at all locations except the plate center where they are equal. For any radial position, the peak tangential stress in the plane of the plate occur at the <110> directions, whereas the peak radial stress occurs along <100> directions.

The stress resulting in a NiAl plate as calculated from the series and approximate solutions are compared to the isotropic solution in Figure 4.4.2.2 for a (001) plate of unit radius and thickness subjected to a unit pressure. The approximate and isotropic solutions predict higher stresses (~10%) near the plate center, with the isotropic solution decaying more rapidly than either of the anisotropic solutions. Thus, for an anisotropic plate, greater care in preparation of the test specimen edges is needed.

As Okubu's solutions were derived for a plate of unit radius, thickness and applied pressure, generalization for application to real specimens is needed.

4.4.3 Generalization of Okubu's Solution to Variable Radius

For a disk of any radius, the equations defining the boundaries and displacement are function of the radius. The terms relating c' and a' in Eq. (124) become

$$c' \cosh a' = r_p, \quad c' \sinh a' = r_p k_1, \quad c'' \cosh a'' = r_p, \quad c'' \sinh a'' = r_p k_2. \quad (125)$$

This leads to

$$w = \frac{c'}{4} \sum_2^{\infty} A_n \left\{ \frac{\cosh(2n+2)\alpha'}{(2n+2)(2n+1)} \cos(2n+2)\beta' - \left[\frac{1}{(2n+1)2n} + \frac{1}{2n(2n-1)} \right] \cosh 2n\alpha' \cos 2n\beta' \right. \\ \left. + \frac{\cosh(2n-2)\alpha'}{(2n-1)(2n-2)} \cos(2n-2)\beta' \right\} +$$

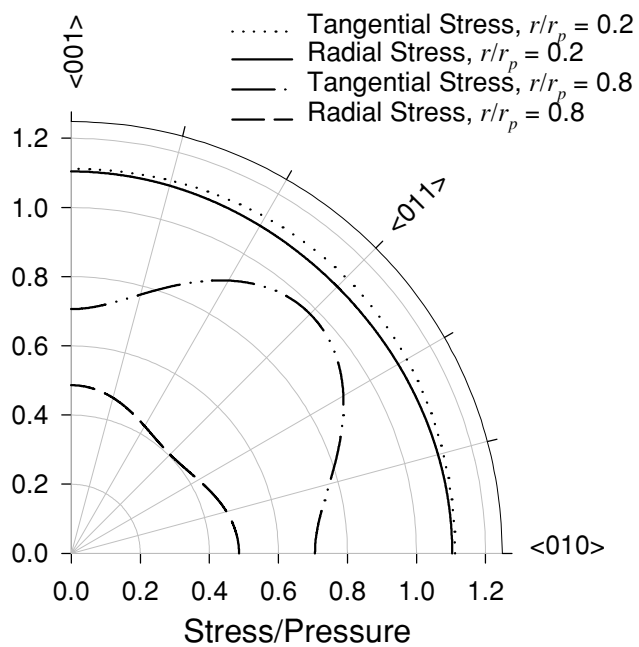
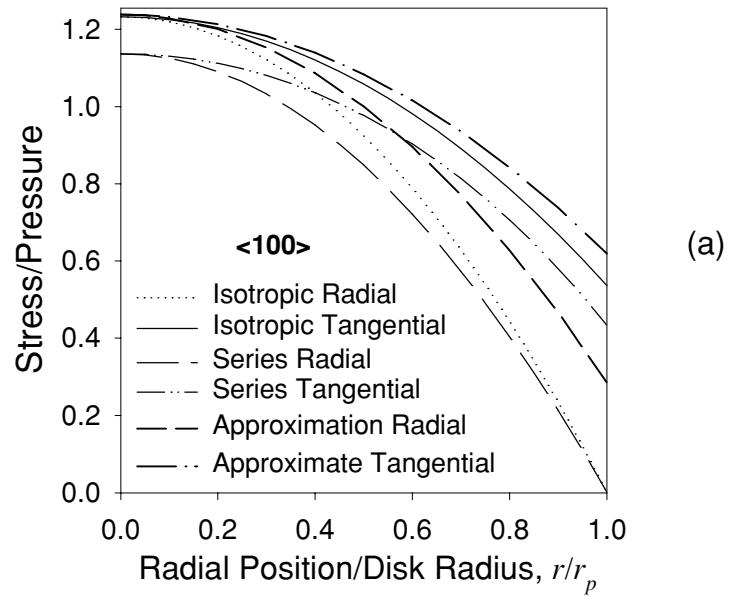
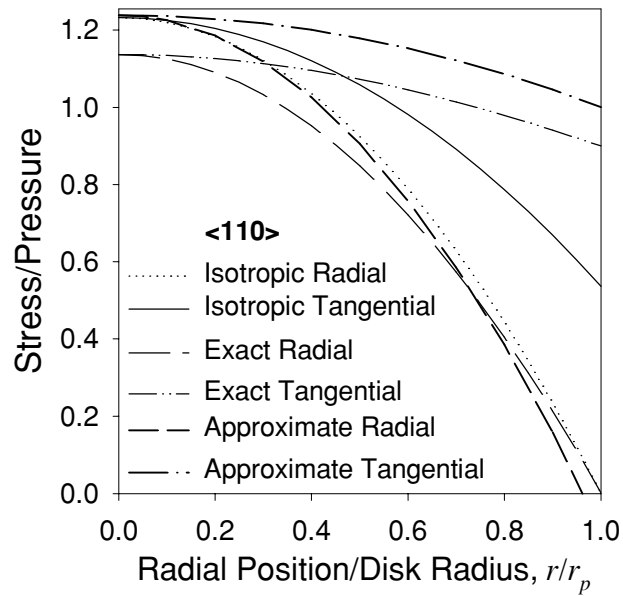


Figure 4.4.2.1: Stresses in a $\{100\}$ plate of unit radius and thickness subjected to a unit uniform pressure as calculated with Okubu's (Okubu 1949) series solution.



(a)



(b)

Figure 4.4.2.2: Comparison of the stresses in a {100} plate of unit radius and thickness subjected to a unit uniform pressure as calculated with isotropic and anisotropic solutions: <100> direction and (b) <110> direction.

$$\frac{c''}{4} \sum_z B_n \left\{ \frac{\cosh(2n+2)\alpha''}{(2n+2)(2n+1)} \cos(2n+2)\beta'' - \left[\frac{1}{(2n+1)2n} + \frac{1}{2n(2n-1)} \right] \cosh 2n\alpha'' \cos 2n\beta'' \right. \\ \left. + \frac{\cosh(2n-2)\alpha''}{(2n-1)(2n-2)} \cos(2n-2)\beta'' \right\} \quad (126)$$

$$+ C_1 x^4 + C_2 x^2 y^2 + C_3 y^4 + C_4 x^2 + C_5 y^2 + C_6$$

as in the original solution. The condition that w vanishes at the plate boundary r_p gives

$$(3C_1 + C_2 + 3C_3)r_p^4 + 4(C_4 + C_5)r_p^2 + 8C_6 = 0$$

$$(C_1 - C_3)r_p^4 + (C_4 - C_5)r_p^2 + \frac{1}{12}c'^2 A_2 \cosh 2a' + \frac{1}{12}c''^2 B_2 \cosh 2a'' = 0 \quad (127)$$

$$\frac{1}{8}(C_1 - C_2 + C_3)r_p^4 - \frac{1}{30}c'^2 A_2 \cosh 4a' - \frac{1}{30}c''^2 B_2 \cosh 4a'' + \frac{1}{80}c'^2 A_3 \cosh 4a' + \frac{1}{80}c''^2 B_3 \cosh 4a'' = 0$$

.

.

.

$$\frac{I}{2n} \left\{ \frac{A_{n-1}}{2n-1} - \left(\frac{1}{2n+1} + \frac{1}{2n-1} \right) A_n + \frac{A_{n+1}}{2n+1} \right\} c'^2 \cosh 2na' \\ + \frac{I}{2n} \left\{ \frac{B_{n-1}}{2n-1} - \left(\frac{1}{2n+1} + \frac{1}{2n-1} \right) B_n + \frac{B_{n+1}}{2n+1} \right\} c''^2 \cosh 2na'' = 0 \quad \text{for } n = 3, 4, \dots$$

.

.

.

The condition that the moment also vanishes at the edge gives

$$\left\{ 3(3D_1 + D_2)C_1 + \left(\frac{D_1}{2} + 3D_2 + 2D_4 + \frac{D_3}{2} \right) C_2 + 3(3D_3 + D_2)C_3 \right\} r_p^2 + 2(D_1 + D_2)C_4 + 2(D_2 + D_3)C_5 = 0,$$

$$(12D_1C_1 - 12D_3C_3)r_p^2 + 2(D_1 - D_2)C_4 + 2(D_2 - D_3)C_5 \\ + \left\{ \frac{1}{2}(D_1 - D_2) \cosh 4a' - \frac{1}{2}(D_2 - D_3)k_1^2 \cosh 4a' - D_4k_1 \sinh 4a' \right\} A_2 \\ + \left\{ \frac{1}{2}(D_1 - D_2) \cosh 4a' - \frac{1}{2}(D_2 - D_3)k_2^2 \cosh 4a'' - D_4k_2 \sinh 4a'' \right\} B_2 = 0,$$

$$\begin{aligned}
& \left\{ 3(D_1 - D_2)C_1 - \left(\frac{D_1 + D_3}{2} - D_2 + 2D_4 \right) C_2 + 3(D_3 - D_2)C_3 \right\} r_p^2 \\
& + A_2 \left\{ D_1 + D_2 - (D_2 + D_3)k_1^2 \right\} \cosh 4a' + B_2 \left\{ D_1 + D_2 - (D_2 + D_3)k_2^2 \right\} \cosh 4a'' \\
& + A_3 \left\{ \frac{1}{2}(D_1 - D_2) \cosh 6a' - \frac{1}{2}(D_2 - D_3)k_1^2 \cosh 6a' - D_4 k_1 \sinh 6a' \right\} \\
& + B_3 \left\{ \frac{1}{2}(D_1 - D_2) \cosh 6a'' - \frac{1}{2}(D_2 - D_3)k_2^2 \cosh 6a'' - D_4 k_2 \sinh 6a'' \right\} = 0, \\
& \cdot \\
& \cdot \\
& \cdot \\
& A_{n+1} \left\{ \frac{(D_1 - D_2)}{2} \cosh(2n+2)a' - \frac{D_2 - D_3}{2} k_1^2 \cosh(2n+2)a' - D_4 k_1 \sinh(2n+2)a' \right\} \\
& + A_n \left\{ D_1 + D_2 - (D_2 + D_3)k_1^2 \right\} \cosh 2na' \\
& + A_{n-1} \left\{ \frac{(D_1 - D_2)}{2} \cosh(2n-2)a' - \frac{D_2 - D_3}{2} k_1^2 \cosh(2n-2)a' + D_4 k_1 \sinh(2n-2)a' \right\} \\
& B_{n+1} \left\{ \frac{(D_1 - D_2)}{2} \cosh(2n+2)a'' - \frac{D_2 - D_3}{2} k_2^2 \cosh(2n+2)a'' - D_4 k_2 \sinh(2n+2)a'' \right\} \\
& + B_n \left\{ D_1 + D_2 - (D_2 + D_3)k_2^2 \right\} \cosh 2na'' \\
& + B_{n-1} \left\{ \frac{(D_1 - D_2)}{2} \cosh(2n-2)a'' - \frac{D_2 - D_3}{2} k_2^2 \cosh(2n-2)a'' + D_4 k_2 \sinh(2n-2)a'' \right\} = 0, \\
& \cdot \\
& \cdot \\
& \cdot
\end{aligned} \tag{128}$$

and the general curvatures for any radial position become

$$\begin{aligned}
\frac{\partial^2 w}{\partial x^2} &= \sum_{n=2}^{\infty} (A_n \cosh 2n\alpha' \cos 2n\beta' + B_n \cosh 2n\alpha'' \cos 2n\beta'') + 12C_1 x^2 + 2C_2 y^2 + 2C_4 \\
\frac{\partial^2 w}{\partial y^2} &= -\sum_{n=2}^{\infty} (A_n k_1^2 \cosh 2n\alpha' \cos 2n\beta' + B_n k_2^2 \cosh 2n\alpha'' \cos 2n\beta'') + 2C_2 x_1^2 + 12C_3 x_2^2 + 2C_5 \\
\frac{\partial^2 w}{\partial x \partial y} &= -\sum_{n=2}^{\infty} (A_n k_1 \sinh 2n\alpha' \sin 2n\beta' + B_n k_2 \sinh 2n\alpha'' \sin 2n\beta'') + 4C_2 xy
\end{aligned} \tag{129}$$

or in curvilinear coordinates

$$\frac{\partial^2 w}{\partial x^2} = \sum_{n=2}^{\infty} (A_n \cosh 2n\alpha' \cos 2n\beta' + B_n \cosh 2n\alpha'' \cos 2n\beta'') + (6C_1 + C_2)r^2 + 2C_4 + (6C_1 - C_2)r^2 \cos 2\beta$$

$$\begin{aligned} \frac{\partial^2 w}{\partial y^2} = & - \sum_{n=2}^{\infty} (A_n k_1^2 \cosh 2n\alpha' \cos 2n\beta' + B_n k_2^2 \cosh 2n\alpha'' \cos 2n\beta'') + (6C_3 + C_2)r^2 \\ & + 2C_5 - (6C_3 - C_2)r^2 \cos 2\beta \end{aligned} \quad (130)$$

$$\frac{\partial^2 w}{\partial x \partial y} = - \sum_{n=2}^{\infty} (A_n k_1 \sinh 2n\alpha' \sin 2n\beta' + B_n k_2 \sinh 2n\alpha'' \sin 2n\beta'') + 2C_2 r^2 \sin 2\beta.$$

The constants A_n 's, B_n 's, and C_i 's are noted to be functions of q/t^3 and various powers of r_p . Thus the q , t and r_p terms can be factored from the curvature equations and the curvatures written in a form more typically used to describe plates. This also allows the constants for a given crystal system to be determined only once by setting the terms to unity in Equations (109), (118), (125), (127) and (128) (i.e. solving Okubu's boundary equations). The curvatures in a general format with q , r and t factored become

$$\begin{aligned} \frac{\partial^2 w}{\partial x^2} &= \frac{qr_p^2}{t^3} \left[\sum_2^{\infty} (A_n \cosh 2n\alpha' \cos 2n\beta' + B_n \cosh 2n\alpha'' \cos 2n\beta'') \right. \\ &\quad \left. + (6C_1 + C_2 + (6C_1 - C_2)\cos 2\beta) \frac{r^2}{r_p^2} + 2C_4 \right] \\ \frac{\partial^2 w}{\partial y^2} &= \frac{qr_p^2}{t^3} \left[- \sum_2^{\infty} (A_n k_1^2 \cosh 2n\alpha' \cos 2n\beta' + B_n k_2^2 \cosh 2n\alpha'' \cos 2n\beta'') \right. \\ &\quad \left. + (6C_3 + C_2 - (6C_3 - C_2)\cos 2\beta) \frac{r^2}{r_p^2} + 2C_5 \right] \end{aligned} \quad (131)$$

$$\frac{\partial^2 w}{\partial x \partial y} = \frac{qr_p^2}{t^3} \left[- \sum_2^{\infty} (A_n k_1 \sinh 2n\alpha' \sin 2n\beta' + B_n k_2 \sinh 2n\alpha'' \sin 2n\beta'') + 2C_2 \frac{r^2}{r_p^2} \sin 2\beta \right]$$

and the displacement function becomes

$$w = \frac{q}{t^3} + \frac{c'^2}{4} \sum_{n=2}^{\infty} A_n \left\{ \frac{\cosh(2n+2)\alpha'}{(2n+2)(2n+1)} \cos(2n+2)\beta' - \left[\frac{1}{(2n+1)2n} + \frac{1}{2n(2n-1)} \right] \cosh 2n\alpha' \cos 2n\beta' \right. \\ \left. + \frac{\cosh(2n-2)\alpha'}{(2n-1)(2n-2)} \cos(2n-2)\beta' \right\} \\ + \frac{c''^2}{4} \sum_{n=2}^{\infty} B_n \left\{ \frac{\cosh(2n+2)\alpha''}{(2n+2)(2n+1)} \cos(2n+2)\beta'' - \left[\frac{1}{(2n+1)2n} + \frac{1}{2n(2n-1)} \right] \cosh 2n\alpha'' \cos 2n\beta'' \right. \\ \left. + \frac{\cosh(2n-2)\alpha''}{(2n-1)(2n-2)} \cos(2n-2)\beta'' \right\} \\ + C_1 x^4 + C_2 x^2 y^2 + C_3 y^4 + (C_4 x^2 + C_5 y^2) r_p^2 + C_6 r_p^2 \quad (132)$$

in Okubu's format or

$$w = \frac{qr_p^4}{8t^3} + 2(1-k_1^2) \sum_{n=2}^{\infty} A_n \left\{ \frac{\cosh(2n+2)\alpha'}{(2n+2)(2n+1)} \cos(2n+2)\beta' + \frac{\cosh(2n-2)\alpha'}{(2n-1)(2n-2)} \cos(2n-2)\beta' \right. \\ \left. - \left[\frac{1}{(2n+1)2n} + \frac{1}{2n(2n-1)} \right] \cosh 2n\alpha' \cos 2n\beta' \right\} \\ + 2(1-k_2^2) \sum_{n=2}^{\infty} B_n \left\{ \frac{\cosh(2n+2)\alpha''}{(2n+2)(2n+1)} \cos(2n+2)\beta'' + \frac{\cosh(2n-2)\alpha''}{(2n-1)(2n-2)} \cos(2n-2)\beta'' \right. \\ \left. - \left[\frac{1}{(2n+1)2n} + \frac{1}{2n(2n-1)} \right] \cosh 2n\alpha'' \cos 2n\beta'' \right\} \\ + \{(C_1 - C_2 + C_3)(\cos 4\beta + 3) + 4(C_1 - C_3)\cos 2\beta + 4C_2\} \frac{r_p^4}{r_p^4} \\ + 4\{(C_4 - C_5)\cos 2\beta + C_4 + C_5\} \frac{r_p^2}{r_p^2} + 8C_6 \quad (133)$$

in curvilinear coordinates only and a form more similar to that used to express the displacements of circular plates.

The constants for both NiAl and an orthotropic graphite epoxy composite are given in Table 4.4.3.1. As can be seen from Table 4.4.3.1, the solution converges rapidly, especially for {100} plates of NiAl. The computer code used to calculate the constants is given in Appendix B.

Note that Okubu's model is capable of analyzing only {100} or {110} plates and cannot be used for generally anisotropic plates (e.g. {111} or {511} plates) because they have fully populated stiffness

matrices and exhibit bend/twist coupling which complicates the elastic solution due to ill-defined boundary conditions. However, fully anisotropic plates are of interest because they are more representative of a complex component. Thus, the finite element analysis method with gap elements at the supports might be used for analysis of such general cases. The gap elements should account for “lift off” from the supports as necessary. Another minor complication with Okubu’s solution is that it does not consider the stiffening effect of overhang, which occurs when the plate is larger than the support. Practically, overhang is necessary to prevent the test specimen from falling off the support and to minimize the tangential stresses at the test specimen edge and thereby avoid edge failures. Based on the isotropic solution, if the support diameter is within 95% of the specimen diameter the error in the maximum stress is less than 2% and if the support diameter is within 90% of the test specimen diameter the error is less than 4%.

Table 4.4.3.1: Displacement solution constants ($\times 10^{-6}$) for NiAl and graphite/epoxy plates of unit thickness and radius subjected to a unit lateral pressure.

NiAl:									
$S_{22} = S_{11} = 1.0428, S_{12} = -0.421, S_{66} = 0.892 \text{ (} \times 10^{-5} \text{ m}^2/\text{MN) (Wasilewski 1966)}$									
C_1	C_2	C_3	C_4	C_5	C_6	A_2	B_2	A_3	B_3
1.392	2.009	1.392	-7.253	-7.253	5.958	0.474	-0.105	10^{-15}	10^{-16}
Graphite Epoxy:									
$S_{11} = 0.6667, S_{22} = 11.11, S_{12} = -0.2000, S_{66} = 14.08 \text{ (} \times 10^{-5} \text{ m}^2/\text{MN) (Lee and Saravanos 1995)}$									
C_1	C_2	C_3	C_4	C_5	C_6	A_2	B_2	A_3	B_3
2.741	9.046	4.080	-15.52	-16.34	12.24	0.385	0.385	0.079	0.079

4.5 BIAXIAL RIG VERIFICATION

4.5.1 The Isotropic Case

Ideally, the test rig will generate stresses described by simple plate theory. A comparison was made between isotropic plate theory (Szilard 1974) and the stresses measured with stacked,

rectangular strain gage rosettes³ placed at eight radial positions on the tensile surfaces of two 4340 steel disk test specimens as shown in Figure 4.5.1.1. The strain-gaged biaxial flexure test specimens were inserted in the test fixture, pressurized and removed repeatedly while the strain was recorded as a function of pressure. The average of at least three slopes, as determined by linear regression of strain as function of pressure, were used to calculate the mean strains and stresses (Measurements Group Tech Note TN 509 and TN 15). A maximum pressure level of 6.90 MPa (1000 psig) was deemed adequate because the strains developed approached the strain limit of the gages and the errors were noted to decrease as the pressure increased.

Because the calculation of stress from strain via constitutive equations requires the elastic modulus and Poisson's ratio, measurements were made by the flexural resonance of the disk test specimens (ASTM C 1259 1995). The estimated elastic moduli and Poisson's ratio were 204.0 ± 0.4 GPa and 0.29, in good agreement with handbook values (CINDAS/USAF 1997).

During pressurization cycles, the rig was noted to exhibit a significant hysteresis when the support ring was not lubricated. The loading slope was very linear and the unloading cycle very nonlinear, particularly near the load reversal. However, if the specimen - support ring interface was lubricated with an anti-seizing compound⁴, the hysteresis was substantially reduced and the strains increased. This behavior can be explained by the specimen slipping across the support ring during loading but sticking briefly upon load reversal. Because strength measurement only involves the loading slope only, loading data was regressed for comparison to plate theory. The slopes of the loading curves typically exhibited correlation coefficients greater than $R^2 = 0.999$. The application of hydraulic oil to the specimen - support ring interface had little effect on the measured stresses, as shown in Table 4.5.1.1.

For the lubricated condition and a pressure of 6.90 MPa agreement between plate theory and the measurements was within ~1% at the disk center, within ~2% at 55% of the support radius and within 9% at 75% of the support radius. In general, the errors increase with increasing radial position, particularly for the tangential component. The results are summarized in Table 4.5.1.1 and shown in Figure 4.5.1.2 along with 95% confidence intervals.

³ Gage designation WA-06-030WR-120, Measurement Group, Raleigh, NC.

⁴ Never-Seez, Never-Seez Compound Corp., Broadview, IL.

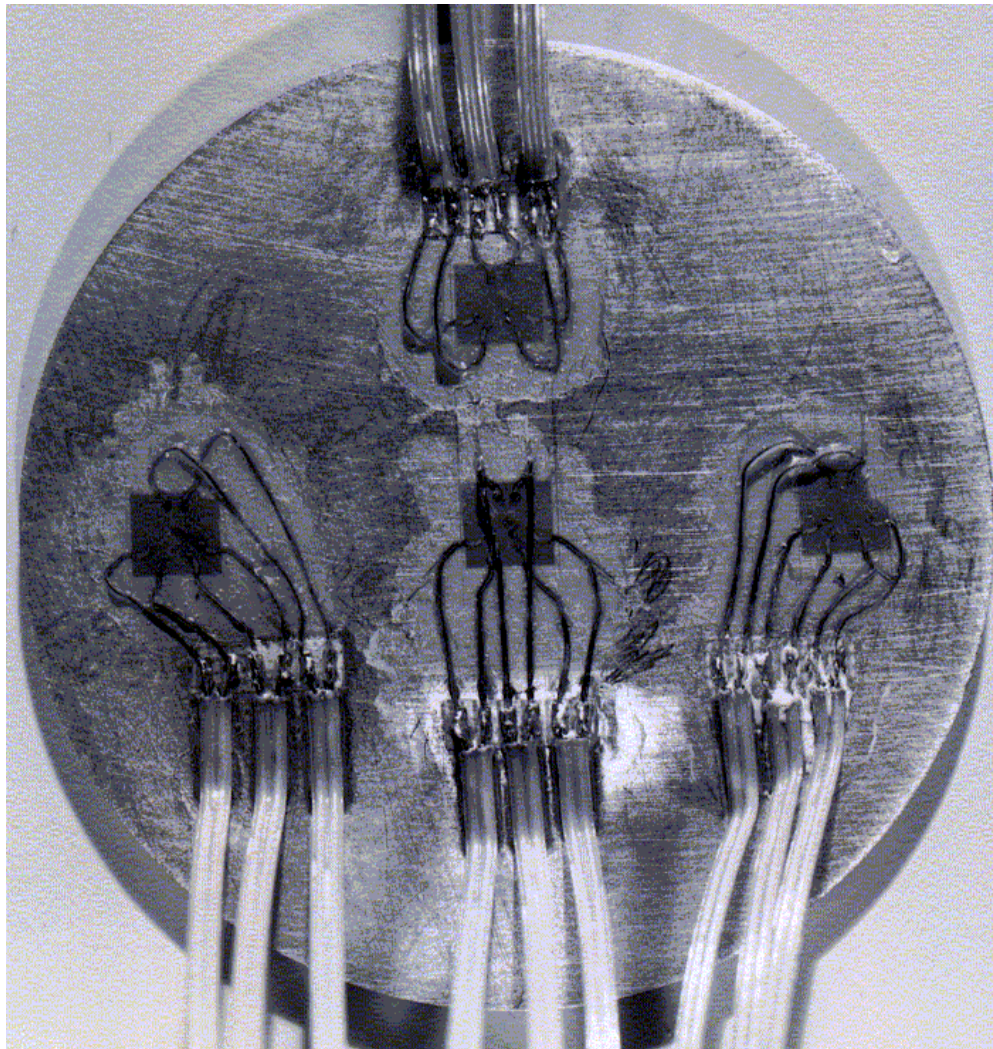


Figure 4.5.1.1: 4340 steel plate with strain gage rosettes attached.

The significance of the differences between the plate theory and the measured stresses can be assessed by estimating the standard deviations and confidence intervals of the measurements. The standard deviations of the strains and stresses were calculated from the apparent strain variances by applying a truncated Taylor series approximation (Haugen 1980) to the transverse sensitivity correction equations, the strain transformation equations and the stress-strain relations. For a rectangular strain rosette, the standard deviations of principal stress, principal strain and principal strain uncorrected for transverse strain errors are

$$\begin{aligned}
 SD_{\sigma_p} &= \frac{E}{1-\nu^2} \sqrt{SD_{\epsilon_p}^2 + \nu^2 SD_{\epsilon_q}^2} \\
 SD_{\sigma_q} &= \frac{E}{1-\nu^2} \sqrt{\nu^2 SD_{\epsilon_p}^2 + SD_{\epsilon_q}^2} \\
 SD_{\epsilon_p} &= \frac{1-\nu_o k_t}{1-k_t^2} \sqrt{SD_{\hat{\epsilon}_p}^2 + k_t^2 SD_{\hat{\epsilon}_q}^2} \\
 SD_{\epsilon_q} &= \frac{1-\nu_o k_t}{1-k_t^2} \sqrt{k_t^2 SD_{\hat{\epsilon}_p}^2 + SD_{\hat{\epsilon}_q}^2} \\
 SD_{\hat{\epsilon}_{p,q}} &= \sqrt{\left(\frac{1}{2} - \frac{\hat{\epsilon}_1 - \hat{\epsilon}_2}{\sqrt{\beta}}\right)^2 SD_{\hat{\epsilon}_1}^2 + \frac{(2\hat{\epsilon}_2 - \hat{\epsilon}_1 - \hat{\epsilon}_3)^2}{\beta} SD_{\hat{\epsilon}_2}^2 + \left(\frac{1}{2} \pm \frac{\hat{\epsilon}_3 - \hat{\epsilon}_2}{\sqrt{\beta}}\right)^2 SD_{\hat{\epsilon}_3}^2} \\
 \beta &= (\hat{\epsilon}_1 - \hat{\epsilon}_2)^2 + (2\hat{\epsilon}_2 - \hat{\epsilon}_1 - \hat{\epsilon}_3)^2
 \end{aligned} \tag{134}$$

where E and ν are the elastic modulus and Poisson's ratio of the test material, ν_o is Poisson ratio of the strain gage manufacturers calibration material, is the transverse sensitivity of the strain gage, $\hat{\epsilon}_1, \hat{\epsilon}_2, \hat{\epsilon}_3$ are the apparent strains and SD_{x_i} is the standard deviation of the x_i variables: $\hat{\epsilon}_p$ and $\hat{\epsilon}_q$ being the uncorrected principal strains, ϵ_p and ϵ_q being the corrected principal strains, and σ_p and σ_q being the corrected principal stresses. The elastic constants in Equation (134) are assumed to be exact for a single test specimen.

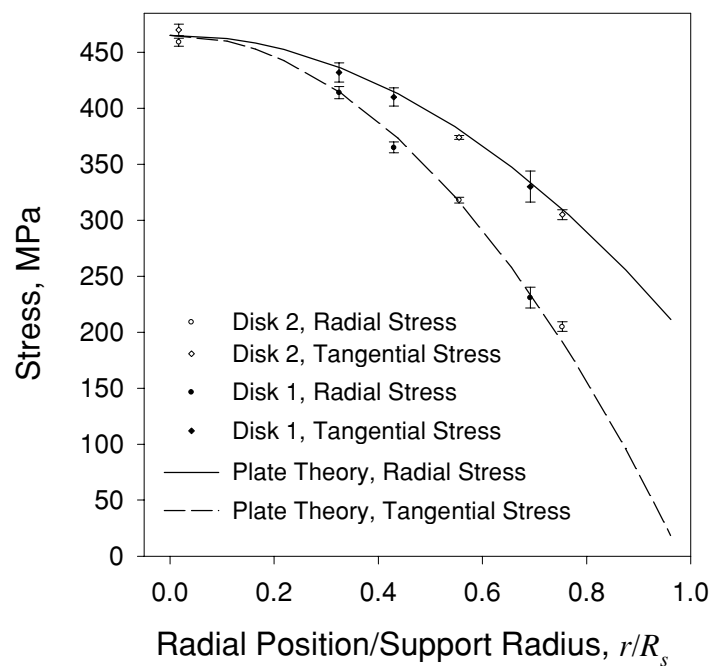


Figure 4.5.1.2: Measured and theoretical stresses for a 4340 steel disk as a function of normalized radial position. Error bars indicate the 95% confidence intervals.

Table 4.5.1.1: Measured stresses, standard deviations and theoretical stresses for a 25 mm diameter, 4340 steel disk subjected to 6.90 MPa uniform pressure.

Radial Position	Radial Stress, MPa			Tangential Stress, MPa		
Percent of Support	Theory [2]	Measured ^[3]	Percent Difference	Theory [2]	Measured ^[3]	Percent Difference
1.7, Unlubricated	465	418±0.6	-10	465	432±0.9	-7.0
33, Unlubricated	415	393±0.2	-3.3	436	409±0.3	-6.4
43, Unlubricated	377	348±0.3	-6.1	415	391±0.4	-5.8
55, Unlubricated	318	278±3.6	-12	382	336±2.3	-12
69, Unlubricated	237	209±3.6	-9.2	335	311±0.1	-7.1
75, Unlubricated	194	162±1.3	-16	311	265±1.3	-15
1.7, Oil	465	418±2.9	-10	465	432±1.6	-7.2
33, Oil	415	398±2.7	-3.9	436	311±2.9	-5.0
43, Oil	377	351±3.2	-6.9	415	396±1.3	-5.2
56, Oil	318	277±1.5	-13	383	336±1.8	-11.2
69, Oil	237	211±0.9	-11	335	310±1.5	-7.4
75, Oil	194	161±0.6	-17	311	266±0.6	-15
1.7, Anti-Seize ^[1]	465	459±2.2	-1.3	465	470±3.0	1.1
33, Anti-Seize	415	414±3.2	-0.2	436	432±5.1	-1.0
43, Anti-Seize	377	365±2.9	-3.1	415	410±4.8	-1.1
55, Anti-Seize	318	318±1.5	0	383	374±1.0	-2.0
69, Anti-Seize	237	231±5.5	-2.2	335	330±8.2	-1.5
75, Anti-Seize	194	205±2.5	5.6	311	305±2.7	-1.9
1.7, Clamping	----	-4.9±1.0	----	----	0.9±1.0	----
33, Clamping	----	0.5±0.1	----	----	2.3±0.3	----
43, Clamping	----	0.2±0.2	----	----	2.8±0.4	----
69, Clamping	----	0.5±0.4	----	----	3.6±0.5	----

[1] Never-Seez, Never-Seez Compound Corp., Broadview, IL.

[2] See (Szilard 1974).

[3] Mean ± one standard deviation.

The clamping forces exerted by the O-ring and cap on the specimen resulted in stresses on the specimen surface. The level and consistency of these stresses were measured by repeatedly inserting and removing a strain-gaged specimen from the fixture. The stresses generated by clamping varied with orientation and radial position. During three clampings, the principal stresses averaged -4.9 ± 1.0 and 0.9 ± 1.0 MPa, respectively at the disk center, and 2.3 ± 0.3 and 0.5 ± 0.1 MPa, respectively at 33% of the support radius. The maximum principal stresses observed in the unlubricated condition were 5.5 and 1.3 MPa at the disk center. As the specimens deflect and slide across the support ring during pressurization, these clamping stresses may be relieved.

Thus, stresses generated by the test rig in a lubricated, isotropic plate can be described (Szilard 1974) by

$$\begin{aligned}\sigma_{rr} &= \frac{3qR_s^2}{8t^2} \left[(1-\nu) \frac{R_s^2}{R_d^2} + 2(1+\nu) - (3+\nu) \frac{r^2}{R_s^2} \right] + \sigma_s \\ \sigma_{\theta\theta} &= \frac{3qR_s^2}{8t^2} \left[(1-\nu) \frac{R_s^2}{R_d^2} + 2(1+\nu) - (1+3\nu) \frac{r^2}{R_s^2} \right] + \sigma_s \\ \sigma_s &= \frac{q(3+\nu)}{4(1-\nu)}\end{aligned}\tag{135}$$

where q is the applied pressure, R_s is the support ring radius, t is the disk thickness, R_d is the disk radius and r is the radius of interest. The term σ_s is a small correction factor to the simple plate theory for the effects of the shearing stresses and lateral pressure on the plate deflection (Timoshenko and Woinowsky-Krieger 1959).

4.5.2 The Anisotropic Case

To compare the test rig with the solutions of Okubu, single crystal NiAl disk test specimens were machined with the face of the disk corresponding to the {100}. One specimen was strain gaged at four locations and pressurized to 4.8 MPa in the rig with anti-seizing lubricant on the boundary. The strain gage positions corresponded to ~50% of the support radius (*i.e.* $r/r_p = 0.5$) with one gage located along the <100> and the others along the stiffer <110> directions. The resulting

stresses are shown in Figure 4.5.2.1 and summarized to Table 4.5.2.1. The stresses calculated with the series solution are within 2% of the measured stresses at the plate center and within 6% at approximately 50% of the support radius.

To further verify the test rig, nine disk test specimens were strain gaged and pressurized to failure. The maximum strain at failure is compared to those calculated with Eqs. (114), (115) and (131) in Figure 4.5.2.2. The strains generated in the rig lie between those of the solutions, with the approximate solution overestimating the average measured strains by ~5% and the series solution underestimating the rig data by approximately 3%. However, neither the approximate or series solutions consider the effect of lateral pressure and shear on the strains and stresses. If the isotropic correction term, σ_s , in Equation (135) is used with the Poisson's ratio of polycrystalline NiAl ($\nu \approx 0.31$ (Noebe et al. 1993)) to approximate the error, an addition strain of

Table 4.5.2.1: Measured stresses, standard deviations and theoretical stresses for a 25 mm diameter, {100} NiAl single crystal plate supported on a lubricated^[1] steel ring and subjected to a 4.8 MPa uniform pressure.

Radial Position	Radial Stress, MPa			Tangential Stress, MPa		
	Plate Theory ^[2] MPa	Measured ^[3] MPa	Percent Difference	Plate Theory ^[2] MPa	Measured ^[3] MPa	Percent Difference
2, center	305.7	300.1±1.0	-1.8	305.7	311.2±1.2	+1.8
44, <100>	259.8	251.3±3.1	-3.3	272.2	264.4±1.7	-2.9
51, < $\bar{1}10$ >	234.2	232.9±1.0	-5.6	274.8	262.8±1.0	-4.4
50, < $\bar{1}\bar{1}0$ >	215.9	223.7±1.0	+3.6	299.3	288.8±1.0	-3.6

[1] Never-Seez, Never-Seez Compound Corp., Broadview, IL.

[2] See (Okubu 1949).

[3] Mean ± one standard deviation.

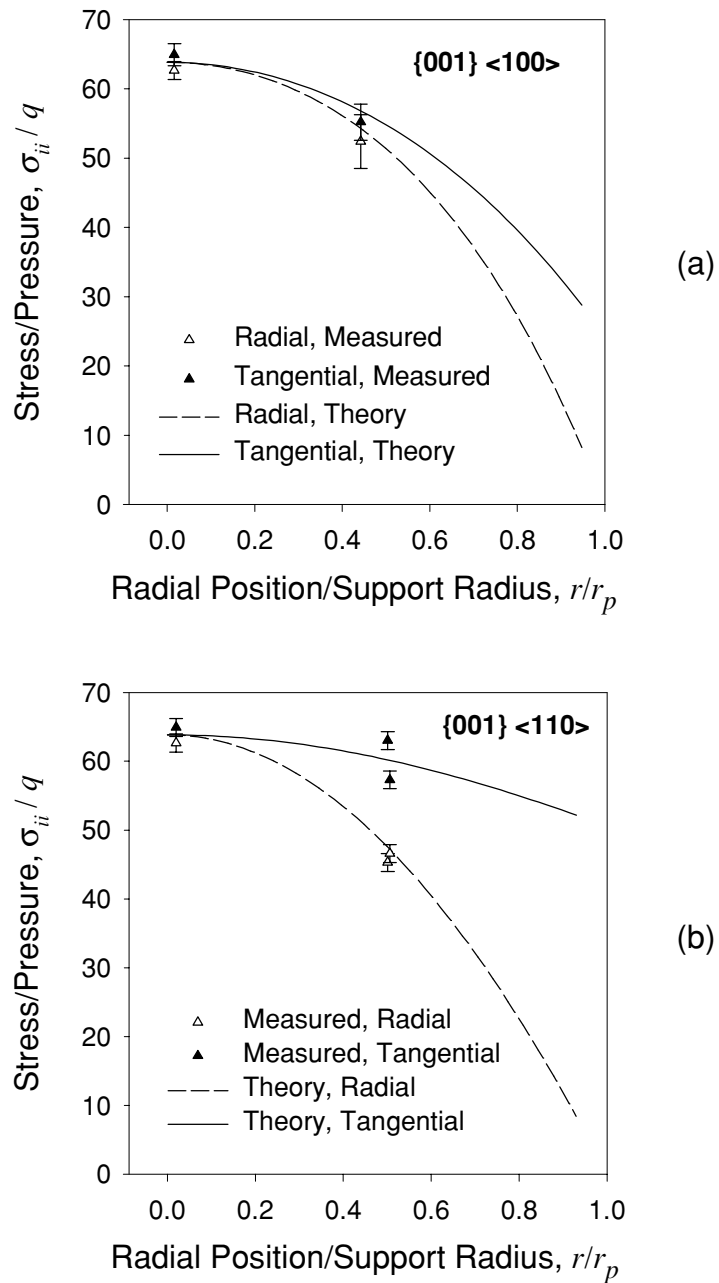


Figure 4.5.2.1: Measured and theoretical stresses for a {100} NiAl disk test specimen as a function of normalized radial position. The support ring was lubricated with anti-seizing compound. Error bars indicate the 95% confidence intervals: (a) <100> direction and (b) <110> direction.

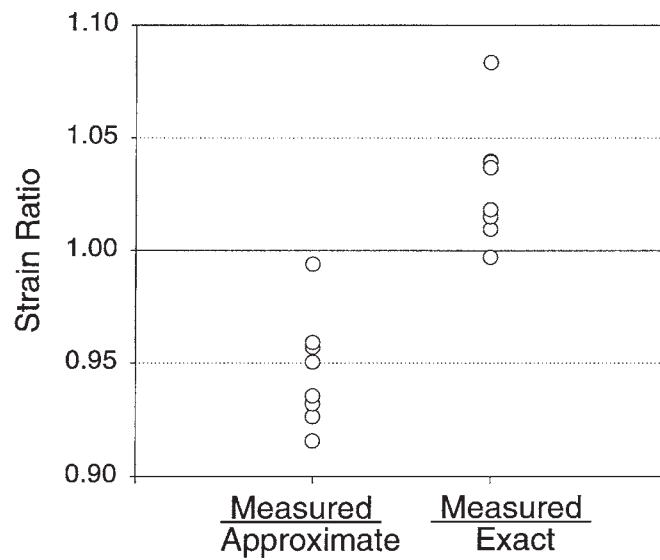


Figure 4.5.2.2: Measured strain at failure normalized to theoretical strain as calculated from Okubu's (Okubu 1949) approximate and exact solutions.

approximately 1.7% is expected, implying that the bending stress components generated by the test rig closely approximate the series solution. However, the beneficial effect of the lateral strains are mitigated by the effect of overhang.

Thus, considering the complexity of the series solution relative to the approximate solution, the use of the approximate solution for practical engineering purposes is reasonable.

4.6 BIAXIAL STRENGTH TESTING

4.6.1 Isotropic Material

The biaxial strengths of ten WC test specimens were measured using the pressure-on-ring (POR) test rig as discussed in Section 4.4. Table 4.6.1.1 summarizes the test specimen dimensions. The strength was calculated from the maximum value of Eq. (135):

$$S_{UTS}^{POR} = \frac{3qR_s^2}{8t^2} \left[(1-\nu) \frac{R_s^2}{R_d^2} + 2(1+\nu) \right] + \sigma_s \quad (136)$$

where the symbols are as defined in Eq. (135).

Table 4.6.1.1: Test specimen dimensions for the isotropic case.

Specimen Configuration (number tested)	Mean ^[1] Thickness or height mm	Mean Width or Radius mm	Support Span or Radius mm
Three-point, "A" Beams (29)	1.50 ± 0.002	1.98 ± 0.07	20.02
Biaxial, POR (10)	2.22 ± 0.004	25.40 ± 0.005	22.74

[1] Mean ± one standard deviation.

4.6.2 Anisotropic Material

Thirteen NiAl disk test specimens with {100} orientation were pressurized to failure in the POR test apparatus. Table 4.6.2.1 summarizes the test specimen dimensions. A nominal pressure rate resulting in a strain rate corresponding to that used in the flexure testing was applied (10^{-4} /s). The support ring was lubricated in order to minimize the effects of friction. For the approximated solution, the strength was calculated from the maximum values of Eq. (116):

$$S_{UTS,cubic}^{POR} = \frac{qtr_p^2}{64D^{*cubic}} \left[\frac{(k^{*cubic} + 1)}{S_{I1} + S_{I2}} \right] \quad (137)$$

where the symbols are as defined in Eqs. (109) to (113).

Table 4.6.2.1: Test specimen dimensions for AFN12 single crystal NiAl specimens tested in biaxial flexure.

Specimen Configuration (number tested)	Mean ^[1] Height or Thickness mm	Mean Depth or Diameter mm	Support Span or Diameter mm
Biaxial, POR (13)	1.49 ± 0.004	25.22 ± 0.15	23.19

[1] Mean ± one standard deviation

CHAPTER 5: EXPERIMENTAL RESULTS: MATERIAL PROPERTIES AND VERIFICATION TESTING

5.1 ELASTIC PROPERTIES

The elastic modulus of the WC was 607 ± 3 GPa and Poisson's ratio was 0.22.

A mean and standard deviation of 96.9 ± 1.0 GPa was measured on the $\langle 100 \rangle$ and 187 ± 2.7 GPa on the $\langle 110 \rangle$ orientation of the NiAl. These results are in good agreement with the published values of 95.9 and 187.3 GPa (Wasilewski 1966) and within 10% of the published values of 86.0 and 205.0 GPa (Rusovic' and Warlimont 1977), implying that the small percentage of alloying elements has not substantially altered the elastic properties.

5.2 UNIAXIAL STRENGTH

5.2.1 Isotropic Material

Table 5.2.1.1 summarizes the measured uniaxial strength of the WC test specimens. The 90% confidence intervals (Abernathy et al. 1983) are included. The maximum likelihood method was used to calculate the Weibull parameters (Jakus et al. 1981 and Sonderman et al. 1985).

Table 5.2.1.1: Measured flexural strength statistics and 90% confidence intervals for WC.

Specimen Configuration (number tested)	Mean ^[1] Strength MPa	Characteristic Strength, σ_θ MPa	90% Confidence Bands on σ_θ	Weibull Modulus m	90% Confidence Bands on m
Three-point, "A" (29)	2910 ± 223	3001	2950, 3053	19.0	14.9, 24.2

[1] \pm one standard deviation.

5.2.2 Anisotropic Material

Tables 5.2.2.1 and 5.2.2.2 summarize the measured uniaxial strength of the NiAl test specimens. Detailed test results are given in Appendix C. The 90% confidence bands (Abernathy et al. 1983) are included for the determination of the statistical significance of the observed differences in measured strength. The mean strength and standard deviation of the specimens from each billet is shown in Figures 5.2.2.1 and 5.2.2.2. Note that two of the $\langle 100 \rangle$ billets exhibit an average strength somewhat significantly greater than the remaining billets. The resulting probabilities of failure as a function of stress are shown in Figure 5.2.3 for $\langle 100 \rangle$ and $\langle 110 \rangle$ orientations. Censored Weibull statistics were used to rank the data (Jakus et al. 1981) and the maximum likelihood estimator (MLE) (Sonderman et al. 1985) was used to calculate the Weibull parameters. The characteristic strength and mean strength as a function of orientation in the $\{100\}$ plane are shown in Figures 5.2.2.3 and 5.2.2.4.

5.3 FRACTOGRAPHY OF THE FLEXURE SPECIMENS

Scanning electron microscopy was performed to determine the source of test specimen fracture. The results are summarized in Table 5.2.2.2. The $\langle 100 \rangle$ specimens fractured predominately from inclusions protruding from the machined surface, Figure 5.3.1. However, the $\langle 110 \rangle$ specimens failed from a mixture of inclusions and electro-discharge machining damage (EDM), even though all the flexure specimens were prepared together in a like manner. Energy and wavelength dispersive analyses⁵ of the inclusions typically indicated large amounts of hafnium (Hf) with smaller amounts of titanium (Ti) and carbon (C), implying complex carbides of the form (HfTi)C. Occasionally a significant oxygen peak was obtained, implying the presence of both HfO and (HfTi)C. However, because the dominant signal indicated Hf with the presence of C, the inclusions will be referred to as HfC. Thus, as carbide are the inherent strength limiting mechanism, lowering the Carbon content during processing should reduce the frequency and/or size of HfC inclusions and thereby increase strength.

Note that the inclusions are three dimensional and bonded to the matrix and therefore probably support significant tractions. Further, the thermal and elastic constants may be substantially different from those of the NiAl matrix. Thus the flaws are not the ideal, classical concept of open closed cracks.

⁵ IMIX-PC Prism Digital Spectrometer, Princeton Gamma Physics, Princeton, NJ.

Table 5.2.2.1: Flexural strength of AFN12 single crystal NiAl - normal statistics.

Orientation and Flexural Configuration	Failure ^[1] Location and Type	Number of Tests	Mean Strength MPa	Standard Deviation of Strength MPa	Coefficient of Variation
<100> 3-point	S-HfC	15	1261	209	0.17
<100> 4-Point	S-HfC	32	1010	202	0.20
<110> 3-Point	S-HfC	9	767	177	0.23
<110> 4-Point	S-HfC	15	629	130	0.21
<110> 3-Point	S-EDM	3	466	69	0.15
<110> 4-Point	S-EDM	19	340	107	0.31

[1] S = surface; EDM = electro-discharge machining scar. HfC = Hafnium carbide inclusion.

Table 5.2.2.2: Flexural strength of AFN12 single crystal NiAl - Weibull statistics.

Orientation and Flexural Configuration	Failure ^[1] Location and Type	Characteristic Strength σ_θ , MPa	90% Confidence Bands for σ_θ	Weibull ^[2] Modulus m	90% Confidence Bands for m
<100> 3-point	S-HfC	1350	1258 to 1475	6.1	4.4 to 8.5
<100> 4-Point	S-HfC	1094	1032 to 1158	5.4	4.3 to 6.8
<110> 3-Point	S-HfC	843	754 to 933	4.8	2.2 to 9.2
<110> 4-Point	S-HfC	689	642 to 735	5.5	3.5 to 8.2
<110> 3-Point	S-EDM	---	---	---	---
<110> 4-Point	S-EDM	474	---	4.6	---

[1] S = surface; EDM = electro-discharge machining scar. HfC = Hafnium carbide inclusion.

[2] Weibull modulus and characteristic strength were determined with the maximum likelihood method.

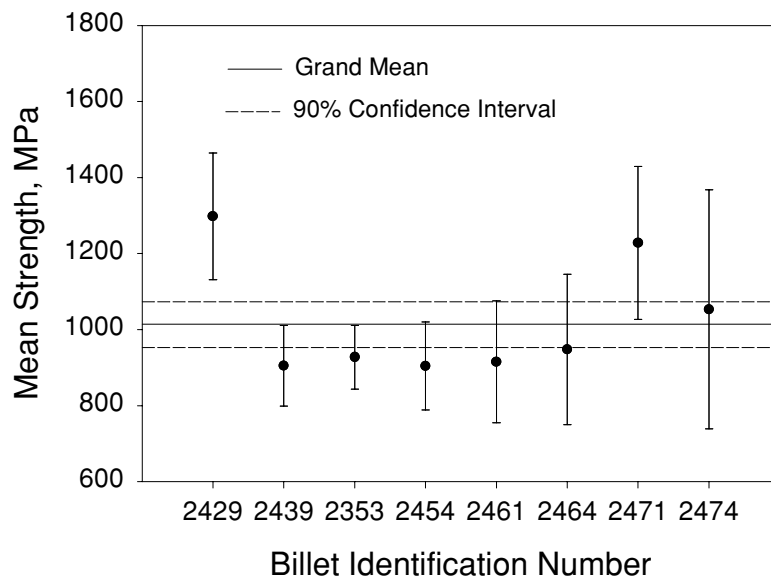


Figure 5.2.2.1: Average <100> four-point flexural strengths and 90% confidence intervals for AFN12 single crystal NiAl billets.

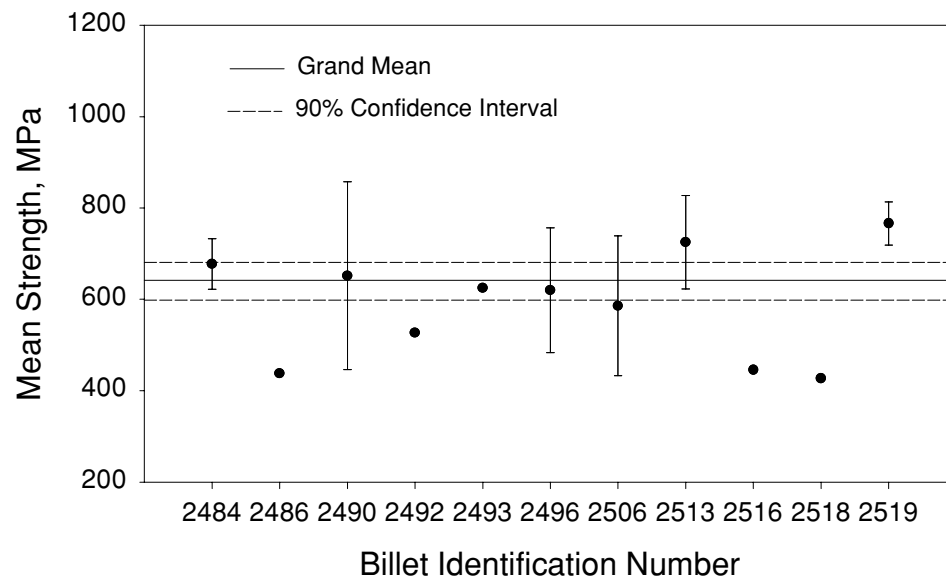


Figure 5.2.2.2: Average $\langle 110 \rangle$ four-point flexural strengths and 90% confidence intervals for AFN12 single crystal NiAl billets.

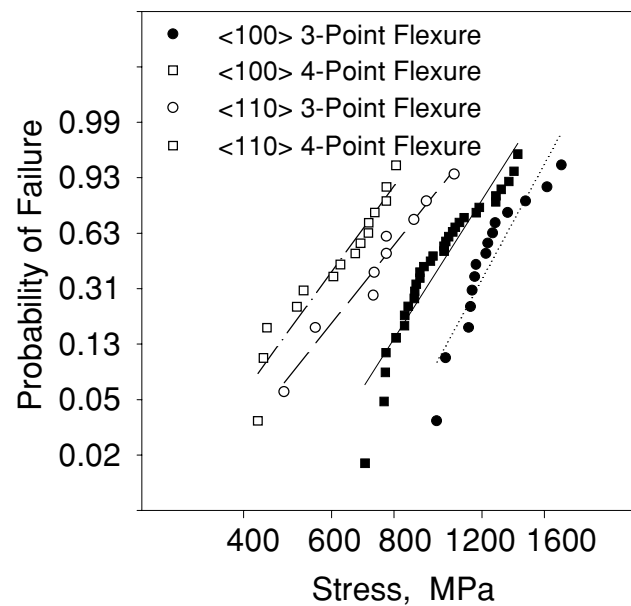


Figure 5.2.2.3: Weibull distributions for the $\langle 100 \rangle$ and $\langle 110 \rangle$ orientations of AFN12 single crystal NiAl tested in three and four-point flexure.

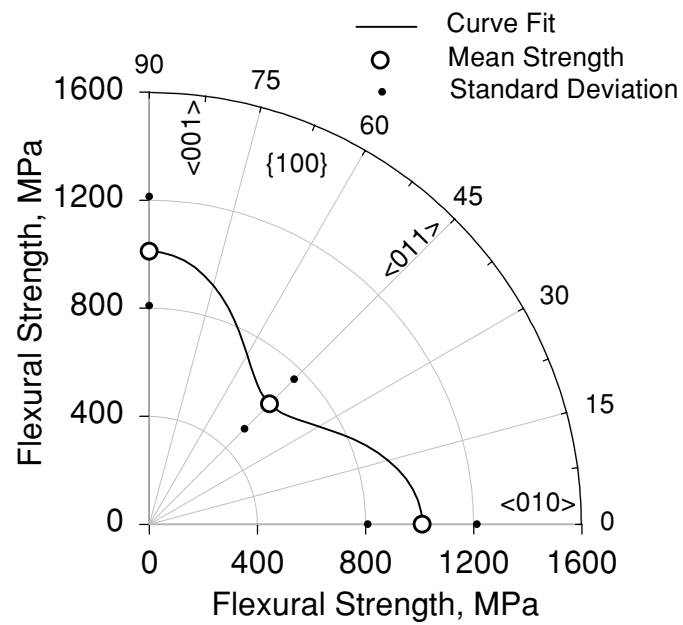


Figure 5.2.2.4: Mean strength as a function of orientation on the {100} for AFN12 single crystal NiAl tested in four-point flexure.

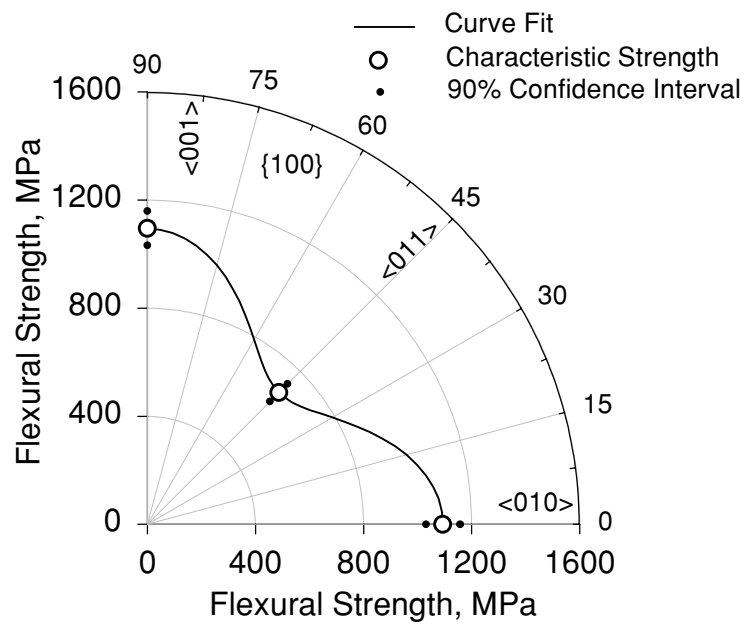
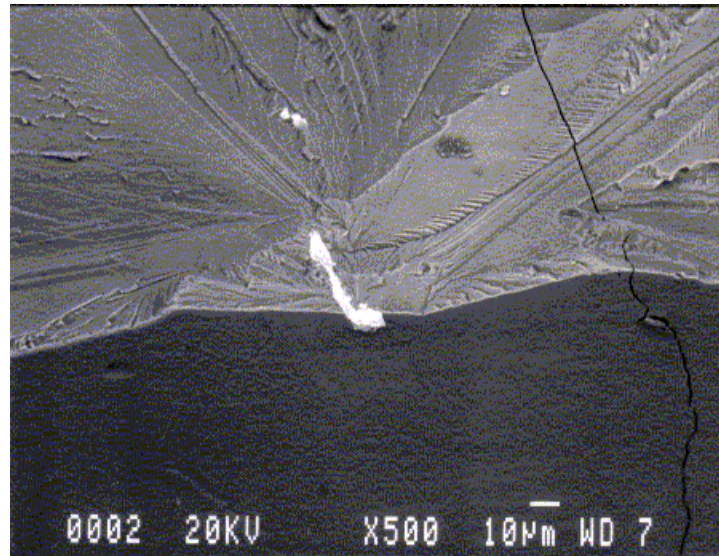


Figure 5.2.2.5: Characteristic strength as a function of orientation on the $\{100\}$ for AFN12 single crystal NiAl tested in four-point flexure.

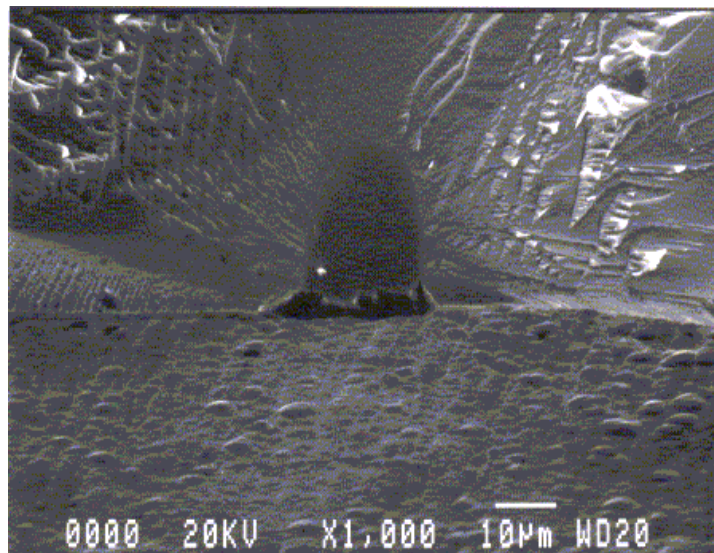
Despite the fact that the principal stress was oriented to induce cleavage along a low index plane, the test specimens did not appear to macroscopically cleave on the cleavage plane common to cubic crystals (*i.e.* $\{100\}$ and $\{110\}$), as shown in Figures 5.3.2 and 5.3.3. However, the fractures (due to EDM scars or HfC inclusions) appeared to have occurred on a specific plane, rather than conchoidally as facets extending from the HfC inclusion are apparent. This was in contrast to observations on test specimens that failed during machining or handling: these exhibited macroscopic cleavage along the $\{110\}$. For some materials cleavage only occurs in a well-defined manner when appropriate conditions of stress and or crack velocity exists. If these conditions do not exist, then conchoidal fracture occurs. In order to determine the orientation of the fracture facets, Laue X-ray analysis of selected cleavage facets was performed. The specimens were mounted on a holder with two mutually perpendicular axes of rotation and examined with a microscope that had a collimated light aligned with the microscope axis. The light source was used to align the facet normal to the axis of the microscope and holder by seeking the fullest reflection. The holder was then transferred to an X-ray machine.

X-ray analysis did not identify a dominant crystal plane associated with the facets. Instead the fracture facets near the origin of these samples appeared to propagate along various high index planes. Figure 5.3.4 is a summary of the major crystal planes identified in six different $\langle 110 \rangle$ four-point flexure specimens. The only similarities associated with these cleavage planes are the fact that they are all high index, consist of near center-triangle orientations, and are all far from (011). This is nominal agreement with Blankenship's results that show facets from several families of planes.

The test specimens that were fractured in four-point flexure and those that fractured during the machining and handling process were subjected to substantially different stress states, strain energies and loading velocities. Thus the effect of impact and crack velocity were briefly investigated to determine if more defined facets could be generated. Additional flexure tests were run at stress rates of 13,270 MPa/s and 27,930 MPa/s. In addition, several Charpy impact tests were run at both room and liquid nitrogen temperatures. Again, fracture occurred on high index planes with similar bifurcation angles as those shown in Figure 5.3.2.



(a)



(b)

Figure 5.3.1: Failure origins in AFN12 NiAl single crystal flexure specimens: (a) Hf rich inclusion in a $\langle 100 \rangle$ test specimen, and (b) EDM damage in a $\langle 110 \rangle$ test specimen.

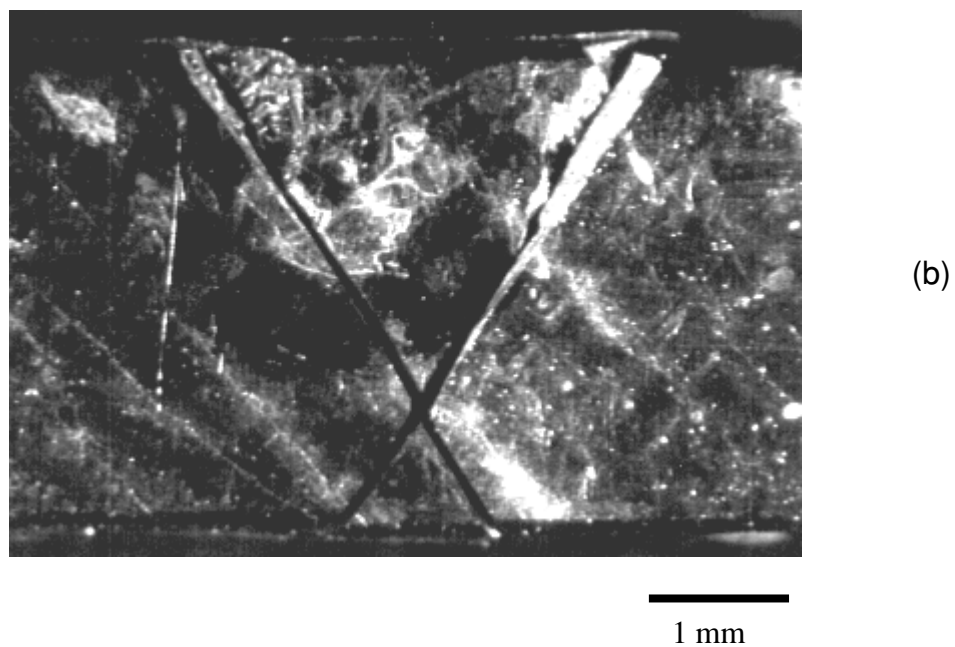
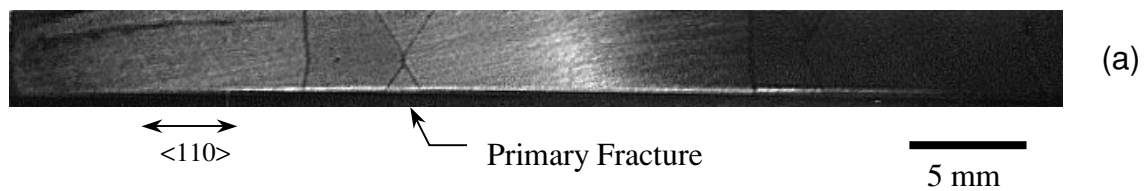


Figure 5.3.2: Typical bifurcation pattern observed on the surface of $\langle 110 \rangle$ flexure test specimens: (a) overall flexure test specimen and (b) detail of a fracture location.

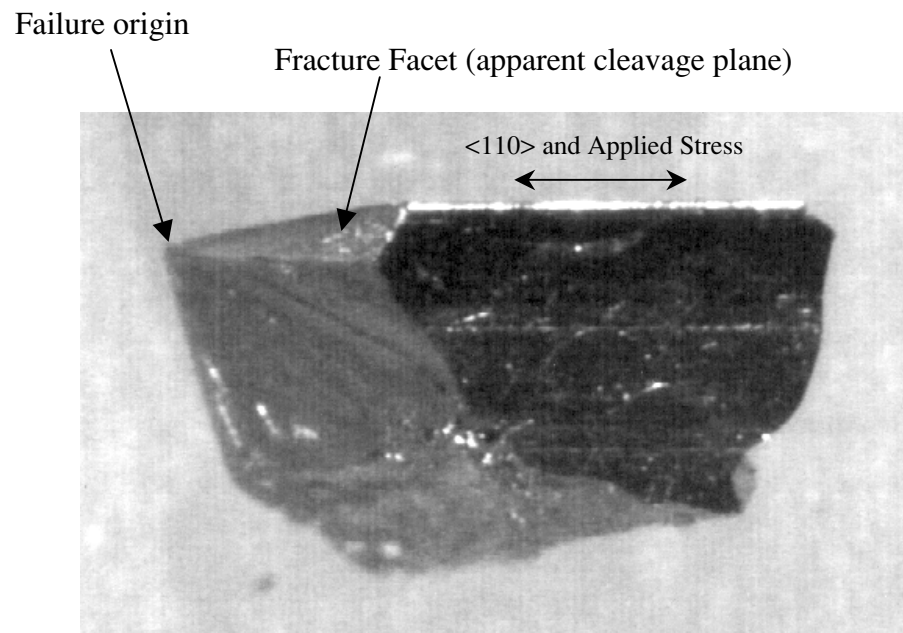


Figure 5.3.3: Side view of a segment from a fractured AFN12 <110> four-point flexure test specimen.

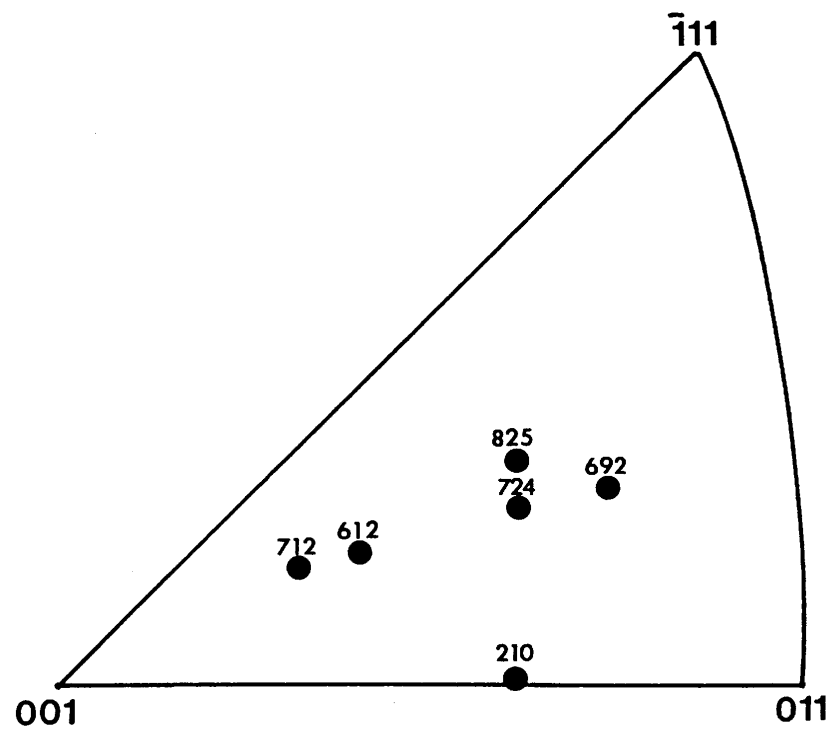


Figure 5.3.4: Summary of cleavage planes in $\langle 110 \rangle$ four-point flexure test specimens. Numbers are crystal $\langle hkl \rangle$ directions associated with fracture facets.

It should be noted that the fracture mirrors about the EDM origins are nominally $\{110\}$, and the crack bifurcation is symmetric about the $\{110\}$ in all cases. Because substantial strain energy is stored during flexural testing but typically not during failure due to machining/handling (which occur via local contact stresses), the crack may be "over driven" during flexural fracture and thus turns off the $\{110\}$. The stored strain energy can be reduced by stiffening the specimen, fixtures and load cell. Limited proof of this concept is shown in Figure 5.3.5, where the bifurcation angle is plotted as a function of fracture stress, indicating that the bifurcation angle tends to increase with increasing fracture stress and thus stored energy.

An alternative explanation (Darolia et al. 1993) for the lack of $\{110\}$ cleavage is that under conditions where microplasticity occurs, cleavage deviates from $\{110\}$ to a series of high index planes centered around $\{511\}$ and $\{711\}$, which is somewhat consistent with the observed cleavage planes summarized in Figure 5.3.4. In the absence of microplasticity, cleavage will occur along $\{110\}$. In some respects, these two explanations are complimentary since greater strain energy can be stored in the material as microplasticity occurs.

Another explanation for the variation in cleavage angle observed on the specimen tensile surface is the variation in secondary orientation. Unless the cleavage planes are orthogonal to the test specimen orientation (i.e. $\langle 110 \rangle$), variation in the secondary orientation will cause a variation in the angle traced on the tensile surface of the specimen. The correlation of strength with observed angle could also imply an effect of secondary orientation on strength.

imparting damage in the grinding direction, allows accurate tolerances while imparting minimal damage in the test direction (ASTM C 1161 1990).

5.4 BIAXIAL STRENGTH

5.4.1 Isotropic Material

Table 5.4.1.1 summarizes the measured uniaxial and biaxial strength of the WC test specimens. The 90% confidence intervals (Abernathy et al. 1983) are included for the determination of the statistical significance of the observed differences in measured characteristic strength and Weibull modulus. The mean strength of the disk test specimens is 20% less than that of the uniaxial test

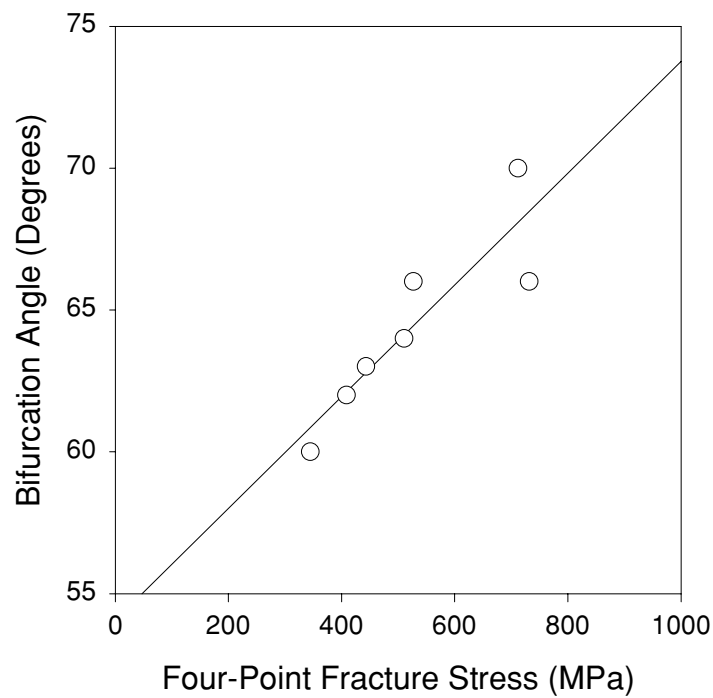


Figure 5.3.5: Bifurcation angle plotted as a function of fracture stress in <110> four-point flexure test specimens.

specimens and the difference is statistically significant. The difference between the Weibull moduli for uniaxial and biaxial data is not statistically significant at 90% confidence. The maximum likelihood method was used to calculate the Weibull parameters (Jakus et al. 1981 and Sonderman et al. 1985).

5.4.2 Anisotropic Material

Table 5.4.2.1 summarizes the measured biaxial strength of the NiAl test specimens. Detailed test results are given in Appendix D. The 90% confidence intervals (Abernathy et al. 1983) are included for the determination of the statistical significance of the observed differences in measured characteristic strength and Weibull modulus.

Table 5.4.1.1: Measured strength statistics and 90% confidence intervals for WC.

Specimen Configuration (number tested)	Mean ^[1] Strength MPa	Characteristic Strength, σ_θ MPa	90% Confidence Bands on σ_θ	Weibull Modulus m	90% Confidence Bands on m
Three-point, "A" (29)	2910 \pm 223	3001	2950, 3053	19.0	14.9, 24.2
Biaxial, POR (10)	2320 \pm 144	2379	2323, 2436	23.0	15.3, 34.5

[1] Mean \pm one standard deviation.

Table 5.4.2.1: Measured strength statistics and 90% confidence intervals for AFN12 single crystal NiAl tested in biaxial flexure.

Stress Solution	Mean ^[1] Strength MPa	Characteristic Strength, σ_θ MPa	90% Confidence Bands on σ_θ	Weibull Modulus m	90% Confidence Bands on m
Approximate	470 \pm 109	511	466, 559	5.3	3.7, 7.6
Series	431 \pm 100	469	428, 513	5.3	3.7, 7.6
Approximate ^[2]	477 \pm 111	519	473, 568	5.3	3.7, 7.6
Series ^[2]	439 \pm 102	478	436, 524	5.2	3.6, 7.4

[1] Mean \pm one standard deviation.

[2]. Estimate includes the effect lateral pressure as calculated from Eq. (135).

The strength distributions of the uniaxial and biaxial flexure strength data are shown in Figure 5.4.2.1. The mean strength of the NiAl biaxial test specimens is 431 MPa. The Weibull modulus is 5.3, implying the same flaw population as measured in the uniaxial specimens. The maximum likelihood method was used to calculate the Weibull parameters (Jakus et al. 1981 and Sonderman et al. 1985). Also included in the table is the effect of lateral pressure on the plate deflection, assuming that the isotropic solution in Eq. (135) is applicable.

5.4.3 Macroscopic Failure Analysis of the Disk Test Specimens

One advantage of biaxial specimens is the multiplicity of planes subjected to large stress over a large area, thereby sampling many flaws and allowing any cleavage plane to induce fracture and be followed for a macroscopically observable distance.

The disk test specimens exhibit a distinct, macroscopic failure pattern as shown in Figure 5.4.3.1. Fracture, as viewed on the {100}, typically occurs along a single direction and rapidly branches in three other directions: one at 90° to the main direction and two other directions that form a 90° angle to each other and 60° and 150° angles to the initial direction. Essentially the traces on the {100} form two sets of orthogonal directions rotated 60° to each other. The pattern is repeated across the disk in a varying degree until the edges are approached and the pattern becomes conchoidal. The angles between the <100> and the observed cleavage traces are listed in Table 5.4.3.1 and plotted with the 90% confidence intervals on a (001) pole figure in Figure 5.4.3.2 for eight of the test specimens. The macroscopic cleavage directions in the (001) nearly correspond to the <310> directions. However, because the planes forming the directions are not normal to the (001) surface, the actual cleavage planes are located in the interior of the pole figure along the line emanating from the <310> directions intersecting the perimeter of the pole figure (i.e. the <310> “great circle”). This implies that the preferred set of macroscopic planes for crack extension is not one of the typical {001}, {110} or {111} sets.

The radial failure position and angle relative to the <100> direction was measured on eight of the disk surfaces, as shown in Figure 5.4.3.3. The data is plotted in a single quadrant as the crystal symmetry repeats every 90°. The radial positions of failure relative to the support ring radius ranged from 0.20 to 0.55 wherein the stresses are greater than 70% of the maximum, equibiaxial stress. The minimum angle from the <100> associated with the dendrite growth direction to the

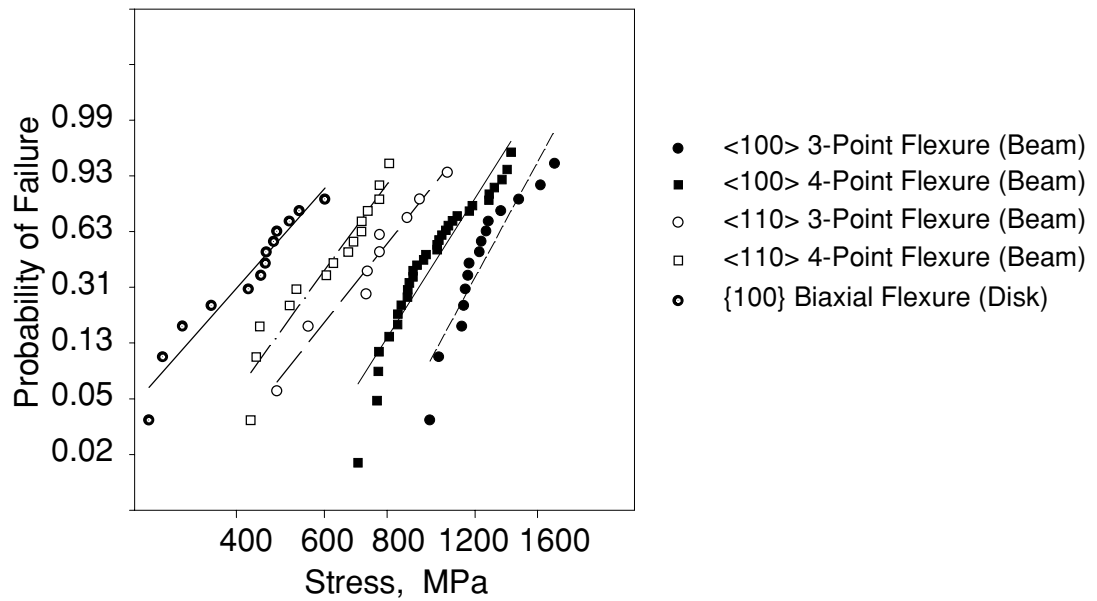
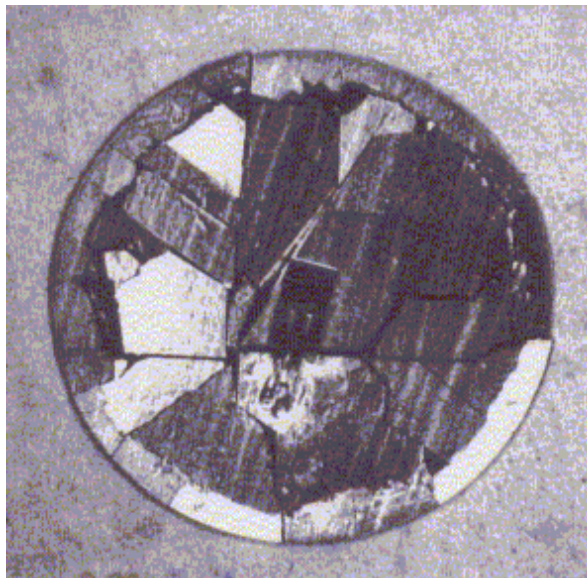
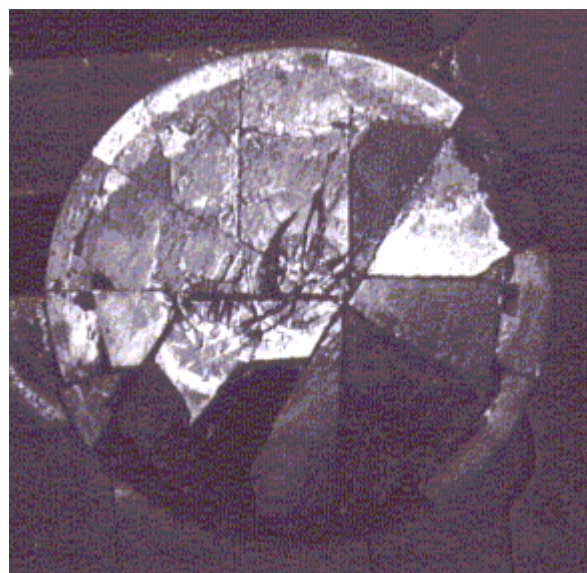


Figure 5.4.2.1: Weibull distributions for the flexural strength of AFN12 single crystal NiAl. Included in the plot are the data for the $\langle 100 \rangle$ and $\langle 110 \rangle$ tested in three and four-point flexure (beams) and the {100} tested in biaxial flexure (disks) by application of a uniform pressure.



(a)



(b)

Figure 5.4.3.1: NiAl single crystal disk test specimens failed by application of a uniform pressure: (a) specimen B11 and (b) specimen B5.

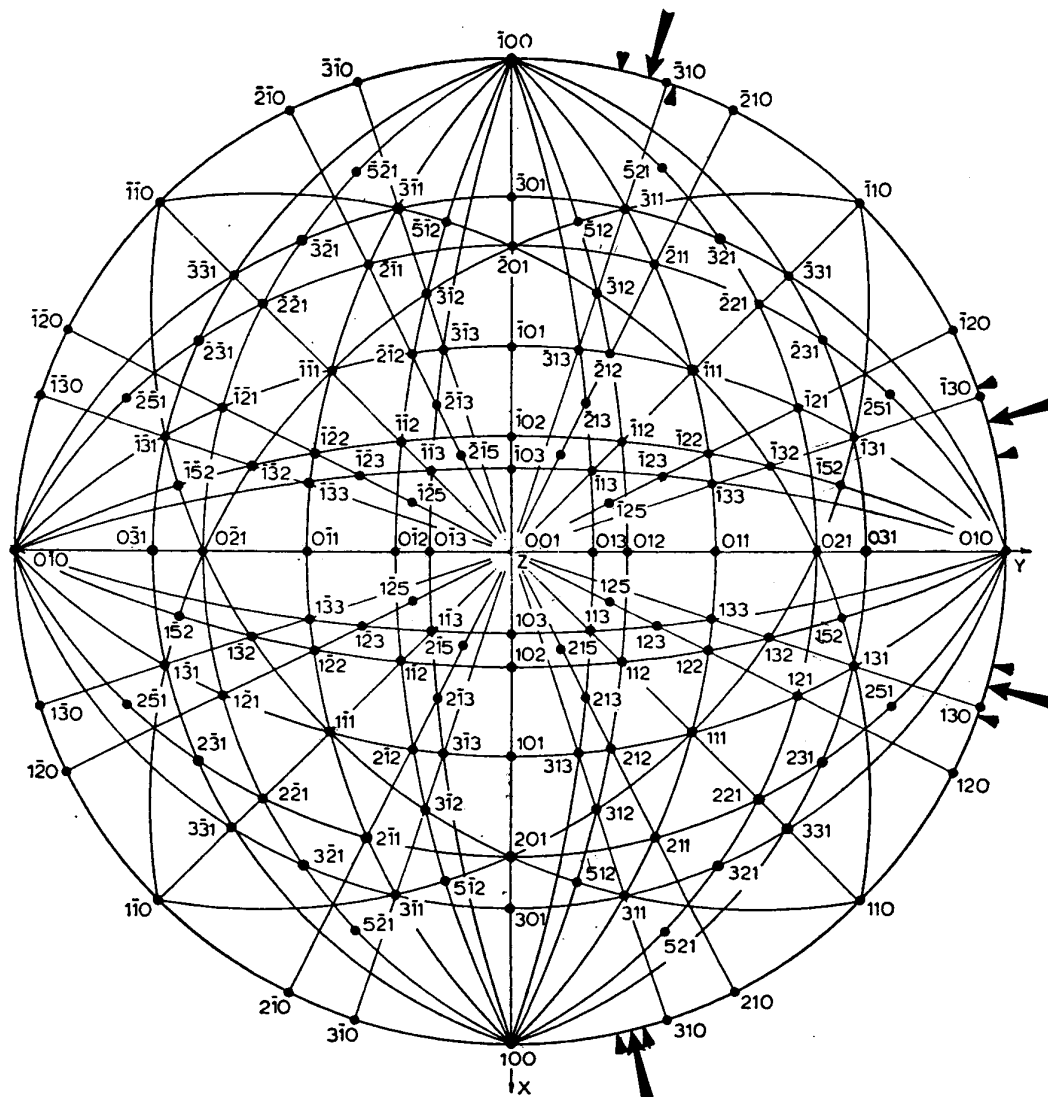


Figure 5.4.3.2: Standard (001) pole figure showing the macroscopic failure directions exhibited by AFN12 single crystal NiAl biaxial test specimen. Arrows on the perimeter indicate the measured mean directions and standard deviations of the cleavage directions observed on the (001).

Table 5.4.3.1: Macroscopic cleavage directions and 90% confidence intervals in the (001) plane of single crystal NiAl tested in biaxial flexure. Measurements are clockwise from the $\bar{1}00$ direction. Also listed are the angles from the $\bar{1}00$ to the $\langle 310 \rangle$.

Mean, degrees	16 ± 3	75 ± 4	106 ± 3	166 ± 1
90% Confidence	2	2	2	1
Angles to $\langle 310 \rangle$	18	72	108	162

failure location ranged from 18° to 62° with a mean of $41 \pm 16^\circ$. Also plotted in Figure 5.4.3.3 in the direction of the macroscopic cleavage plane relative to the $\langle 100 \rangle$ dendrite growth direction. In all but two of the test specimens, the minimum angle was toward the $\langle 310 \rangle$ associated with the $\langle 100 \rangle$ direction corresponding to the dendrite growth direction instead of its complement. This implies a preference or bias in the properties toward the $\langle 100 \rangle$ associated with dendrite growth.

The bias of the failure position to the $\langle 110 \rangle$ directions implies that the larger tangential stress or lower strength associated with the $\langle 110 \rangle$ influences failure. Because the $\langle 110 \rangle$ are orthogonal in the {001}, the $\langle 110 \rangle$ directions are subjected to both the radial and tangential stress components at any radial location along a $\langle 110 \rangle$. Thus, failure would be expected to initiate and propagate along the $\langle 110 \rangle$ radial directions if the $\langle 110 \rangle$ is the weak plane and the maximum principal stress dominated failure. However, as shown in Table 5.4.3.1 and Figure 5.4.3.2, the macro extension plane is not the $\langle 110 \rangle$ and either a weaker cleavage plane exists or the combined stresses cause propagation elsewhere.

Particularly noteworthy is a slight jog in the direction of crack propagation at the failure origin. The failure origins observed in the flexure specimens are finite and three-dimensional HfC inclusions.

Thus, the jog may be a result of the failure initiating on one side of an inclusion and traveling around or through it. The jogs are relatively small and optical measurement of the associated angles was not feasible. Detail electron fractography is required to determine the exact failure location and the cause of the jog. The failures could initiate within the inclusion, outside of the inclusion, or at the inclusion-NiAl interface.

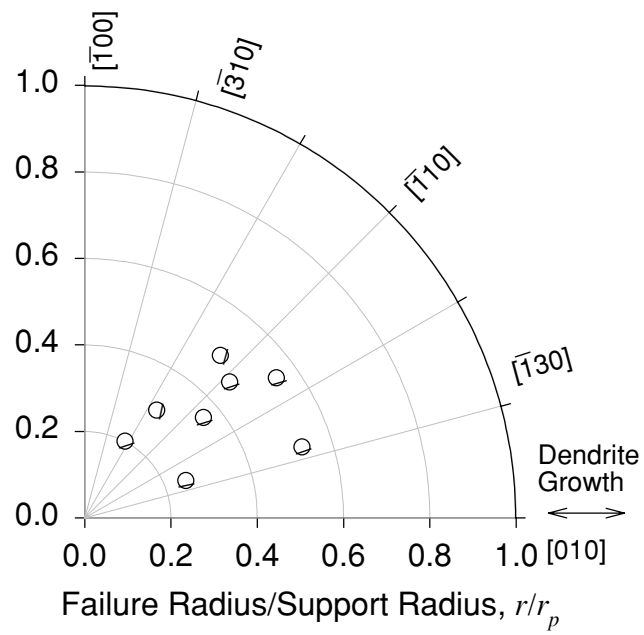


Figure 5.4.3.3: Macroscopic failure locations and planes exhibited by AFN12 single crystal biaxial test specimens.

5.4.4 Fractography of the Disk Test Specimens

As in the flexure test specimens, failure occurred from coarse Hf rich inclusions, as shown in Figure 5.4.4.1. Energy dispersive analysis of the inclusions indicated Hf, Ti and C, as shown in Figure 5.4.4.2, implying complex (HfTi)C carbides as in the uniaxial test specimens.

The river marks and tail next to the inclusion imply that fracture initiates along the interface of the inclusion at or near tensile surface, Figure 5.4.4.3. In some cases, a second smaller tail is apparent on the other side of the inclusion implying the initiation of a second crack immediately after the initial failure. The primary crack wraps around the inclusion and either meets the secondary fracture or jumps across the HfC inclusion as it fails. Exactly when the inclusion fractures is not clear, however, observation of both the uniaxial and biaxial flexure test specimens indicate that the inclusions typically fail instead of pulling out of the NiAl matrix, as shown in Figure 5.4.4.4.

The initiation at the interface between the inclusion and the matrix can be explained by the residual stresses that result from the thermal and elastic differences between HfC and NiAl. The residual stresses are estimated and discussed in Section 6.

In order to measure the jog angle relative to the applied stress and crystal structure and determine its source, the tensile surface of eight of the specimens were observed with in the electron microscope. A typical jog and the corresponding fracture surface are shown in Figure 5.4.4.5. The inclusions are typically located at one end of the jog with the initiation of fracture occurring on the jog side of the inclusion. Thus the jog is not caused by the crack passing through or initiating within the inclusion. The average angle of the jog direction relative to the <100> and the radial direction of the disk are summarized in Table 5.4.4.1 and are plotted in Figure 5.4.4.6. The jogs

Table 5.4.4.1: Orientation of failure relative to the crystal structure and stress state.

Jog Length μm	Jog Angle From <100> Degrees	Jog Angle from Radial Direction Degrees
62 ± 28	44 ± 5	45 ± 34

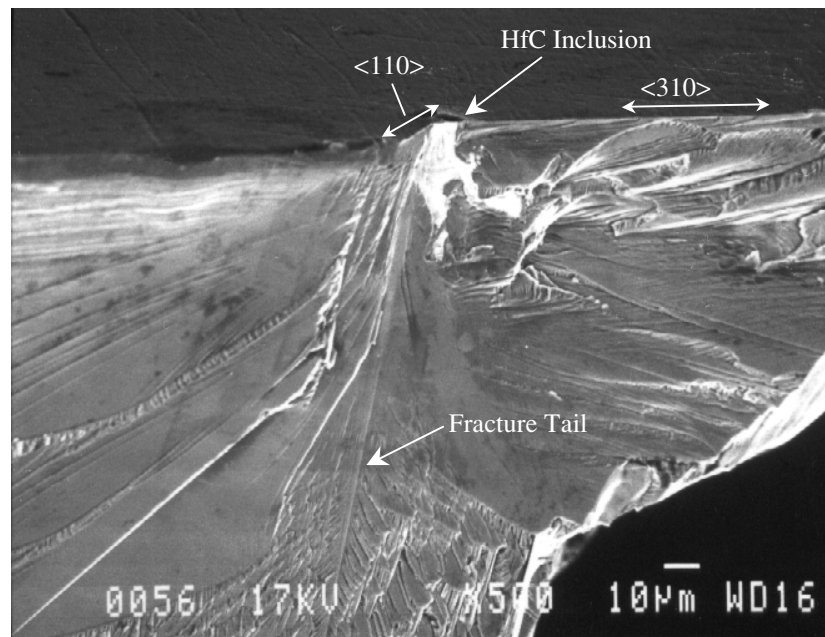


Figure 5.4.4.1: Failure origin in an AFN12 single crystal biaxial test specimen.

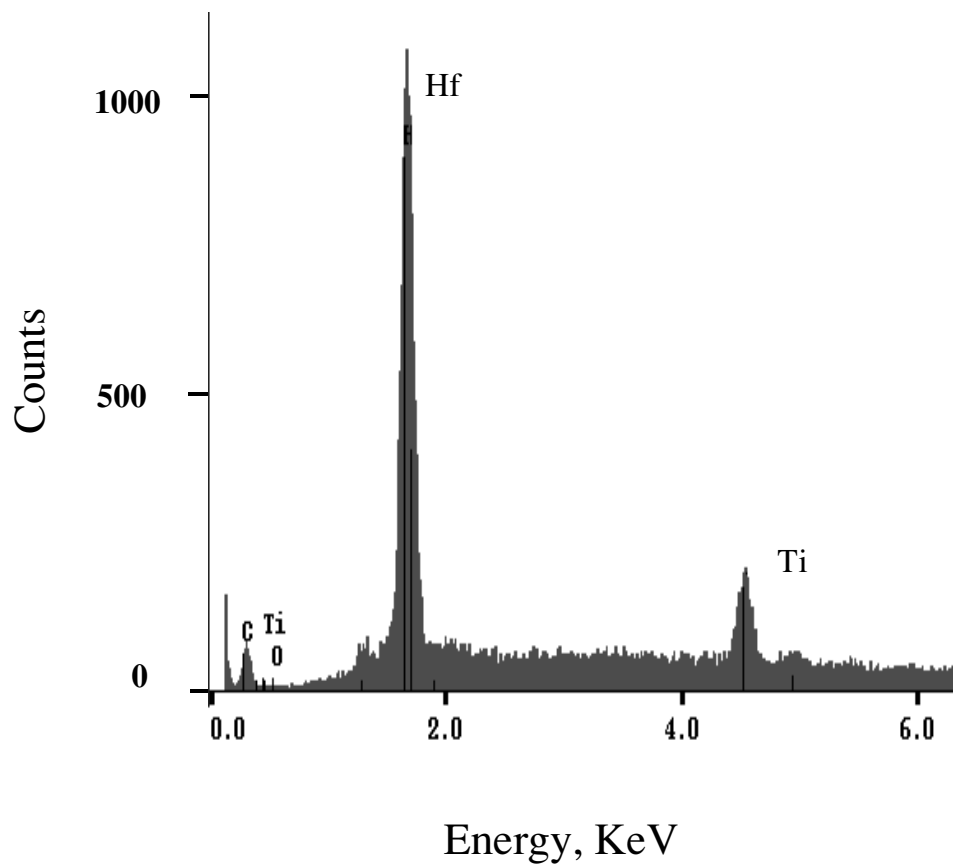


Figure 5.4.4.2: Energy dispersive analysis of a failure origin in an AFN12 single crystal NiAl biaxial test specimen. Hafnium, titanium and carbon are indicated, implying (HfTi)C.

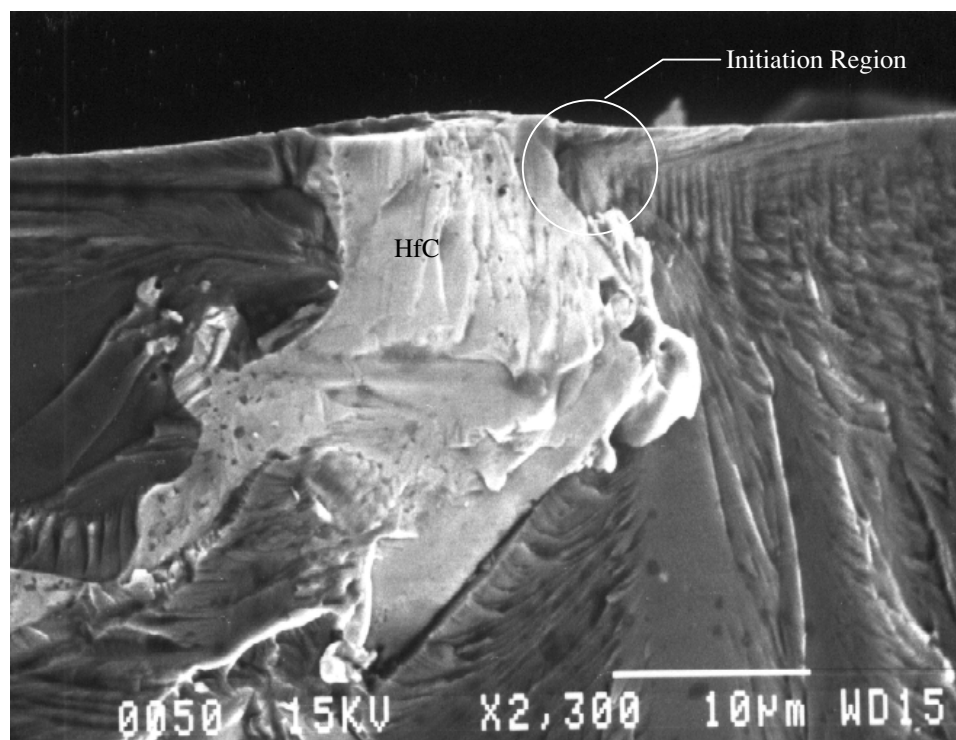
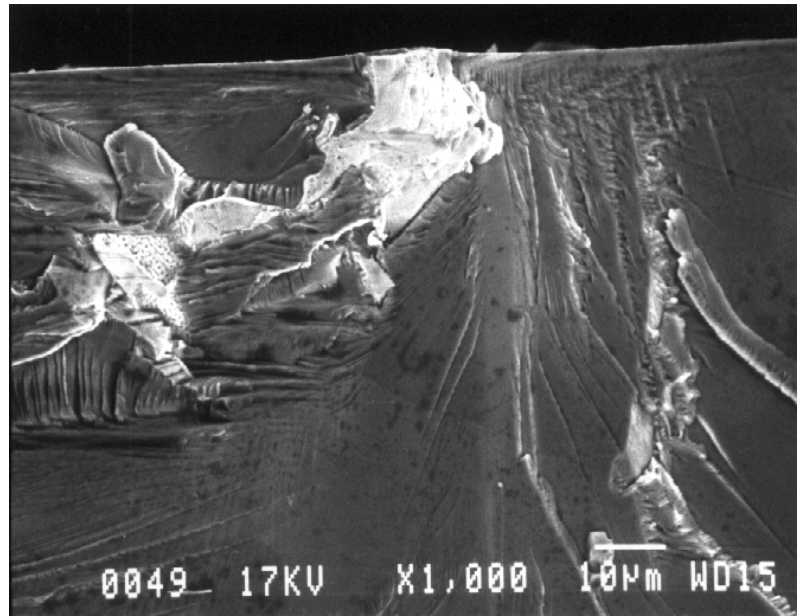
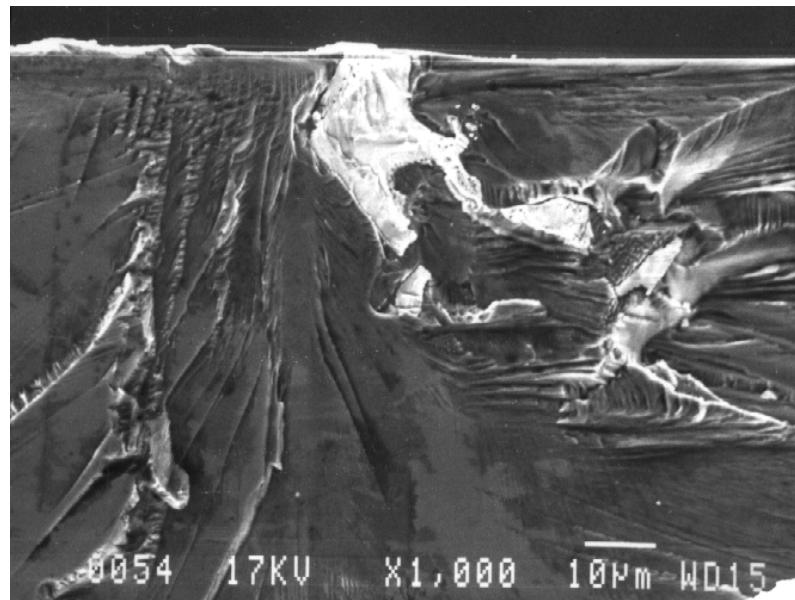


Figure 5.4.4.3: Detail of a failure origin in an AFN12 single crystal NiAl biaxial test specimen. A mixture of secondary and back-scattered electrons were used for imaging.

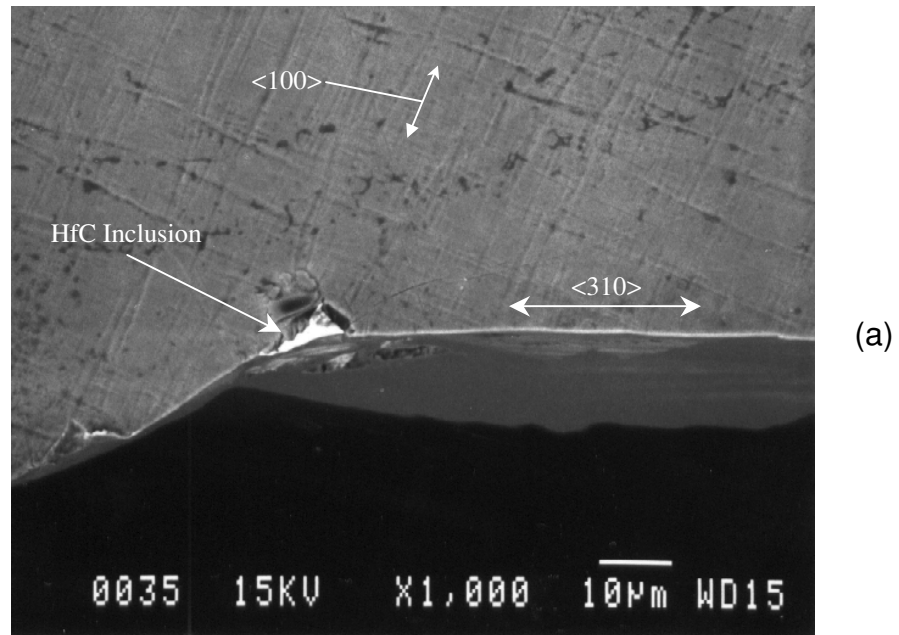


(a)

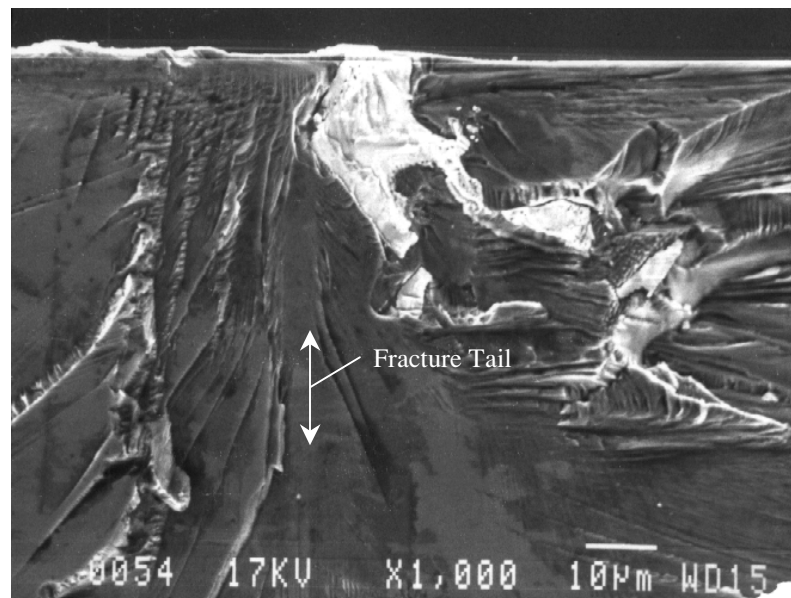


(b)

Figure 5.4.4.4: Mating fracture surfaces of an AFN12 single crystal biaxial test specimen. Fractured inclusion can be observed on both halves, implying inclusion fracture instead of pullout.



(a)



(b)

Figure 5.4.4.5: (a) Tensile surface of an AFN12 single crystal NiAl biaxial test specimen and (b) corresponding fracture surface. Jog angle relative to the macroscopic failure plane and $\langle 100 \rangle$ etch lines that resulted from chemical milling are shown.

have a mean length of $62 \pm 28 \mu\text{m}$ on the tensile surface and extend along a $44 \pm 5^\circ$ angle to the $\langle 100 \rangle$ in the surface of the plate, which corresponds to the $\langle 110 \rangle$ trace. The jog planes are nominally normal to plate surface, implying jog planes of $\{110\}$ orientation. Note from Figure 5.4.4.6 that both tangentially and radially oriented $\langle 110 \rangle$ jog planes have produced failure (three of radial orientation and five of tangential orientation), implying that neither the radial or tangential stress component-dominated failure. As noted previously, the radial and tangential stresses at the failure locations were within 70% of the equibiaxial stress and therefore similar. Also summarized in Table 5.4.4.1 is the jog angle relative to the radial direction in the disk test specimen. Note that the standard deviation of the angle of failure relative to the radial direction is quite large as a result of the failure planes being either nearly radial or tangential. Thus failure appears to be controlled locally by the crystal structure and location of the largest flaw dimension in a multiaxial stress state in which the principal stresses are nearly equal.

Apparently fracture initiates at the interface of the HfC and NiAl matrix on the $\{110\}$ and rapidly branches onto a set of high-index planes associated with the $\langle 310 \rangle$ trace in the $\{100\}$. The $\langle 110 \rangle$ extension on the plate surface occurs predominantly on the initiation side of the inclusion. Little extension on the other side of the inclusion is observable on the plate surface because the crack transits onto the $\langle 310 \rangle$ trace as it wraps around or travels through the inclusion. One explanation for the branching is the multiplicity of low index planes available for the crack to extend on and thereby dissipate energy. Figure 5.4.4.7 shows the idealized fracture pattern based on the average crack angles measured.

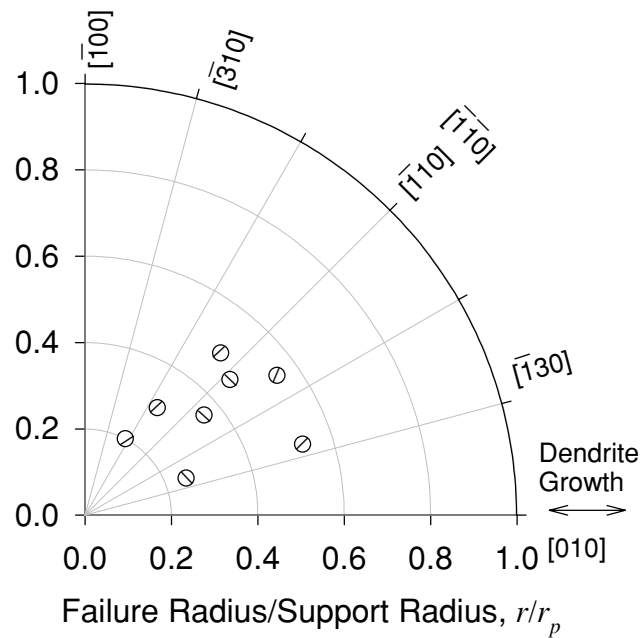


Figure 5.4.4.6: Failure locations in an AFN12 single crystal NiAl biaxial test specimen. Symmetry was invoked and the positions plotted in a single quadrant. The lines within the circles represent the local direction of failure (i.e. the jog direction) extending from the HfC origin.

CHAPTER 6: VERIFICATION OF THE ANISOTROPIC RELIABILITY MODEL

The formulations developed in Chapter 3 and the experimental results detailed in Chapter 5 provide a basis for verification of the reliability model given in Eq. (74). For isotropic materials, Eqs. (88) and (89) are generally considered capable of predicting four-point strengths from three-point strength data for brittle, isotropic materials such as polycrystalline ceramics and glasses. The next section investigates that capability.

6.1 RELIABILITY-BASED STRENGTH PREDICTIONS FOR ISOTROPIC MATERIALS

The equivalent stress failure criteria given in Eqs. (29) to (32) and (44) and (45) were employed to predict the biaxial strength of the WC disk test specimens from the measured strength parameters of the smaller, uniaxial flexure specimens (Tables 5.4.1.1 and 5.2.1.1).

The resulting strength predictions from the uniaxial data and the associated 90% confidence bands are compared to the 90% confidence bands of the measured biaxial data in Figures 6.1.1 for the SIFCs given in Equations (21) to (23).

The PIA and the maximum principal stress criteria, which are based only on the principal stresses, were reasonable predictors of the materials measured biaxial flexure strength, despite the in-plane shear stresses generated in the outer region of the plate. The normal stress criterion, which implies that the normal stresses at any angle reduces reliability, was the most conservative of any criteria considered and underestimated the data by approximately 8%. The ability of the fracture mechanics failure criterion to predict the multiaxial strength data was dependent upon the SIFC chosen, however, for all the SIFCs considered, the coplanar energy release rate was a slightly conservative estimator of the biaxial strength data. In contrast, the noncoplanar energy release rate and the maximum hoop stress factor resulted in predictions not statistically significantly

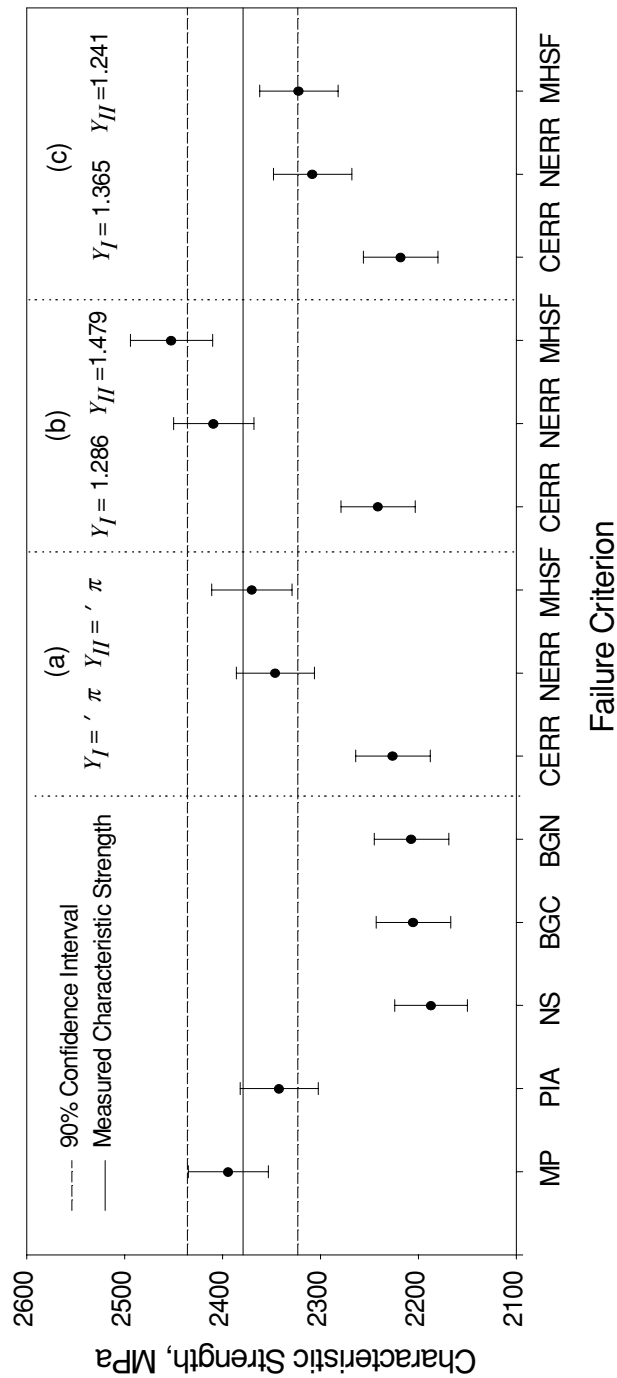


Figure 6.1.2: Measured and predicted characteristic strength for tungsten carbide. The stress intensity factor coefficients of (a) a Griffith crack, (b) of Thiemeier et al. (Thiemeier 1991) and (c) Smith et al. (Smith 1967) and Smith and Sorensen (Smith and Sorensen 1994) were used. The maximum principal stress (MP), principle of independent action (PIA), normal stress (NS), coplanar energy release rate (CERR), non-coplanar energy release rate (NERR), maximum hoop stress factor (MHSF), Batdorf's for a Griffith crack (BGC) and Batdorf's for a Griffith notch (BCN) were considered.

different from the biaxial strength data. Use of the SIFCs of Smith et al. (Smith et al. 1967) resulted in more conservative estimates from the shear sensitive failure theories. The criteria of Batdorf for Griffith cracks and notches resulted in underestimates (-7%) similar to the coplanar energy release rate (-6%) and the normal stress criterion. The characteristic strength predictions were noted to be independent of the value of h used (for $h = 0.5$ to 20), however, the scale parameter was a function of h .

6.2 RELIABILITY-BASED STRENGTH PREDICTIONS FOR ANISOTROPIC MATERIALS: UNIAXIAL STRESS STATES

As shown in Section 3.4.2, the predicted characteristic strength of a uniaxial test specimen is independent of failure criterion and only a function of the ratio of effective areas. To determine the applicability of the scaling equations (i.e. Eqs. (89) and (95) in Section 3.4.1 and 3.4.2) to this single crystal NiAl alloy, the average Weibull modulus in Table 5.2.2 ($m \approx 5.5$) was used to calculate the effective areas and predict the four-point flexural characteristic strength from the three-point flexural data. The results are listed in Table 6.2.3. The predictions are well with the standard deviations of the experimental results for both the $\langle 100 \rangle$ and the $\langle 110 \rangle$ orientations. Thus, the probability of failure for uniaxial flexural of this NiAl can adequately be described by

$$P_{FA} = 1 - \exp \left(- \int_A \left(\frac{\sigma_I}{\sigma_o(\theta_I)} \right)^m dA \right) \quad (138)$$

or as follows in crystallographic notation

$$P_{FA} = 1 - \exp \left(- \int_A \left(\frac{\sigma_{n\langle hkl \rangle}}{\sigma_{o\langle hkl \rangle}} \right)^m dA \right) \quad (139)$$

or in terms of a “crack density coefficient” (Batdorf and Crose 1974) as

$$P_{FA} = 1 - \exp \left(- \int_A k_{ws} (\sigma_{n\langle hkl \rangle})^m dA \right) \quad (140)$$

where the subscript $\langle hkl \rangle$ specifies the crystal direction parallel to the applied stress and k_{ws} is a crack density coefficient now dependent on the stress orientation:

$$k_{ws} = (\sigma_{\langle hkl \rangle})^{-m}. \quad (141)$$

The scaling function becomes

$$(\sigma_{\theta 1} / \sigma_{\theta 2})_{\langle hkl \rangle} = (A_{e2} / A_{e1})_{\langle hkl \rangle}^{1/m}. \quad (142)$$

Note that this material does exhibit yield in compression at approximately 1650 MPa in the $\langle 100 \rangle$ and at 1050 MPa in the $\langle 110 \rangle$ direction (Noebe and Garg 1995). It is unknown if this phenomenon is volume dependent, however, deformation is typically not viewed as a volume dependent process. Thus, for a sufficiently small test volume subjected to tension, yield, rather than brittle fracture, might occur. Equations (89) and (142) indicate that a miniature, $\langle 100 \rangle$ three-point flexure specimen with 1 by 1.5 mm cross-section and a 6 mm support span would fail by brittle fracture at a tensile stress greater than the compressive yield stress 90% of the time. The implication is that very localized (e.g. contact) stresses, such as those at the root of a blade or vane, might cause yield rather than fracture.

Table 6.2.3: Measured and predicted strength for AFN12 single crystal NiAl tested in uniaxial flexure.

Orientation and Failure Criterion	Measured Characteristic Strength σ_{θ} , MPa	90% Confidence Bands, σ_{θ}	Predicted Characteristic Strength σ_{θ}
$\langle 100 \rangle$	1094	1032 to 1158	1040
$\langle 110 \rangle$	689	642 to 735	653

6.3 ESTIMATION OF THE SCALE PARAMETER

The estimated scale parameter constants are given in Table 6.3.1 for maximum principal stress criterion, the PIA criterion and the normal stress criterion. The computer code used to make the estimates is given in Appendix E. For the more advanced criteria, values of $\sigma_{o<100>}$ and $\sigma_{o<110>}$ satisfying Equations (100) and (101) could not be numerically determined by using the form of Equation (98) to describe the scale parameter. In order to determine if another function describing the scale parameter as a function of orientation was more tractable, several other functions were considered without success:

$$\begin{aligned}
 \sigma_{o(100)<hkl>}(\theta) &= \sigma_{o<100>} \cos^2(2\theta) + \sigma_{o<110>} \sin^2(2\theta) \pm \sigma_{o<100>} \\
 \sigma_{o(100)<hkl>}(\theta) &= \sigma_{o<100>} \cos^2(2\theta) + \sigma_{o<110>} \sin^2(2\theta) \pm \sigma_{o<110>} \\
 \sigma_{o(100)<hkl>}(\theta) &= \sigma_{o<100>} \cos^2(2\theta) + \sigma_{o<110>} \sin^2(2\theta) \pm \sigma_{o<110>} \sigma_{o<100>} \\
 \sigma_{o(100)<hkl>}(\theta) &= \sigma_{o<100>} \cos^2(2\theta) + \sigma_{o<110>} \sin^2(2\theta) \pm \sigma_{o<110>} \sin^2(\theta) \cos^2(\theta) \\
 \sigma_{o(100)<hkl>}(\theta) &= \sigma_{o<100>} \cos^2(2\theta) + \sigma_{o<110>} \sin^2(2\theta) \pm \frac{\sigma_{o<100>}}{\sigma_{o<110>}} \sin^2(\theta) \cos^2(\theta)
 \end{aligned} \tag{143}$$

However, it was noted that if the degree of strength anisotropy was reduced such that $\sigma_{o<110>} / \sigma_{o<100>} \geq 0.8$, solutions for $\sigma_{o<100>}$ and $\sigma_{o<110>}$ could be found.

Table 6.3.1: Scale parameters estimated from Eqs. (98), (100) and (101) for various failure criteria.

Failure Criterion	$\sigma_{o<100>}, \text{MPa}(\text{mm}^2)^{1/m}$	$\sigma_{o<110>}, \text{MPa}(\text{mm}^2)^{1/m}$
Maximum Principal	2516	1574
PIA	2516	1574
Normal Stress	4038	976
Coplanar Energy Release Rate	----	----
Noncoplanar Energy Release Rate	----	----
Maximum Hoop Stress	----	----

Although Eqs (100) and (101) could not be solved for the fracture mechanics based failure criteria, the scale parameters $\sigma_{o<100>}$ and $\sigma_{o<110>}$ can be estimated by another approach. If the parameters are treated as average values of the strength variation about the unit circle for a uniaxial stress state, then the functions can be solved independently as for the PIA model. This is similar to the approach used in Eq. (39) to calculate an average normal stress for the Weibull model. The new functions are

$$\sigma_{\theta<100>} = \left(2 \frac{A_e}{\pi} \int_0^{\pi/2} \left(\frac{f(\theta)}{\bar{\sigma}_{o<100>}} \right)^m d\theta \right)^{-1/m} \quad (144)$$

and

$$\sigma_{\theta<110>} = \left(2 \frac{A_e}{\pi} \int_0^{\pi/2} \left(\frac{f(\theta)}{\bar{\sigma}_{o<110>}} \right)^m d\theta \right)^{-1/m}. \quad (145)$$

The scale parameters estimated from Eq. (144) and (145) are listed in Table 6.3.2.

Table 6.3.2: Scale parameters estimated from Eqs. (144) and (145) for various failure criteria.

Failure Criterion	$\bar{\sigma}_{o<100>}, \text{MPa}(\text{mm}^2)^{1/m}$			$\bar{\sigma}_{o<110>}, \text{MPa}(\text{mm}^2)^{1/m}$		
Maximum Principal	2516			1574		
PIA	2516			1574		
Normal Stress	1934			1210		
SIFCs Used	$Y_I = \sqrt{\pi}$ $Y_I = \sqrt{\pi}$	$Y_I = 1.286$ $Y_I = 1.479$	$Y_I = 1.365$ $Y_I = 1.241$	$Y_I = \sqrt{\pi}$ $Y_I = \sqrt{\pi}$	$Y_I = 1.286$ $Y_I = 1.479$	$Y_I = 1.365$ $Y_I = 1.241$
Coplanar Energy Release Rate	2051	2097	2028	1283	1312	1269
Noncoplanar Energy Release Rate	2223	2309	2175	1390	1444	1360
Maximum Hoop Stress	2265	2375	2205	1417	1486	1379
Batdorf – Griffith Crack	1985			1242		
Batdorf – Griffith Notch	2230			1395		

6.4 RELIABILITY PREDICTION FOR ANISOTROPIC MATERIALS: MULTIAXIAL STRESS STATES

The probability of failure and characteristic strength of a component subjected to multiaxial stresses, such a biaxial disk test specimen, can be estimated from Eqs. (74) and (91). The functions can be applied in the general form or a variety of simplifying assumptions can be used. Three cases and the associated assumptions were considered in predicting the strength of the disk test specimens from the uniaxial test data: (1) complete isotropy; (2) anisotropic elasticity with strength isotropy; and (3) complete anisotropy. A Weibull modulus of 5.4 was used in the analyses because it corresponded to that of the largest test population (i.e. the <110> four-point flexure specimens) and the average value for the measured uniaxial and biaxial data. The approximate solution of Okubu (Okubu 1949) was used to minimize the computational time.

6.4.1 Assumption of Complete Isotropy

If the material's elasticity and strength are assumed to be isotropic, then Eq. (135) applies for the stress analysis and Eqs. (82) and (87) apply for the reliability and characteristic strength analyses. The resulting strength predictions from the 90% confidence bands on the uniaxial data are compared to the 90% confidence bands of the measured biaxial flexure strength data in Figure 6.4.1.1 for the various failure criteria and the SIFCs given in section 2.5.2. The computer code used to make the estimates is given in Appendix F.

6.4.2 Assumption of Strength Isotropy

If the strength is assumed to be isotropic but the elasticity anisotropic, Eqs. (114) to (117) or (131), (114), (116) and (117) apply for stress analysis depending on whether Okubu's approximate or series solutions are applied. For the reliability analysis, Eqs. (82) and (87) apply. The resulting strength predictions from the 90% confidence bands on the uniaxial data and Okubu's approximate solution are compared to the 90% confidence bands of the measured biaxial data in Figure 6.4.2.1 for various failure criteria and the SIFCs given in section 2.5.2. The difference between the predictions in this section and section 6.4.1 reflect the effects of anisotropic elasticity in the solution, which improves all the predictions except Batdorf's criterion for a Griffith crack. The computer code used to make the estimates is given in Appendix G.

6.4.3 Assumption of Complete Anisotropy

If complete anisotropy is assumed, Eqs. (114) to (117) or (131), (114), (116) and (117) apply for stress analysis depending on whether Okubu's exact or approximate solutions are applied. Note that this is the most general case and would be expected to best describe single crystal NiAl. For reliability analysis, Eqs. (74) and (91) apply. The scale parameter is calculated from (100) and (101) or (144) and (145). The resulting strength predictions from the 90% confidence bands on the uniaxial data and Okubu's approximate solution are compared to the 90% confidence bands of the measured biaxial data in Figure 6.4.3.1 for various failure criteria and the scale parameters in Table 6.3.1 (i.e. Eq. (98). The prediction based on the scale parameters in Table 6.4.3.2 (i.e. from Eqs. (144) and (145)) are given in Figure 6.4.3.2. The difference between the predictions in this section and section 6.3.1 reflect the effects of anisotropic elasticity and strength in the solution. The computer code used to make the estimates is given in Appendix H.

6.4.4 Flaw Distribution Anisotropy

A fourth case, in which an anisotropic flaw distribution exists within an isotropic material, can be envisioned. In such a case Eq. (135) applies for the stress analysis and Eqs. (74) and (91) apply for the reliability and characteristic strength analyses. The strength distribution function would have to be determined from experimental measurements of strength as a function of orientation.

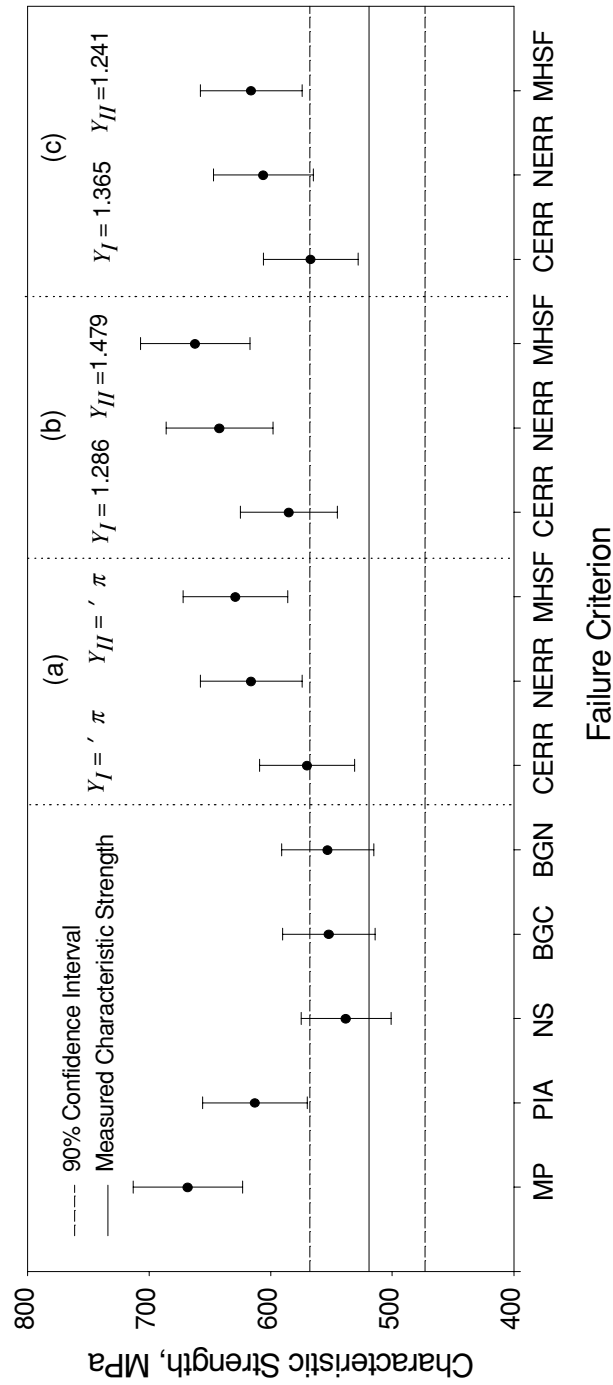


Figure 6.4.1.1: Measured and predicted characteristic strength for AFN12 single crystal NiAl. Elastic and strength isotropy were assumed. The stress intensity factor coefficients of (a) a Griffith crack, (b) of Thiemeier et al. (Thiemeier 1991) and (c) Smith et al. (Smith 1967) and Smith and Sorensen (Smith and Sorensen 1994) were used. The maximum principal stress (MP), principle of independent action (PIA), normal stress (NS), coplanar energy release rate (CERR), non-coplanar energy release rate (NERR) and maximum hoop stress factor (MHSF) were considered.

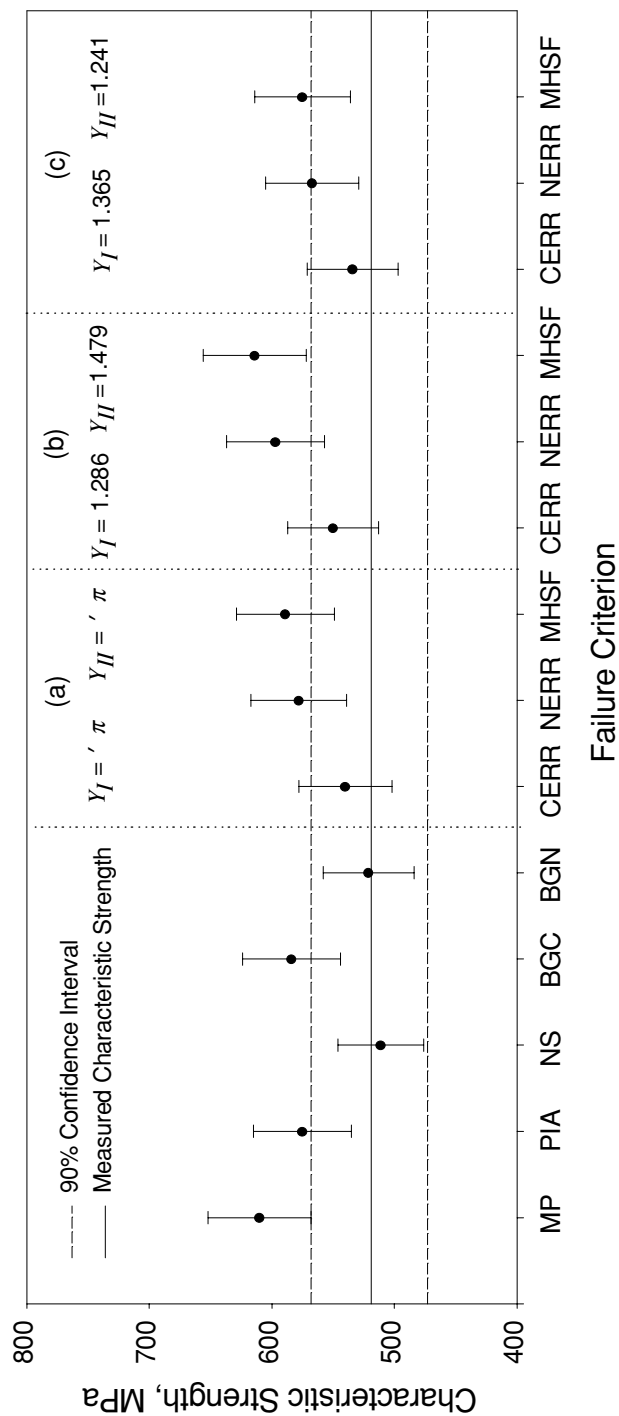


Figure 6.4.2.1: Measured and predicted characteristic strength for AFN12 single crystal NiAl. Strength isotropy with anisotropic elasticity was assumed. The stress intensity factor coefficients of (a) a Griffith crack, (b) Thiemeier et al. (Thiemeier 1991) and (c) Smith et al. (Smith 1967) and Smith and Sorensen (Smith and Sorensen 1994) were used. The maximum principal stress (MP), principle of independent action (PIA), normal stress (NS), coplanar energy release rate (CERR), non-coplanar energy release rate (NERR), maximum hoop stress factor (MHSF), Batdorf's for a Griffith crack (BGC) and Batdorf's for a Griffith notch (BCN) were considered.

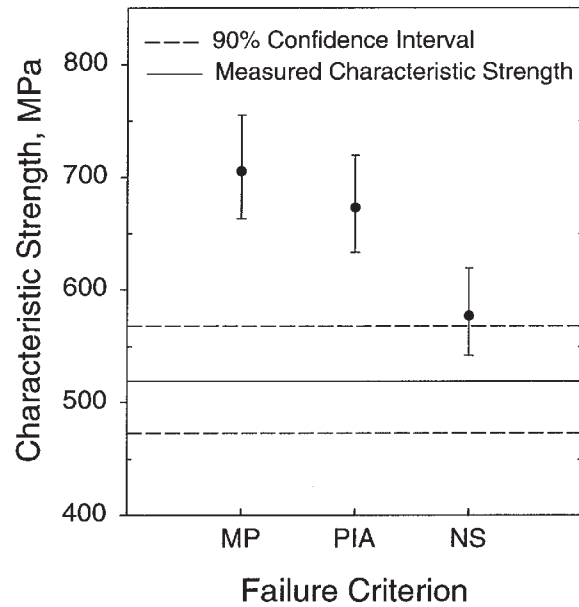


Figure 6.4.3.1: Measured and predicted characteristic strength for single crystal AFN12 NiAl. Elastic and strength anisotropy were applied. The maximum principal stress (MP), principle of independent action (PIA) and normal stress (NS) were analyzed using Equation (98) for the functional form of the scale parameter.

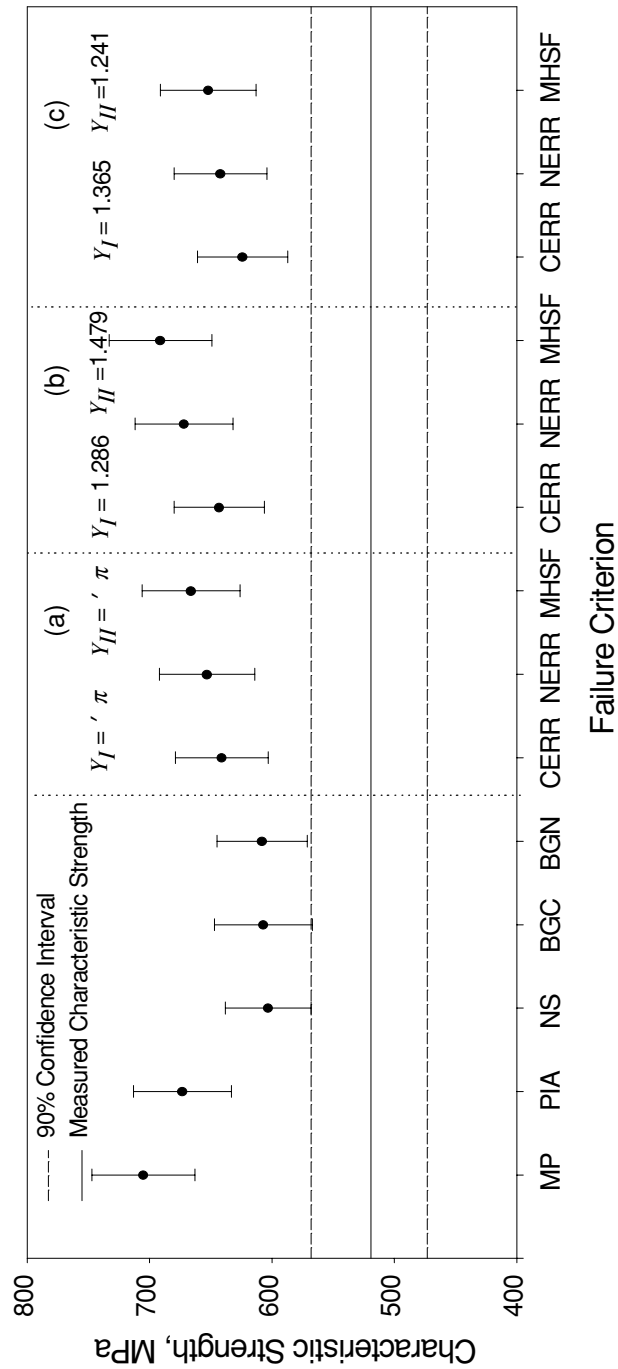


Figure 6.4.3.2: Measured and predicted characteristic strength for AFN12 single crystal NiAl. Elastic and strength anisotropy were assumed. The stress intensity factor coefficients of (a) a Griffith crack, (b) Thiemeier et al. (Thiemeier 1991) and (c) Smith et al. (Smith 1967) and Smith and Sorensen (Smith and Sorensen 1994) were used. The maximum principal stress (MP), principle of independent action (PIA), normal stress (NS), coplanar energy release rate (CERR), non-coplanar energy release rate (NERR), maximum hoop stress factor (MHSF), Batdorf's for a Griffith crack (BGC) and Batdorf's for a Griffith notch (BCN) were considered. Equations (144) and (145) were used for the functional form of the scale parameter.

CHAPTER 7: DISCUSSION OF THE RESULTS

7.1 DISCUSSION OF THE EXPERIMENTAL RESULTS

7.1.1 Strength and Weibull Modulus

The data in Table 5.2.2.2 and 5.4.2.1 indicate significant strength differences between the three- and four-point flexure test configurations for both orientations, and between orientations for the same test configuration, implying effects of scale and orientation. The data also indicates a significant strength difference between the uniaxial strength in either the $\langle 100 \rangle$ or $\langle 110 \rangle$ and the biaxial strength. However, significant differences could not be detected between the Weibull moduli for the three- and four-point configurations for either orientation, or between orientations for the same configuration, implying a statistically homogeneous flaw distribution and an independence of the Weibull modulus on crystal orientation. Also, the Weibull modulus of the biaxial data is not statistically significantly different from that of the uniaxial data.

The apparent independence of Weibull modulus as calculated from the MLE (Abernathy et al. 1983) on test specimen orientation can also be examined from the Gaussian statistics of the data. The Weibull modulus of a brittle material can be estimated from Gaussian statistics by using (Ritter et al. 1981)

$$m \cong \frac{1.2}{CV} \quad (146)$$

where CV is the coefficient of variation (i.e. mean divided by the standard deviation). Thus Equation (146) and the nearly identical coefficients of variation in Table 5.2.2.1 also imply that the Weibull modulus does not vary with orientation.

This conclusion can be examined further from an analytical standpoint by using a truncated Taylor series expansion for estimating the statistics of a random variable that is a function of other independent variables (Haugen 1980), and the fracture mechanics equation

$$SD_y = \left[\sum_i \left(\frac{\partial y}{\partial x_i} \right)^2 (SD_{x_i})^2 \right]^{1/2} \quad (147)$$

and

$$K_{IC} = S_{uts} \sqrt{\pi a} \quad (148)$$

where SD_y is the standard deviation of the y variable, x_i is the i^{th} independent variable, and K_{IC} is the fracture toughness and a the crack length. Solving Equation (148) for fracture strength and Equation (147) for standard deviation of strength leads to

$$SD_\sigma = \left\{ \left[\frac{SD_{K_{IC}}^2}{\pi a} \right] + \left[\frac{K_{IC}^2 SD_a^2}{4\pi a^3} \right] \right\}^{1/2} \quad (149)$$

Dividing Equation (149) by the expected (i.e. mean) value of strength gives

$$CV_{S_{uts}} = \left\{ \left[\frac{SD_{K_{IC}}^2}{K_{IC}^2} \right] + \left[\frac{SD_a^2}{4a^2} \right] \right\}^{1/2} \quad (150)$$

or

$$CV_{S_{uts}} = \left\{ CV_{K_{IC}}^2 + \frac{CV_a^2}{4} \right\}^{1/2} \quad (151)$$

For small standard deviations of crack size or a single flaw population, Equation (151) implies that the coefficient of variation of strength, and thus the Weibull modulus, is approximated by that of the fracture toughness. Note that the mean fracture toughness of single crystal NiAl varies with orientation (Chang et al. 1992) but the CV s do not. To further illustrate the relationship between CV and fracture toughness, the $CV_{K_{IC}}$ for several brittle ceramics and binary single crystal NiAl is plotted in Figure 7.1.1.1. No strong function of $CV_{K_{IC}}$ with fracture toughness, as measured with the single-edged-precracked-beam technique (ASTM C 1421 1999, Nose and Fuji 1988), is exhibited, implying that Weibull modulus via Equation (146) is not dependent on the fracture toughness. The $CV_{K_{IC}}$ is probably more a function of the material's inherent variability and the test error than of the fracture toughness. Thus, Weibull modulus should not vary with orientation in a material with fracture toughness anisotropy, if the same flaw population controls failure.

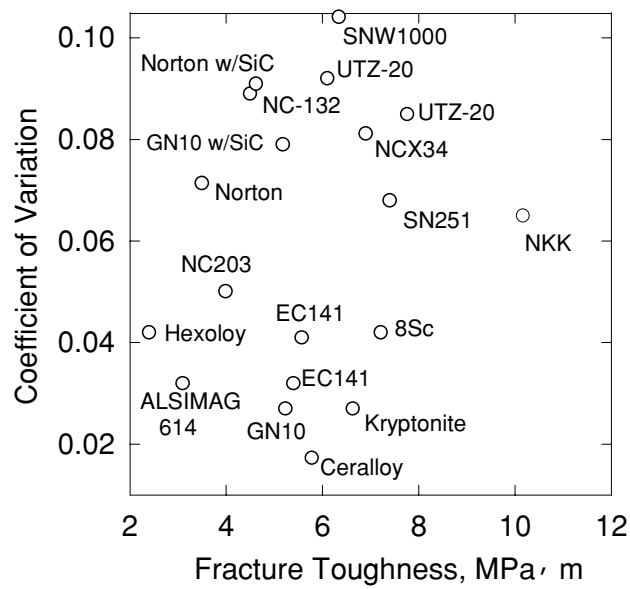


Figure 7.1.1.1: Coefficient of variation of the fracture toughness of various commercially available ceramics. No correlation between fracture toughness and coefficient of variation is apparent.

Thus, the strength of single crystal NiAl is a function of test specimen orientation, test specimen size and stress state for tensile loading. However, the Weibull modulus is not a function of test specimen orientation, size or stress state for tensile loading. This is in agreement with the generalized Weibull model proposed in Eq. (74).

7.1.2 Correlation of billet Chemistry to Flexural Strength

Because C is a “tramp” element in the alloy and its presence results in strength-limiting HfC inclusions, the strength of a given billet was speculated to correlate to the carbon content: smaller or fewer HfC inclusions might develop for decreased carbon content. Carbon content of the billets and an additional billet (HP252) believed to be of low carbon content (Darolia 1996) were measured. The data is summarized in Table 7.1.2.1 and is plotted in Figure 7.1.2.1 along with 90% confidence intervals. The average strength as a function carbon content is shown in Figure 7.1.2.2. No trend is detectable and the strongest billets have similar carbon content as the weak billets. Improvement of the NiAl’s strength might be pursued by reduction of Hf.

Table 7.1.2.1: Billet chemistry (weight %) and <100> four-point flexure strength with 90% confidence intervals.

Ingot Designation	Ni	Al	Hf	Ti	Si	C	O	Fracture Strength MPa
2429	66.4	29.7	2.2	1.1	0.082	0.0034	0.0044	1298 ± 167
2439	66.5	30.3	2.1	1.1	0.110	0.0041	0.0047	904 ± 106
2454	66.4	30.0	2.4	1.2	0.120	0.0030	0.0043	904 ± 116
2461	66.7	30.0	2.1	1.1	0.120	0.0032	0.0033	915 ± 161
2464	68.3	28.4	2.1	1.1	0.120	0.0030	0.0030	948 ± 198
2471	69.3	26.7	3.2	1.4	0.120	0.0034	0.0046	1228 ± 201
2474	66.4	30.3	2.2	1.1	0.074	0.0035	0.0050	1053 ± 315
HP252	66.4	30.2	2.2	1.1	0.067	0.0039	0.0043	1226 ± 33

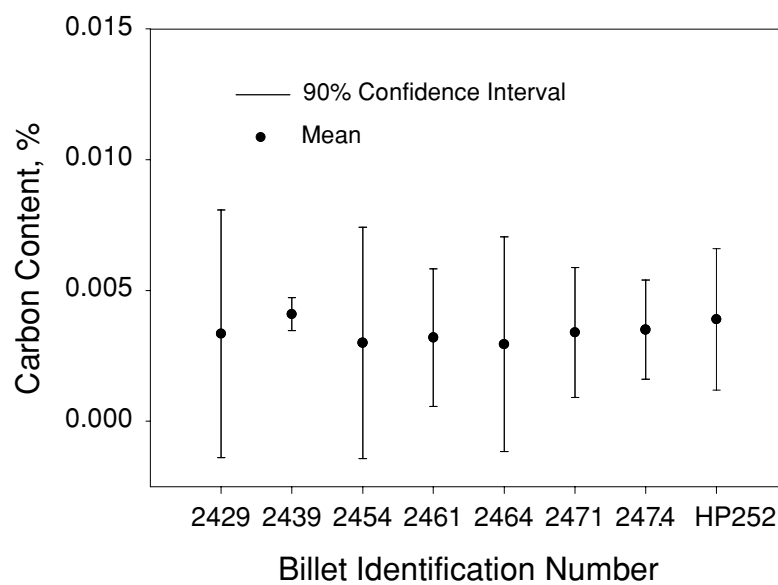


Figure 7.1.2.1: Mean carbon content (weight %) and 90% confidence interval for the <100> billets.

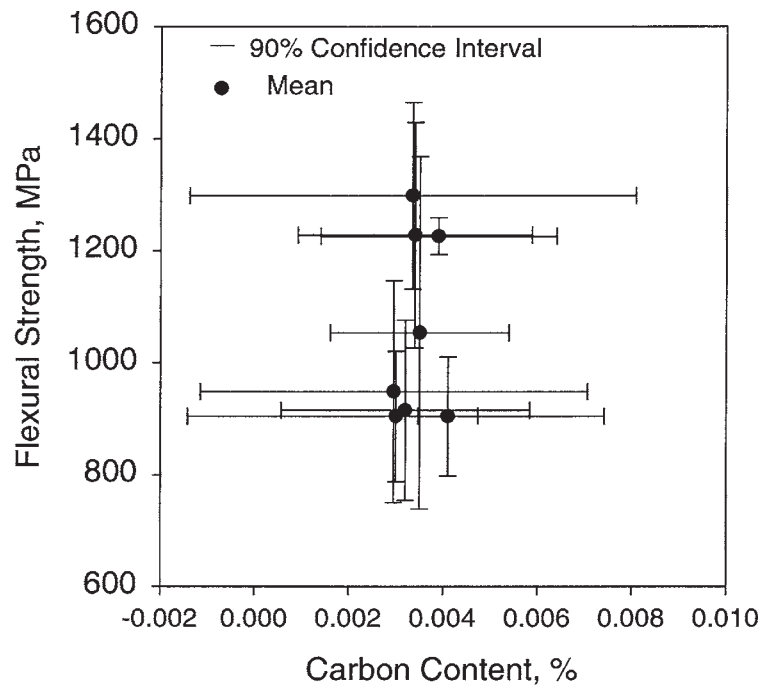


Figure 7.1.2.2: Mean strength and 90% confidence interval as a function of <100> billet carbon content (weight %).

7.1.3 Test Specimen Preparation

Ideally, better specimen preparation is needed to minimize machining damage and maximize the number of failures from inherent flaws. This is especially true if NiAl is to be used as a structural component. It is recommended that lower voltages be used during EDM in order to minimize pitting. Further, the chemical milling procedure did not eliminate EDM damage from as-machined surface as shown in Figures 4.1.2.1 and 5.3.1, but tended to extend the existing pits into the material. However, elimination of EDM pits by hand sanding prior to chemical milling did eliminate EDM related failures. Unfortunately, this is not a practical approach for manufacturing components. A procedure such as electro-polishing might produce a smoother surface from a pitted surface made via EDM. Also, if possible, a grinding procedure should be developed. However, typical uniaxial grinding of ceramic materials does leave damage in the direction transverse to the grinding direction, and may do so in NiAl's.

7.2 DISCUSSION OF THE PREDICTIONS

The predictions shown in Figures 6.4.1.1 to 6.4.3.1 imply that the normal stress criterion (NS), in which the normal stress acting on each plane of the crystal reduces reliability, is the best choice regardless of assumptions regarding anisotropy. Further, the best agreement occurs if the strength associated with the strong $\langle 100 \rangle$ directions is ignored and strength properties associated with the weak $\langle 110 \rangle$ direction are applied (see Fig. 6.4.2.1) with anisotropic stress analysis. This implies that either the strong directions do little to enhance reliability or that a discrepancy between the model and the data exists. Because disk data was taken from only one billet, one source of discrepancy between the model and the disk data is billet-to-billet variation. The effect of billet-to-billet variation can be investigated somewhat by eliminating the billets that exhibited significantly greater strengths (numbers 2429, 2471 and 2474 in Figure 5.2.2.1 and Table 7.1.2.1) from the flexural test data used as input into the model. The resulting predictions for elastic and strength anisotropy are only slightly improved, as shown in Figure 7.2.1. The normal stress criterion is the only criteria exhibiting a statistically insignificant difference between measured and predicted strengths.

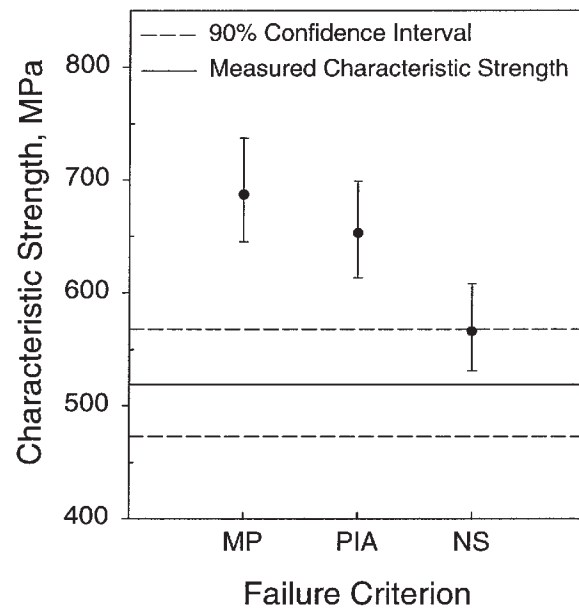


Figure 7.2.1: Measured and predicted characteristic strength for single crystal AFN12 NiAl. Elastic and strength anisotropy were applied. The three strongest $\langle 100 \rangle$ billets were not used in the predictions. The maximum principal stress (MP), principle of independent action (PIA) and normal stress (NS) were considered.

Another aspect of statistical variation from billet-to-billet that affects the predictions is the estimated Weibull modulus. For the largest test population (i.e. the <100> four-point flexure specimens), the estimated Weibull modulus is between 4.3 to 6.8 with 90% confidence, in relatively good agreement with the estimated parameter for the disk test specimens (5.3). Thus little justification exists for varying Weibull modulus in the predictions.

Interestingly, none of the other failure theories reviewed predict as much weakening of a material due to a second principal stress as the Weibull based theories (Giovan and Sines 1979). Another aspect of the material behavior that may have contributed to the discrepancy between the predictions employing strength anisotropy and the biaxial test data is the consistent failure of the disk test specimens along the <110> planes. Such a failure pattern implies a dominance of the <110> strength properties in biaxial stress states and an influence on the strength predictions.

Note also that in the highly stressed central region of the disk test specimens, the principal stresses are nearly equal thereby subjecting all planes to large nearly equal normal stresses. Although the model accounts for the stress variation, it assumes randomly distributed planar flaws. However, based on the fractography, the actual flaws are three-dimensional inclusions. Conceptually this implies a flaw on each crystal plane thereby allowing a higher frequency of a large flaw dimension to intersect a highly stressed or weak direction and thereby allowing the weak planes to dominate strength. However, because the measured uniaxial data used in the model is a sample of the same flaw distribution on a specific plane, the effect should be taken into account for uniaxial cases, as the state of stress does not change with test specimen size. This is supported by the accuracy of the predictions for the uniaxial cases. Thus fault does not seem to lie with the origins of the model, but more with the choice of flaw type.

However, for multiaxial cases, the three-dimensionality of the flaws implies that all planes at the point of a flaw are exposed to a similar flaw size distribution and the stresses resolved on all planes should reduce reliability. This is supported by the ability of the normal stress criterion to predict biaxial strength and explains why the PIA and MP criteria do not. However, this does not explain the poor results for the shear sensitive theories.

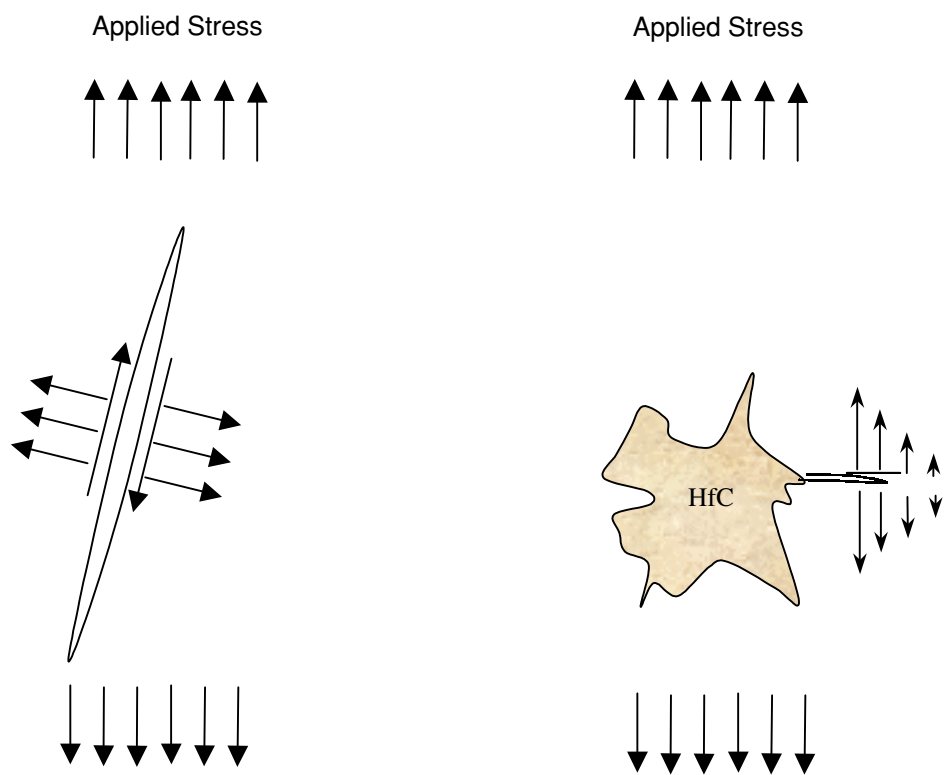


Figure 7.2.2: Effect of flaw type on the loading mode resulting from application of a uniaxial stress state: (a) randomly oriented planar crack and (b) three-dimensional inclusion.

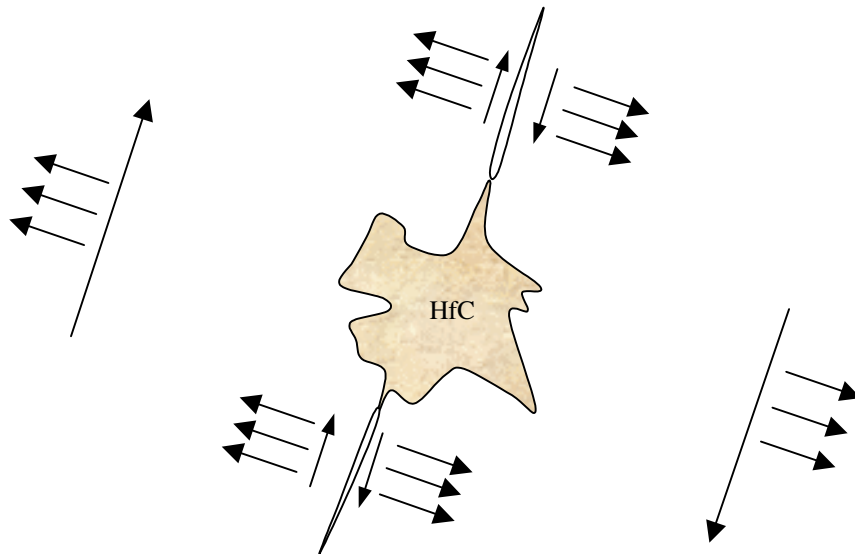


Figure 7.2.3: Illustration of an inclusion shielding a crack from an applied, remote shear stress.

The poorer agreement between the data and predictions using shear sensitive criteria, and the inability to solve for anisotropic scale parameters for shear sensitive failure criterion, may also be explained by the nature of the flaws. Because the flaws are three-dimensional, uniaxial test data tends to sample a cross-section of a three-dimensional flaw by way of the principal stress instead of sampling randomly oriented planar flaws that are inclined to the uniaxial (principal stress) and subject to shear and normal stresses. Thus the data is unrepresentative of shear induced failure, as shown in Figure 7.2.2, and shear sensitive criteria are less applicable. Further, inclusions tend to resist shear as they “bridge” any crack emanating from them and thereby “shield” the crack tip as shown in Figure 7.2.3.

It might be speculated that materials with many randomly oriented planar flaws always fail from a flaw oriented normal to the applied stress. This would be the case if all the flaws were of the same size, however, a random size distribution results in some large flaws at significant angles to the applied stress and thus shear can influence the sampling in uniaxial strength testing. For three-dimensional flaws, the off axis shear may be ineffective as compared to the principal stress.

Because the flaws are three dimensional, the failure criterion for open pores given by Babel and Sines (Babel and Sines 1968) might appear applicable. However, the flaws causing failure are cavities filled with HfC and therefore carry tractions. Further, the failure criterion for pores predicts equibiaxial strengthening and should result in prediction larger than those for planar cracks.

Another aspect of the inclusions that may have resulted in the failure locations being associated with $\langle 110 \rangle$ directions is residual stresses generated by an inclusion in matrix.

7.3 Residual Stresses

The HfC inclusions are well bonded to the NiAl matrix, as described above, and have different thermal and elastic properties than the matrix. As a result, when the NiAl billets are cooled from the heat treatment temperature, residual stresses should be developed within and around the inclusions. The magnitude of these thermo-elastic stresses can be estimated from the models of Selsing or Bussem and Lange (Selsing 1961, Bussem and Lange 1966) if isotropic behavior is assumed. The reported properties of polycrystalline HfC are quite variable, with the reported elastic modulus varying from 316 to 461 GPa. The properties of HfC are summarized in Table 7.3.1 and those of NiAl alloys in Table 1.1.1. The single crystal NiAl considered herein is heat-treated at $\sim 1000^\circ\text{C}$ prior to cooling to room temperature, however, the lower limit for bulk creep

deformation is considered to be $\sim 800^{\circ}\text{C}$ (Nathal 1999) and thus a temperature difference of 775°C was used in the calculations. This estimate is probably high as local deformation and stress relaxation might occur on cooling. The resultant residual stresses are summarized in Table 7.3.2 for both the polycrystalline properties of NiAl and the elastic moduli associated with specific single crystal directions. The resultant stresses are estimated to be quite large, with the peak tensile stress for any assumed properties occurring in the matrix at the interface. In terms of crystal direction the peak stress are associated with the stiffest directions, this being the $\langle 110 \rangle$ in the plane of the plate and the $\langle 111 \rangle$ in general. The residual stresses should interact with the applied macroscopic stresses; however, determination of the exact, net resultant stresses requires analysis of the general cases of an inclusion in a single crystal matrix.

Based on the estimated residual stresses, the location of fracture initiation seems to be most probable at the tensile surface where on the $\{110\}$ plane intersects an inclusion.

Table 7.3.1: Mechanical Properties of HfC (MCIC 1979).

Young's Modulus, E GPa	Poisson's Ratio, ν	Coefficient of Thermal Expansion $\times 10^{-6}/^{\circ}\text{C}$
316 to 460	0.17 to 0.18	6.6 to 7.3

Table 7.3.2: Estimated residual stresses at the interface of an HfC inclusion in an NiAl matrix. The stresses were calculated using the data in Table 7.3.1 and Table 1.1.1, and the equations of Selsing (Selsing 1961).

Matrix Properties Considered	NiAl Matrix		HfC Inclusion	
	Radial Stress	Tangential Stress	Radial Stress	Tangential Stress
	σ_{rr} MPa	$\sigma_{\theta\theta}$ MPa	σ_{rr} MPa	$\sigma_{\theta\theta}$ MPa
Polycrystalline	-932	466	-932	-932
<100>	-583	291	-583	-583
<011>	-929	464	-929	-929
<111>	-1162	581	-1162	-1162

CHAPTER 8: SUMMARY

A general methodology for analyzing the reliability of brittle single crystals was developed and experimentally investigated. Procedures and analyses for specimen preparation, uniaxial and multiaxial testing and failure source identification were developed in order to supply verification data for the model. The reliability model employs the Weibull distribution and strength or fracture mechanics based failure criteria. The results of this study can be summarized as follows:

- 1) A procedure for preparing the surfaces single crystal NiAl test specimens was developed.
- 2) The elastic moduli in the $\langle 100 \rangle$ and $\langle 110 \rangle$ directions were measured by impulse excitation. The measured values agreed well with published values for binary NiAl.
- 3) The uniaxial flexure strength in three and four-point flexure were determined for $\langle 100 \rangle$ and $\langle 110 \rangle$ orientations.
- 4) A test apparatus for measuring the biaxial flexure strength of isotropic and anisotropic materials was developed and verified. The test rig subjects a circular plate to a uniform pressure and is capable of generating equibiaxial stresses within $\sim 2\%$ of theoretical predictions for cubic single crystal NiAl.
- 5) The formulas for estimating the standard deviations of strain and stress from apparent strains measured with stain gage rosettes were derived.
- 6) The displacement solution for an anisotropic plate subjected to uniform pressure was generalized to the case of variable radius, pressure and thickness. The resultant curvature functions were derived in a general format more commonly used for plate analysis.
- 7) The multiaxial strength of single crystal NiAl was measured for the $\{100\}$ orientation.
- 8) A reliability model was developed for brittle materials that exhibit elastic and strength anisotropy. The model was used to predict the characteristic strength associated with uniaxial and biaxial stress states.

- 9) An equivalent stress solution for the coplanar energy release rate of an anisotropic material was derived.
- 10) The source of failure in AFN12 single crystal NiAl was identified via fractographic and energy dispersive analyses.

CHAPTER 9: CONCLUSIONS

- (1) The source of failure in AFN12 single crystal NiAl was identified to be either machining damage or coarse, three-dimensional HfC inclusions. Biaxial test specimens cleaved on the {110} plane, implying a dominance of that plane in the strength of the material when subjected to multiaxial stresses.
- (2) Fracture in a biaxial stress state occurs on the {110} because of four factors: (1) the low fracture toughness (Chang and Darolia 1992), (2) the higher residual stresses associated with the stiff <110>, (3) the large area of {110} planes subjected to large applied stresses, and (4) the three-dimensional shape of the inclusions.
- (3) The three-dimensional flaw shape has specific implications on the measure characteristic strength. In uniaxial stress states, the effects of off-axis shear are mitigated because the nominal cross-section of the flaw is subjected to the principal stress regardless of orientation. In contrast, planar flaws of random size are subjected to a mix of shear and normal stress depending on orientation of the critical flaw. Thus, uniaxial test data does not detect the shear sensitivity of the brittle materials failing from inclusions.
- (4) The flaw shape also has implications on multiaxial failure. Because all crystal planes at the point of a three-dimensional flaw intersect the cross-section of the flaw, the weak crystal planes tend to dominate the failure behavior in near equibiaxial stress states. Further, because the flaws are inclusions, they may “mechanically” resist remotely applied shear. Thus shear-sensitive criteria are less applicable than criteria related to normal stresses.
- (5) EDM machining leaves significant surface damage on test specimens. A significant amount of this damage remains even after chemical milling. Removal of the EDM layer by sanding with 400 grit silicon carbide paper prior to chemical milling produced acceptable surfaces on test specimens.
- (6) An effect of stressed test volume and test specimen orientation exists for AFN12 single crystal NiAl. The effect of specimen scale on the probability of failure and characteristic strength for uniaxial stresses can be described by the Weibull distribution.

- (7) No statistically significant difference in Weibull moduli between $\langle 110 \rangle$ and $\langle 100 \rangle$ orientations could be detected at 90% confidence, implying that the Weibull modulus is not a function of orientation. Analytical derivations support this conclusion.
- (8) The biaxial strength of AFN12 single crystal NiAl is significantly less than that measured with uniaxial test specimens of similar dimensions. The Weibull modulus of the biaxial test specimens was not statistically significantly different from that of the uniaxial test specimens.
- (9) The same flaw population and failure mechanism (brittle failure without macroscopic ductility) controls failure in both uniaxial and biaxial test specimens. Cleavage in biaxial stress state appears to initiate on the $\langle 110 \rangle$ plane and rapidly branch in the $\langle 310 \rangle$ directions.
- (10) The displacement of a circular, single crystal NiAl plate subjected to a uniform pressure can be accurately described by the solutions of Okubu (Okubu 1949). For practical purposes, the approximate solution is adequate for the estimation of stress and strain in engineering applications.
- (11) The fractography and predictions point out the critical nature of understanding the flaw type in modeling the brittle failure of single crystals. Inclusions interact with remote stresses differently than planar cracks.
- (12) Based on the current data, the best design approach for AFN12 single crystal NiAl components involving multiaxial stresses is to employ anisotropic stress analysis with the normal stress criterion and $\langle 110 \rangle$ strength statistics in the reliability model. Adequate results can also be attained by using anisotropic strength and elasticity with the normal stress criterion in the reliability model.

CHAPTER 10: RECOMMENDATIONS AND FUTURE WORK

Based on the present analytical and empirical research, the following extension of the present investigation recommended:

- (1) Multiaxial testing of additional billets of AFN12 {100} single crystals. The addition of data from other billets would clarify the role of billet-billet variation in the predictions.
- (2) Multiaxial testing of different orientations (e.g. {110}) of single crystal NiAl in order to test different and more general cases.
- (3) Determine functions that allow a generalized scale parameter as a function of orientation to be determined for advanced fracture mechanics criterion such as the coplanar energy release rate.
- (4) Develop an equivalent stress failure criterion for an inclusion embedded in a cubic matrix
- (5) Optimization of the materials strength and Weibull modulus by using the test and fractographic methods applied herein. Ultimately, processing refinement that eliminate Hafnium carbides are required.
- (6) Testing of miniature flexure specimen to determine if localized yield can occur prior to fracture via brittle cleavage.
- (7) Apply the model to other cases such as strength anisotropy due to machining damage associated with uniaxial grinding.

REFERENCES

Abernethy, R. B., Breneman, J. E., Medlin, C. H., Reinman, G. L., Weibull Analysis Handbook, AFWAL-TR-83-2079, 1983.

Adams, M., and Sines, G., "Determination of Biaxial Compressive Strength of a Sintered Alumina Ceramics," *Journal of the American Ceramic Society*, Vol. 59, No. 7-8, pp. 300-304, 1976.

Adler, W. F. and Mihora, D. J., "Biaxial Flexure Testing: Analysis and Experimental Results," pp. 227-246 in Fracture Mechanics of Ceramics, Vol. 10, eds. Bradt, R.C., Hasselman, D. P. H., Munz, D., Sakai, M., and Shevchenko, V., Plenum Press, New York, 1991.

CINDAS/USAF, Aerospace Structural Metals Handbook, CINDAS/USAF CRDA Handbook Operations, West Lafayette, IN, p. 41, Vol. 1, 1997.

ASTM C 1161 "Standard Test Method for Flexural Strength of Advanced Ceramics at Ambient Temperature," American Society for Testing and Materials Annual Book of ASTM Standards, Vol. 15.01, pp. 333-339, ASTM, West Conshohocken, PA , 1990.

ASTM C 1259 "Standard Test Method for Dynamic Young's Modulus, Shear Modulus, and Poisson's Ratio for Advanced Ceramics by Impulse Excitation of Vibration," American Society for Testing and Materials Annual Book of ASTM Standards, Vol. 15.01, pp. 336-384, ASTM, West Conshohocken, PA, 1995.

ASTM C 1273-95a "Standard Practice for Tensile Strength of Monolithic Ceramics at Ambient Temperature," American Society for Testing and Materials Annual Book of ASTM Standards, Vol. 15.01, pp. 401-418, ASTM, West Conshohocken, PA , 1999.

ASTM E 399 "Standard Test Method for Plane-Strain Fracture Toughness of Metallic Materials," American Society for Testing and Materials Annual Book of ASTM Standards, Vol. 03.01, ASTM, West Conshohocken, PA, 1990.

ASTM F 394 "Standard test method for Biaxial Flexure Strength (Modulus of Rupture) of Ceramic Substrates," American Society for Testing and Materials Annual Book of ASTM Standards, Vol. 15.02, pp. 446-450, 1999.

Babel, H. W. and Sines, G. "A Biaxial Fracture Criterion for Porous Brittle Materials," Journal Basic Eng., Vol. Paper No. 68-WA/Met-12, pp. 1-7, 1968.

Bain, K. and Darolia, R., unpublished work, GE Aircraft Engines, Evendale, Ohio.

Baratta, F. I., and Dunlay, W. I., "Crack Stability in Simply Supported Four-Point and Three-Point Loaded Beams of Brittle Materials," *Mechanics of Materials*, **10**, 149-159, 1990.

Baratta, F. I., Matthews, W. T., and Quinn, G. D., "Errors Associated with Flexure Testing of Brittle Materials," U. S. Army Materials Technology Laboratory, MTL TR 87-35, July 1987.

Barnett, R. L., Connors, C. L., Hermann, P.C., and Wingfield, J. R., "Fracture of Brittle Materials Under Transient Mechanical and Thermal Loading," U.S. Air Force Flight Dynamics Laboratory. AFFDL-TR-66-220, March 1967.

Batdorf, S. B., and Crose, J. G., "A Statistical Theory for the Fracture of Brittle Structures Subjected to Nonuniform Polyaxial Stresses," *Journal Applied Mechanics*, Vol. 41, No. 2, pp. 459-464, June 1974.

Batdorf, S. B. "Some approximate Treatments of Fracture Statistics for Polyaxial Tension," *International Journal Fracture*, Vol. 13, No. 1, pp. 5-11, February 1977.

Batdorf, S. B., "Fundamentals of the Statistical Theory of Fracture," pp. 1-30 in Fracture Mechanics of Ceramics, Vol. 3, eds. Bradt, R.C., Hasselman, D. P. H., Lange, F. F. Plenum Press, New York, 1978.

Batdorf, S.B. and Heinisch, " Fracture Statistics of Brittle Materials with Surface Cracks," *Engineering Fracture Mechanics*, Vol, 10, pp. 831-841, 1978.

Batdorf, S. B. and Heinisch, H. L., "Weakest Link Theory Reformulated for Arbitrary Fracture Criterion," Journal American Ceramic Society, Vol. 61, No. 6-7, July-August, pp. 355-358, 1978.

Blankenship, C. P., JR, Larsen, M., Sutliff, J. A., "Deformation and Fracture of NiAl Single Crystals Tested in Torsion," Acta Metall. Mater., Vol. 43, No. 4, pp. 1549-1558, 1995.

Broek, D., Elementary Engineering Fracture Mechanics, Martinus Nijhoff Publishers, 1982.

Buch, J. D, "Mechanical Behavior Model for Graphite's," in Properties Related to Fracture Toughness, ASTM STP 605, American Society for Testing and Materials, ASTM, West Conshohocken, PA, pp. 124-144, 1976.

Bussem, W. R., and Lange F. F, "Residual Stresses in Anisotropic Ceramics," Interceram, Vol. 15, [3], pp. 229-231, 1966.

Chang, K. M., Darolia, R. and Lipsitt, H. A., "Cleavage Fracture in B2 Aluminides," Acta Metall. Mater., 40, pp. 2727-2737 1992.

Chen, C. P., and Leipold, M. H., "Stress Rate and Proof-Testing of Silicon Wafers," Journal of the American Ceramic Society, 68, [2], pp. C-54-C-55, 1985.

Darolia, R., private communication, 1996.

Darolia, R., Chang, K. M., and Hack, J. E., Intermetallics, Vol. 1, pp. 65-78, 1993.

DeMarco, H, and Ardell, A. J., "Preferential Cleavage Planes in Biaxially Stressed, Vickers-Indented NiAl Monocrystals," Scripta Materialia, Vol. 34, No. 7, pp. 1107-1113, 1996.

Duffy, S. F., and Arnold, S. M., "Noninteractive Macroscopic Reliability Model for Whisker-Reinforced Ceramic Composites," Journal of Composite Materials, Vol. 24, pp. 293-308, March 1990.

Ellis, R. and Gulick, D., Calculus with Analytic Geometry, Harcourt Brace Jovanovich, New York, 1978.

Erdogan, F. and Sih, G. C. "On the Crack Extension in Plates Under Plane Loading and Transverse Shear," Journal Basic Eng., Vol. 85, pp. 519 - 27, 1963.

Evans, A. G., "A General Approach for the Statistical Analysis of Multiaxial Fracture," Journal of the American Ceramic Society, 61, 7-8, pp. 302-308, 1978.

Fessler, H., and Fricker, D.C., "A Theoretical Analysis of the Ring-on-Ring Loading Disk Test," Journal American Ceramic Society, Vol. 67, No. 9, pp. 582-588, 1984.

Fischer, J. J., and Weber, J. H., "Mechanical Alloying Spreads its Wings," Advanced Materials and Processes, 10, pp. 43-49, 1990

Freudenthal, A. M. "Statistical Approach to Brittle Fracture," in Fracture, An Advanced Treatise, Vol. 2, Mathematical Fundamentals, H. Liebowitz, ed. Academic Press, pp. 510-515, 1968.

Frechette, V. D., Failure Analysis of Brittle Materials, Advances in Ceramics, Vol. 28, The American Ceramic Society, Westerville, Ohio, 1990.

Godfrey, D. J. and John, S., "Disc Flexure Test for the Evaluation of Ceramic Strength," pp. in 657–665 in Proceedings of the 2nd International Symposium on Ceramic Materials and Component for Engines, W. Bunk and H Hausner, eds., Lubeck-Travenmunde, FGR, 1986.

Gross, B, and Gyekenyesi, J. P. "Weibull Crack Density Coefficients for Polydimensional Stress States," Journal American Ceramic Society, 72, 3, 506-507, 1989.

Haugen, E. B., Probabilistic Mechanical Design, John Wiley and Sons, 1980.

Hayashi, K., Ashizuka, M., Bradt, R. C. "Cleavage of Gallium Phosphide," Materials Letters., Vol. 1, No. 3,4, pp. 116-118, 1982.

Hearmon, R. F. S., An Introduction to Applied Anisotropic Elasticity, Oxford University Press, 1961.

Hellen, T. K. and Blackburn, W. S. "The Calculation Stress Intensity Factors for Combine Tensile and Shear Loading," International Journal Fracture, Vol. 5, pp. 605 - 17, 1975.

Hirsch, P.B., Booth, A. S., Ellis, M., Roberts, S. G. "Dislocation-Driven Stable Crack Growth by Microcleavage in Semi-Brittle Crystals," Scripta Metall. et Mater., Vol. 27, pp. 1723-1728, 1992.

Hoagland, R. G., Marschall, C. W., and Duckworth, W. H., "Reduction in Errors in Ceramic Bend Tests," Journal American Ceramic Society, Vol. 59, No. 5-6, pp. 189-192, 1976.

Jakus, K., Ritter, J. E., Jr., Service, T., and Sonderman, D., Evaluation of Bimodal Concurrent Flaw Distributions, Communications of American Ceramic Society, 64, C-174, 1981.

Kanninen, M. F. and Popelar, C. H., Advanced Fracture Mechanics, Oxford Engineering Science Series 15, Oxford Press, 1985.

Lamon, J., "Statistical Approaches to Failure for Ceramic Reliability Assessment," Journal American Ceramic Society, Vol. 71, No. 2, pp. 106-112, 1988.

LeMay, I., Principles of Physical Metallurgy, Elsevier, New York, pp. 217 - 218, 1981.

Lee H. J. and Saravanos, D. A., "Generalized Finite Element Formulation for Smart Multilayered Thermal Piezoelectric Composite Plates," International Journal Solids Structures, Vol. 34, No. 26, pp. 3355-3371, 1997.

Lekhnitskii, S. G., Theory of Elasticity of an Anisotropic Body, Holden-Day, San Francisco, 1963.

Li, C. W., and Yamanis, J., "Super-Tough Silicon Nitride with R-curve Behavior," Ceramic Engineering Science Proceedings., 10, [7-8], pp. 632-645, 1989.

Margetson, J. "A statistical Theory of Brittle Failure for an Anisotropic Structure Subjected to a Multiaxial Stress State," paper No. 76-632, in the American Institute of Aeronautics and Astronautics/Society for Automotive Engineers 12th Propulsion Conference, July, 1976.

MCIC-HB-07, "Engineering Property Data on Selected Ceramics, Vol. 2, Carbides", Metals and Ceramics Information Center, Columbus, Ohio, August 1979.

Mechtly, E. A. "Physical Constants and Conversion Factors," NASA SP-7012, 1973.

Military Handbook 790 "Fractography and Characterization of Fracture Origins in Advanced Structural Ceramics," MIL-HDBK-790, July 1992.

Miller, H. E. and Chambers, W. L., pp. 27-57 in Superalloys II, Sims, C. T., Stoloff, N. S., and Hagel, W. C., eds., John Wiley & Sons, New York, NY, 1987.

Miller, I. and Freund, J. E., Probability and Statistics for Engineers, 3rd edition, Prentice-Hall, 1977.

Molloy W. J., "Investment-Cast Superalloys, a Good Investment," Advanced Materials and Processes, 10/90, pp. 23-30, 1990.

Nemeth, N., Manderscheid, J., Gyekenyesi, J., "CARES Users and Programmers Manual," NASA Technical Paper TP2916, 1990.

Noebe, R. D., Bowman, R. R. and Nathal, M. V., "Physical and Mechanical Properties of the B2 Compound NiAl," International Materials Review, Vol. 38, No. 4, pp. 193-232, 1993.

Noebe, R. D. and Garg, A., "Deformation Behavior of Single Crystal NiAl Alloy D176," NASA Technical Memorandum 106891, 1995.

Nose, T. and Fuji, T. "Evaluation of Fracture Toughness for Ceramic Materials by a Single-Edge-Precracked-Beam Method, Journal American Ceramic Society, Vol. 71, No. 5, 328-333, 1988.

Oda, I., Matsui, M., Soma, T., Yamada, N., "Fracture Behavior of Sintered Silicon Nitride under Multiaxial Stress States," Journal of the Ceramic Society of Japan International Edition, Vol. 96, pp. 523-539, 1988.

Oh, K. P. L., "On the Statistical Nature of Brittle Fracture, Ph.D. Thesis, University of California, Berkeley, 1970.

Oh, K. P. L., Vardar, O. and Finnie, I. "Failure of Brittle Solids on Biaxial Stresses," International Journal Fracture, Vol. 9, 372, 1973.

Okubu, H. "Bending of a Thin Circular Plate of an Aeolotropic Material under Uniform Lateral Load (Supported Edge), Journal of Applied Physics, Vol. 20, December 1949.

Pagano, N. C., and Halpin, J. C., "Influence of End Constraints in the Testing of Anisotropic Bodies," Journal Comp. Materials, Vol. 2, No. 1, pp. 19-31, 1968.

Paris, P. C., and Sih, G. C. in Fracture Toughness Testing and its Applications, ASTM STP 381, American Society for Testing and Materials, pp. 30-83, 1965.

Pascoe, R. T. and Newey, C. W. A., "The Mechanical Behavior of the Intermediate Phase NiAl," Met. Sci. J., 2, pp. 138-143, 1968.

Peterson, R. E., Stress Concentration Factors, Wiley, New York, 1974.

Petrovic, J. J. and Stout, M. G., "Fracture of Al_2O_3 in Combined Tension/Torsion: I, Experiments," Vol. 64, No. 11, pp. 656-660, November 1981.

Price, J. R., Jimenez, O., Parthasarathy, V., and Miriyala, N., "Ceramic Stationary Gas Turbine Development Program – Sixth Annual Summary," proceedings of the 1999 International Gas Turbine and Aeroengine Congress, paper No. 99-GT-351, Indianapolis, Indiana, June 7 – 10, 1999.

Priddy, T. G. "A Fracture Theory for Brittle Anisotropic Materials," Journal of Engineering Materials and Technology, pp. 91-96, April 1974.

Quinn, G., "Flexural Strength of Advanced Structural Ceramics: A Round Robin," Journal American Ceramic Society, Vol. 73, No. 8, pp. 2374-2384, 1990.

Reissner, E., Stavsky, Y. "Bending and Stretching of Certain Types of Aeolotropic Elastic Plates," Trans. ASME, pp. 402-408, Sept. 1961.

Reuss, S. and Vehoff, H., in "Intermetallische Phasen Strukturwerkstoffe fur hohe Temperature," ed. F. J. Brewer, Forschungszentrum Julich GmbH, pp. 65-73, 1991.

Richard, H. A. "Prediction of Fracture of Cracks Subjected to Combined Tensile and Shear Loads," VDI Research Report 631/85 (in German), Dusseldorf, FGR, 1985.

Rickerby, D. G., "Weibull Statistics for Biaxial Strength Testing," in Fracture 1977, Vol. 2, ICF4, Waterloo, Canada, June 19-24, pp. 1133 -1141, 1977.

Ritter, J. E. Bandyopadhyay, N., Jakus, K. "Statistical Reproducibility of Dynamic and Static Fatigue Experiments," *Ceramics Bulletin*, Vol. 60, No. 8, pp. 798-806, 1981.

Ritter, J. E., Jr., Jakus, K., Batakis, A., Bandyopadhyay, N., "Appraisal of Biaxial Strength Testing," *Journal Non-Crystalline Solids*, 38 & 39, pp. 419-242, 1980.

Roark, R. J., and Young, W. C., Formulas for Stress and Strain, 5th ed., McGraw-Hill, 1975.

Rusovic', N. and Warlimont, H., "The Elastic Behavior of β_2 -NiAl Alloys," *Phys. Stat. Sol. (a)*, 44, pp. 609-619, 1977.

Sauthoff, G., Intermetallics, VCH publishers, New York, NY 1995.

Schneibel, J. C., Darolia, R., Lahrman, D. F., and Schmauder, J. C., *Metall. Trans.*, 24A, 1363, 1993.

Selsing, J., "Internal Stresses in Ceramics," *Journal of the American Ceramic Society-Discussions and Notes*, Vol. 44, No. [8], pp. 419, 1961.

Schenl, B., "Ceramic Gas Turbine Technology Development" proceedings of the 1999 International Gas Turbine and Aeroengine Congress, paper No. 99-GT-315, Indianapolis, Indiana, June 7 – 10, 1999.

Shigley, J. E. and Mischke, C. R., Mechanical Engineering Design, McGraw Hill, New York, 1968.

Sih, G. C. and Liebowitz, H. "Mathematical Theories of Brittle Fracture," in *Fracture*, ed. H. Liebowitz, Vol. 2, Academic Press, NY, pp. 67-190, 1967.

Sih, G. C., Paris, P. C., and Irwin, G. R., "On Cracks in Rectilinearly Anisotropic Bodies," International Journal Fracture Mech. Vol. 1, No. 3. 1964.

Sih, G. C., "Some Basic Problems in Fracture Mechanics and New Concepts," Engineering Fracture Mechanics., Vol. 52(2), pp. 365-377, 1973.

Sih, G. C. "Strain-Energy Density Factor Applied to Mixed Mode crack Problems," International Journal Fracture Vol. 10, pp. 305-21, 1974.

Sih, G. C., "Fracture Mechanics of Composite Materials," pp. 111-131 in Fracture of Composite Materials, eds. G. C. Sih and V. P. Tamuzs, Sijthoff & Noordhoff, The Netherlands, 1979.

Sims, C. T. pp. 3-26 in Superalloys II, Sims, C. T., Stoloff, N. S., and Hagel, W. C., eds., John Wiley & Sons, New York, NY, 1987.

Schultz, R. A., Jensen, M. C., Bradt, R. A. "Single Crystal Cleavage of Brittle Materials,' International Journal Fracture, 65, pp. 291-312, 1994.

Shetty, D. K., Rosenfield, A. R., Duckworth, W. H., Held, P. R., "A Biaxial Test for Evaluating Ceramic Strengths," Journal American Ceramic Society, Vol. 66, No. 1, pp. 36-42, Jan. 1983.

Shetty, D. K., "Mixed-Mode Fracture Criteria for reliability Analysis and Design with Structural Ceramics," Journal Engineering for Gas Turbines and Power, Vol 109, pp. 284-289, 1987.

Sonderman, D., Jakus, K., Ritter, J. E., Jr., Yuhaski, S., Jr., Maximum Likelihood Estimation Techniques for Concurrent Flaw Subpopulations, Journal of Materials Science, 20, pp. 207-212, 1985.

Szilard, R., Theory and Analysis of Plates, Classical and Numerical Methods, Prentice-Hall, Englewood Cliffs, NJ, 1974.

Smith, F. W., Emery, A. F., Kobayashi, A. S., "Stress Intensity Factors for Semicircular Cracks," Journal Applied Mechanics, Vol. 34, pp. 953-59, 1967.

Smith, F. W., Sorensen, D. W., "Mixed Mode Stress Intensity Factors for Semielliptical Surface Cracks," NASA CR-134684, June 1974

Measurements Group Tech Note TN-509, "Errors Due to Transverse Sensitivity in Strain Gages," Measurements Group, Raleigh N.C.

Measurements Group Tech Note TN-515, "Strain Gage Rosettes - Selection, Application and Data Reduction," Measurements Group, Raleigh N.C.

Thiemeier, T., Bruckner-Foit, A., and Kolker, H., "Influence of the Fracture Criterion on the Failure Prediction of Ceramics Loaded in Biaxial Flexure," Journal American Ceramic Society 74 [1] pp. 48-52, 1991.

Timoshenko, S. P., and Woinowsky-Krieger, S., p. 72 in Theory of Plates and Shells, 2^{ed}, McGraw-Hill, New York, NY, 1959.

Tsai, S. W. and Wu, E. M. "A General Theory of Strength for Anisotropic Materials," Journal of Composite Materials, Vol. 5, pp. 58-80, January 1971.

Turley, J. and Sines, G., "The Anisotropy of Young's Modulus, Shear Modulus and Poisson's Ratio in Cubic Materials," Physics D: Applied Physics, Vol. 4, pp. 264-271, 1971.

Wortman, J. J. and Evans, R. A., "Young's Modulus, Shear Modulus, and Poisson's Ratio in Silicon and Germanium," Journal of Applied Physics, Vol. 36, No. 1, pp. 153-156, 1965.

Van Vlack, L. H., Elements of Materials Science and Engineering, 3rd edition, Addison-Wesley, Reading MA, 1975.

Vehoff, H., "Fracture Mechanisms in Intermetallics," in Ordered Intermetallics - Physical Metallurgy and Mechanical Behavior, eds. C. T. Liu, Kluwer Academic Publishers, pp. 299-320, 1992.

Vitmar, F. F., and Pukh, V. P., "A Method for Determining the Strength of Sheet Glass," *Aavodskaya Laboratoriya*, 19, pp. 863-867, 1963.

Walsh, P. F., "Linear Fracture Mechanics in Orthotropic Materials," *Engineering Fracture Mechanics*, Vol. 4, pp. 533-541, 1972.

Walston, W. S., General Electric Aircraft Engines, Evendale, Ohio, private communication, July, 1995.

Walston, W. S., Darolia, R. "Effect of Alloying on Physical Properties of NiAl," in *High-Temperature Ordered Intermetallic Alloys V*, ed. I. Baker et al., Materials Research Society Symposium Proceedings, Vol. 288, pp. 237-242, 1993.

Wasilewski, R. J., "Elastic Constants and Young's Modulus of NiAl," *Transactions of the Metallurgical Society of AIME*, Vol. 236, pp. 455-456, 1966.

Weibull, W., "A Statistical Theory of the Strength of Materials," *Ingeniors Vetenskaps Akademien Handlingar*, No. 151, 1939.

Whitney, J. M., and Dauksys, R. J., "Flexure Experiments on Off-Axis Composites," *Journal Composite Materials*, Vol. 4, pp. 135-137, 1970.

APPENDIX A: BIAXIAL TEST APPARATUS

A.1 DESCRIPTION OF THE TEST APPARATUS

An assembly drawing for the biaxial flexure test apparatus capable of applying a uniform pressure to a disk test specimen is shown in Figures A.A.1 and A.A.2. Design drawings of the components for testing a 25.4 mm disk test specimen are shown in Figures A.A.3 to A.A.6. The rig consists of a test chamber, reaction ring and cap, capacitance extensometer⁶, and oil inlet and drain ports. The desired pressurization cycle is supplied to the test chamber and specimen via a hydraulic actuator placed in line with a servo-hydraulic actuator connected to a closed loop controller⁷. The feedback to the controller is supplied by a commercial pressure transducer⁸ connected to the oil inlet line. Although the chamber could be pressurized manually via a hydraulic hand pump, the use of a servo-hydraulic actuator and closed loop controller allows any load rate or load cycle to be applied.

The test chamber and cap are 304 stainless steel, and the reaction ring is either cold rolled, half-hard copper or an appropriate material (e.g. steel) depending on the pressures required for specimen failure. The pressures required to fail the tungsten carbide specimen (~21 MPa) required a steel disk. Copper, having a lower elastic modulus and being somewhat ductile, might be used to accommodate any minor misalignments or specimen curvatures in as-processed specimens or very compliant specimens. The hydraulic oil is contained on the compressive face of the specimen by a nitrile O-ring⁹ retained in a groove.

A 4340 steel disk test specimen design used for rig verification is shown in Figure A.A.7.

⁶ Bentley-Nevada Corp., Minden, Nevada.

⁷ Model 8521, Instron Corp., Canton MA.

⁸ Model 204, Setra Corp., Acton, MA.

⁹ Parker, #5-273, 70 Durometer Buna-N compound N507-70.

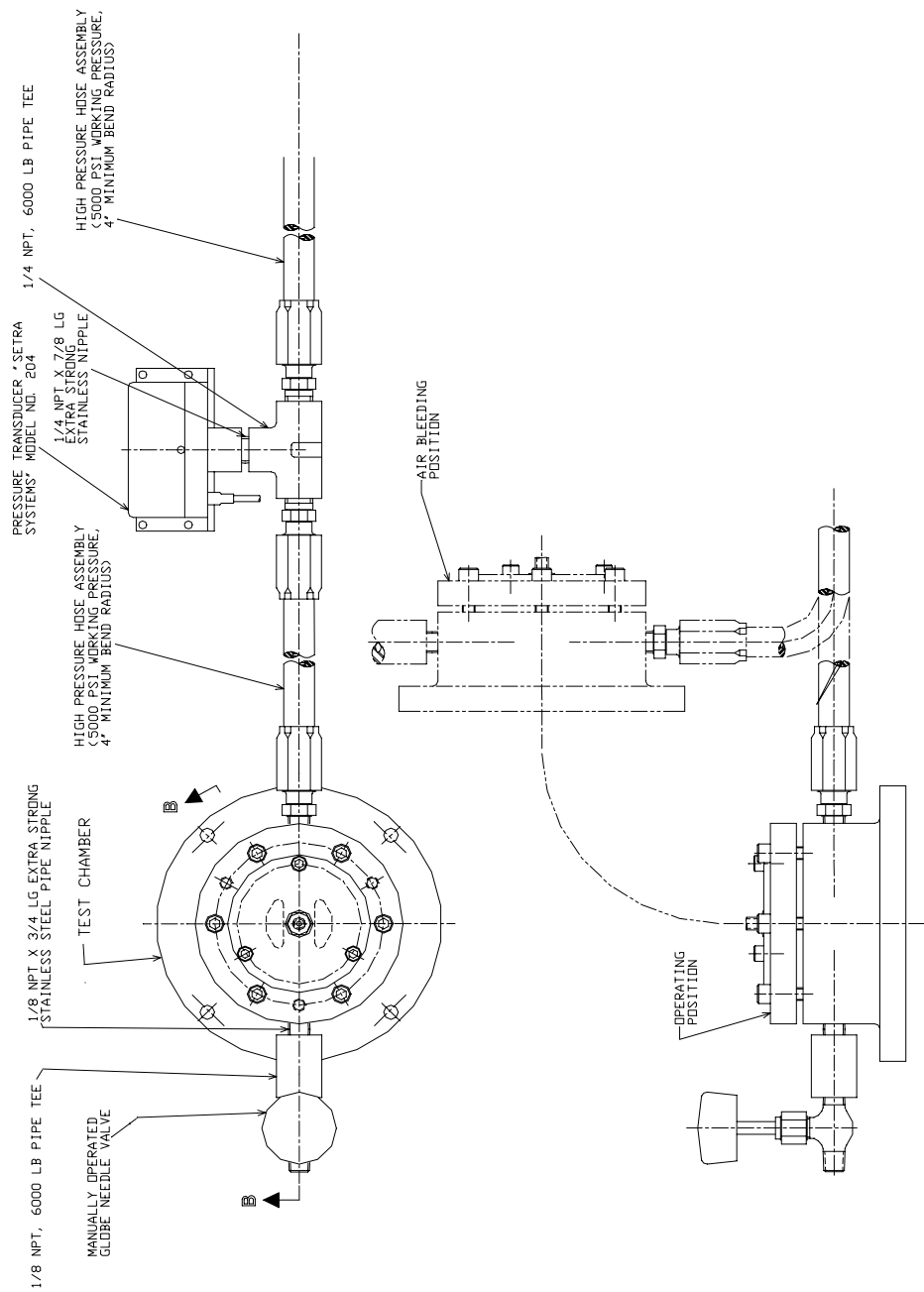


Figure A.A.1.: Assembly drawing for a biaxial test apparatus capable of applying a uniform pressure to a disk test specimen.

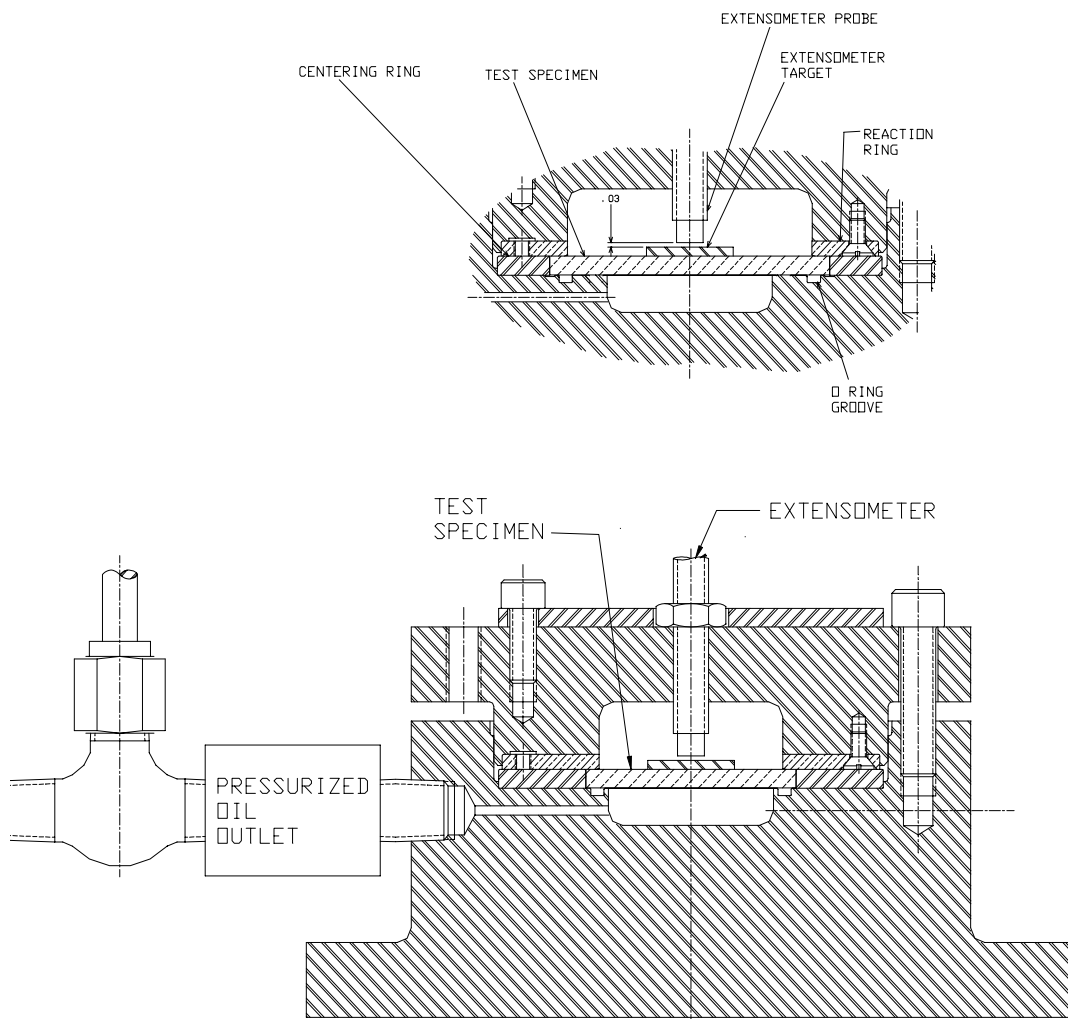


Figure A.A.2 Section view assembly drawing for a biaxial test apparatus capable of applying a uniform pressure to a disk test specimen.

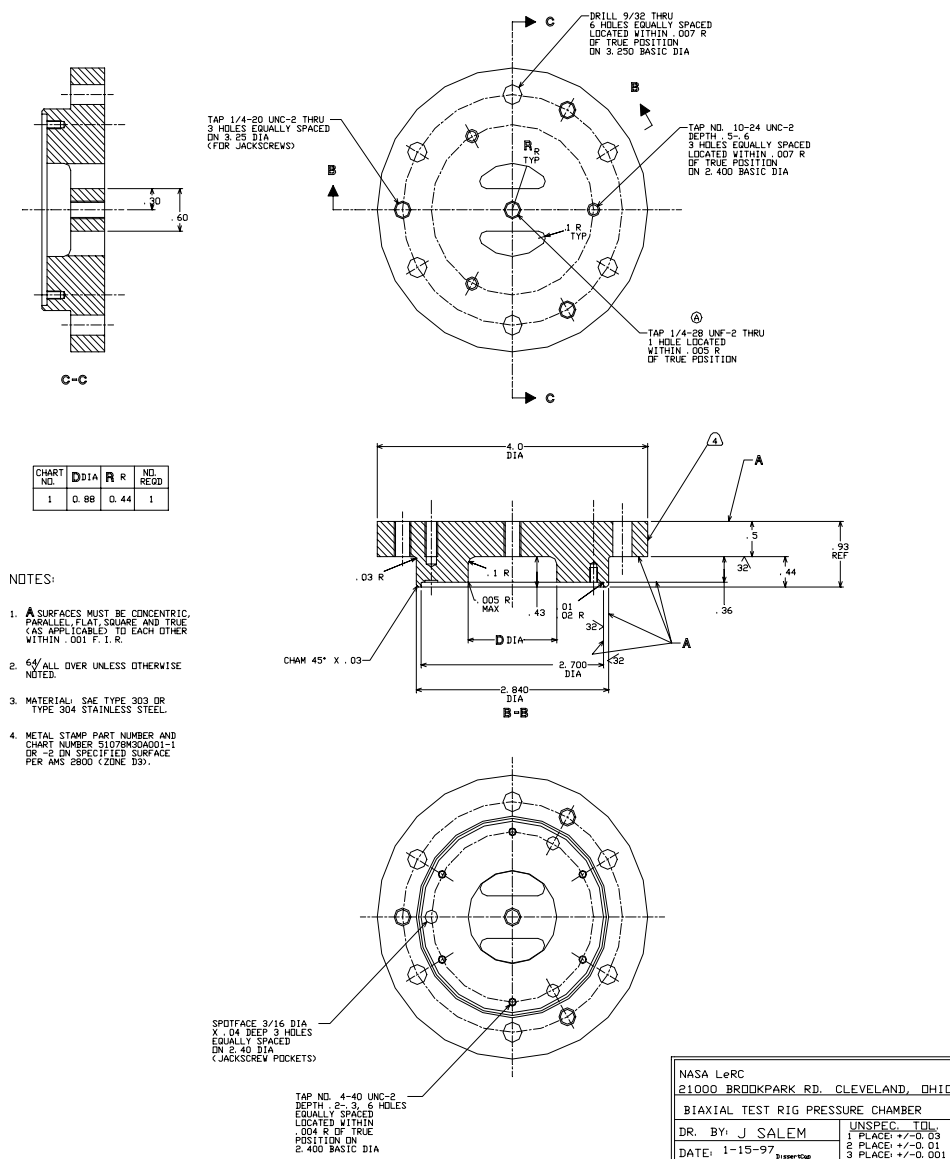
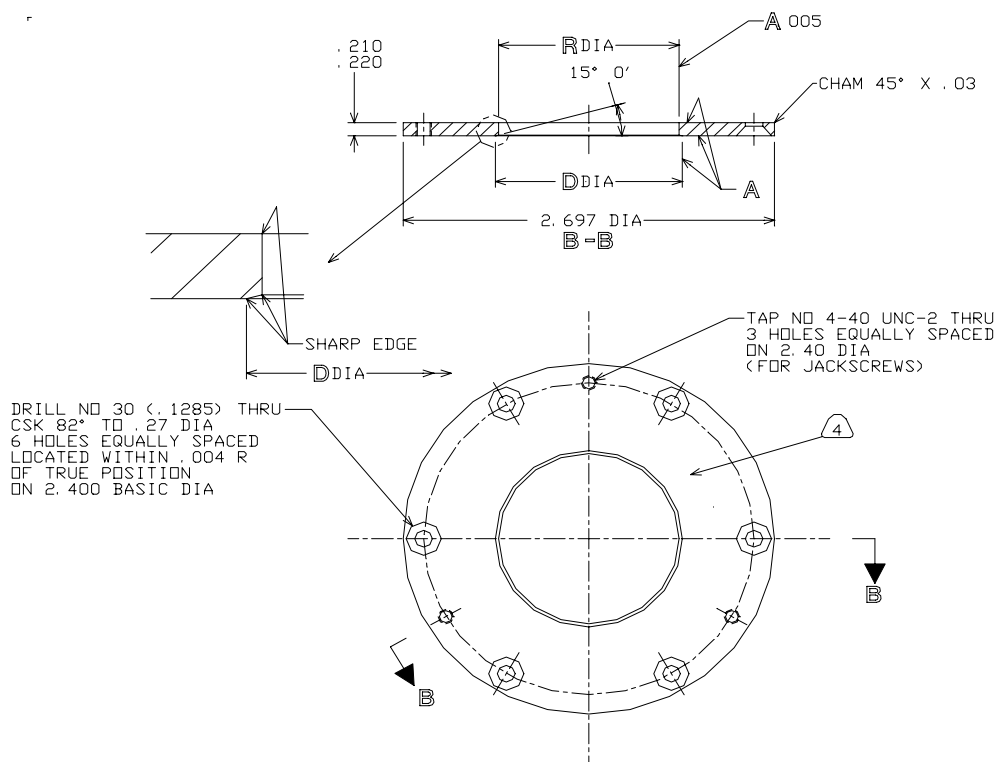


Figure A.A.4: Test chamber cap for a biaxial test apparatus capable of applying a uniform pressure to a 25.4 mm disk test specimen. Units are in inches for ease of machining and minimization of cost.

CHART NO.	DDIA	RDIA	NO. REQD
1	0.911	0.88	2
2	0.931	0.88	2



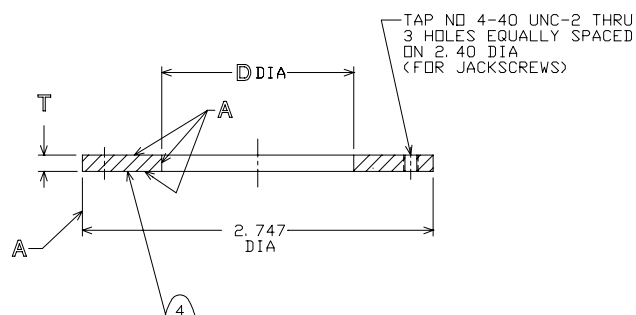
NOTES:

1. A SURFACES MUST BE CONCENTRIC, PARALLEL, FLAT, SQUARE AND TRUE (AS APPLICABLE) TO EACH OTHER WITHIN .001 F. I. R. UNLESS OTHERWISE NOTED.
2. 3ϕ ALL OVER.
3. MATERIAL: ASTM B152, HALF HARD, COLD ROLLED COPPER

NASA LeRC	
21000 BROOKPARK RD. CLEVELAND, OHIO	
BIAXIAL TEST RIG PRESSURE CHAMBER	
DR. BY: J SALEM	UNSPEC. TOL.
DATE: 1-15-97	1 PLACE: ± 0.03
DissertSuppRing	2 PLACE: ± 0.01
	3 PLACE: ± 0.001

Figure A.A.5: Test chamber reaction ring for a biaxial test apparatus capable of applying a uniform pressure to a 25.4 mm disk test specimen. Units are in inches for ease of machining and minimization of cost.

CHART NO.	D DIA	T	NO. REQD
1	1.006	.0595 .0605	1
2	1.006	.0625 .0635	1
3	1.006	.0655 .0665	1
4	1.001	.0595 .0605	1
5	1.001	.0625 .0635	1
6	1.001	.0655 .0665	1
7	0.999	.0595 .0605	1
8	0.999	.0625 .0635	1
9	0.999	.0655 .0665	1



NOTES:

1. A SURFACES MUST BE CONCENTRIC, PARALLEL, FLAT, SQUARE AND TRUE (AS APPLICABLE) TO EACH OTHER WITHIN .001 F. I. R.
2. $\sqrt[32]{}$ ALL OVER.
3. MATERIAL: SAE TYPE 303 OR TYPE 304 STAINLESS STEEL.

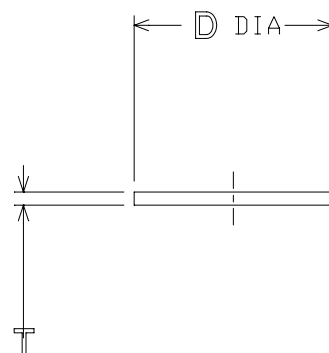
NASA LeRC 21000 BROOKPARK RD. CLEVELAND, OHIO	
BIAXIAL TEST RIG PRESSURE CHAMBER	
DR. BY: J SALEM	UNSPEC. TOL.
DATE: 1-15-97	1 PLACE: +/-0.03
	2 PLACE: +/-0.01
	3 PLACE: +/-0.001

Figure A.A.6: Test chamber centering ring for a biaxial test apparatus capable of applying a uniform pressure to a 25.4 mm disk test specimen. Units are in inches for ease of machining and minimization of cost.

CHART NO.	D DIA	T	NO. REQD
1	0.996 0.998	.0605 .0615	4

NOTES:

1. 32/ ALL OVER
2. Material is 4340 steel heat treated to 280 ksi nominal tensile strength.



NASA LeRC 21000 BROOKPARK RD. CLEVELAND, OHIO	
BIAXIAL TEST RIG PRESSURE CHAMBER	
DR. BY: J SALEM	UNSPEC. TOL. 1 PLACE: +/-0.03 2 PLACE: +/-0.01 3 PLACE: +/-0.001
DATE: 1-15-97 <small>DissentSteelDisk</small>	

Figure A.A.7: 25.4 mm disk test specimen. Units are in inches for ease of machining and minimization of cost.

A.2 SEAL ANALYSIS

The O-ring seal is somewhat compliant and thus the pressure generated at the interface between it and the test specimen is of interest. Because the relatively compliant seal is compressed into the groove via the test specimen, it nominally assumes orthogonal faces as shown in Figure A.A.8 and is constrained from movement. This is a somewhat tenuous assumption, because with sufficient pressures the O-ring seal will be extruded out of the groove. The resulting boundary conditions are

$$\begin{aligned}\sigma_x &= P \\ \varepsilon_y &= \varepsilon_z = 0\end{aligned}\quad . \quad \text{AC.1}$$

From Hooke's law we have

$$\varepsilon_y = \frac{1}{E}(\sigma_y - \nu(\sigma_x + \sigma_z)) \quad \text{AC.2}$$

$$\varepsilon_z = \frac{1}{E}(\sigma_z - \nu(\sigma_x + \sigma_y)) \quad \text{AC.3}$$

The strains are zero in equations AC.2 and AC.3, and they can be equated and solved to show that the y and z stresses are equivalent. Setting AC.2 to zero and substituting σ_z for σ_y and the pressure for σ_x results in

$$\sigma_z = \left(\frac{\nu}{1-\nu} \right) P. \quad \text{AC.4}$$

Because Poisson's ratio for most elastomer materials is ~ 0.5 , Equation AC.5 implies that the pressure on all faces of the seal are equivalent to the hydraulic pressure within the chamber.

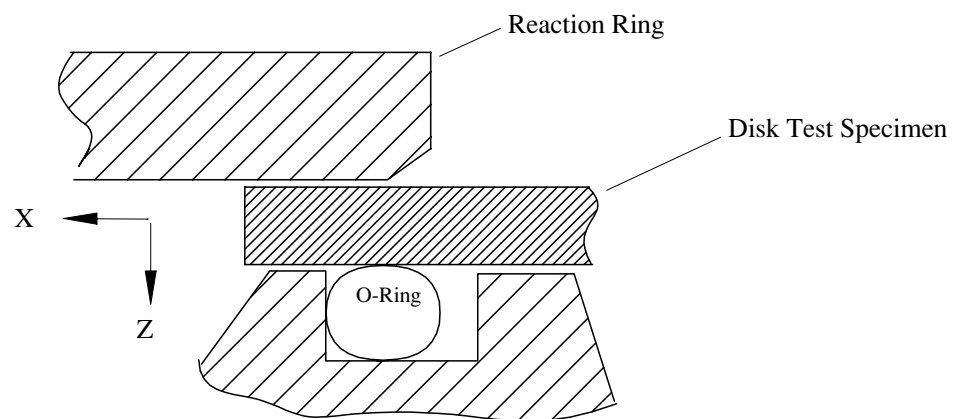


Figure A.A.8: Cross-sectional view of the test specimen, reaction ring, O-ring and groove.

APPENDIX B: CODE FOR CALCULATION OF STRESSES AND STRAINS IN ANISOTROPIC CIRCULAR PLATES SUBJECTED TO UNIFORM PRESSURE

The series constants for Okubu's solution (Okubu, 1949) and the stresses and strains at any point in the disk test specimen were determined by a program written in the Maple V[®] programming language¹⁰. The Maple V code, which is listed below, has two main parts: that solving a selected number of equations for the corresponding constants and that determining the stresses and strains at a specified Cartesian location. As the crystal symmetry is orthogonal, the elastic constants and solutions are in Cartesian form. However, as the plate is circular, stress and strain in polar coordinates are more informative and output is given in both Cartesian and polar systems.

The plates is assumed to be of cubic symmetry, {100} orientation and subjected to a uniform pressure with support on the periphery. Any plate radius, thickness and pressure can be specified, however, the solution assumes that the plate is thin and the displacements small. The code can be generalized to plate of orthotropic symmetry such as a plate of {110} orientation.

Okubu's Solution Generalized for the Case of a {001} Plate of Variable Radius

Determination of Constants

Displacement Equations and Curvatures

```
> restart: with (linalg):
```

```
> n[t]:=4;
```

```
> wc:=C1*x^4+C2*x^2*y^2+C3*y^4+C4*x^2+C5*y^2+C6;
```

```
>w:=wc+cp^2/4*sum(A[n]*(cosh((2*n+2)*ap)*cos((2*n+2)*bp)/((2*n+2)*(2*n+1))-  
(1/(2*n*(2*n+1))+1/(2*n*(2*n-1)))*cosh(2*n*ap)*cos(2*n*bp)+cosh((2*n-2)*ap)*cos((2*n-  
2)*bp)/((2*n-1)*(2*n-  
2))),n=2..n[t])+cpp^2/4*sum(B[n]*(cosh((2*n+2)*app)*cos((2*n+2)*bpp)/((2*n+2)*(2*n+1))-  
(1/(2*n*(2*n+1))+1/(2*n*(2*n-1)))*cosh(2*n*app)*cos(2*n*bpp) +cosh((2*n-2)*app)*cos((2*n-  
2)*bpp)/((2*n-1)*(2*n-2))),n=2..n[t]):
```

```
> dwdxx:=sum((A[n]*cosh(2*n*ap)+B[n]*cosh(2*n*app))*cos(2*n*b),n=2..n[t])+diff(wc,x$2);
```

¹⁰ Maple V, release 5, Waterloo Maple Software, Ontario, Canada.


```

>dwdyy:=-
sum((A[n]*k1^2*cosh(2*n*ap)+B[n]*k2^2*cosh(2*n*app))*cos(2*n*b),n=2..n[t])+diff(wc,y$2);

> dwdxdy:=-sum((A[n]*k1*sinh(2*n*ap)+B[n]*k2*sinh(2*n*app))*sin(2*n*b),n=2..n[t])+diff(wc,y,x);

> a:=ln(rp);x:=exp(a)*cos(b);y:=exp(a)*sin(b);bp:=b;bpp:=b;

> w:=combine(w,trig):

```

Equation 11 Of Okubu:

```

> EQ11a:=collect(simplify(w-sum('coeff(w,cos(2*n*b))*cos(2*n*b)',n'=1..n[t]+1)=0),rp);
> EQ11b:=simplify(coeff(w,cos(2*b))=0);
> EQ11c:=simplify(coeff(w,cos(4*b))=0);
> EQ11d:=simplify(coeff(w,cos(6*b))=0);
> EQ11e:=simplify(coeff(w,cos(8*b))=0);

```

Moment Equation and Equation 12 of Okubu:

```

>Ma:=combine((D1+D2+(D1-D2)*cos(2*b))*dwdxx+(D2+D3+(D2-
D3)*cos(2*b))*dwdyy+2*D4*dwdxdy*sin(2*b),trig);

> EQ12a:=collect(simplify(Ma-sum('coeff(Ma,cos(2*n*b))*cos(2*n*b)',n'=1..n[t]+1)=0),rp);

EQ12b:=simplify(coeff(Ma,cos(2*b))=0):EQ12b:=collect(EQ12b,A[2]):EQ12b:=collect(EQ12b,B[2]):
EQ12b:=collect(EQ12b,rp);

EQ12c:=simplify(coeff(Ma,cos(4*b))=0):EQ12c:=collect(EQ12c,A[2]):EQ12c:=collect(EQ12c,B[2]):
EQ12c:=collect(EQ12c,rp);
EQ12d:=simplify(coeff(Ma,cos(6*b))=0):

```

Single Crystal Elastic Constants(m^2/MN):

```

> S11:=1.0428e-5;
> S22:=1.0428e-5;
> S12:=-0.421e-5;
> S44:=0.892e-5;
> b11:=S22/(S11*S22-S12^2);
> b22:=S11/(S11*S22-S12^2);
> b12:=-S12/(S11*S22-S12^2);
> b66:=1/S44;

```

Plate thickness (mm), Radius (mm) and applied pressure (psig):

```

> rp:=11.568;q:=1056*6.8947/1000;h:=1.554;

```

Plate stiffness in Okubu's Notation:

```

> D1:=h^3*S22/(12*(S11*S22-S12^2));
> D2:=-h^3*S12/(12*(S11*S22-S12^2));
> D3:=h^3*S11/(12*(S11*S22-S12^2));

```

```
> D4:=h^3/(6*S44);
```

DEQ Constants:

```
> k1:=D1^0.5/(D2+D4+((D2+D4)^2-D1*D3)^0.5)^0.5;
> k2:=D1^0.5/(D2+D4-((D2+D4)^2-D1*D3)^0.5)^0.5;
> cp:=rp*(1-k1^2)^0.5;
> cpp:=rp*(1-k2^2)^0.5;
> ap:=arccosh(rp/cp);
> app:=arccosh(rp/cpp);
```

Series Constants Set to Zero:

```
> n:='n';A[4]:=0:A[5]:=0:A[6]:=0:B[4]:=0:B[5]:=0:B[6]:=0:
```

Differential Equation of Bending:

```
> EQ10:=3*D1*C1+(D2+D4)*C2+3*D3*C3-q/8;
```

An, Bn and Ci Terms to be Determined from Boundary Equations;

```
> consts:=
solve({EQ10,EQ11a,EQ11b,EQ11c,EQ12a,EQ12b,EQ12c,EQ11d,EQ11e,EQ12d},{C1,C2,C3,C4,
C5,C6,A[2],B[2],A[3],B[3]});
```

STRAINS AND STRESSES FOR A SPECIFIC PLATE LOCATION:

Cartesian Location of Interest (mm):

```
> x:=0.0066;
> y:=0.0067;
> t:=arctan(y/x);
```

Calculation of Alpha and Beta Prime and Double Prime terms:

```
> k:=k1;c:=cp;
> a:=x^2+k^2*y^2-c^2;
> b:=2*k*y*c;
> d:=x^2+k^2*y^2-c^2;
> alp:=evalf(log(1/(c^2^0.5)*(a+(a^2+b^2)^0.5)^0.5+(1/(2*c^2)*(a+(a^2+b^2)^0.5)+1)^0.5));
> betp:=(arcsin(1/(c*(2^0.5))*(-d+(d^2+b^2)^0.5)^0.5));
> k:=k2;c:=cpp;
> a:=evalf(x^2+k^2*y^2-c^2);
> b:=2*k*y*c;
> d:=x^2+k^2*y^2-c^2;
> alpp:=evalf(log(1/(c^2^0.5)*(a+(a^2+b^2)^0.5)^0.5-(1/(2*c^2)*(a+(a^2+b^2)^0.5)+1)^0.5));
> betpp:=(arcsin(1/(c*(2^0.5))*(-d+(d^2+b^2)^0.5)^0.5));
```

Maximum Value of Prime Terms

```
> alpMAX:=log((cos(Pi/4)*(-cp^2+(cp^4)^0.5)^0.5)/cp+(1+(-cp^2+(cp^4)^0.5)/(2*cp^2))^0.5);
> betpMAX:=arcsin((cos(Pi/4)*(cp^2+(cp^4)^0.5)^0.5)/cp);
```

```
>alppMAX:=log((cos(Pi/4)*(-cpp^2+(cpp^4)^0.5)^0.5)/cpp-(1+(-
cpp^2+(cpp^4)^0.5)/(2*cpp^2))^0.5);
>betppMAX:=arcsin((cos(Pi/4)*(cpp^2+(cpp^4)^0.5)^0.5)/cpp);
```

Cartesian MicroStrains:

```
>e11:=Re(-
h/2*(A[2]*cosh(4*alp)*cos(4*betp)+A[3]*cosh(6*alp)*cos(6*betp)+B[3]*cosh(6*Re(alpp))*cos(6*Im(
alpp))*cos(6*betpp)+B[2]*cosh(4*Re(alpp))*cos(4*Im(alpp))*cos(4*betpp)+12*C1*x^2+2*C2*y^2+
2*C4));
```

```
>e22:=Re(-h/2*(-k1^2*A[2]*cosh(4*alp)*cos(4*betp)-k1^2*A[3]*cosh(6*alp)*cos(6*betp)-
k2^2*B[2]*cosh(4*Re(alpp))*cos(4*Im(alpp))*cos(4*betpp)-
k2^2*B[3]*cosh(6*Re(alpp))*cos(6*Im(alpp))*cos(6*betpp)+2*C2*x^2+12*C3*y^2+2*C5));
```

```
>e12:=Re(-h*(-k1*A[2]*sinh(4*alp)*sin(4*betp)-k1*A[3]*sinh(6*alp)*sin(6*betp)-
k2*B[2]*sinh(4*Re(alpp))*cos(4*Im(alpp))*sin(4*betpp)-
k2*B[3]*sinh(6*Re(alpp))*cos(6*Im(alpp))*sin(6*betpp)+4*C2*x*y));
```

```
e11:=evalf(Re(subs(consts,e11)));e22:=evalf(Re(subs(consts,e22)));e12:=evalf(Re(subs(consts,e
12)));
```

```
> eMAX:=Re(-
h/2*(A[2]*cosh(4*alpMAX)*cos(4*betpMAX)+B[2]*cosh(4*Re(alppMAX))*cos(4*Im(alppMAX))*cos
(4*betppMAX)+2*C4));
```

```
> eMAX:=evalf(Re(subs(consts,eMAX)));
```

Cartesian Stresses (MPa):

```
> Sig11:=evalf(b11*e11+b12*e22);
> Sig22:=evalf(b12*e11+b22*e22);
> Sig12:=evalf(b66*e12);
> SigMax:=b11*eMAX+b12*eMAX;
```

Polar MicroStrains and Stresses (MPa):

```
> Sigr:=Sig11*cos(t)^2+Sig22*sin(t)^2+Sig12*sin(2*t);
> err:=e11*cos(t)^2+e22*sin(t)^2+e12*sin(2*t);
> err:=e11*cos(t)^2+e22*sin(t)^2+e12*sin(2*t);
> ett:=e22*cos(t)^2+e11*sin(t)^2-e12*sin(2*t);
> ert:=(e22-e11)*sin(t)*cos(t)+e12*cos(2*t);
> tt:=evalf(t*180/Pi);
```

APPENDIX C: UNIAXIAL TEST SPECIMEN DATA

The following tables give detailed uniaxial test specimen dimensions, failure loads and the calculated strengths based on ASTM C1161 (ASTM C 1161 1990).

Table A.C.1 – <100> three-point flexure test specimen dimensions and failure loads.

Billet Number	Specimen Number	Width 1 mm x	Width 2 mm	Width 3 mm	Height 1 mm x	Height 2 mm	Height 3 mm	Average Width mm	Average Height mm	Load N	Strength MPa	Effective Area mm ²
2461	3fx2	3.862	3.858	3.816	2.797	2.775	2.723	3.845	2.765	1005	1016	21
2429	3fx1t	3.824	3.836	3.821	2.747	2.745	2.721	3.827	2.738	770	1622	21
<100>	3fx2t	3.746	3.777	3.763	2.761	2.771	2.763	3.762	2.765	608	1277	21
	3fx3b	3.798	3.811	3.804	2.767	2.76	2.736	3.804	2.754	827	1732	21
2454	3fx1t	3.864	3.876	3.866	2.876	2.851	2.807	3.869	2.845	601	1162	21
<100>	3fx2b	3.865	3.837	3.788	2.829	2.84	2.835	3.830	2.835	623	1224	21
	3fx3b	3.83	3.853	3.861	2.845	2.867	2.842	3.848	2.851	760	1469	21
2464	3fx1	3.854	3.832	3.799	2.791	2.798	2.799	3.828	2.796	578	1168	21
<100>	3fx2	3.817	3.827	3.829	2.801	2.835	2.84	3.824	2.825	623.6	1235	21
												21
2471	3fx1t	3.745	3.829	3.852	2.808	2.874	2.883	3.809	2.855	694.9	1353	21
2474	3fx1t	3.848	3.849	3.839	2.825	2.842	2.845	3.845	2.837	498.9	975	21
<100>	3fx2b	3.796	3.799	3.788	2.799	2.828	2.836	3.794	2.821	568.3	1139	21
	3fx3b	3.81	3.844	3.878	2.818	2.818	2.795	3.844	2.810	633.8	1262	21
2439	3fx1t							3.776	2.755	543.7	1148	21
<100>	3fx2b	3.729	3.754	3.786	2.815	2.834	2.832	3.756	2.827	560.2	1129	21

Table A.C.2 – <100> four-point flexure test specimen dimensions and failure loads.

Billet # Number	Specimen Number	Width 1 mm x	Width 2 mm	Width 3 mm	Height 1 mm x	Height 2 mm	Height 3 mm	Average Width mm	Average Height mm	Load N	Strength MPa	Effective Area mm ²
2461 <001>	4fx1	3.922	3.922	3.907	2.901	2.914	2.915	3.917	2.910	860	771	101
	4fx2	3.937	3.94	3.93	2.908	2.902	2.873	3.936	2.894	776	700	102
	4fx3	3.926	3.892	3.835	2.936	2.921	2.889	3.884	2.915	1203	1082	100
	4fx4	3.855	3.854	3.824	2.894	2.935	2.952	3.844	2.927	1117	1008	100
	3fx2	3.862	3.858	3.816	2.797	2.775	2.723	3.845	2.765	1005	1016	99
2429 <001>	4fx3b	3.636	3.699	3.735	2.713	2.726	2.7	3.690	2.713	1273	1392	95
	4fx1t	3.771	3.779	3.766	2.708	2.769	2.766	3.772	2.748	1207	1259	97
	4fx2t	3.727	3.735	3.704	2.71	2.758	2.737	3.722	2.735	1306	1393	95
	4fx4b	3.704	3.748	3.747	2.698	2.722	2.686	3.733	2.702	998	1088	95
2353 <100>	4fx1t	3.569	3.593	3.567	2.74	2.75	2.738	3.576	2.743	784	880	92
	4fx2t	3.788	3.75	3.722	2.839	2.842	2.836	3.753	2.839	1032	1030	96
	4fx3b	3.991	4.049	4.09	2.747	2.776	2.787	4.043	2.770	903	879	103
	4fx4b	3.493	3.465	3.412	2.636	2.59	2.53	3.457	2.585	702	919	89
2454 <100>	4fx1t	3.879	3.883	3.876	2.85	2.859	2.846	3.879	2.852	926.7	887	99
	4fx2t	3.814	3.836	3.836	2.681	2.689	2.649	3.829	2.673	761	841	98
	4fx3b	3.805	3.834	3.851	2.826	2.837	2.824	3.830	2.829	852.5	840	98
	4fx4b	3.818	3.833	3.838	2.819	2.825	2.812	3.830	2.819	1057	1049	98
2464 <100>	4fx1	3.786	3.792	3.799	2.81	2.812	2.802	3.792	2.808	893	902	97
	4fx2	3.815	3.834	3.85	2.811	2.819	2.797	3.833	2.809	764	764	98
	4fx3	3.738	3.742	3.724	2.827	2.827	2.804	3.735	2.819	941	958	96
	4fx4	3.859	3.848	3.83	2.801	2.829	2.847	3.846	2.826	1189	1169	99
2471 <100>	4fx1t	3.882	3.86	3.85	2.858	2.862	2.873	3.864	2.864	1378	1312	99
	4fx2t	3.944	3.939	3.915	3.023	2.996	2.982	3.933	3.000	1503	1281	101
	4fx4b	3.7	3.758	3.807	2.834	2.858	2.860	3.755	2.851	1103	1091	97
2474 <100>	4fx1t	3.81	3.826	3.819	2.855	2.854	2.822	3.818	2.844	1390	1359	98
	4fx2t	3.873	3.87	3.84	2.816	2.849	2.874	3.861	2.846	933.8	902	99
	4fx3b	3.749	3.77	3.794	2.788	2.815	2.836	3.771	2.813	1171	1185	97
	4fx4b	3.811	3.794	3.762	2.707	2.766	2.756	3.789	2.743	725	769	97
2439 <100>	4fx1t	3.85	3.855	3.833	2.864	2.855	2.832	3.846	2.850	883	854	99
	4fx2t	3.755	3.766	3.784	2.755	2.791	2.803	3.768	2.783	780.8	808	97
	4fx3b	3.789	3.794	3.775	2.736	2.736	2.728	3.786	2.733	944.5	1008	97
	4fx4b	3.857	3.869	3.877	2.802	2.825	2.822	3.868	2.816	962.4	947	99

Table A.C.3 – <110> three-point flexure test specimen dimensions and failure loads.

Billet Number	Specimen Number	Width 1 mm x	Width 2 mm	Width 3 mm	Height 1 mm x	Height 2 mm	Height 3 mm	Average Width mm	Average Height mm	Failure Load N	Strength MPa	Effective Area mm ²	Failure Source
2492	3fx1	3.734	3.725	3.706	2.742	2.756	2.753	3.722	2.750	338	727	20	HfC
<110>	3fx2	3.627	3.643	3.663	2.701	2.695	2.667	3.644	2.688	317	731	20	HfC
2490	3fx1	3.789	3.803	3.811	2.795	2.788	2.772	3.801	2.785	427	877	21	HfC
<110>	3fx2	3.748	3.779	3.776	2.751	2.762	2.753	3.768	2.755	499	1057	21	HfC
2496	3fx2	3.802	3.801	3.774	2.804	2.811	2.81	3.792	2.808	251.2		21	EDM
<110>	3fx3	3.873	3.866	3.858	2.767	2.715	2.752	3.706	2.745	356.1	773	20	HfC
2518	3fx1	3.783	3.784	3.771	2.808	2.803	2.775	3.779	2.795	237.4		21	EDM
<110>	3fx2	3.737	3.754	3.803	2.788	2.819	2.837	3.765	2.815	236.6	482	21	HfC
2519	3fx1	3.709	3.709	3.709	2.78	2.771	2.741	3.709	2.764	434.7	929	20	HfC
<110>	3fx3	3.714	3.754	3.766	2.792	2.754	2.707	3.745	2.751	361.3	773	20	HfC
2493	3fx1	3.74	3.695	3.65	2.808	2.78	2.735	3.695	2.774	178		20	EDM
<110>	3fx2	3.638	3.676	3.684	2.75	2.753	2.752	3.666	2.752	254.4	557	20	HfC

Table A.C.4 – <110> four-point flexure test specimen dimensions and failure loads.

Billet Number	Specimen Number	Width 1 mm x	Width 2 mm	Width 3 mm	Height 1 mm x	Height 2 mm	Height 3 mm	Average Width mm	Average Height mm	Failure Load N	Strength MPa	Effective Area mm ²	Failure Source
2492 <110>	4fx1	3.868	3.872	3.874	2.849	2.855	2.841	3.871	2.848	391.8	372	105	EDM
	4fx2	3.891	3.886	3.881	2.891	2.9	2.88	3.886	2.890	310.1	285	105	EDM
	4fx3	3.732	3.751	3.742	2.839	2.826	2.804	3.742	2.823	519.5	527	101	HfC
	4fx4	3.742	3.761	3.768	2.775	2.77	2.735	3.757	2.760	418.6	443	101	EDM
2486 <110>	4fx2	3.873	3.884	3.886	2.802	2.819	2.836	3.881	2.819	351.3	345	105	EDM
	4fx4	3.861	3.852	3.804	2.746	2.76	2.752	3.839	2.753	420.3	438	103	HfC
2490 <110>	extra	3.834	3.775	3.803	2.705	2.701	2.661	3.804	2.689	464.6	511	102	HfC
	4fx2	3.839	3.847	3.819	2.783	2.809	2.813	3.835	2.802	406.7	409	103	EDM
	4fx1	3.824	3.836	3.843	2.801	2.812	2.795	3.834	2.803	729.1	732	103	HfC
	4fx2	3.734	3.735	3.725	2.708	2.704	2.682	3.731	2.698	639.3	712	101	HfC
	CN1	3.712	3.746	3.74	2.777	2.775	2.766	3.733	2.773	191.7	204	101	EDM
2496 <110>	4fx2	3.776	3.811	3.839	2.907	2.909	2.887	3.809	2.901	334.5	316	103	EDM
	4fx3	3.833	3.842	3.831	2.831	2.866	2.881	3.835	2.859	365.9	354	104	EDM
	4fx4	3.853	3.859	3.857	2.878	2.884	2.883	3.856	2.882	420.9	398	104	EDM
2518 <110>	4fx1	3.757	3.778	3.795	2.816	2.823	2.807	3.777	2.815	336.0	340	102	EDM
	4fx2	3.825	3.831	3.842	2.736	2.721	2.709	3.833	2.722	322.8	345	103	EDM
	4fx3	3.705	3.694	3.645	2.77	2.732	2.677	3.681	2.726	339.7	376	100	EDM
	4fx4	3.695	3.712	3.728	2.818	2.822	2.815	3.712	2.818	415.9	427	101	HfC
2506 <110>	4fx1	3.647	3.647	3.599	2.733	2.781	2.814	3.631	2.776	404.4	438	99	EDM
	4fx4	3.76	3.745	3.741	2.856	2.831	2.782	3.749	2.823	358.1	363	102	EDM
	4fx2	3.635	3.636	3.643	2.66	2.71	2.737	3.638	2.702	426.9	487	98	EDM
	4fx3	3.656	3.644	3.576	2.821	2.808	2.766	3.625	2.798	567.9	605	98	HfC
2516 <110>	4fx1	3.791	3.734	3.654	2.759	2.712	2.674	3.726	2.715	404.9	447	101	EDM
	4fx2	3.67	3.646	3.612	2.72	2.752	2.776	3.643	2.749	404.6	445	99	HfC
	4fx3	3.803	3.779	3.737	2.821	2.836	2.847	3.773	2.835	373.4	373	102	EDM
	4fx4	3.746	3.724	3.714	2.787	2.763	2.746	3.728	2.765	295.9	315	101	EDM
2519 <110>	4fx1	3.667	3.685	3.704	2.787	2.711	2.62	3.685	2.706	634.9	711	100	HfC
	4fx3	3.626	3.627	3.622	2.728	2.687	2.63	3.625	2.682	665.6	772	98	HfC
	4fx4	3.586	3.617	3.619	2.651	2.694	2.726	3.607	2.690	667.8	773	98	HfC
	4fx2	3.68	3.711	3.72	2.742	2.746	2.741	3.704	2.743	745.0	808	100	HfC
2484 <110>	4fx3	3.747	3.763	3.777	2.784	2.776	2.744	3.762	2.768	637.4	669	102	HfC
	4fx4	3.684	3.687	3.695	2.758	2.746	2.731	3.689	2.745	630.7	686	100	HfC
2493 <110>	4fx1	3.832	3.821	3.801	2.809	2.833	2.847	3.818	2.830	632.4	625	103	HfC
	4fx2	3.787	3.785	3.786	2.797	2.831	2.847	3.786	2.825	184.5	186	102	EDM
	4fx3	3.797	3.803	3.796	2.852	2.836	2.794	3.799	2.827	267.5	268	103	EDM

APPENDIX D: BIAXIAL TEST SPECIMEN DATA

The following tables give detailed biaxial test specimen dimensions, failure pressures and the calculated strengths based on Okubu's (Okubu 1949) approximate and series solutions.

Table A.D.1 – Biaxial disk test specimen dimensions and failure pressures.

Test Specimen ID	Thickness 1	Thickness 2	Thickness 3	Thickness 4	Thickness Center	Average Thickness	Diameter 1	Diameter 2	Disk Average Diameter	Support Radius	Applied Pressure
	mm	mm	mm	mm	mm	mm	mm	mm	mm	mm	MPa
B4	1.541	1.558	1.546	1.555	1.548	1.550	25.318		25.318	11.568	4.92
B5	1.548	1.552	1.544	1.547	1.544	1.547	25.303	25.308	25.306	11.568	8.40
B6	1.499	1.476	1.455	1.514	1.486	1.486	25.307	25.301	25.304	11.568	4.13
B7	1.555	1.549	1.563	1.552	1.549	1.554	25.292	25.292	25.292	11.568	7.28
B8	1.539	1.547	1.549	1.552	1.542	1.546	25.278	25.290	25.284	11.685	7.31
B9	1.549	1.544	1.539	1.552	1.539	1.545	24.303	25.288	24.796	11.777	7.29
B10	1.529	1.542	1.542	1.544	1.534	1.538	25.296	25.293	25.295	11.568	9.33
B11	1.544	1.539	1.534	1.542	1.539	1.540	25.277	25.266	25.272	11.568	6.59
B12	1.265	1.273	1.270	1.268	1.265	1.268	25.077	25.008	25.043	11.568	4.83
B13	1.499	1.511	1.488	1.529	1.509	1.507	25.304	25.328	25.316	11.568	5.32
B14	1.448	1.435	1.443	1.430	1.448	1.441	25.243	25.211	25.227	11.568	3.65
e3	1.440	1.448	1.453	1.435	1.445	1.444	25.222	25.228	25.225	11.568	7.00
e4	1.438	1.425	1.422	1.440	1.430	1.431	25.207	25.210	25.209	11.568	6.03
Average						1.492			25.222	11.593	
Standard Deviation						0.081			0.148	0.064	

Table A.D.2 – Biaxial disk test specimen dimensions and failure pressures.

Test Specimen ID	D*	C*	Displacement	Maximum	Approximate Solution Stress MPa	Series Solution Stress MPa	<i>Lateral Correction:</i>	
			w mm	micro Strain			Approximate Solution Stress MPa	Series Solution Stress MPa
B4	47611	5.30	0.154	2113	339.7	311.8	343.4	315.5
B5	47372	5.30	0.263	3618	581.8	534.3	588.1	540.6
B6*	41976	5.30	0.146	1929	310.3	284.9	313.4	288.0
B7	47981	5.30	0.225	3107	499.8	458.6	505.2	464.1
B8*	47266	5.30	0.239	3214	517.0	474.7	522.4	480.2
B9*	47170	5.30	0.247	3264	524.8	481.8	530.3	487.3
B10*	46572	5.30	0.297	4061	653.1	601.3	660.1	608.3
B11*	46708	5.30	0.209	2862	460.3	422.6	465.2	427.5
B12*	26084	5.30	0.275	3095	497.8	457.1	501.4	460.7
B13*	43813	5.30	0.180	2412	387.9	356.4	391.9	360.4
B14*	38261	5.30	0.142	1811	291.2	267.2	294.0	269.9
e3*	38547	5.30	0.269	3456	555.8	510.6	561.0	515.8
e4*	37496	5.30	0.239	3033	487.8	447.8	492.3	452.3
Average					470	431	477	439
Standard Deviation					109	100	111	102
90% Confidence Interval					54	49	55	50

APPENDIX E: CODE FOR ESTIMATION OF THE SCALE PARAMETER OF ANISOTROPIC MATERIALS

In order to estimate the characteristic strength of disk test specimens exhibiting elastic and strength anisotropy, the scale parameter function must be estimated from uniaxial test data. The following program, which is written in the Mathematica® programming language¹¹, estimates the constant for the scale parameter function given in Equation (98). The normal stress criterion is used.

ESTIMATION OF SCALE PARAMETER CONSTANTS FOR NiAl SINGLE CRYSTAL: NORMAL STRESS CRITERION.

```
(* INPUT WEIBULL MODULUS *)
(* INPUT <100> AND <110> 4-POINT FLEXURE EFFECTIVE AREAS (mm):*)

m=5.5
Ae100=97.6
Ae110=94

(* DEFINE SCALE PARAMETER SHAPE FUNCTIONS AND CONSTANTS TO BE SOLVED
(Equations 128 and 129) *)

scaleparameter100=(AA*Cos[2*t]^2+BB*Sin[2*t]^2)

scaleparameter110=(AA*Cos[2*(t+Pi/4)]^2+BB*Sin[2*(t+Pi/4)]^2)

(* CHARACTERISTIC STRENGTH INTEGRATIONS RELATING SCALE PARAMETER FUNCTION
TO MEASURED CHARACTERISTIC STRENGTH BY AREA INTEGRATION ( Equations 130 and
131). INPUT CHARACTERISTIC STRENGTHS ARE NORMALIZED TO THAT OF THE <100> FOR
COMPUTATIONAL EFFICIENCY. *)

EQ100=2*NIntegrate[Ae100/Pi*(Cos[t]^2/scaleparameter100)^m,{t,0,Pi/2}]

EQ110=2*NIntegrate[Ae110/Pi*(0.6298*Cos[t]^2/scaleparameter110)^m,{t,0,Pi/2}]

FindRoot[Print[InputForm[{AA,BB,EQ100,EQ110}]];{1.0==EQ100,1.0==EQ110},{
AA,{3.4,3.8}},{BB,{0.7,1}},MaxIterations->150]

`DigitsOfAccuracy==Accuracy[%]
```

¹¹ Mathematica 3.0, Wolfram Research, Champaign, Illinois.

APPENDIX F: CODE FOR ESTIMATION OF THE CHARACTERISTIC STRENGTH OF ISOTROPIC DISK TEST SPECIMENS

The characteristic strength of isotropic disk test specimens (e.g. tungsten carbide) can be determined from uniaxial test data and the following program, which is written in the Mathematica® Programming Language¹². The Mathematica code has two main parts: that solving for the scale parameters associated with various failure criteria and that determining the characteristic strength of the disk test specimens.

The material is assumed to be isotropic. The disk test specimen is assumed to be subjected to a uniform pressure within a circular support of diameter less than or equal to that of the disk periphery. Any plate radius, thickness and pressure can be specified, however, the solution assumes that the plate is thin and the displacements small. The code was used to calculate the characteristic strengths of the tungsten carbide specimens and the NiAl specimens with the assumptions of elastic and strength isotropy.

ESTIMATION OF THE CHARACTERISTIC STRENGTH OF ISOTROPIC DISK TEST SPECIMENS

(* ESTIMATION OF SCALE PARAMETER *)

(* INPUT <110> 4-POINT FLEXURE DATA (MPa):*)

m=5.5;
CS=689;

(* MEAN EFFECTIVE AREA OF THE TESTED BEAMS (mm):*)

AePIA = 94;

(* STRESS INTENSITY FACTOR COEFFICIENTS:*)

Y1=1.365;
Y2= 1.241;

(* TRIGONOMETRIC FUNCTION FOR UNIT CIRCLE INTEGRATION:*)

¹² Mathematica 3.0, Wolfram Research, Champaign, Illinois.

```

fthetaPIA=1;
fthetanormal=Cos[t]^2;
fthetacoplanar=(Cos[t]^4+0.25*Y2^2/Y1^2*Sin[2*t]^2)^0.5;
fthetaNoncop=(
    Cos[t]^8+1.5*Y2^2/Y1^2*Cos[t]^4*Sin[2*t]^2+
    Y2^4/Y1^4/16*Sin[2*t]^4)^0.25;
fthetaHoop=
    8^(-0.5)*Y2^3*
    Sin[2*t]^3*(
        2*Cos[t]^2+6*(Cos[t]^4+2*Sin[2*t]^2*Y2^2/Y1^2)^0.5)/(
        Y1^2*Cos[t]^4+3*Y2^2*Sin[2*t]^2-
        Y1*Cos[t]^2*(Y1^2*Cos[t]^4+2*Y2^2*Sin[2*t]^2)^0.5)^1.5;

```

(* ESTIMATION OF SCALE PARAMETER *)

```

SPpia=CS*(NIntegrate[AePIA/Pi*(fthetaPIA)^m,{t,0,Pi},Method->Trapezoidal])^(
    1/m)
SPnormal=CS*(
    NIntegrate[AePIA/Pi*(fthetanormal)^m,{t,0,Pi},Method->Trapezoidal])^(
    1/m)
SPcoplanar=
    CS*(NIntegrate[AePIA/Pi*(fthetacoplanar)^m,{t,0,Pi},Method->Trapezoidal])^(
    1/m)
SPnoncop=CS*(
    NIntegrate[AePIA/Pi*(fthetaNoncop)^m,{t,0,Pi},Method->Trapezoidal])^(
    1/m)
SPhoop=CS*(
    2*NIntegrate[AePIA/Pi*(fthetaHoop)^m,{t,0.0001,Pi/2},
    Method->Trapezoidal])^(1/m)

```

DigitsOfAccuracy=Accuracy[%]

(* ESTIMATION OF CHARACTERISTIC STRENGTH OF DISK TEST SPECIMENS *)

(* MEAN DISK DIMENSIONS (mm): *)

```

Rs=11.592;
Rd=25.229/2;
v=0.31;
h = 1.495;

```

(* DISK STRESSES WITH LATERAL CORRECTION TERM OF TIMOSHENKO: *)
 (* TO IGNORE CORRECTION TERM, SET THICKNESS h TO 0: *)

```

Sig1=(1-v)*Rs^2/Rd^2+2*(1+v)-(1+3*v)*r^2/Rs^2+2/3*h^2/Rs^2*(3+v)/(1-v);
Sig2=(1-v)*Rs^2/Rd^2+2*(1+v)-(3+v)*r^2/Rs^2+2/3*h^2/Rs^2*(3+v)/(1-v);
SigMax=(1-v)*Rs^2/Rd^2+2*(1+v)+2/3*h^2/Rs^2*(3+v)/(1-v);

```

(* CALCULATION OF CHARACTERISTIC STRENGTH OF DISK (MPa): *)

(* MAXIMUM PRINCIPAL STRESS: *)

```

f1pia=1;
f2pia=1;

cspresdiskmaxprin=
  SPpia*(2*NIntegrate[
    NIntegrate[r*((Sig1*f1pia/SigMax)^m),{t,0,Pi}],{r,0,Rs}])^(-1/m)

(* PIA: *)

cspresdiskpia=
  SPpia*(2*NIntegrate[
    r*Pi*((Sig1*f1pia/SigMax)^m+(Sig2*f2pia/SigMax)^m),{r,0,Rs}])^(-1/
    m)

(* NORMAL STRESS CRITERION: *)

f1nor=Cos[t]^2;
f2nor=Sin[t]^2;

cspresdisknormal=
  SPnormal*(
    2*NIntegrate[
      NIntegrate[r*((Sig1*f1nor/SigMax+Sig2*f2nor/SigMax)^m),{t,0,Pi}],{
        r,0,Rs}])^(-1/m)

(* COPLANAR ENERGY RELEASE RATE: *)

f1nor=Cos[t]^2;
f2nor=Sin[t]^2;

cspresdiskcoplanar=
  SPcoplanar*(
    2*NIntegrate[
      NIntegrate[
        r*(((Sig1*Cos[t]^2+Sig2*Sin[t]^2)^2+
          Y2^2/Y1^2/4*(Sig1-Sig2)^2*Sin[2*t]^2)^0.5)/
          SigMax)^m,{t,0,Pi}],{r,0,Rs}])^(-1/m)

(* NONCOPLANAR ENERGY RELEASE RATE: *)

SigN=Sig1*Cos[t]^2+Sig2*Sin[t]^2;
SigS=(Sig1-Sig2)/2*Sin[2*t];

cspresdisknoncop=
  SPnoncop*(
    2*NIntegrate[
      NIntegrate[
        r*((SigN^4+6*Y2^2/Y1^2*SigN^2*SigS^2+Y2^4/Y1^4*SigS^4)^0.25/
          SigMax)^m,{t,0,Pi}],{r,0,Rs}])^(-1/m)

```

(* HOOP STRESS FACTOR: *)

```

cspresdisHoop=
  SPhoop*(2*
    NIntegrate[
      NIntegrate[
        2*r*((8^0.5*(2*SigN+6*(SigN^2+8*Y2^2/Y1^2*SigS^2)^0.5)*Y2^3*
          SigS^3/(
            Y1^2*SigN^2+12*Y2^2*SigS^2-
            Y1*SigN*(
              Y1^2*SigN^2+8*Y2^2*SigS^2)^0.5)^1.5)/
          SigMax)^m,{t,0.005,0.99*Pi/2}],{r,0.05,Rs}]]^(-1/m)

```

APPENDIX G: CODE FOR ESTIMATION OF THE CHARACTERISTIC STRENGTH OF ELASTICALLY ANISOTROPIC DISK TEST SPECIMENS

The characteristic strength of disk test specimens exhibiting elastic anisotropy and strength isotropy can be determined from uniaxial test data and the following program, which is written in the Mathematica® Programming Language¹³. The Mathematica code has two main parts: that solving for the scale parameters associated with various failure criteria and that determining the characteristic strength of the disk test specimens.

The disk test specimen is subjected to a uniform pressure within a circular support of diameter less than or equal to that of the disk periphery. Any plate radius, thickness and pressure can be specified, however, the solution assumes that the plate is thin and the displacements small. The code was used to calculate the characteristic strengths of the NiAl specimens with the assumptions of elastic anisotropy and strength isotropy (i.e. section 5.3.2).

ESTIMATION OF THE CHARACTERISTIC STRENGTH OF DISK TEST SPECIMENS **ASSUMING ELASTIC ANISOTROPY AND STRENGTH ISOTROPY**

(* ESTIMATION OF SCALE PARAMETER *)

(* INPUT <110> 4-POINT FLEXURE DATA (MPa):*)

m=5.5;
CS=689;

(* MEAN EFFECTIVE AREA OF THE TESTED BEAMS:*)

AePIA = 94;

(* STRESS INTENSITY FACTOR COEFFICIENTS:*)

Y1=1.365;
Y2=1.241;

(* TRIGONOMETRIC FUNCTION FOR UNIT CIRCLE INTEGRATION:*)

fthetaPIA=1;
fthetanormal=Cos[t]^2;
fthetacoplanar=(Cos[t]^4+0.25*Y2^2/Y1^2*Sin[2*t]^2)^0.5;

¹³ Mathematica 3.0, Wolfram Research, Champaign, Illinois.

```

fthetaNoncop=(
  Cos[t]^8+1.5*Y2^2/Y1^2*Cos[t]^4*Sin[2*t]^2+
  Y2^4/Y1^4/16*Sin[2*t]^4)^0.25;

fthetaHoop=
  8^(-0.5)*Y2^3*
  Sin[2*t]^3*(
    2*Cos[t]^2+6*(Cos[t]^4+2*Sin[2*t]^2*Y2^2/Y1^2)^0.5)/(
    Y1^2*Cos[t]^4+3*Y2^2*Sin[2*t]^2-
    Y1*Cos[t]^2*(Y1^2*Cos[t]^4+2*Y2^2*Sin[2*t]^2)^0.5)^1.5;

```

(* SCALE PARAMETER ESTIMATION *)

```

SPpia=CS*(NIntegrate[AePIA/Pi*(fthetaPIA)^m,{t,0,Pi},Method->Trapezoidal])^(
  1/m)
SPnor=CS*(
  NIntegrate[AePIA/Pi*(fthetanormal)^m,{t,0,Pi},Method->Trapezoidal])^(
  1/m)
SPcoplanar=
  CS*(NIntegrate[AePIA/Pi*(fthetacoplanar)^m,{t,0,Pi},Method->Trapezoidal])^(
  1/m)
SPnoncop=CS*(
  NIntegrate[AePIA/Pi*(fthetaNoncop)^m,{t,0,Pi},Method->Trapezoidal])^(
  1/m)
SPhoop=CS*(
  2*NIntegrate[AePIA/Pi*(fthetaHoop)^m,{t,0.0001,Pi/2},
  Method->Trapezoidal])^(1/m)

```

(* ESTIMATION OF CHARACTERISTIC STRENGTH OF DISK TEST SPECIMENS *)

(* DISK DIMENSIONS *)

```

Rs=11.592;
Rd=25.229/2;
v=0.31;
h = 1.495;

```

(* DISK STRESSES FROM OKUBU'S APPROXIMATE SOLUTION*)

```

S11=1.0428*10^-5;
S22=1.0428*10^-5;
S12=-0.421*10^-5;
S44=0.892*10^-5;
b11=S22/(S11*S22-S12^2);
b22=S11/(S11*S22-S12^2);
b12=-S12/(S11*S22-S12^2);
b66=1/S44;
(* Plate stiffness in Okubu's Notation: *)
D1=h^3*S22/(12*(S11*S22-S12^2));
D2=h^3*(-S12)/(12*(S11*S22-S12^2));
D3=h^3*S11/(12*(S11*S22-S12^2));
D4=h^3/(6*S44);
DD=(3*D1+2*D2+2*D4+3*D3)/8;

```



```

k=(7*D1+10*D2+6*D4+7*D3)/(2*(D1+2*D2+D3));
x=(r^2/(1+Tan[t]^2))^0.5;
y=x*Tan[t];
a=Rs;
(* Cartesian Strains: *)
e11=h/2*(2*a^2*(k+1)-12*x^2-4*y^2)/(64*DD);
e22=h/2*(2*a^2*(k+1)-12*y^2-4*x^2)/(64*DD);
e6=-h*x*y/(8*DD);
(* Cartesian Stress: *)
Sig11=b11*e11+b12*e22;
Sig22=b12*e11+b22*e22;
Sig12=b66*e6;
(* Principal Stress: *)
Sig2=Sig11*cos[t]^2+Sig22*sin[t]^2+Sig12*sin[2*t];
Sig1=Sig22*cos[t]^2+Sig11*sin[t]^2-Sig12*sin[2*t];
Shear=(Sig22-Sig11)*sin[t]*cos[t]+Sig12*cos[2*t]
SigMax=h*a^2*(k+1)/(64*DD)*(b11+b12);
(* Normal and Shear Stresses: *)
SigN=Sig1*cos[t1]^2+Sig2*sin[t1]^2;
SigS=(Sig1-Sig2)/2*sin[2*t1];

(* CALCULATION OF CHARACTERISTIC STRENGTH OF DISK (MPa): *)

(* MAXIMUM PRINCIPAL STRESS: *)

f1pia=1;
f2pia=1;

cspressdiskMP=(
  NIntegrate[
    NIntegrate[r*((Sig1*f1pia/(SPpia*SigMax))^m),{r,0,Rs}},{t,0,
      2*Pi}]]^(-1/m)

cspressdiskpia=(
  NIntegrate[
    NIntegrate[
      r*((Sig1*f1pia/(SPpia*SigMax))^
        m+(Sig2*f2pia/(SPpia*SigMax))^m),{r,0,Rs}},{t,0,
      2*Pi}]]^(-1/m)

(* NORMAL STRESS CRITERION: *)

f1nor=Cos[t1]^2;
f2nor=Sin[t1]^2;

cspressdisknormal=(
  NIntegrate[
    8*NIntegrate[
      NIntegrate[
        r/Pi*((Sig1*f1nor+Sig2*f2nor)/(SPnor*SigMax))^m,{r,0,Rs}},{t,
        0,Pi/4}},{t1,0,Pi}]]^(-1/m)

(*COPLANAR ENERGY RELEASE RATE: *)

```

```

cspresdiskcoplanar=(
  NIntegrate[
    8*NIntegrate[
      NIntegrate[
        r/Pi*(((Sig1*Cos[t1]^2+Sig2*Sin[t1]^2)^2+
          Y2^2/Y1^2/4*(Sig1-Sig2)^2*
            Sin[2*t1]^2)^0.5)/(SPcoplanar*SigMax))^
        m,{r,0,Rs}},{t,0,Pi/4}},{t1,0,Pi}]]^(-1/m)

```

(* NONCOPLANAR ENERGY RELEASE RATE: *)

```

cspresdisknoncop=(
  NIntegrate[
    8*NIntegrate[
      NIntegrate[
        r/Pi*(((SigN^4+6*Y2^2/Y1^2*SigN^2*SigS^2+
          Y2^4/Y1^4*SigS^4)^0.25)/(SPnoncop*SigMax))^
        m,{r,0,Rs}},{t,0,Pi/4}},{t1,0,Pi}]]^(-1/m)

```

(* HOOP STRESS FACTOR: *)

```

cspresdiskHoop=(
  NIntegrate[
    2*8*NIntegrate[
      NIntegrate[
        r/Pi*((8^0.5*(2*SigN+6*(SigN^2+8*Y2^2/Y1^2*SigS^2)^0.5)*Y2^3*
          SigS^3/(
            Y1^2*SigN^2+12*Y2^2*SigS^2-
              Y1*SigN*(
                Y1^2*SigN^2+8*Y2^2*SigS^2)^0.5)^1.5)/((
                SPhoop*SigMax))^m,{r,0.04,Rs}},{t,0,Pi/4}},{t1,0.005,
                0.998*Pi/2}]]^(-1/m)

```

```

time = TimeUsed[]/60
memor = MemoryInUse[]

```

APPENDIX H: CODE FOR ESTIMATION OF THE CHARACTERISTIC STRENGTH OF ANISOTROPIC DISK TEST SPECIMENS

The characteristic strength of disk test specimens exhibiting elastic and strength anisotropy can be determined from uniaxial test data and the following program, which is written in the Mathematica® Programming Language¹⁴. The Mathematica code has two main parts: that calculating stresses at any Cartesian location and that determining the characteristic strength of the disk test specimens. The scale parameter constants as estimated from the code in Appendix E are used as input to this code.

The disk test specimen is subjected to a uniform pressure within a circular support of diameter less than or equal to that of the disk periphery. Any plate radius, thickness and pressure can be specified, however, the solution assumes that the plate is thin and the displacements small. The code was used to calculate the characteristic strengths of the NiAl specimens with the assumptions of elastic and strength anisotropy (i.e. section 5.3.3).

ESTIMATION OF THE CHARACTERISTIC STRENGTH OF DISK TEST SPECIMENS **ASSUMING ELASTIC AND STRENGTH ANISOTROPY**

(* ESTIMATION OF SCALE PARAMETER *)

(* WEIBULL MODULUS *)
m=5.5

(*STRESS INTENSITY FACTOR COEFFICIENTS:*)

Y1=(Pi)^0.5
Y2=(Pi)^0.5

(* DISK DIMENSIONS *)

Rs=11.592
Rd=25.229/2
v=0.31
h = 1.495

(* DISK STRESSES FROM OKUBU'S APPROXIMATE SOLUTION*)

S11=1.0428*10^-5;

¹⁴ Mathematica 3.0, Wolfram Research, Champaign, Illinois.

```

S22=1.0428*10^-5;
S12=-0.421*10^-5;
S44=0.892*10^-5;
b11=S22/(S11*S22-S12^2);
b22=S11/(S11*S22-S12^2);
b12=-S12/(S11*S22-S12^2);
b66=1/S44;
(* Plate stiffness in Okubu's Notation: *)
D1=h^3*S22/(12*(S11*S22-S12^2));
D2=h^3*(-S12)/(12*(S11*S22-S12^2));
D3=h^3*S11/(12*(S11*S22-S12^2));
D4=h^3/(6*S44);
DD=(3*D1+2*D2+2*D4+3*D3)/8;
k=(7*D1+10*D2+6*D4+7*D3)/(2*(D1+2*D2+D3));
x=(r^2/(1+Tan[t]^2))^0.5;
y=x*Tan[t];
a=Rs;
(* Cartesian Strains *)
e11=h/2*(2*a^2*(k+1)-12*x^2-4*y^2)/(64*DD);
e22=h/2*(2*a^2*(k+1)-12*y^2-4*x^2)/(64*DD);
e6=-h*x*y/(8*DD);
(* Cartesian Stresses *)
Sig11=b11*e11+b12*e22;
Sig22=b12*e11+b22*e22;
Sig12=b66*e6;
Sig2=Sig11*cos[t]^2+Sig22*sin[t]^2+Sig12*sin[2*t];
Sig1=Sig22*cos[t]^2+Sig11*sin[t]^2-Sig12*sin[2*t];
SigMax=h*a^2*(k+1)/(64*DD)*(b11+b12);

(* SCALE PARAMETER FUNCTION FOR PIA AND MAX PRINCIPAL FAILURE CRITERION *)

SPpia1=2516*cos[2*t]^2+1574*sin[2*t]^2
SPpia2=2516*cos[2*t]^2+1574*sin[2*t]^2
f1pia=1
f2pia=1

(* ESTIMATION OF CHARACTERISTIC STRENGTH BY MAX PRINCIPAL CRITERION *)
cspressdiskmaxprin=(
  NIntegrate[
    NIntegrate[r*((Sig1*f1pia/(SPpia1*SigMax))^m),{r,0,Rs}],{t,0,
      2*Pi}]]^(-1/m)

(* ESTIMATION OF CHARACTERISTIC STRENGTH BY PIA PRINCIPAL CRITERION *)
cspressdiskpia=(
  NIntegrate[
    NIntegrate[
      r*((Sig1*f1pia/(SPpia1*SigMax))^m+(Sig2*f2pia/(SPpia2*SigMax))^m),{
        r,0,Rs}],{t,0,2*Pi}]]^(-1/m)

(* SCALE PARAMETER FUNCTION FOR NORMAL STRESS CRITERION *)

```

```

f1nor=Cos[t1]^2
f2nor=Sin[t1]^2
t2=t+t1
SPnor=4038*Cos[2*t2]^2+976*Sin[2*t2]^2

(* ESTIMATION OF CHARACTERISTIC STRENGTH BY NORMAL STRESS CRITERION *)

cspressdisknormal=(
  NIntegrate[
    8*NIntegrate[
      NIntegrate[
        r/Pi*((Sig1*f1nor+Sig2*f2nor)/(SPnor*SigMax))^m,{r,0,Rs}],{t,0,
        Pi/4}],{t1,0,Pi}]]^(-1/m)

```

REPORT DOCUMENTATION PAGE			Form Approved OMB No. 0704-0188	
Public reporting burden for this collection of information is estimated to average 1 hour per response, including the time for reviewing instructions, searching existing data sources, gathering and maintaining the data needed, and completing and reviewing the collection of information. Send comments regarding this burden estimate or any other aspect of this collection of information, including suggestions for reducing this burden, to Washington Headquarters Services, Directorate for Information Operations and Reports, 1215 Jefferson Davis Highway, Suite 1204, Arlington, VA 22202-4302, and to the Office of Management and Budget, Paperwork Reduction Project (0704-0188), Washington, DC 20503.				
1. AGENCY USE ONLY (Leave blank)	2. REPORT DATE February 2002	3. REPORT TYPE AND DATES COVERED Technical Memorandum		
4. TITLE AND SUBTITLE Generalized Reliability Methodology Applied to Brittle Anisotropic Single Crystals		5. FUNDING NUMBERS WU-708-31-13-00		
6. AUTHOR(S) Jonathan A. Salem				
7. PERFORMING ORGANIZATION NAME(S) AND ADDRESS(ES) National Aeronautics and Space Administration John H. Glenn Research Center at Lewis Field Cleveland, Ohio 44135-3191		8. PERFORMING ORGANIZATION REPORT NUMBER E-12486		
9. SPONSORING/MONITORING AGENCY NAME(S) AND ADDRESS(ES) National Aeronautics and Space Administration Washington, DC 20546-0001		10. SPONSORING/MONITORING AGENCY REPORT NUMBER NASA TM-2002-210519		
11. SUPPLEMENTARY NOTES This report was submitted as a dissertation in partial fulfillment of the requirements for the degree Doctor of Philosophy to University of Washington, Washington, Seattle, Washington, 1999. Responsible person, Jonathan A. Salem, organization code 5920, 216-433-3313.				
12a. DISTRIBUTION/AVAILABILITY STATEMENT Unclassified - Unlimited Subject Categories: 38 and 39 Available electronically at http://gltrs.grc.nasa.gov/GLTRS This publication is available from the NASA Center for AeroSpace Information, 301-621-0390.		12b. DISTRIBUTION CODE		
13. ABSTRACT (Maximum 200 words) A generalized reliability model was developed for use in the design of structural components made from brittle, homogeneous anisotropic materials such as single crystals. The model is based on the Weibull distribution and incorporates a variable strength distribution and any equivalent stress failure criteria. In addition to the reliability model, an energy based failure criterion for elastically anisotropic materials was formulated. The model is different from typical Weibull-based models in that it accounts for strength anisotropy arising from fracture toughness anisotropy and thereby allows for strength and reliability predictions of brittle, anisotropic single crystals subjected to multiaxial stresses. The model is also applicable to elastically isotropic materials exhibiting strength anisotropy due to an anisotropic distribution of flaws. In order to develop and experimentally verify the model, the uniaxial and biaxial strengths of a single crystal nickel aluminide were measured. The uniaxial strengths of the <100> and <110> crystal directions were measured in three and four-point flexure. The biaxial strength was measured by subjecting <100> plates to a uniform pressure in a test apparatus that was developed and experimentally verified. The biaxial strengths of the single crystal plates were estimated by extending and verifying the displacement solution for a circular, anisotropic plate to the case of a variable radius and thickness. The best correlation between the experimental strength data and the model predictions occurred when an anisotropic stress analysis was combined with the normal stress criterion and the strength parameters associated with the <110> crystal direction.				
14. SUBJECT TERMS Flexural strength; Weibull modulus; Weibull density function; Reliability analysis; Single crystals; Nickel aluminides; Anisotropic plates; Failure criteria; Tungsten carbides; Fractography; Fracture mechanics; Brittle materials; Component reliability; Biaxial stresses; Stress analysis; Fracture toughness			15. NUMBER OF PAGES 222	
			16. PRICE CODE	
17. SECURITY CLASSIFICATION OF REPORT Unclassified	18. SECURITY CLASSIFICATION OF THIS PAGE Unclassified	19. SECURITY CLASSIFICATION OF ABSTRACT Unclassified	20. LIMITATION OF ABSTRACT	